I would like to dedicate this thesis to my children Alexander and Sophia, my wife Oksana and my family for their support over the years.

UNIVERSITY OF BIRMINGHAM

University of Birmingham

MECHANICAL ENGINEERING FACULTY

Thermal Management and control of a Homogeneous Charge Compression Ignition (HCCI) Engine

by George Constandinides

A thesis submitted to

The University of Birmingham

For the degree of

DOCTOR OF PHILOSOPHY

The University of Birmingham

School of Engineering

October 2013

Abstract

Homogeneous Charge Compression Ignition (HCCI) is the process which a relatively homogeneous mixture of air and fuel auto ignites through compression. HCCI engines can have high thermodynamic cycle efficiencies, with low levels of emissions of nitrogen oxides (NOx) and particulate matter (PM). However due to the nature of the combustion the operating envelope is quite small compared to conventional internal combustion engines.

An efficient powertrain system centred on a supercharged HCCI (Homogeneous Charge Compression Ignition) engine with on-board thermal management was developed that extends the operating envelope of an HCCI engine. To achieve controlled auto-ignition across a wide range of engine conditions, a system for management of flow and temperature was installed at the air intake to enable the necessary regulation of temperatures and pressures at the inlet ports. The system includes a heat exchanger to heat the charge air, a supercharger to boost the charge air pressure, supercharger bypass and finally an intercooler, so that a wide range of combinations of pressures and temperatures can be achieved at the intake ports.

In order to facilitate this control, a complete simulation model of the thermal system for a pressure-boosted multi-cylinder HCCI engine was developed that investigates the physical behaviour of the HCCI test engine and auxiliary components and can easily be implemented for a forward predicting control strategy. This work presents a dynamic mass and enthalpy balance model running in real time for the air intake system of the multi-cylinder HCCI gasoline engine and auxiliary components. The model is capable to calculate heat flux, mass flow, pressure and gas temperature distribution for the whole engine thermal management system however it does not take into account the turbulent nature of flow especially where hot and cold gas mix.

Therefore an elaborate CFD model of the Thermal Management system has been compiled for evaluation of the computed flow field and analysis of the thermal system performance by the use of the CFD tool ANSYS CFX.

Furthermore utilising the Thermal Management System, the upper operating range was increased by using an intercooler and supercharging the inlet air. Special care had to be exerted while cooling the charge air as the appropriate amount of energy for auto-ignition had to be delivered to initiate HCCI combustion. Applying inlet air heating was regarded as to be one of the most popular ways of reducing the achieved load under HCCI combustion, however during the presented tests the impact of heating on the lowest achievable load seems to be somehow reduced. In order to expand the low HCCI boundary even further, the combined effect of heating and throttling of inlet air has been incorporated. By applying both of these techniques the lowest achievable load during HCCI combustion was increased by 0.25 (of NMEP) from the baseline at 1000rpm and by 0.5bar (of NMEP) from the baseline at 1500rpm. Unfortunately, this approach is accompanied with the penalty of higher fuel consumption.

Finally an HCCI control strategy has been proposed aiming to reduce emissions and in particular NOx and HC. It has been shown that by applying thermal management on both load regimes (the lowest and the highest) an improvement in both $NSNO_x$ and NSHC emissions was achieved.

Acknowledgments

The author gratefully acknowledge financial help of EPSRC, DTI and Jaguar Cars and would like to extend special thanks to all staff in The University of Birmingham and Jaguar Cars for their effort and support in this project.

Furthermore the author would also like to show his grateful appreciation to Professor Mirosław L. Wyszyński for his guidance and supervision during his PhD course. Furthermore I'd like to thank my friend and colleague Dr Jacek Misztal for his assistance during the experimental phase of this work. Dr Jonahan Hartland from Jaguar Cars is also greatly appreciated, for his guidance, help and support during the early development of this project.

Last, Technical support by Peter Thornton, Carl Hingley and Lee Gauntlett from The University of Birmingham was highly valuable and appreciated.

Nomenclature

List of Figures

List of Tables

Algebraic Symbols and Abbreviations Table

$\dot{m}$	: mass flow rate	[kg/s]
m	: mass in a finite volume	[kg]
m_{gas}	: mass of mixed charge air with exhaust gas (due to EGR)	[kg]
m_{air}	: mass of charge air avaiable for combustion	[kg]
p	: pressure	[N/m^2]
T	: temperature	[K]
R	: ideal gas constant for air	[J/kgK]
ρ	: density	[kg/m^3]
μ	: kinematic viscosity	[kg/ms]
v	: air velocity	[m/s]
q_v	: volumetric flow rate	[m^3/s]
u	: spesific internal energy	[J/kg]
h	: spesific enthalpy	[J/kgK]
c_v	: constant-volume specific heat	[J/kgK]
c_p	: constant-pressure specific heat	[J/kgK]
P	: Power	[J/s]
$\dot{U}$	: rate of change of internal energy of the system	[J/s]
$\dot{Q}$	: rate of change of heat transfer of the system	[J/s]
$\dot{W}$	: rate of work transfer out of the system	[J/s]
Q_{comb}	: heat available for combustion	[J]
Q_{lcv}	: lower calorific heat for petrol	[J/kg]
A	: area of a component	[m^2]
D	: throttle/cylinder bore diameter	[m]
S_{str}	: piston stroke	[m]
N	: engine speed	[RPM]
γ	: specific heat ratio	[-]
n_{vol}	: engine pumping efficiency (inlet and valve ports only)	[-]
n_{comb}	: combustion efficiency	[-]
rc	: compression ratio	[-]
AFR	: stochiometric air to fuel ratio	[-]
K	: loss coefficient	[-]
$K_{laminar}$	: laminar loss coefficient	[m^3]
$K_{turbulant}$	: turbulant loss coefficient	$[\frac{1}{m^2}]$
λ	: relative air to fuel ratio	[-]

BDC :Bottom Dead Centre

BDSCac :Blow Down Super-Charging by accumulation

BDSCpw :Blow Down Super-Charging by pressure wave

BP :Boost Pressure

BSCO :Brake Specific Carbon Monoxide Emission

BSFC :Brake Specific Fuel Consumption

BSHC :Brake Specific Hydrocarbons Emission

CAD :Crank Angle Degree

CAI :Compression Auto-Ignition

CCD :Combustion Chamber Deposits

CFD :Computational Fluid Dynamic

CHARGE : Compression Homogeneous Auto-ignition Reformed Gas Engine

CHASE :Controlled Homogeneous Auto-ignition Supercharged Engine

CI :Compression Ignition

CN :Cetane Number

CO :Carbon Monoxide

CO2 :Carbon Dioxide

COV :(of NMEP) Coefficient of Variations

CPS :Cam Profile Switch

CR :Compression Ratio

CTCV :Cylinder to Cylinder Variations

DI :Direct Injection

DME :Dimethyl Ether

DMS500 :Fast Particulate Spectrometer

EGR :Exhaust Gas Recirculation

EVC :Exhaust Valve Closing

EOI :End of injection before TDC combustion phase

FID :Flame Ionization Detector

FS :Full Scale

FSD :Full Scale Deflection

FSO :Full Scale Output

HC (UHC) :Hydrocarbons (Unburned Hydrocarbons)

HCCI :Homogeneous Charge Compression Ignition

HLL :High Load Limit

HTHR :High Temp Heat Release

HP :Heated Air Path

HP-H :Heated Air Path with Heating

IMEP :Indicated Mean Effective Pressure

IC :Internal Combustion

IVC :Inlet Valve Closing

IVO :Inlet Valve Opening

LLL :Low Load Limit

LTHR :Low Temperature Heat Release

MFB :Mass Fraction Burnt

$MFB_{10\%}$:10% of Mass Fraction Burnt

$MFB_{10\text{-}50\%}$:Duration of 10% to 50% of MFB

$MFB_{10\text{-}90\%}$:Duration of 10% to 90% of MFB

$MFB_{50\%}$:50% of Mass Fraction Burnt

$MFB_{50\text{-}90\%}$:Duration of 50% to 90% of MFB

$MFB_{90\%}$:90% of Mass Fraction Burnt

MON :Motor Octane Number

MRG :Methanol Reformed Gas

NA :Naturally Aspirated

NDIR :Non-Dispersive Infrared

NMEP :Nett Mean Effective Pressure

NOx :Nitric Oxides

NP :Normal Air Path

NP-C :Normal Air Path with Cooling

NVO :Negative Valve Overlap

^{o}aTDCc :Crank angle degrees after Top Dead Centre of combustion

^{o}bTDCc :Crank angle degrees before Top Dead Centre of combustion

OHC :Oxygenated Hydrocarbons

OI :Octane Index

PFI :Port Fuel Injection

PID :Proportional-Integral-Derivative controller

PM :Particulate Matter

PRF50 :Primary Reference Fuel (mixture of n-heptane and iso-octane)

PWM :Pulse-Width Modulation

REGR :Reformed Exhaust Gas Recirculation

RH :Relative Humidity

ROHR :Rate of Heat Release

RON :Research Octane Number

SACI :Spark Assisted Compression Ignition

SI :Spark Ignition

SI-CI :Spark Ignited Compression Ignition

SOF :Soluble Organic Fraction

TDC :Top Dead Centre

T.M. :Thermal Management

TR :Trapped Residuals

TWC :Three-Way Catalyst

List of Publications

1) Influence of Inlet Air Temperature on Gasoline HCCI Particulate Emissions

   Jacek Misztal, George Constandinides, Hongming Xu, Athanasios Tsolakis, Miroslaw L. Wyszynski, Philip Price, Richard Stone, Jun Qiao;

   Journal of Combustion Science and Technology, Volume 181, Issue 5 May 2009 , pages 695 – 70, DOI**:** 10.1080/00102200902851610

2) Modelling and Experimental Study of Thermal Management System for HCCI

   George Constandinides, Jacek Misztal, 10th International Conference on Engines & Vehicles, Engine Modelling for Management, Control and Diagnostics , SAE Technical Paper, 2011-24-0160

Chapter 1. Introduction

1.1 Introduction to HCCI and Thermal Management

During many years of HCCI research this new mode of combustion has been described by a variety of terms; Active Thermo-Atmosphere Combustion (ATAC), Activated Radicals Combustion (ARC) and Toyota Soken Combustion, to name a few. Finally, two names became widely accepted by the research community: Homogeneous Charge Compression Ignition (HCCI) and Compression Auto-Ignition (CAI). HCCI in essence brings the best of both SI and CI engine modes together. The homogeneous mixture (as in an SI engine) is compressed and auto-ignited (similarly to a CI engine). This allows achieving an efficiency close to the diesel engine efficiency, but a reduction in gaseous emissions can be met as well. It can also be said that the combustion process is related more closely to the ideal Otto Cycle because HCCI combustion is fast and violent. The combustion takes place due to the relative pressure and temperature in the chamber and the fuel mixture auto-ignition point. The definitive characteristic of HCCI is that ignition occurs at several places at a time which makes the air/fuel mixture burn spontaneously and homogeneously without flame propagation. Thus heterogeneous air/fuel mixtures are eliminated and Nitrogen oxide emissions (NO_x) are greatly reduced. The unburned hydrocarbons and carbon monoxide emissions are still high, due to lower peak temperatures, and must be treated with catalytic converters to meet emission regulations. Because HCCI operation involves such violent and rapid combustion, the disadvantage is that HCCI engines have high in cylinder peak pressures and high heat release rates. In addition because the fuel mixture autoignites it inherently lacks of an event directly triggering

combustion,. Thus the operational range and power output an engine can run in HCCI mode, without any means of control, is limited.

At The University of Birmingham successful attempts to implement the HCCI combustion on a four-stroke engine was performed. However quickly it became clear that the new combustion mode could not cover the full load/speed map of the modern passenger car engine. Therefore a mix of SI/HCCI or diesel/HCCI operation would be required in order to obtain the best engine performance. The number of factors limiting HCCI operation was quickly quantified. The limitation at the low load is mainly due to the lack of sufficient energy for autoignition (combustion peak temperature becomes too low). At high load a low dilution ratio leads to rapid and violent combustion (a very high rate of pressure rise).

1.2 Thermal Management Objectives and HCCI Control

Unlike a typical gasoline engine the charge is not ignited by spark, instead the homogeneous mixture is ignited when the appropriate conditions in the combustion chamber are reached (sufficient energy for autoignition). This makes the combustion process challenging for control because there is no well-defined combustion initiator that can be directly controlled. An engine can be designed so that the ignition conditions occur at a desirable timing, however limiting the engine operation range and power output only at a specific operating point. This approach could potentially work well in a REEV hybrid (range-extended electric vehicle) where the main drive is provided by the electric motors and the internal combustion engine is operated at a set design point either to provide power or supplement the power provided by the batteries. However these type of hybrid cars have higher manufacturing costs.

In normal vehicular applications an internal combustion engine is required to increase/decrease its speed, power and torque production to meet user demands. In

order to apply HCCI in such vehicles and fulfil the user/load demands, a control system needs to dynamically change the conditions that induce combustion and allow changing between SI/HCCI or CI/HCCI operation modes. Thus a complete control system must change either compression ratio, induced gas temperature and pressure, quantity and temperature of re-induced exhaust gas (EGR).

1.3 Jaguar V6 HCCI Engine

The multi-cylinder engine at The University of Birmingham is a prototype of a production engine modified to facilitate HCCI. This modification focussed mainly on the installation of the cam profile switching system on both inlet and exhaust cams. HCCI is achieved by deploying Negative Valve Overlap strategy (NVO). The engine is equipped with a thermal management system in order to control the inlet pressure and air temperature. A thermal management model was created in Simulink and run in parallel with the engine in order to validate and predict its operation point, however control of the engine remained a manual process. A secondary Simulink model has been used for control data acquisition and investigating the HCCI operation boundaries. This model was also used to explore effects of different parameters including inlet and exhaust valve timing (dilution ratio), inlet temperature, boost pressure, air to fuel ratio, exhaust throttling, hydrogen addition and others. The findings that are not related to this project such as spark assisted HCCI, split injection strategy, cylinder to cylinder variations and particulate matter emissions have been described by Dr. Jacek W. Misztal in his PhD thesis [1].

1.4 Thermal Management for HCCI

For the CHASE project (shown in Figure 3) the thermal system of the powertrain unit includes a supercharger, intercooler, intake manifold, engine, exhaust manifold,

fuel reformer and the after-treatment system. The heat flux in this thermal system (Figure 1) and the effect on the HCCI engine performance is quite complicated. Thus it is important to study the thermal energy distribution and plan/control the heat flux in an intelligent way to facilitate HCCI combustion and also to benefit of the after-treatment of exhaust gases.

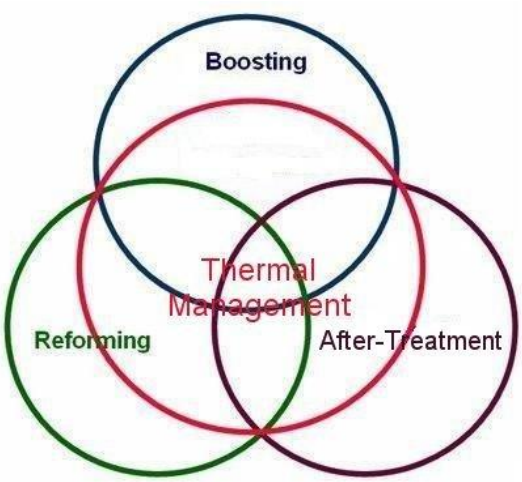

Figure 1: CHASE Thermal Management

1.5 Thermal Management Study and Control Strategy Implementation.

The heat exchange process in the system, was studied particularly the intercooling/supercharging system. The following were investigated:

a) How much energy is available from the coolant if it is used as an air-intake "inter-heater"?

b) How much temperature rise from the supercharger one can utilise while boosting? Excess energy can/will be rejected through the intercooler.

The heat-exchange process in the engine thermal management was examined in conjunction with the heat addition using the air heater and the heat exchanger. The thermal management control strategy leading to the best thermal efficiency of the system is proposed so that to use the thermal energy available in the supercharging /

intercooling / heat addition systems in an optimized way for the best thermal efficiency of the system.

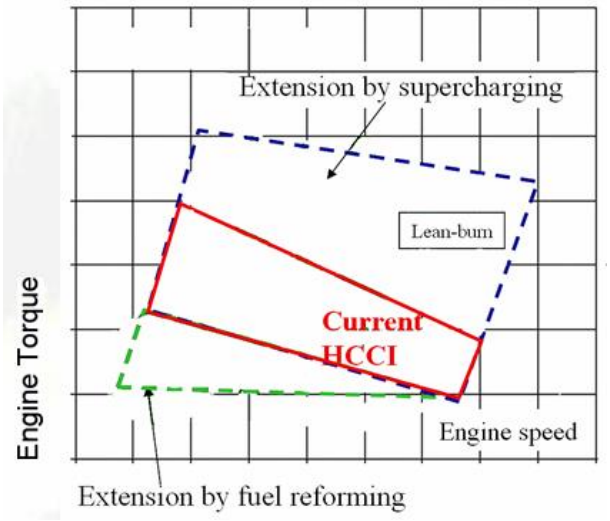

Figure 2: Proposal for expanding the HCCI Operational Envelope

HCCI Operational Envelope Extension by Supercharging

One of the major problems associated with HCCI combustion has been the relatively small operating envelope (speed/load map) as shown in Figure 2. Supercharging addresses the problem of the limited HCCI window by 3 aspects:

a) To achieve early exhaust valve closing for EGR trapping used in HCCI engines, the valve opening duration is reduced and the valve lift is lowered. Using this configuration at higher engine speeds, the intake air flow would be consequently restricted thus a cam profile switching mechanism for both intake and exhaust cams has been used to avoid engine breathing limitations. However in HCCI mode the upper boundary could be extended using forced induction, thus a supercharger would help reduce engine breathing problems.

b) At lower engine speeds, the combustion of HCCI can become very violent at higher loads. This problem is more prominent when the mixture is stoichiometric for obtaining higher IMEP near upper load boundary because there is less dilution

by reduced internal EGR. This situation may improve if lean operation is made possible by boosting.

c) It is known that HCCI cycle efficiency close to the CI engine cycle efficiency, but also offers reduction in gaseous emissions. However this combustion mode cannot cover the full load/speed map of the modern passenger car engine and a mix of SI/HCCI or diesel/HCCI operation would be required in order to obtain the best engine performance. It is advantageous to implement HCCI/SI dual combustion mode for boosted engines, as pressure charged SI engines usually have a relatively lower compression ratio in order to eliminate knock at full load, which results in lower fuel economy at low loads due to the reduced thermal efficiency.

HCCI Operational Envelope Extension by Fuel Reforming

Fuel reforming has been proven to be quite effective in reducing the auto-ignition temperature of hydrocarbon fuels (thus the control of HCCI combustion), using natural gas in the CHARGE project [2]. It has been shown that the reformed gas reduces the required charge temperature for auto-ignition (with a conventional engine compression ratio) by 40-70°C, depending on engine conditions. This makes the auto-ignition of charge relatively less dependent on the thermal factor, leading to reduced limitation to the HCCI operation window.

Exhaust Gas After-Treatment

After-treatment development with low temperature catalysis for HCCI engines has been widely recognized and is receiving significant attention. The development of exhaust gas after-treatment catalysis for HCCI engines is sustained in parallel with the development of the catalyst for fuel reforming because both catalytic processes require further investigation in:

1. Exhaust gas composition and temperature.
2. Surface chemical reactions.
3. Design of hardware in the same/close location(s), with possible combination of both in the same unit.

The targeted new after-treatment system combined with boosting is expected to achieve much improved HC and CO emission levels for the HCCI engines.

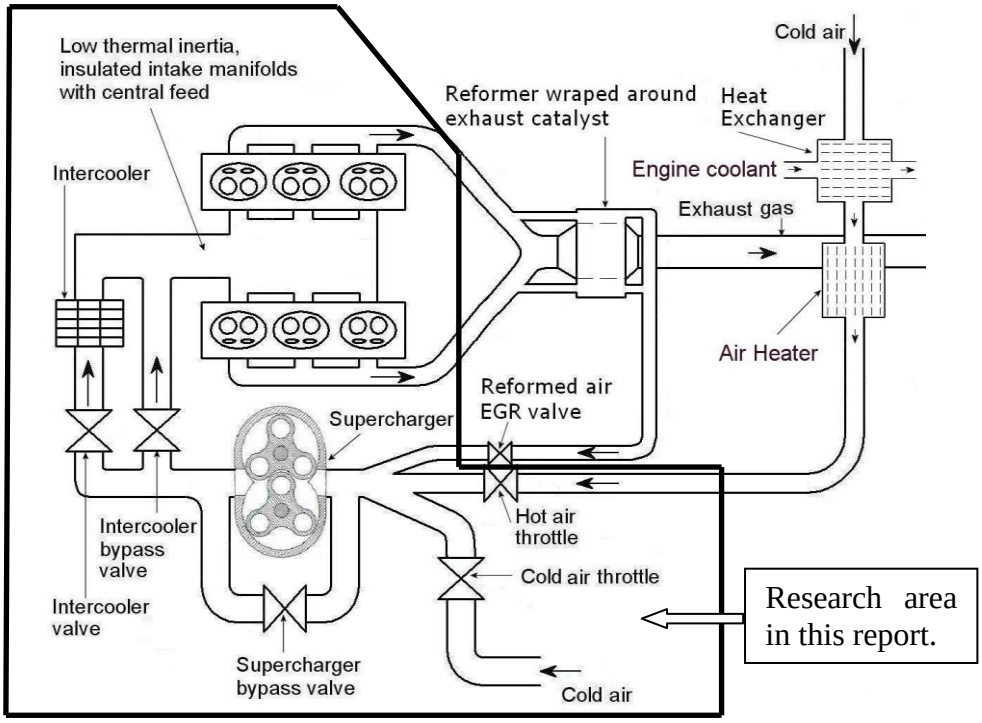

Figure 3: CHASE thermal system arrangement and research area

1.6 Objectives and Approaches

The aim of the CHASE (Controlled Homogeneous Auto-ignition Supercharged Engine) project was to develop a clean and efficient powertrain system based on supercharged HCCI with on board fuel reforming and thermal management. The main objective of multi-cylinder HCCI operation was to confirm findings by Yap et al. [2] previously reported on single cylinder engines and to extend the knowledge towards solutions closer to those realistically implemented in the production engine. One of the problems attributed to multi-cylinder HCCI operation has been cylinder-to-

cylinder variations which have made the operating envelope smaller. Cylinder-to-cylinder variation refers to the combustion differences in specific cylinders e.g. one of the cylinders approaching the misfire limit earlier than others. Additionally, when the upper boundary is investigated, one cylinder will approach the knocking limit earlier than others as well. These two factors restrict the operating envelope for the whole engine. Another area of concern is that of HCCI sensitivity to ambient conditions (i.e. humidity and temperature) which affect the lowest and highest achievable loads. Yap et al. [2] conducted single cylinder engine tests at The University of Birmingham however was no equipment for charge air preparation. Variations in inlet air temperature was up to 15ºC and variations in the relative humidity could reach 30%. These two parameters affect combustion air properties, but also the heat transfer between the engine and the environment.

The aim of the thermal management system was the means for the CHASE project to achieve its target. The CHASE project extends the work by Yap et al. [2] from the CHARGE project by:

a) defining the operating map of Naturally Aspirated HCCI in a multi-cylinder Jaguar V6 engine. The thermal management system helped stabilise ambient conditions in order to have repetitive HCCI test results.
b) investigate the possibility of expanding high load limit by supercharging.
c) investigate the possibility of expanding high load limit by combining supercharging with thermal management.
d) investigating the possibility of expanding low load limit by thermal management. Expansion of the low load limit has been a combination of more than one factor, including: heating of inlet air, increasing air-to-fuel ratio, and the throttling effect of the thermal management system.

e) emissions measurements, including HCCI PM emissions.

1.7 Thesis Outline

The research presented in this thesis has been performed at The University of Birmingham in collaboration with Jaguar Cars Ltd. and EPSRC under the CHASE (Controlled Homogeneous Auto-ignition Supercharged Engine) project. The aim of the CHASE project was to develop a clean and efficient powertrain system based on a supercharged multi-cylinder HCCI engine with on board fuel reforming and thermal management.

The aim of the thermal management system was the means for the CHASE project to achieve its target as outlined in Section 1.6. The extension of the multi-cylinder HCCI operating range has been investigated based on the combination of boosted operation, and total thermal management.

In terms of providing control a mathematical model describing the Thermal Management system installed on a multi-cylinder HCCI engine at The University of Birmingham has been developed and verified over the HCCI engine extended operational envelope. The mathematical model can run in real time and can be implemented for a forward predicting control strategy. This model can be used for predicting the multi-cylinder HCCI engine load and operating conditions within the tested HCCI region.

Subcomponents of the mathematical model were gradually developed and matured towards the current implementation of the Thermal Management system currently installed on a multi-cylinder HCCI engine at The University of Birmingham.

However the zero dimensional model does not take into account the turbulent nature of flow especially where hot and cold gas mix. Therefore an elaborate CFD model of the Thermal Management system has been compiled for evaluation of the

computed flow field and thermal system performance. This allowed a deeper understanding of the behaviour and performance of the Thermal Management system. This study was divided into three phases:

a) Mathematical model development of conceptual design.
b) Experimental multi-cylinder engine tests comprising the Thermal Management system. This system enabled stabilisation of ambient conditions in order to have repetitive HCCI test results and control of the air intake of the engine operating in HCCI mode and extension of its operating envelope. With this phase the mathematical model is also validated with experimental data.
c) CFD investigation of thermal management system and the system performance.

The thesis is divided into seven chapters each covering a different aspect of research. A quick overview of the contents of each chapter is provided below:

Chapter 1 – Introduction – Introduction to HCCI , Thermal management Objectives and HCCI Control

Chapter 2 – Literature Review – The publications of other researchers' work have been studied prior the author's own research. Special interest has been placed on parameters affecting HCCI performance, thermal conditions suitable for HCCI operation, expansion of an HCCI engine operating window and gaseous emissions. A brief extract of the most important publications has been described in this chapter.

Chapter 3 – Engine Thermal Management System – Description of design rationale behind the thermal management system, design calculations, operational objectives and operating strategy were described. A detailed description of the research engine as well as auxiliary equipment has been provided. Procedures used for data processing were quoted and explained. A report of uncertainties in recorded

data was also provided. A detailed description of the thermal management engine model is presented together with the various mathematical relationships for the components used within the HCCI test-rig. Assumptions and programming routines were quoted and explained. A comprehensive description of the Ricardo Wave model was provided along with its validation with experimental results and its limitations.

Chapter 4 – Experimental Resutls – The naturally aspirated (NA) HCCI window for the research engine was identified, including discussion of problems related to NA HCCI window definition. Expansion of high load limit for HCCI operation upwards by means of boosting was studied. It included the effect of different parameters such as inlet air temperature and air to fuel ratio. An attempt to expand low load limit of HCCI operation was made by a combination of throttling and thermal management. The effect of inlet air temperature as well as injection strategies on HCCI emissions were studied.

Chapter 5 – CFD Investigation – CFD was used to study the computed flow field, thermal system performance, thermal energy distribution and heat flux flow in the proposed T.M. system. This was required as components of the T.M. system did not perform as expected.

Chapter 6 – Analysis - Thermal Management System as a Tool for HCCI Window Expansion and Emission Comparison – Expansion of load limit for HCCI operation and the impact of inlet air heating and cooling on the engine operation with set valve timing was studied. During the work on HCCI boundary expansion, gas emissions were carefully studied as emission reduction was one of the reasons for introducing the HCCI combustion.

Chapter 7 – Conclusions – Conclusions from all work were summarised. Future work recommendations were also outlined.

Chapter 2. Literature Review

Over the years there has been a significant number of discussions regarding various environmental situations such as “Green House Effect” and “Global Warming” and suggest links to increasing exhaust gases originating from the transport sector. As a result research into emissions reduction, alternative power systems and energy conservation has intensified. Automobiles being one of the major sources of energy consumption and urban emissions, automobile manufacturers are under scrutiny and continuous pressure to improve efficiency and reduce exhaust emissions levels. The fundamental reason of worldwide HCCI research is meeting the increasingly stringent emission legislation for vehicles; one such example is the Euro emission standards presented in Table 1. Note that up and until Euro 5, there were no PM limits for gasoline powered vehicles.

Tier	Date	CO	HC	HC+NOx	NOx	PM
Compression Ignition (Diesel)						
Euro 1†	1992.07	2.72 (3.16)	-	0.97 (1.13)	-	0.14 (0.18)
Euro 2, IDI	1996.01	1.0	-	0.7	-	0.08
Euro 2, DI	1996.01[a]	1.0	-	0.9	-	0.10
Euro 3	2000.01	0.64	-	0.56	0.50	0.05
Euro 4	2005.01	0.50	-	0.30	0.25	0.025
Euro 5	2009.09[b]	0.50	-	0.23	0.18	0.005[e]
Euro 6	2014.09	0.50	-	0.17	0.08	0.005[e]
Positive Ignition (Gasoline)						
Euro 1†	1992.07	2.72 (3.16)	-	0.97 (1.13)	-	-
Euro 2	1996.01	2.2	-	0.5	-	-
Euro 3	2000.01	2.30	0.20	-	0.15	-
Euro 4	2005.01	1.0	0.10	-	0.08	-
Euro 5	2009.09[b]	1.0	0.10[c]	-	0.06	0.005[d,e]
Euro 6	2014.09	1.0	0.10[c]	-	0.06	0.005[d,e]

* At the Euro 1..4 stages, passenger vehicles > 2,500 kg were type approved as Category N1 vehicles
† Values in brackets are conformity of production (COP) limits
a - until 1999.09.30 (after that date DI engines must meet the IDI limits)
b - 2011.01 for all models
c - and NMHC = 0.068 g/km
d - applicable only to vehicles using DI engines
e - 0.0045 g/km using the PMP measurement procedure

Table 1: EU Emission Standards for Passenger Cars (Category M_1*), g/km [3]

As mentioned in Section 1.1 HCCI brings the best of both SI and CI engine modes together. The homogeneous mixture (as in an SI engine) is compressed and auto-ignited (similarly to a CI engine). It can also be said that the combustion process is related more closely to the ideal Otto Cycle because HCCI combustion is fast and violent. In HCCI engine operation mode and similarly to an SI engine, the in-cylinder mixture is homogeneous, therefore fuel-rich zones are eliminated as result to have lower particulate emissions. However in an SI engine the ignition is generated from a spark source thus a flame front will exist. In HCCI engine operation mode and similarly to DI engines, auto-ignition occurs through the entire combustion chamber; the ignition is spontaneous and does not propagate as a flame front thus reducing the creation of nitric oxides.

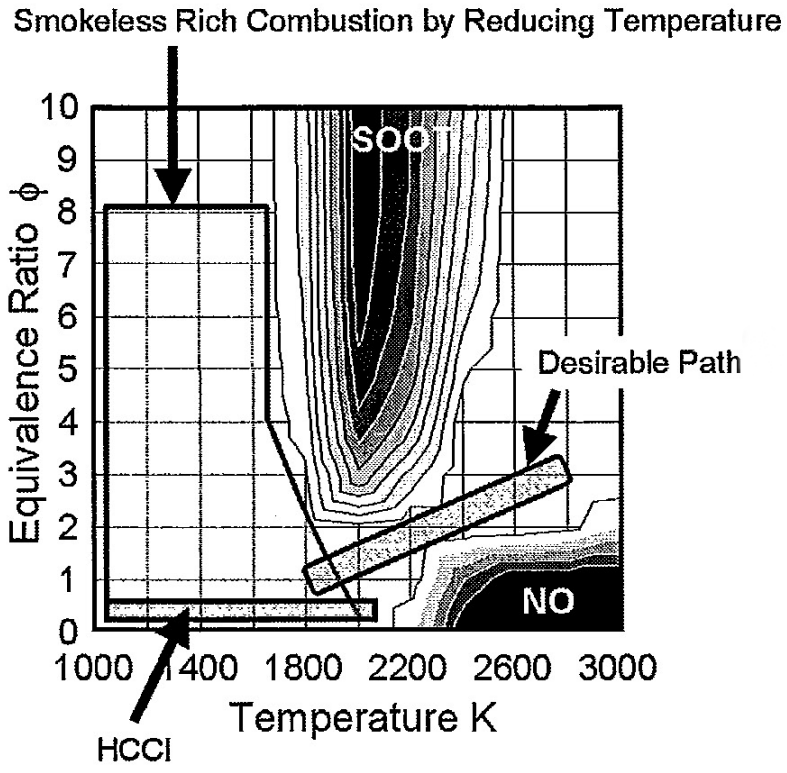

Figure 4: Soot and NOx formation regions as functions of equivalence ratio and temperature [4]

HCCI technology is compatible with a wide variety of fuels, such as gasoline, diesel, biofuels, E85 etc [8]. The characteristic features for HCCI combustion is low

NOx because generally the maximum combustion temperatures is below 1900[K]. Furthermore with homogeneously premixed fuels and high air/fuel ratios the combustion is generally regarded without particulates. However as shown in Figure 4, in order to avoid Soot and NOx formation some combustion regions have to be avoided. It is known [5] that the higher the burned gas temperature the higher the rate of NOx formation and as burned gases cool down the NOx chemistry and then the CO rate of production freezes. Hyvönen [4] reported that the thermal NOx formation region is at combustion temperatures above 1900[K] and also notes that the NOx formation rate is exponential, hence a small increase in combustion temperature results in a large increase in NOx formation. Hyvönen [4] also reported that the Soot formation region, where high temperature and lack of oxygen favours the build-up of long hydrocarbon chains, is at equivalence ratios φ above 2 and temperatures between 1700[K] to 2500[K], where $\varphi = 1/\lambda$, and λ the air to fuel ratio. The HCCI region shown in Figure 4 is plotted up to $\varphi \leq 0.5$ (equivalent to $\lambda \leq 2$). If residual gas is used which is the case for air-diluted HCCI then $\lambda < 1$. Rich combustion are not an interest with HCCI since the combustion efficiency deteriorates due to lack of oxygen [4].

The definition of residual gas is “already burned gas” from previous engine cycles that is left in the cylinder. The main reason to use residual gas is to lower the amount of NOx formed. The temperature in the cylinder can be high enough so that nitrogen and oxygen react and form NOx. By introducing residual gas there is less oxygen in the combustion chamber since the amount of charge air is reduced and consequently the amount of fuel has to be decreased. The exhaust temperature decreases with the amount of trapped residuals at the same engine speed thus less NOx is formed. There are two ways to increase the amount of residual gas in the combustion chamber. Either a) through Exhaust Gas Recirculation (EGR) which exhaust gases are bled

back to the combustion chamber, or b) closing the exhaust valve early thus some exhaust gas remains in the combustion chamber. The second alternative is commonly referred to as "internal EGR". One of the problems with residual gas diluted HCCI is at low engine speeds and loads because the temperature of trapped residuals is too low to initiate auto-ignition. The definition of residual gas fraction is the ratio between the mass of residual gas and the total mass of gas and fuel mixture in the combustion chamber.

HCCI was first implemented on a two-stroke engine cycle [20, 50] mainly because of the inherently high fraction of trapped residual gas found in two-stroke engines, which also slows down the rate of heat release, and thus the knock intensity of the engine. A four-stroke engine does not by design have trapped residual gas rates similar to that of a two-stroke engine and as such, control of the heat release rate becomes a factor for achieving HCCI operation mode.

It has been widely recognised that charge temperature control is one of the key contributors for successful HCCI engine operation. Indeed, complete thermal management has been proposed as a control method in many supercharged / turbocharged / force induction HCCI engine studies. Research has been reported in Germany [6], Sweden [8 – 14] USA [15 – 18] Japan [20] and UK [22 – 32] in which thermal management was used to enable the control of HCCI and also emission improvement by using after-treatment systems. It has been demonstrated [25 – 27] that a moderate increase (e.g., by 60 °C) in intake air temperature can substantially increase the size of HCCI envelope. With the "Total Thermal Management" concept the aim is to collectively join the efforts of the research areas mentioned above for the most efficient operation of the engine with the maximum HCCI envelope. This

chapter will present the up to date knowledge concerning Thermal Management and HCCI control.

2.1 Impact of Fuel type on HCCI Combustion

Shibata et al. [45-47] has presented a series of tests correlating air/fuel chemistry for the HCCI ignition process with Low Temperature Heat Release (LTHR) and High Temperature Heat Release (HTHR). Shibata et al. [45-47] found that the allowable HCCI range in a load/speed engine map is strongly related to HTHR phasing (more precisely to crank angle at which 50% of HTHR is completed). They also showed that HTHR phasing is a function of LTHR phasing and heat release at crank angle at which 50% of LTHR is completed. Further on it was also presented that automotive IC engine fuels can be divided into groups depending on their tendency to advance HTHR. Shibata et al. [45-47] has reported that even a small change in the fuel chemical composition can change the HCCI combustion characteristics, including the amount of LTHR phasing that will significantly affect HTHR. Their results show that n-paraffin hydrocarbons will have the biggest tendency to advance the HTHR, olefins second most and aromatics will exhibit the least advance of HTHR. Finalising a correlation between the start of HTHR, temperature and pressure was proposed as the Shibata-Urushihara Model.

Besides fuel type it has previously been mentioned that auto ignition is dependent on the time history of the temperature and pressure in the combustion chamber. An engine with high compression ratio and low inlet air temperature can exhibit two stage ignition at low speeds where as an engine with low compression ratio and high inlet temperature does not have any low temperature reactions at the same speed [4].

2.2 Means of HCCI Control

Controlling of HCCI combustion in four-stroke engine is extremely difficult primarily because there isn't a direct parameter (or event) that triggers HCCI combustion. Every parameter which can affect temperature and pressure at the end of compression stroke is of potential interest for the purpose of HCCI control. The auto ignition process for HCCI combustion is controlled by the time history of temperature and pressure which changes the ignition properties of the fuel. The said time parameters are a function of the load (among others) and some of these parameters are relatively easy to control during engine operation. However some of these parameters are subject of a wider agreement between researchers and some of them are strictly related to basic engine design and cannot be changed during engine operation [1].

Several potential control methods can be applied to control HCCI combustion; for example varying the amount of exhaust gas recirculation (EGR), using a variable compression ratio (VCR), and/or using variable valve timing (VVT) to change the effective compression ratio and/or the amount of hot exhaust gases retained in the cylinder and/or multi fuel blending to adjust fuel properties. The chemistry of the air/fuel mixture can be affected by dual-fuel injection systems [13] which the ignitability of the mixture can be dynamically changed while the engine is operational. The ignitability of the mixture can also be changed by fuel reforming through injection during NVO [50,51]. However the use of hydrogen as a fuel of vehicular applications introduces several challenges, as one of the main drawbacks is the difficulty of storing onboard hydrogen. Exhaust gas reforming is a promising technique for on board production of hydrogen from fuels [35]. Mixture composition can be affected by fuel stratification in Direct Injection (DI) engines [53].

Last combustion wall temperature which is directly linked to the cooling water temperature can have an effect on HCCI combustion [48]. VCR and VVT technologies are favourable because of their fast time response and can potentially handle rapid transients. Intake air heating as a method of controlling combustion phasing needs to use methods such as flow mixing so that the response times are comparable than that of VCR and VVT [2]. Some means of control variables that have been mentioned above can have long term effects that can last from several engine cycles for example fuel reforming up to several hundred engine cycles such as combustion wall temperature control.

2.3 Charge Air Thermal Conditions Control and Effects on HCCI Combustion

It has already been mentioned that HCCI ignition depends on the time history of the temperature and pressure in the combustion chamber that change the auto-ignition properties of the fuel. The impact of fuel type on HCCI combustion has also been reviewed thus the sensitivity of the control mechanism is also dependant on the fuel type and needs to be tightly controlled as in some cases a temperature difference of a few degrees can lead to early auto-ignition or misfire. There are many ways to adjust the intake temperature and as such researchers [54 – 56] have published results of the effect of inlet temperature on HCCI combustion. However continuous control mechanisms are necessary and for vehicular applications an onboard Thermal Management (T.M.) system is required. The fundamentals of such a system have been installed on the authors' engine test rig. The T.M. system comprises of a supercharger, intercooler integrated to the intake manifold with hot/cold air mixing passages, Jaguar V6 multi-cylinder HCCI engine, exhaust manifold, fuel reformer and an exhaust gas after-treatment system.

Modelling results of a T.M. system have been described by Martinez-Frias et al. [52]. They showed that thermally controlled HCCI can be successfully implemented over a wide range of conditions with high efficiency and low emissions.

Persson et al.[57] simulated the realistic changes in the ambient temperature for HCCI and concluded that the variations in ambient temperature are insignificant due to the effects of NVO, as long as the engine operates within the HCCI operating window. However closer to the load limit, the effect of the intake temperature becomes more significant but when HCCI operation is spark assisted the sensitivity to inlet temperature is reduced. The in cylinder temperature also depends on the residual fraction; at low load operation (high residual fraction) the intake temperature does not have a great effect since there is little fresh air at a lower temperature compared to the higher temperature of trapped EGR. However when the load is increased (low residual fraction), this leads to a situation where the high inlet temperature stabilises HCCI combustion. As mentioned earlier the correlation between in cylinder temperature and residual gas fraction is primarily due to the mass of fresh air in the combustion chamber mixing with the higher temperature trapped EGR.

The relationship between measured inlet temperature, in cylinder temperature at BDC and combustion phasing has been investigated by Sjöberg et al. [58]. They observed that due to heat transfer during the intake cycle the effective inlet port temperature will be different from the temperature measured in the inlet intake runners. In addition, dynamic flow effects also affect the level of charge heating, and the amount of residuals from previous cycles affect the temperature at the end of compression stroke. They published correlations between heat transfer during the intake period and volumetric efficiency and for the effect of charge cooling due to direct fuel injection. The amount of heat required for fuel evaporation changes with

injection timing and volumetric efficiency. The above observations led to the development of correlations in which one can use to estimate the mixture temperature at the end of the compression stroke. Further observations link this temperature with HCCI combustion phasing. Further conclusions from their work, state that: intake heat transfer changes linearly with intake temperature and increasing engine speed does not diminish the intake heat transfer effect. The amount of dynamic heating of the incoming charge increase with increasing engine speed, especially if injection is retarded and applied during the induction stroke and leads to increased charge cooling. The published correlations show to have good agreement with experimental results and good correlation was achieved between BDC temperature and ignition phasing. Finally their work can be used not only for HCCI engines but also in CI and SI engines to prevent knock and NOx formation.

Chang et al. [59] considered how the intake charge temperature and cylinder wall temperature affects the thermal conditions in the cylinder. Their results show great sensitivity of HCCI combustion to changes in the wall temperature and weak correlation to inlet charge temperature. This observation led to the conclusion that decreasing the intake temperature retards the timing and the burn rates change, primarily as a function of ignition timing. Furthermore reducing the wall temperature leads to a greater reduction in the bulk burn rate and higher combustion variation, as one can expect from retarded ignition.

Hyvönen et al.[14] used inlet temperature control as an effective tool for cylinder-to-cylinder balancing. They concluded that it is possible to balance Cylinder-To-Cylinder Variations (CTVC) by individually adjusting the temperature to each cylinder. It also leads to highest brake efficiency and the lowest NOx emissions compared with other tested methods such as individually adjusting the amount of fuel

injected into the combustion chamber. Unfortunately, air density and therefore the load will vary between individual cylinders. On the other hand it has been shown that simply maintaining inlet temperature at the same level for all cylinders will not guarantee the same combustion phasing since other parameters will affect HCCI operation. Furthering Hyvönen et al.[61] discussed the operating range in a multi-cylinder HCCI engine incorporating variable compression ratio. He concluded that CTCV due to differences in compression ratio and inlet air temperature would prevent achieving high loads.

Morgan et al.[60] concluded that by increasing the inlet temperature to about 70ºC this will cause a decrease of NMEP by 7%, advance the timing of $MFB_{50\%}$ by approximately 2.5º and will increase pressure rise rate per crank angle degree (dP/dCA) by 7%.

Iida et al.[55] showed that by increasing the inlet air and coolant temperature this will cause an earlier start of heat release. This effect is also dependent on the engine speed and the higher speed the more pronounced the effect will be.

The experimental work of Misztal [1] investigated the impacts of inlet air temperature and injection timing. By reducing charge air temperature HCCI particulate matter (PM) emissions (by mass) was increased. This observation was also related to the engine load, where the higher the load the lesser the effect to PM emissions by charge air temperature. When the injection timing effect was studied it was observed that the earlier the injection the more particulates HCCI combustion will produce. It was also observed that by increasing engine speed this effect was somewhat diminished

2.4 Effect of Compression Ratio on HCCI mode

HCCI combustion is highly dependent on the effective compression ratio because it directly influences the pressure at the start of compression and as such the maximum in-cylinder pressure. Hyvönen et al.[14] researched the effect of manufacturing tolerances on the effective compression ratio. They concluded that the resulting effect on combustion phasing could be anything between 10 ºC to 20ºC. They also stated that if the effect of these differences cannot be removed, active cylinder balancing will be required. The effective compression ratio will be affected not only by these mechanical parameters, but other factors as well such as blow-by losses, heat transfer through the wall geometry and volumetric efficiency.

Iida et al.[55] identified that the compression ratio has a high effect on the mixture temperature and pressure at the end of the compression stroke and as such the start of heat release. Increasing the compression ratio would increase the temperature at the end of the compression stroke and as such the requirement to provide higher inlet temperature decreases. This effect is more pronounced compared to the effect the inlet temperature and coolant temperature has on the start of heat release. They also concluded that the start of heat release could be advanced by about 15º when the compression ratio was increased by a factor of 4. The effect of compression ratio on HCCI operation shows only a restricted sensitivity to engine speed.

Haraldsson et al.[63] proved that there is a correlation between compression ratio (CR) and brake thermal efficiency, CO and NOx emissions. Increasing the CR will increase brake thermal efficiency and lower NOx emissions, while CO emissions would increase most likely because of the faster expansion, thereby resulting in a shortened reaction time.

2.5 Effect of Boost Pressure on HCCI mode

Applying boost pressure mechanisms for increasing the upper load boundary for HCCI was investigated by a number of researchers. A review of the notable advances for increasing the upper load boundary using increased boost pressure is provided below by the author.

Hyvönen et al.[12] successfully applied supercharging with a turbocharger and a mechanical supercharger on a 1.6 litre multi-cylinder VCR engine running on HCCI increasing the operating range. They concluded that turbocharged HCCI has better brake efficiency as compared to naturally aspirated HCCI through the load range (up to 10 bar BMEP). Furthermore they reported that with turbocharging they obtained both higher maximum load and brake efficiency than with supercharging, due to the high parasitic losses in case of supercharging. Furthermore they concluded that by applying throttling at zero loads results for greater brake efficiency compared to unthrottled HCCI operation due to the increase in combustion efficiency offsetting the increase in pumping losses.

Yap et al.[29,31] conducted tests on boosted gasoline HCCI. They concluded that by boosting a substantial increase of the high load limit can be achieved without any auxiliary heating, while keeping low NOx emissions. The indicated load reached 7.6 bar at 1.4 bar maximum boost pressure which is approximately 75% of the total engine load. In a parallel work they investigated the changes of boost pressure with inlet valve timing and trapped residual gas. They concluded that during the combustion stroke, combustion phasing is dependent on the temperature of the gas inside the cylinder and the trapped residual gas which remains from the previous cycle. They also observed that there is an optimum inlet valve setting for the lowest NOx emissions. When the valve timing is significantly advanced or retarded away

from this optimum, NOx emissions increase due to the richer air / fuel ratios required for stable combustion. This optimum inlet valve timing setting will advance if the boost pressure is increased.

Christensen et al. [64] successfully applied supercharging on HCCI operation with natural gas. They reported that when boost pressure reached 1.5 bar a pilot injection of iso-octane was introduced in the mixture in order to improve its ignition properties. They concluded that the expansion of load limit while supercharging was linked with applied EGR. Last they also observed a reduction of specific HC emissions while increasing EGR rate and load. The specific NOx emissions were below 0.04 [g/kWh] at about 16 [bar] IMEP.

The effect of boost pressure on emissions of CO, UHC and NOx, BSFC, torque, thermal and combustion efficiency was studied by Canakci at al. [69]. They concluded that the maximum engine torque would increase with increasing boost pressure however would decrease with increasing engine speed. They also reported that combustion efficiency would increase with increasing engine speed for all tested boost pressures. However at the region of the highest achieved boost pressure the increase of combustion efficiency would be minimal. Furthering BSCO would increase with increasing engine speed but would decrease with increasing boost pressure. Also they reported that BSHC would decrease with increasing engine speed but would increase while boost pressure was increased. Last they reported that NOx emissions tend to have an inverse trend to the HC emissions.

The potential benefits from using a turbocharger to increase the inlet pressure was also studied by Olsson et al.[65-66]. They concluded that for HCCI combustion that pumping loses could be reduced if turbocharger efficiency would be high. They

suggested the use of a two stage turbocharger with inter-stage cooling if and when a high load demand would exists.

Last Hatamura [68] described a means for applying boost in HCCI called Blow Down Supercharging by accumulation (BDSCac) and Blow Down Supercharging by pressure wave (BDSCpw). These systems are rather unconventional but can achieve a large amount of internal EGR and can deliver high charge pressure increase however without actually implementing a supercharger thus eliminating associated supercharger parasitic losses.

2.6 Gas Emissions on HCCI mode

The characteristic features for HCCI combustion is low NOx but it can potentially produce higher HC and CO emissions. Port injected HCCI was researched by Christensen et al. [67] on a single cylinder engine fuelled with iso-octane. They concluded that most of the UHC emissions can be traced at the crevices within the combustion chamber by varying the size and the geometry of the largest crevice. By increasing the topland width of the piston the UHC emissions were reduced, when engine speed was increased a wider topland was required in order to achieve the same UHC emissions. In most of the test cases, a reduction of UHC emissions by increasing the topland piston width was accompanied by an increase in CO emissions.

Sjöberg et al. [19] performed HCCI combustion with direct injection of gasoline using a standard GDI-injector. EGR and Electric heaters were used to raise the inlet temperature when no EGR was applied. They observed that with increased air swirl HC, CO and smoke was reduced especially when the injection timing was earlier or later than the optimal point. They concluded this was due to improved air-fuel mixing. They also observed that the most homogeneous mixture was for a lambda of 3.4 and

injection during the middle of the intake stroke. This led to low NOx and smoke emissions.

Sjöberg et al. [21] continued both modelling and experimental work on the effect of engine speed and different fuels affecting bulk-gas reactions. They confirmed direct influence of intake temperature on the completeness of combustion because CO–to–CO_2 reactions are highly sensitive to the peak combustion temperatures. They also reported that for fuels with very little cool-flame activity (i.e. gasoline and pure iso-octane), the fuel/air-equivalence ratio for the start of incomplete bulk-gas reactions is independent of the engine speed. For fuels with a significant fraction of n-heptane, the start of incomplete bulk-gas reactions is dependent on engine speed with a shift towards higher fuel/air-equivalence ratios for lower engine speeds. As result of the later lower peak combustion temperatures were reported and CO emissions would rise unless fuelling was increased.

Dec et al. [49] combined experimental and modelling studies and correlated CO and HC emissions with fuelling rate from knocking conditions to very low loads. The results showed that reducing fuelling rate (lambda above 5), CO emissions increase rapidly. Along the same lines combustion efficiency decreased from 94% to 55%. Furthermore they also conducted comparative computations using a single-zone model with the full chemistry mechanisms for iso-octane. The conclusion was that high CO emissions and combustion inefficiency are related to incomplete bulk-gas reactions. High HC emissions were also observed but not only until lambda was increased above 7.1. Furthermore modelling results suggest that significant emissions of oxygenated hydrocarbons such as formaldehyde will form when bulk-gas reactions become less complete. Furthermore they observed that for iso-octane compression ratio and engine speed do not have a significant impact on bulk-gas reactions but inlet

temperature has high impact on those reactions. Finally they observed that fuel stratification by late GDI injection has a good potential for improving combustion efficiency and emissions at low loads.

Marriott et al. [54] performed tests with altered injection parameters to study the effects of charge stratification and the effects of the fuel injection parameters on combustion phasing of normally aspirated HCCI combustion covering the achievable load range. They observed that UHC emissions were reduced with increased load and/or fuel stratification. They also observed two different mechanisms responsible for HC reduction. At higher loads the high combustion temperature promotes complete oxidation. When stratification was applied they concluded that firstly increased stratification means higher fuel concentration in the bulk-gas, therefore higher combustion temperatures and complete combustion is promoted. Secondly, increased stratification leads to reduced amounts of fuel in the quenching zones.

A detailed numerical analysis of HCCI engine operation at low loads was conducted by Aceves et al. [62] to investigate the sources of HC and CO emissions and the associated combustion inefficiencies Their work revealed that localised formation of the pollutants CO and HC shifts from the crevices and/or near wall regions to the bulk-gas as fuelling is reduced.

Dec at al. [70] presented their results on the sources of Hydrocarbon (HC) and Oxygenated Hydrocarbon Emissions (OHC) emissions from an HCCI engine fuelled with iso-octane over a range of fuelling rates, and fuel-stratification levels. They concluded that unreacted fuel (iso-octane) was the most common HC species for all fuelling rates and stratification levels. They also reported that other species of HC and OHC were commonly found and could be identified as breakdown products of iso-octane. They also reported that at the highest lambda the emissions of all species were

low, except iso-octane. As lambda was reduced the emissions of all species increased, but the rate of increase was dissimilar for each the different species. Finally, they concluded that applying stratification improves emissions and combustion efficiency because a) it produces a local richer mixture in the central part of the charge which burns hotter and more completely reducing CO, HC and OHC and b) because fuel penetration to the crevices and cylinder-wall boundary-layer regions is reduced.

Elghawi et al. [71] investigated hydrocarbon emissions from SI and HCCI combustion using commercial gasoline. They observed that light hydrocarbons species C1-C6 such as Butadiene, Ethane etc. are present in SI mode (9 to 32 ppm) for different operation conditions but were below detection levels in HCCI combustion mode and although the engine operating parameters were varied. They reported however that the contribution of heavier hydrocarbons C6 to C12 in HCCI exhaust is higher than in SI exhaust gas. This was attributed to unburned fuel. Their results have shown that the hydrocarbon compounds (C6-C12) are responsible for most of the hydrocarbon emissions, 50 - 70 % in case of SI mode and 69 - 88 % in case of HCCI mode using the same gasoline fuel, speed/load conditions.

Bhave et al. [72] investigated the factors influencing a reliable prediction of CO emissions in an HCCI engine using an improved probability density function (PDF) based engine cycle model. They observed that CO formation is influenced by fluid-wall interactions, mixing of hot and cold air with fuel particles and the wall temperature. Furthermore they concluded that inhomogeneities during the compression stroke, influence the ignition timing of stochastic particles and in turn the rate of CO formation. The inhomogeneities in the exhaust stroke dictate the levels of CO present in the exhaust.

Sjöberg et al. [73] conducted a study where the combustion temperatures required for complete combustion in HCCI engines have been obtained computationally and experimentally. They concluded that for a compression ratio of 18 at an engine speed of 1200 rpm CO oxidation is not complete if the peak temperature is below 1500K, due to too low OH levels. They also found that the required peak combustion temperature was independent of fuel-type and autoignition characteristics because the final CO oxidation process is independent of the original fuel molecule structure. Furthering the combustion phasing (relative to TDC) did not affect the required peak combustion temperature due to the slow, but complete, CO oxidation.

Girard et al.[74] investigated the effect of the fuel-air mixture quality on the emissions from a HCCI engine running on propane. The fuel-air mixing level was changed by adding the fuel into the intake system at different distances from the intake valve (40 cm and 120 cm away). They observed that at a distance of 120 cm between the injector and inlet valve, the mixture homogeneity was increased and therefore, CO, HC and NOx emissions were reduced. They also reported that using a multi-zone combustion model they show that reducing fuel-air mixture non-uniformities increases NOx emissions. The effect of fuel-air mixture non-uniformity on combustion duration and ignition timing was found to be minimal.

Studies by Kaiser et al. [75] performed studies on concentrations of individual species in the exhaust gas from a gasoline-fuelled (101.5 / 91.5 RON), DI HCCI engine for both stratified and nearly homogeneous fuel-air mixtures. They showed that PM emissions from a DI HCCI engine is comparable between emissions from CI and PFI SI engines and therefore PM emissions are not negligible. They also observed that PM emissions show a trend related to air-to-fuel ratio. In detail for air-to-fuel ratios equal to 50 ($\lambda \approx 3$), soot-like PM dominate the spectrum size. When air-to-fuel

ratio was increased to 70 ($\lambda \approx 5$), the overall PM diameter was reduced meaning the PM were mostly semi-volatile.

Kawano et al. [76] studied the effect of various high octane number fuels mixed with diesel fuel as a base fuel, and the mixed fuels were directly applied to an unmodified DI diesel engine. They concluded that low NOx emission can be achieved by HCCI operation using the mixed fuels despite low volatility of base fuel. However they also measured high PM emissions due to the increased Soluble Organic Fraction (SOF) which originated from base (diesel) fuel.

Kim et al. [77] used premixed fuel (diesel, gasoline and n-heptane) via a port fuel injection system located in the intake port of DI diesel engine to improve NOx emissions. Cooled EGR was introduced for the suppression of advanced autoignition of the premixed fuel. They concluded that with increasing premixed ratios (higher n-heptane and lower diesel content) a simultaneous reduction of NOx and soot can be achieved for diesel fuel. However, at higher premixed ratios and higher inlet temperature, the limiting factor for HCCI combustion will be the increased NOx emissions and knock tendency. They also observed that premixing gasoline (mixing of gasoline with n-heptane) provides the highest benefit in terms of NOx and soot emission reductions, compared with the other two base fuels.

Mulenga et al.[78] studied analytically the effects of hydrogen peroxide (H2O2) addition on an iso-octane/air HCCI combustion. Their results show that it is possible to reduce CO and NOx emission by the use of hydrogen peroxide (H2O2). The CO emissions improvement is due to the decomposition of H2O2 into OH species, hence reducing the time to ignition and the onset of combustion. The NOx emission reduction was due to the lower inlet temperature required with the addition of H2O2

to attain auto-ignition, therefore reducing the time the mixture has to is above the NOx formation temperature threshold.

Price et al. [79] measured PM emissions from a DI HCCI engine implementing the negative valve overlap method for trapping high levels of residual exhaust gases in the cylinder. In summary, it was shown by experimental measurements that the number concentrations of emitted particles from a DI gasoline HCCI combustion are similar in size and concentration to those from a conventional DI gasoline engine (SI), and as such PM emissions are non-negligible. They also observed that under certain conditions and for the same load, PM concentration of the accumulation mode was higher for HCCI engine mode than from SI engine mode. However PM nucleation mode concentrations was lower for HCCI engine mode. Moreover, the magnitude of the accumulation mode inversely varied with the amount of residual gas trapped, and hence in direct proportion to NOx emissions. This is the opposite of the well known PM/NO trade-off one can observe in conventional CI engines. This is thought to be because of the extra heat during the intake and compression stroke the HCCI mixture preparation was improved.

2.7 Fuel Reforming on HCCI mode

It was mentioned that the ignitability of the mixture can also be changed by fuel reforming through injection during NVO [50,51]. Urushihara et al. [51] injected gasoline fuel directly into the residual in-cylinder gas during the NVO interval for the purpose of reforming it by using the high temperature resulting from exhaust gas recompression. They reported that with this injection strategy, HCCI combustion region was dramatically expanded without any increase in NOx emissions. They also found that the injection timing during the NVO was an important parameter that affected the HCCI operational map.

However the use of hydrogen as a fuel for vehicular applications introduces several challenges, as one of the main drawbacks is the difficulty of storing onboard hydrogen. Therefore many researchers focused on exhaust gas reforming as a technique for onboard production of hydrogen from fuels [35].

Fuel reforming is a process which hydrogen is produced from hydrocarbons or alcohol, Wyszyński et al.[80]. They summarised the information on fuel reforming and reported the main reforming reactions:

$CH_4 + H_2O = CO + 3H_2$ - steam reforming,

$2CH_4 + O_2 = 2CO + 4H_2$ - direct partial oxidation

$CH_3OH = CO + 2H_2$ - thermal decomposition

Exhaust gas reforming is the process which exhaust gas (comprising heat and water) react with fuel over a catalyst and a combination of the above reactions take place, Wyszyński et al.[80]. An example of the reactions that occur is as follows:

$CH_4 + 0.33\ (CO_2 + 2H_2O + 7.52N_2) = 1.33\ (CO + 2H_2 + 1.88N_2)$

The quality and quantity of the reformed fuel depends on a number of parameters such as exhaust gas composition, exhaust gas flow rate, heat in the exhaust gas, the catalyst composition, fuel, air and water input into the reactor. However they reported that the amount of hydrogen produced by the reformer mainly depends on the exhaust temperature. If the exhaust temperature is above 800-900 [ºC] (for example at high engine loads in SI mode) the hydrogen content in the reformed gas can be as high as 30%. If the exhaust temperature is within the range of 500-700 [ºC] (for example

medium to low engine loads in SI mode) the hydrogen content in the reformed gas is below 20%.

The possibility of implementing exhaust gas reforming of some hydrocarbon fuels using a reforming fuel catalyst and exhaust gas generator was studied by Jones [81]. They conducted experiments to produce fuel reforming using unleaded gasoline and n-heptane and they concluded that with the fuel catalyst they used, gasoline was difficult to reform while it was possible to reform n-heptane.

Jamal et al. [82] reviewed the use of hydrogen and hydrogen-enriched gasoline as a fuel for SI engines and the techniques used to generate hydrogen from liquid fuels such as gasoline and methanol, on-board the vehicle. The different fuel reforming techniques used to produce hydrogen from liquid fuels such as gasoline and methanol were also covered. They also summarized and reviewed predictive and experimental results of different investigations. Due to difficulties in reforming gasoline there is a limited amount of published research.

Kopasz et al.[83-84] performed a study for reforming multicomponent fuels. They reported that aromatic, naphthenic, and detergent components adversely affect the reforming of paraffinic species. Reforming of aromatic components require higher temperatures and longer contact times to reform compared to paraffinic components. Napthenic components require higher temperatures to reform, but can be reformed at higher space velocities than paraffinic components. They reported that the effects of sulphur depend on the catalyst used. Last they suggested that further evolution of gasoline could reduce the demands on the reformer and provide a better fuel for hydrogen production. A general conclusion from their work indicates that all major components of gasoline can be auto-thermally reformed to provide hydrogen-reach

gas. However differences in the reformer temperature can produce significantly different results.

Yap et al. [85] documented the experimental results of production of hydrogen using closed loop exhaust gas fuel reforming. It is shown that hydrogen in the form of reformed gas helps in lowering the intake temperature required for stable HCCI operation. Furthermore it was shown that the addition of hydrogen advances the start of combustion in the cylinder as a result of the lowering of the minimum intake temperature required for auto-ignition to occur during the compression stroke, resulting in advanced combustion for the same intake temperature.

Chapter 3. Engine Thermal Management System

3.1 Physical Thermal System

One of the major problems associated with HCCI combustion has been the relatively small operating envelope (speed/load map). During years of HCCI research many solutions to expand the HCCI operating range have been proposed including: inlet air heating, fuel reforming, injection strategy, multi-fuel operation and boosting.

The Thermal system arrangement is presented in Figure 3 (page 23) and Figure 5. The system comprises of a supercharger, water cooled intercooler, heat exchanger, an air heater and a gasoline reformer wrapped around the exhaust catalyst. A number of throttles have been used to control the air flow where as for the hot air reformed stream an EGR valve will be utilised. The heat exchanger transfers heat from the engine coolant and is aided by an air heater when more heat is needed to increase the temperature of charge air.

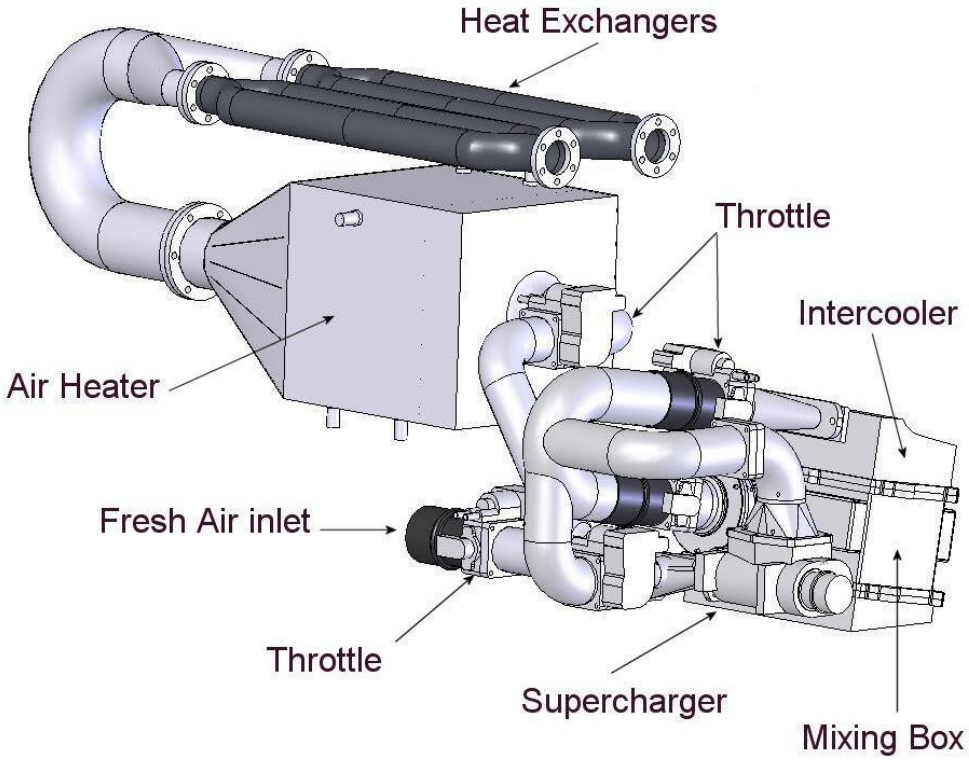

Figure 5: CHASE Thermal management system arrangement

3.2 Reformed Exhaust Gas Recirculation (REGR)

A note to the reader, during our research the reformer research interest by Jaguar Cars, the project sponsor, was postponed as the company decided not to utilise fuel reforming for HCCI. However for research purposes the thermal system has been designed with the capacity to utilise fuel reforming, since fuel reforming research continues at The University of Birmingham. The details of the reactor design and performance optimisation have been described by M.Ashur in his PhD thesis [35]. Therefore in the present work the effect of Reformed Exhaust Gas Recirculation (REGR) on HCCI engine performance will not be examined.

3.3 Thermal Management System Design Rationale

Generally the operating strategy with thermal management was to establish the HCCI multi-cylinder NA baseline with controlled ambient conditions. A series of tests was conducted changing various engine parameters such as intake and exhaust parameters, air to fuel ratio, speed etc. Engine parameter data were monitored such as in-cylinder pressures, load, emissions, temperatures at various points within the engine and thermal management system. At the low load HCCI boundary, engine operation was limited by misfire due to limited tolerance for EGR. Whereas, at the high load HCCI boundary the limitation was typically due to knock tendencies. When the HCCI baseline operation was established then one by one the effect of boosting, throttling and temperature increase was investigated.

The thermal management system comprised mainly of off the shelf components from Jaguar Cars Ltd. The reasoning behind this was a requirement from Jaguar Cars Ltd to use as many production components as possible if the thermal management system were to be tested into a prototype car. Therefore the throttles, supercharger, intercooler and exhaust gas recuperator were off the shelf components provided by

Jaguar Cars Ltd. Packaging was not a concern during the design phase of the thermal management system. The focus instead was the requirement to make the components to work for the intended purpose.

Manufacturers data or measured tests were conducted in order to predict component performance (pressure loss, effectiveness in case of heat exchangers and supercharger performance) in our thermal management system. These data were used in the thermal management model as detailed in Section 3.6.

What follows is design calculations and methodology used to predict the performance of the electric heaters and preliminary exhaust gas recuperator. The later was replaced by a different recuperator however the methodology to predict performance remained the same. Last the reasoning behind using a smaller supercharger than the one originally installed is explained.

3.3.1 Intake air heating

The Thermal Management Intake system was equipped with electric heaters and exhaust gas recuperator to heat intake the air. The calculations estimating component performance follows.

Electric heaters

At 2900rpm the Natural Aspirated engine requires approximately 3.5e-3 kg/s of air per cylinder. This equates to 0.021 kg/s. It can be estimated that in order to heat the air up to 125°C it is required 2.131kW heating (Table 2) if one assumes 100% efficiency of the electric heaters. However to achieve better efficiency it is required to reduce air velocity sufficiently and increase surface area so that the electric heaters would be able to heat the air effectively. Thus a vane diffuser was devised avoiding sudden expansion and the Borda–Carnot effect, that expanded the air from 100mm diameter pipe to a 350x350x350mm box as shown in Figure 5. In the end it was

decided to use use more heating elements to employ rapid heating of the air thus 3*1kW heating elements were installed in the air heating box. Last when the T.M. system was installed it was insulated with 5mm flexible insulation material.

m_{air} [kg/s]	0.021
cp_{air} [J/kgK	1015
T_{in} [°C]	25
T_{out} [°C]	125
Q [W]	2131.5

Table 2: Electric Air Heating

Preliminary Exhaust gas heat recuperator

At the initial stages of this project it was considered to use a TUV NEL exhaust gas heat recuperator. However eventually a Jaguar Cars prototype exhaust gas heat recuperator was used and this is presented in Section 3.6.3.Heat Exchanger and Intercooler What follows is the predicted performance calculations of the TUV NEL exhaust gas heat recuperator if it were to be used in our system.

In Table 3 TUV NEL Ltd provided the performance data for an exhaust gas heat recuperator. The data were obtained from simulated runs with an exhaust gas inlet temperature of 450°C and an air inlet temp of 25°C.

Qexh [W]	Cexh [W/K]	0	24.45781	48.93616	73.40278
Cair [W/K]					
0		0	0	0	0
23.48597222		0	4104.174	5449.215	5870.554
46.99168056		0	5970.293	9488.09	10827.82
70.48611111		0	6656.003	11370.11	13644

Qair [W]	Cexh [W/K]	0	24.45781	48.93616	73.40278
Cair [W/K]					
0		0	0	0	0
23.48597222		0	4077.116	5413.808	5820.84
46.99168056		0	5967.949	9485.786	10795.35
70.48611111		0	6660.594	11381.08	13620.62

Table 3: TUV NEL Exhaust Gas Heat Recuperator Heat Rate Data

Using the heat rate data from Table 3 the heat transfer and temperatures for both sides of the recuperator were calculated as shown in Table 4 and Table 5.

	°C	K		
Tex_in	450	723.15		
Tair_in	25	298.15		
Cp_exh [J/K]	1057			
Cp_air [J/K]	1015			
	m' [kg/Hour]	m' [kg/s]	cp [J/kgK]	C [W/K]
m(dot)_exh[kg/s]	0	0	1057	0
	83.3	0.023139	1057	24.45781
	166.67	0.046297	1057	48.93616
	250	0.069444	1057	73.40278
m(dot)_air[kg/s]	0	0	1015	0
	83.3	0.023139	1015	23.48597
	166.67	0.046297	1015	46.99168
	250	0.069444	1015	70.48611
Q(dot)air [KW]				
		4.1	5.47	5.9
		5.94	9.49	10.86
		6.62	11.35	13.64

Table 4: TUV NEL Exhaust Gas Heat Recuperator Heat transfer

	m(dot)_exh[kg/s]	0	0.023139	0.046297	0.069444
m(dot)_air[kg/s]					
0	Tout °C	237.5	450	450	450
0.023138889	Exhaust side	25	283.3	339.37	370.7
0.046297222		25	205.99	256.16	302.93
0.069444444		25	177.67	217.43	264.44
0	Tout °C	237.5	450	450	450
0.023138889	Air side	25	199.75	257.02	274.96
0.046297222		25	152.05	226.91	255.42
0.069444444		25	119.43	186.31	218.57

Table 5: TUV NEL Exhaust Gas Heat Recuperator Performance

The results shown in Table 4 and Table 5 indicate that some heat loss occurs inside the heat exchanger, and this has been accounted for in the simulated data.

$$\dot{Q}_{air}\left[W\right] = \dot{m}_{air}\, Cp_{air}\left(T_{air\_out} - T_{air\_in}\right)$$

$$\dot{Q}_{exh}\left[W\right] = \dot{m}_{exh}\, Cp_{exh}\left(T_{exh\_in} - T_{exh\_out}\right)$$

Heat capacity "C_{xx}" is defined as:

$$C_{air}\left[\frac{W}{K}\right] = \dot{m}_{air}\, Cp_{air}\left[\frac{kg}{s}\frac{J}{kgK} = \frac{W}{K}\right]$$

$$C_{exh}\left[\frac{W}{K}\right] = \dot{m}_{exh}\, Cp_{exh}\left[\frac{W}{K}\right]$$

In order to simulate the performance of the heat exchanger, the calculated heat rate from Table 3 was normalised by dividing it by the simulated inlet temperature difference that is (450 – 25) = 425 K.

The resulting array can be seen in Table 6.

CQ'hx(exh side) [W/K]	m(dot)_exh[kg/s]	0	0.023139	0.046297	0.069444
m(dot)_air[kg/s]					
0		0.1	0.1	0.1	0.1
0.023138889		0.1	9.656879	12.82168	13.81307
0.046297222		0.1	14.04775	22.32492	25.47723
0.069444444		0.1	15.66118	26.75321	32.10352

CQ'hx(air side) [W/K]	m(dot)_exh[kg/s]	0	0.023139	0.046297	0.069444
m(dot)_air[kg/s]					
0		0.1	0.1	0.1	0.1
0.023138889		0.1	9.593215	12.73837	13.69609
0.046297222		0.1	14.04223	22.3195	25.40082
0.069444444		0.1	15.67199	26.77902	32.04852

Table 6: TUV NEL Exhaust Gas Heat Recuperator Normalised Heat Rate

Figure 6 shows the recuperator duty/K on the exhaust and air side. The resulted surface can be easily extrapolated for data outside the test range. In order to create the simple heat exchanger model all is needed is to interpolate within this array to obtain the duty/K for the air mass flowrate and exhaust gas mass flowrate and multiply the result by the actual inlet temperature difference in the gas streams.

From the predicted duty $\dot{Q}_{air}\ f(\dot{m}_{air})$ and $\dot{Q}_{exh}\ f(\dot{m}_{exh})$ [W] one can then determine the outlet air and exhaust gas temperatures. However the main assumption behind the

above is that the air and exhaust gas properties do not change significantly with temperature.

$$\dot{C}Q_{hx\_air}\ \left[\frac{W}{K}\right]=\frac{\dot{Q}_{air}\ f\left(\dot{m}_{air}\right)}{T_{exh\_in}-T_{air\_in}}\ \text{and}\ \dot{C}Q_{hx\_exh}\ \left[\frac{W}{K}\right]=\frac{\dot{Q}_{exh}\ f\left(\dot{m}_{exh}\right)}{T_{exh\_in}-T_{air\_in}}$$

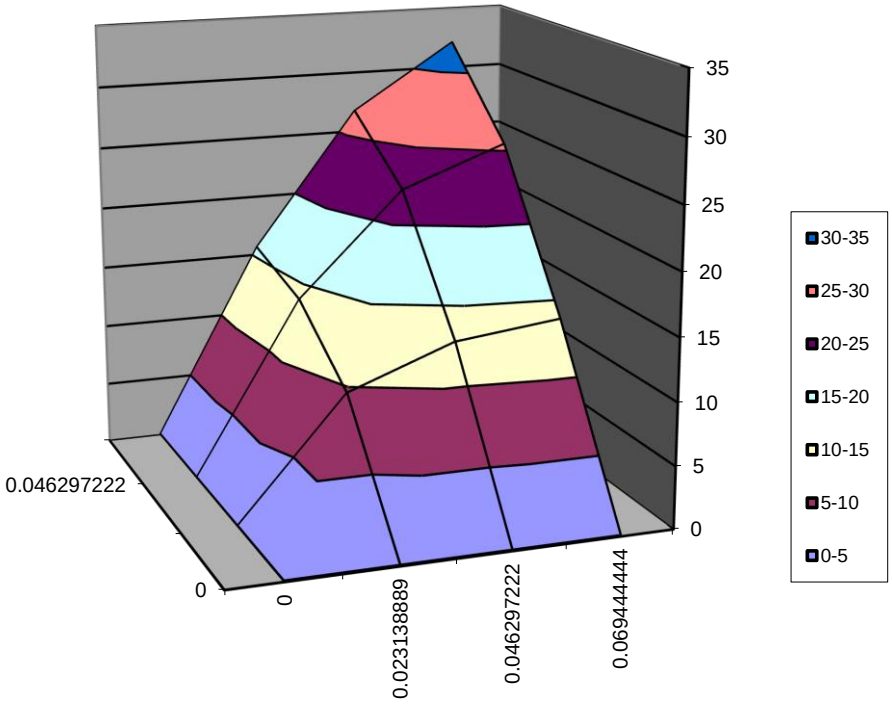

A)

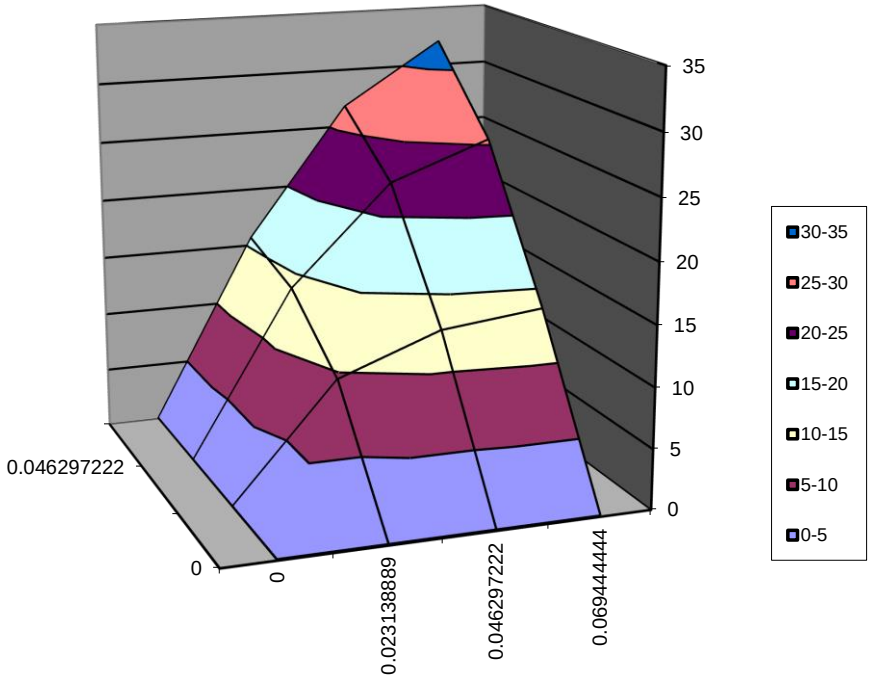

B)

Figure 6: CQ'hx(exh side A),(air side B) [W/K])

3.3.2 Preliminary Matlab/Simulink heat exchanger model

A simple model for the recuperator was created using Matlab/Simulink environment, using manufacturers data from Table 3. The front-end requires mass flows, inlet temperature and pressures and produces the output temperature and pressures. The preliminary heat exchanger model predicts the outlet exhaust and air side temperatures using the inlet exhaust and air side temperatures and an exhaust and air side performance map. However the main assumption is that the air and exhaust gas properties do not change significantly with temperature. Because a simple model was required, there was no account for pressure losses inside the heat exchanger.

Model Validation

Two known operating points were examined. Exhaust gas inlet temperature was kept at 450°C and air inlet temp of 25°C.

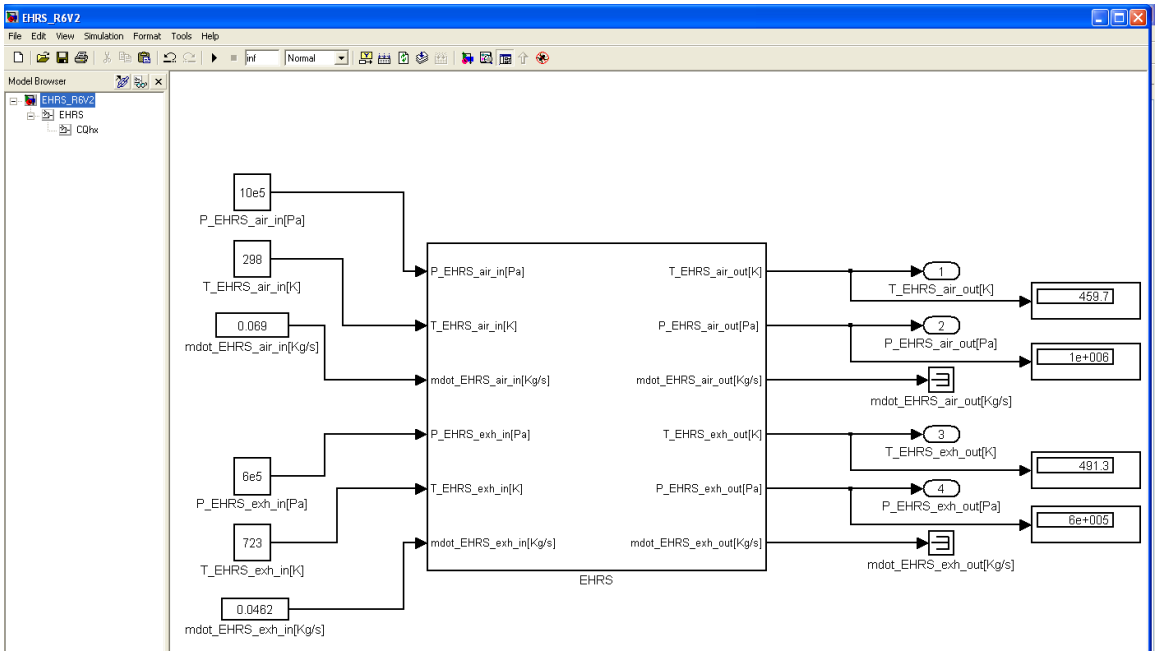

Figure 7: Matlab/Simulink Recuperator (first level)

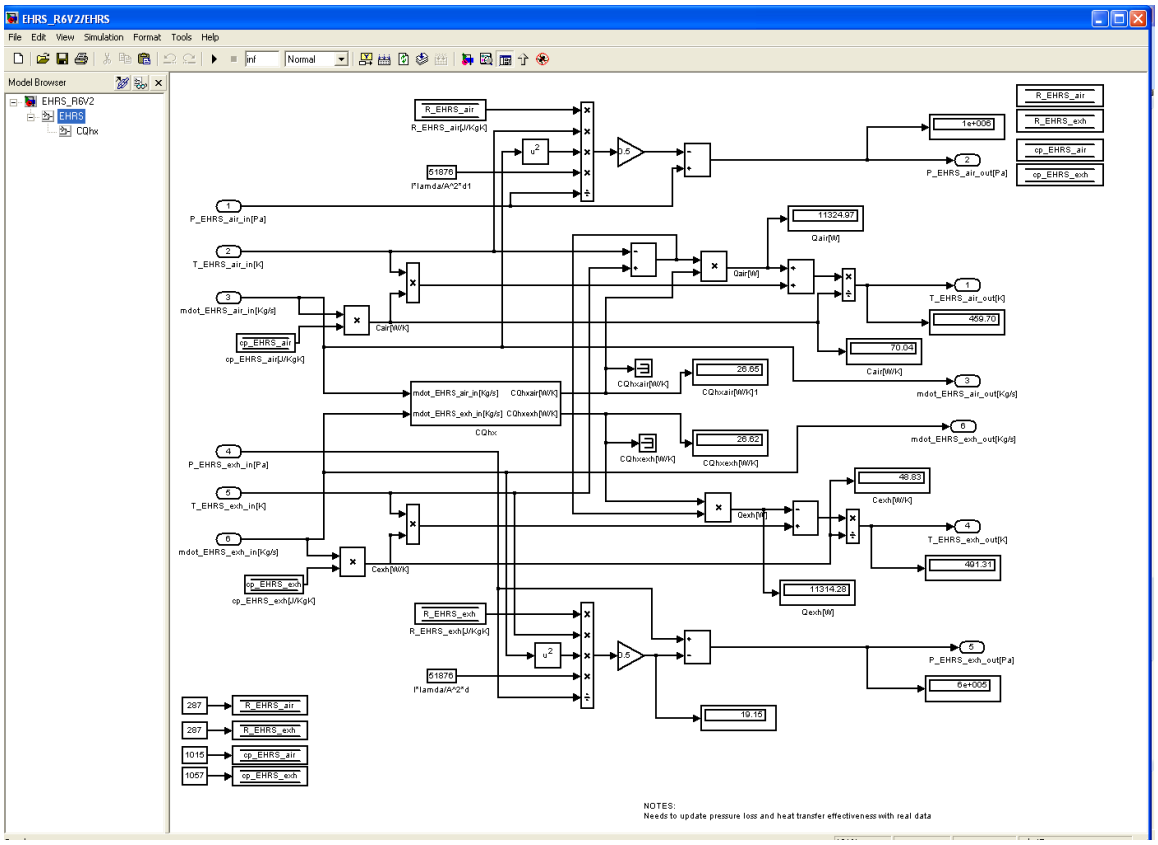

Figure 8: Matlab/Simulink Recuperator (second level)

Case 1

$$T_{air\_in} = 298[K]$$
$$T_{exh\_in} = 723[K]$$

$$\dot{m}_{air} = 0.023139\left[\frac{kg}{s}\right]$$
$$\dot{m}_{exh} = 0.023139\left[\frac{kg}{s}\right]$$

Expected temperatures

$$T_{air\_out} = 199.75\ ^{\circ}C\ \left(472.75\ K\right)$$
$$T_{exh\_out} = 283.3\ ^{\circ}C\ \left(556.3\ K\right)$$

Calculations

Using the above mass flow rates

$$\dot{C}Q_{hx\_air} = 9.5932 \left[\frac{W}{K}\right] = \frac{\dot{Q}_{air}\ f\left(\dot{m}_{air}\right)}{T_{exh\_in} - T_{air\_in}} = \frac{\dot{Q}_{air}\ f\left(\dot{m}_{air}\right)}{425}$$

$$\dot{C}Q_{hx\_exh} = 9.6568 \left[\frac{W}{K}\right] = \frac{\dot{Q}_{exh}\ f\left(\dot{m}_{exh}\right)}{T_{exh\_in} - T_{air\_in}} = \frac{\dot{Q}_{exh}\ f\left(\dot{m}_{exh}\right)}{425}$$

Calculated temperatures

$T_{air\_out} = 471.6\ \text{K}$

$T_{exh\_out} = 555.2\ \text{K}$

Case 2

$T_{air\_in} = 298[K]$

$T_{exh\_in} = 723[K]$

$\dot{m}_{air} = 0.04629\left[\frac{kg}{s}\right]$

$\dot{m}_{exh} = 0.06944\left[\frac{kg}{s}\right]$

Expected temperatures

$T_{air\_out} = 255.42\ ^{\circ}C\ \left(528.75\ K\right)$

$T_{exh\_out} = 302.93\ ^{\circ}C\ \left(575.93\ K\right)$

Calculations

Using the above mass flow rates

$$\dot{C}Q_{hx\_air} = 25.401 \left[\frac{W}{K}\right] = \frac{\dot{Q}_{air}\ f\left(\dot{m}_{air}\right)}{T_{exh\_in} - T_{air\_in}} = \frac{\dot{Q}_{air}\ f\left(\dot{m}_{air}\right)}{425}$$

$$\dot{C}Q_{hx\_exh} = 25.477 \left[\frac{W}{K}\right] = \frac{\dot{Q}_{exh}\ f\left(\dot{m}_{exh}\right)}{T_{exh\_in} - T_{air\_in}} = \frac{\dot{Q}_{exh}\ f\left(\dot{m}_{exh}\right)}{425}$$

Calculated temperatures

$T_{air\_out} = 527.7\ \text{K}$

$T_{exh\_out} = 575.5\ \text{K}$

3.3.3 Eaton M24 Supercharger

During the early stage of the HCCI tests at The University of Birmingham and prior the Thermal Management system was installed, It was discovered that due to the much smaller flow rate on HCCI mode, the operating map of the M62 model does not cover the required flow rate to pressure ratio. During tests with the HCCI engine setup at The University of Birmingham we were aiming to operate HCCI mainly within 1000-3000 rpm. There was a choice from three superchargers and the most suitable was the EATON M24 supercharger. With a pulley ratio 3.5 the supercharger would spin from 3500 to 10500 rpm. From Figure 9 and since it was known it wasn't possible to operate HCCI at high boost pressures, it wasn't expected to operate the supercharger at its maximum efficiency however it was a requirement from Jaguar Cars Ltd to use a supercharger.

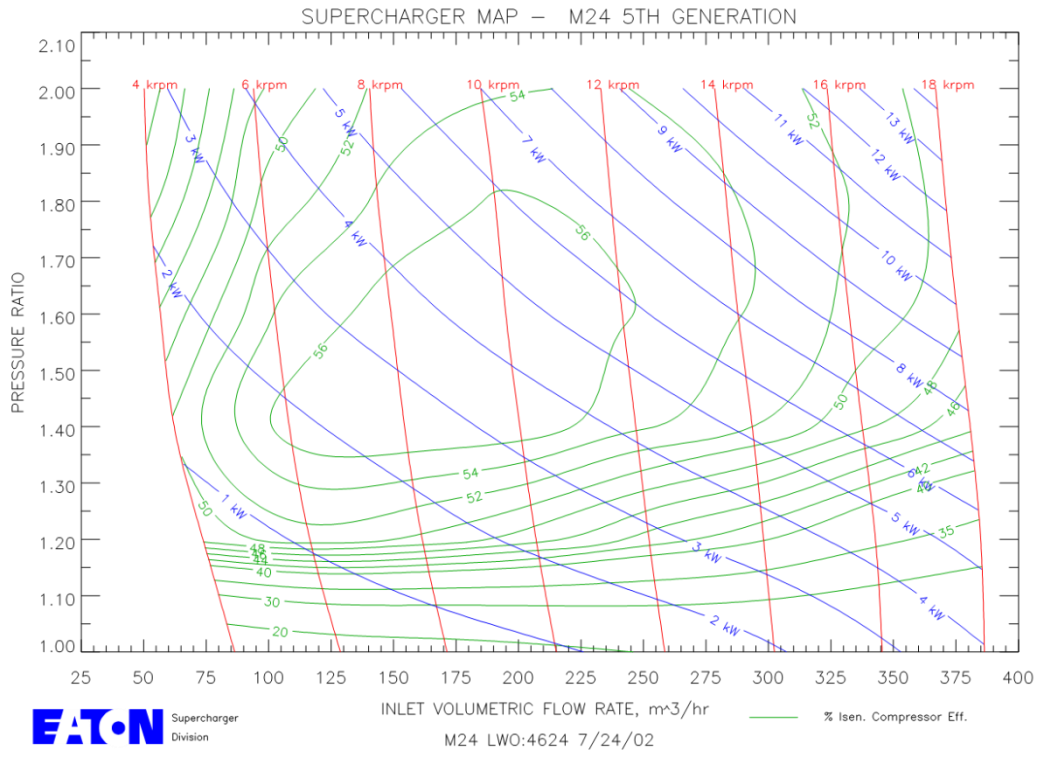

Figure 9: Performance map for EATON M24 supercharger

3.4 Thermal Management System Experimental System

This section describes experimental facilities and procedures used in the presented work. The description will include the experimental engine, control and data acquisition system as well as techniques used for pressure and emission data processing.

3.4.1 Jaguar V6 HCCI Engine

The experimental engine is a Jaguar gasoline V6 direct injection, 4 valves per cylinder and 3 litres swept volume. An engine specification summary has been presented in Table 7. To switch between the SI and HCCI modes of operation, the cam profile switching (CPS) system is used. This system allows on-line switching of valve lift from 9mm (SI operation) to 3mm (HCCI operation) as shown in Figure 10. The variable cam timing system makes it possible to change the cam timing for the inlet and exhaust cams within a 60 crank angle.

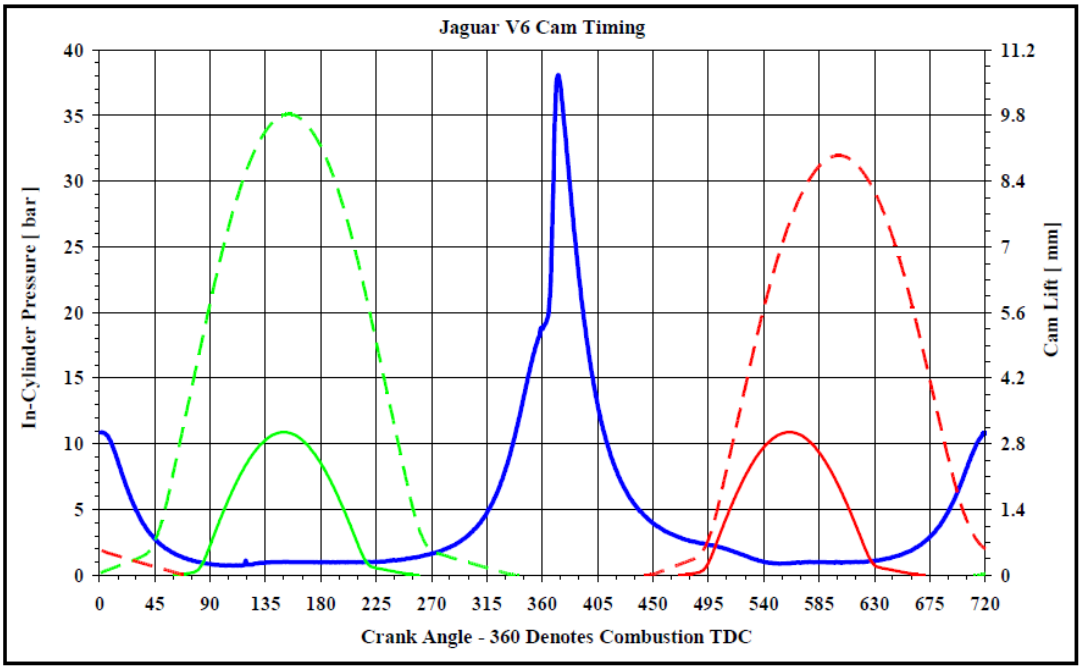

Figure 10: Cam timing for Jaguar research engine

Base Engine	3.0L Jaguar research V6, 24-V, GDI
Fuel	ULG95 (EN228)
Engine Speed	1500, 2000, 2500 rpm
Bore	89 mm
Stroke	79.5 mm
Compression Ratio	11.3
VCT	Intake and Exhaust, variable
CPS	Intake and Exhaust, variable (High and low lift cams)
Internal EGR trapping	Yes, variable
Intake Air Heating/cooling	Yes, variable
Supercharging	Yes, variable

Table 7: Engine specification summary

The HCCI operation is achieved by internal EGR, using negative valve overlap which traps exhaust gasses in order to retain enough energy for auto-ignition. Xu et al.[32] have presented possibilities of controlling HCCI which include: inlet air temperature, compression ratio, high internal EGR rate (trapped residuals), fuel blending, fuel additives and fuel reforming. Residual trapping seems to be an interesting method due its implementation flexibility for many different engine configurations. Furthermore, it can also be combined with the other aforementioned methods for HCCI control. The penalty of HCCI implementation by the residuals trapping is typically the limitation of its operating envelope. At the low load boundary it is limited by misfire due to limited tolerance for EGR. Whereas, at the high load boundary the limitation is typically due to knock tendencies. The restricted operating envelope forces the use of SI combustion outside the HCCI operating region, therefore the CPS system which allows switching to internal EGR trapping has been chosen. Valve timing is defined here by the inlet valve opening (IVO) and the exhaust valve closing (EVC) point: they represent the crank angle measured from TDC at gas exchange denotes as 720(0) deg. Exhaust valve timing is expressed in degrees CA before TDC and inlet valve timing in degrees CA after TDC. The HCCI starting procedure involves a warm-up period when the engine is operated in SI mode until oil and coolant temperature reach 90ºC.

In the HCCI mode the engine is operated with a wide open throttle. The engine is equipped with a thermal management (T.M.) system as shown in Figure 11. By controlling three throttles it is possible to control the air flow and as a result, the air temperature. The first throttle adjusts the amount of air passing through the heating box while the next two control the flow between the intercooler and the mixing box. This solution allows temperature control within a relatively small time constant. A mathematical description of the T.M. system is presented in Sections 3.5 and 3.6.

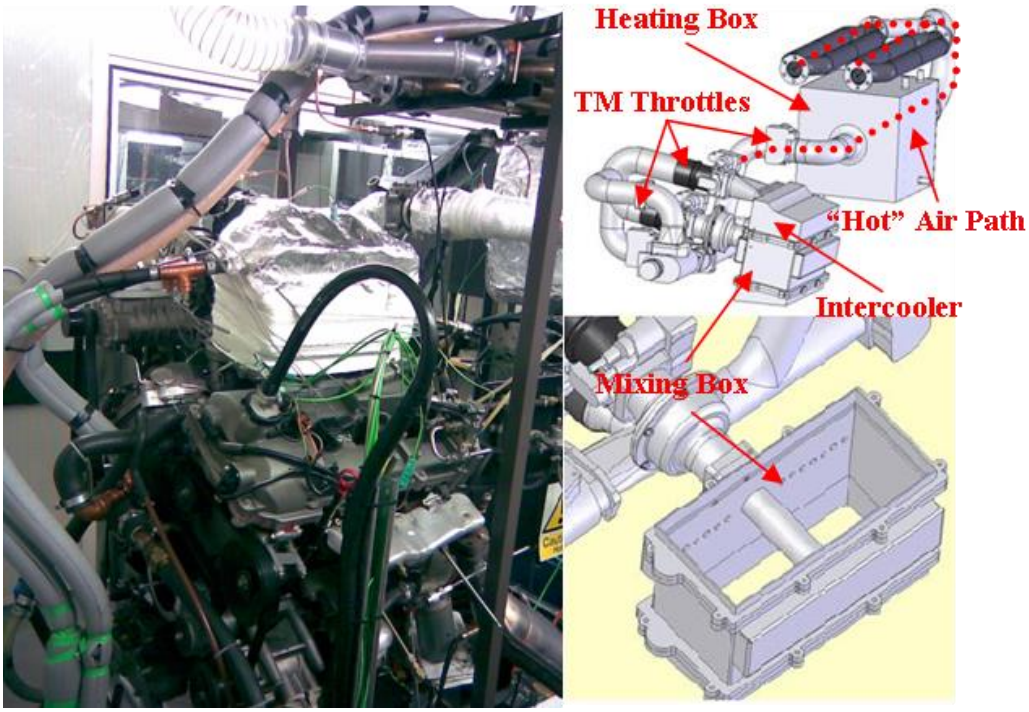

Figure 11: Research engine and thermal management system

The engine is coupled with a Froude EC38 eddy current dynamometer. In addition an electric motor is installed which allows recording of a sample when the engine is motored. Connection between the engine and the dynamometer is made by a shaft with universal CV joints at both ends. During all tests the dynamometer was operated at "constant speed" mode in which the controller keeps to a set speed regardless of engine load. When the engine is powered by the electric motor, the controller keeps a set speed with a 10% offset. This offset allows the system to recognise when the

engine is not firing and electric motor support is required to keep the requested speed The values of trapped residuals (TR) are calculated based on the in-cylinder volume when exhaust valve is closing. In-cylinder pressure is measured and the gas temperature is assumed to be equal to the temperature measured in the exhaust port.

Parameters such as ambient air temperature and humidity have been monitored during testing and kept at the same level for each single group of tests. In order to maintain good quality results, four samples were taken every day; two samples in SI and two in HCCI operation (firing and motoring mode). These samples were used as a measurement validation and engine check. For each day's test, a randomly selected condition has been repeated in order to validate data repeatability. HCCI operation is considered as stable when the coefficient of variation (COV) of net mean effective pressure (NMEP) is below 5%.

3.4.2 Cam Profile Switching System

Figure 12 shows the Cam Profile Switching (CPS) system with its major components. The CPS system is powered from the engine oil rail and by controlling the oil pressure, it is possible to switch cam lift from 9 to 3mm. In Figure 12 (View A and B), the details of the bucket design and configuration are presented. "View – A" represents the bucket configuration when the engine is running in SI mode (9mm cam lift). "View – B" represents the bucket configuration for HCCI mode (low cam lift – 3mm). Closing of the CPS solenoid valves causes an increase (up to 5bars – depending on the oil temperature) in oil pressure in the CPS oil rail. The high oil pressure engages the pin (Figure 12 B) into the slot (Figure 12 A), which in turn does not allow independent movement of the inner and outer bucket. From Figure 10 it can be observed that the SI cam profile completely covers the HCCI profile. Therefore, the high lift cam profile (Figure 13) is forcing the valve to open and there is no

interference between the high and low lift profiles. When HCCI operation is required, solenoid valves are released causing oil pressure in the CPS oil rail to drop to 0 bar (gauge). This allows the spring fitted into the pin, to pull the pin inside the inner bucket.

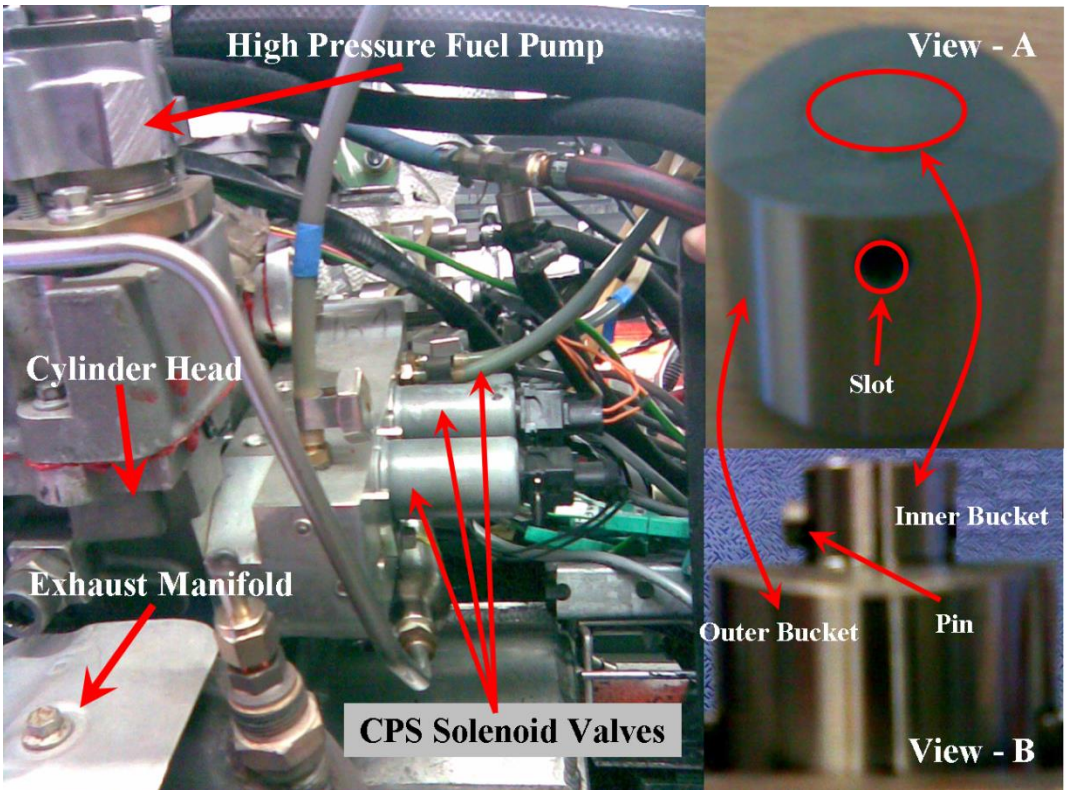

Figure 12: CPS system on the engine and details of the bucket design

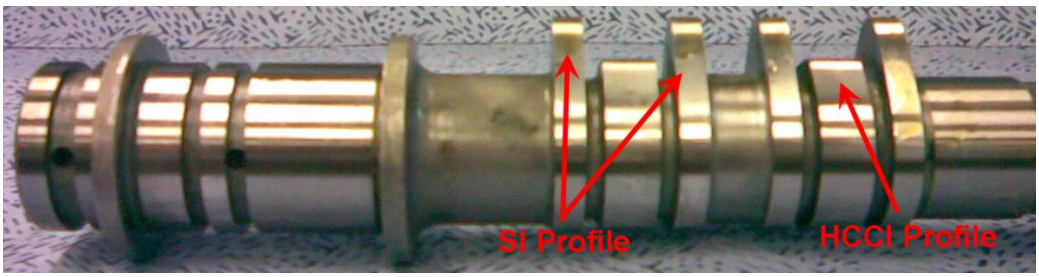

Figure 13: Camshaft with SI and HCCI profiles

When the pin (Figure 12 B) is disengaged from the slot (Figure 12 A), the inner and outer bucket can move independently. The high cam profile (SI) starts to push the outer bucket; however, it slides down without forcing the valve to open, as the valve

stem is connected to the inner bucket. When the low lift cam profile (HCCI) is pressing the inner bucket the valve is forced to open. The cross section of the system in two operating conditions is presented in Figure 14

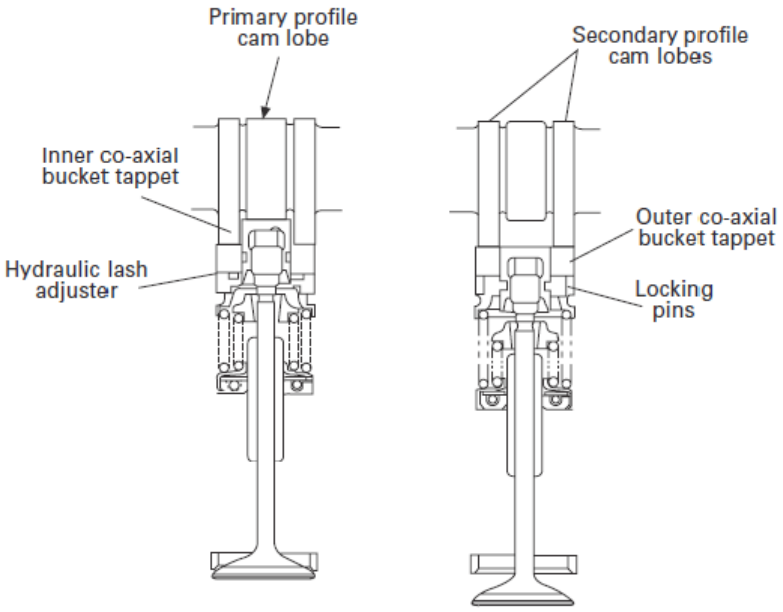

Figure 14: Cross section of CPS system as described by Zhao [94]

3.4.3 Supercharger

The general concept of boost pressure control is shown in Figure 15. When no boosting is required the "Bypass Throttle" stays fully open. When boosting is necessary, the engine operator will close the "Bypass Throttle" gradually, until inlet manifold pressure rises to the required level. Any change in the engine operating conditions (e.g. inlet or exhaust valve timing change) leads to the necessity of adjusting the "Bypass Throttle", in order to keep boost pressure at the set level. Both inlet manifold pressure measurements and "Bypass Throttle" control are maintained electrically through dSPACE system. Through all experiments run on the Jaguar V6 HCCI engine at The University of Birmingham two EATON superchargers were in use (model M62 and M24). Model M62 (Figure 16) was used in the early stage of the HCCI tests and prior the Thermal Management system was installed. It was discovered that due to the much smaller flow rate on HCCI mode, the operating map

of the M62 model does not cover the required flow rate to pressure ratio. Thus the M24 superchargerwas installed, as explained in Section 3.3.3. All HCCI tests with Thermal Management were continued with the M24 supercharger model (Eaton M24 specifications in Figure 9).

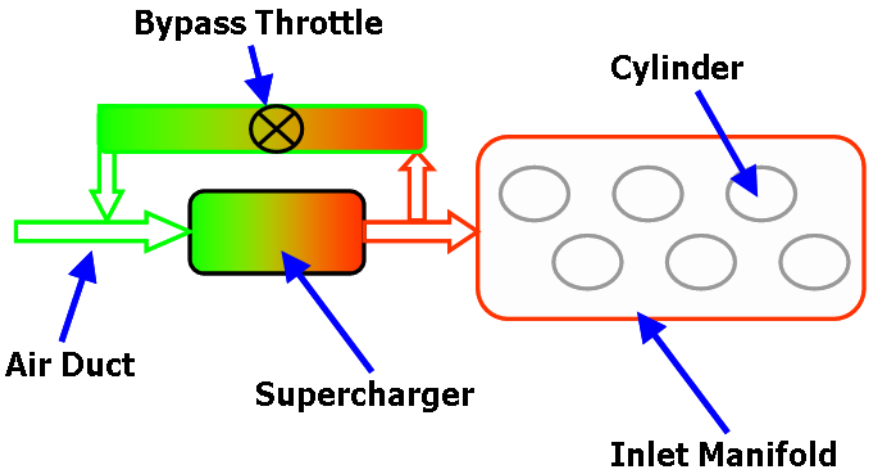

Figure 15: Sketch of boost pressure control

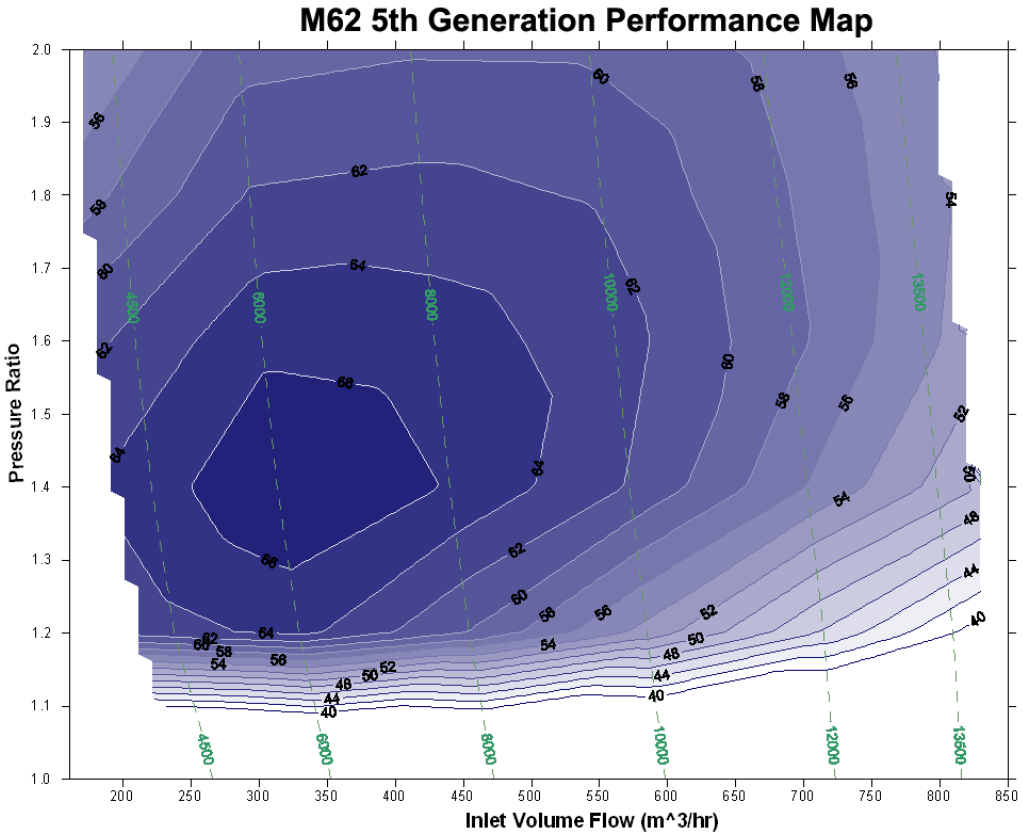

Figure 16: Performance map for EATON M62 supercharger

3.4.4 Thermal Management System

The research engine is equipped with a Thermal Management (T.M.) system. The main purpose of this system is to control the temperature of the charge air. The CAD drawing of the system was installed on the engine is shown in Figure 17. A schematic diagram of T.M. system is presented in Figure 18.

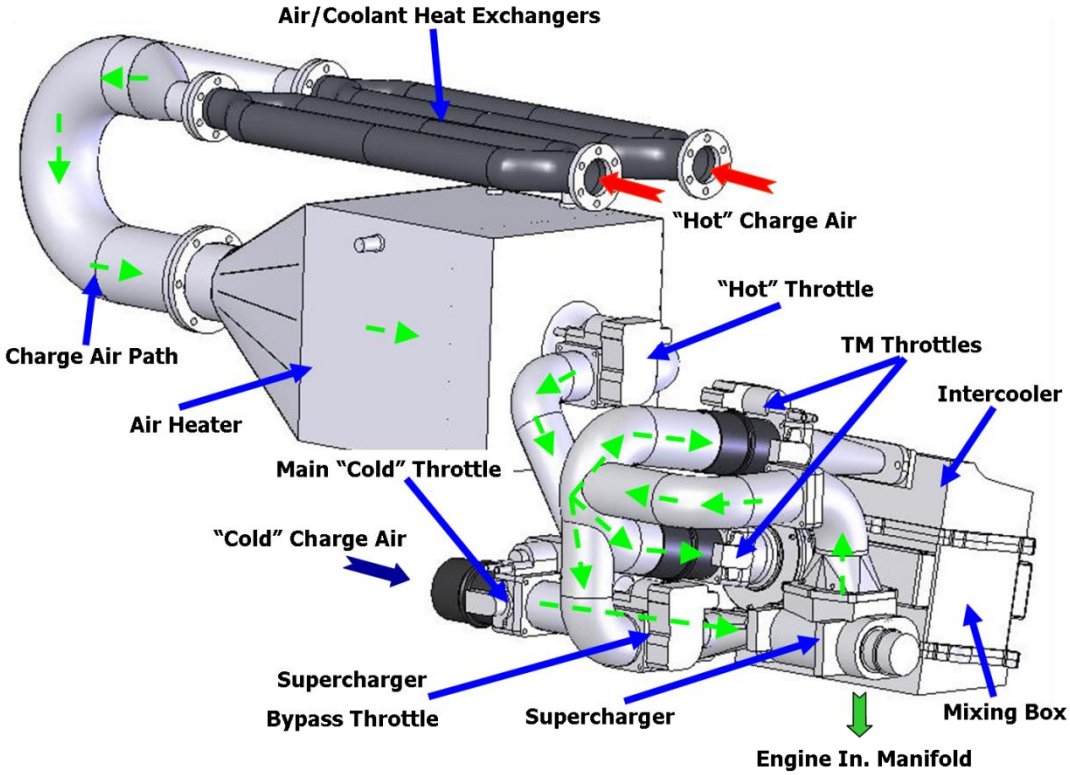

Figure 17: CHASE Thermal management system arrangement with notations

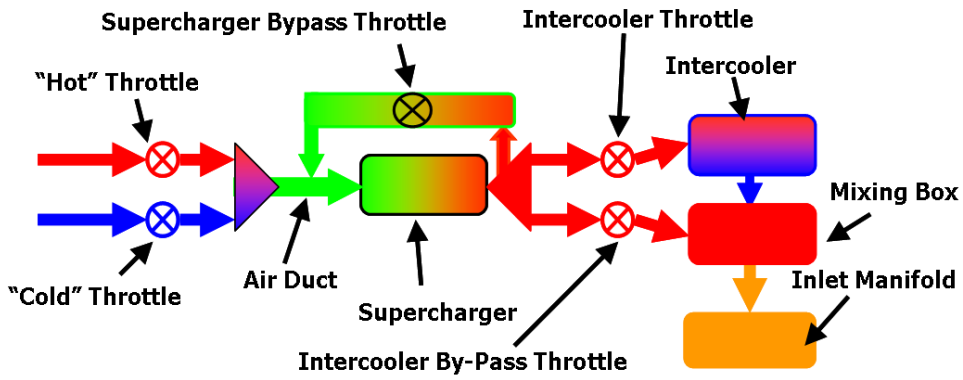

Figure 18: Schematic diagram of Thermal Management system

The components of this system include: an air/coolant heat exchanger, electric heaters, three throttles, a supercharger, intercooler and a mixing box. By opening or closing the main "cold" throttle and the "hot" throttle the charge air will pass through a "cold" or "hot" air path. If the main ("cold") throttle is opened and "hot" throttle is closed air pass without heating into the inlet manifold. When "hot" throttle is opened and the main throttle is closed, air passes through the heat exchanger, electric heaters, by the supercharger and onto a junction in which it can be directed in two paths. Firstly it can be routed directly into the mixing box and into the engine. Secondly it can pass through the intercooler if cooling is required. Charge air diversion is made by two throttles marked as "T.M. Throttles" in Figure 17. During normal SI operation the air can pass via the intercooler by closing one of the throttles (however if cooling is not required the airflow can easily be diverted straight into the mixing box. The temperature of the air leaving the air heater box was controlled by a SIMULINK model through a PID controller. Based on the temperature difference between requested and measured values, a PID controller generates a PWM signal which triggers a relay and in turns the electric heaters. An external controller maintains the constant temperature of water flowing through the intercooler. When the charge air is boosted, air is compressed which increases the temperature and this increase is utilised in that less heat from the heater box is required. As shown in Figure 17, the "hot" part of the thermal management system consists of long pipes which also cause an extra pressure drop. This additional pressure drop appears to be about 0.1 bar in the inlet manifold, compared with the case when air passes through the "cold" part of the T.M. system. A supercharger has been used to maintain the pressure in the inlet manifold when the "hot" part of T.M. system was used. The supercharger bypass throttle has been adjusted to compensate the additional pressure drop.

3.4.5 On Board Fuel Reforming

A sketch presenting principles of an on board fuel reformer structure on the engine, as well as a reactor sketch, has been presented in Figure 19.

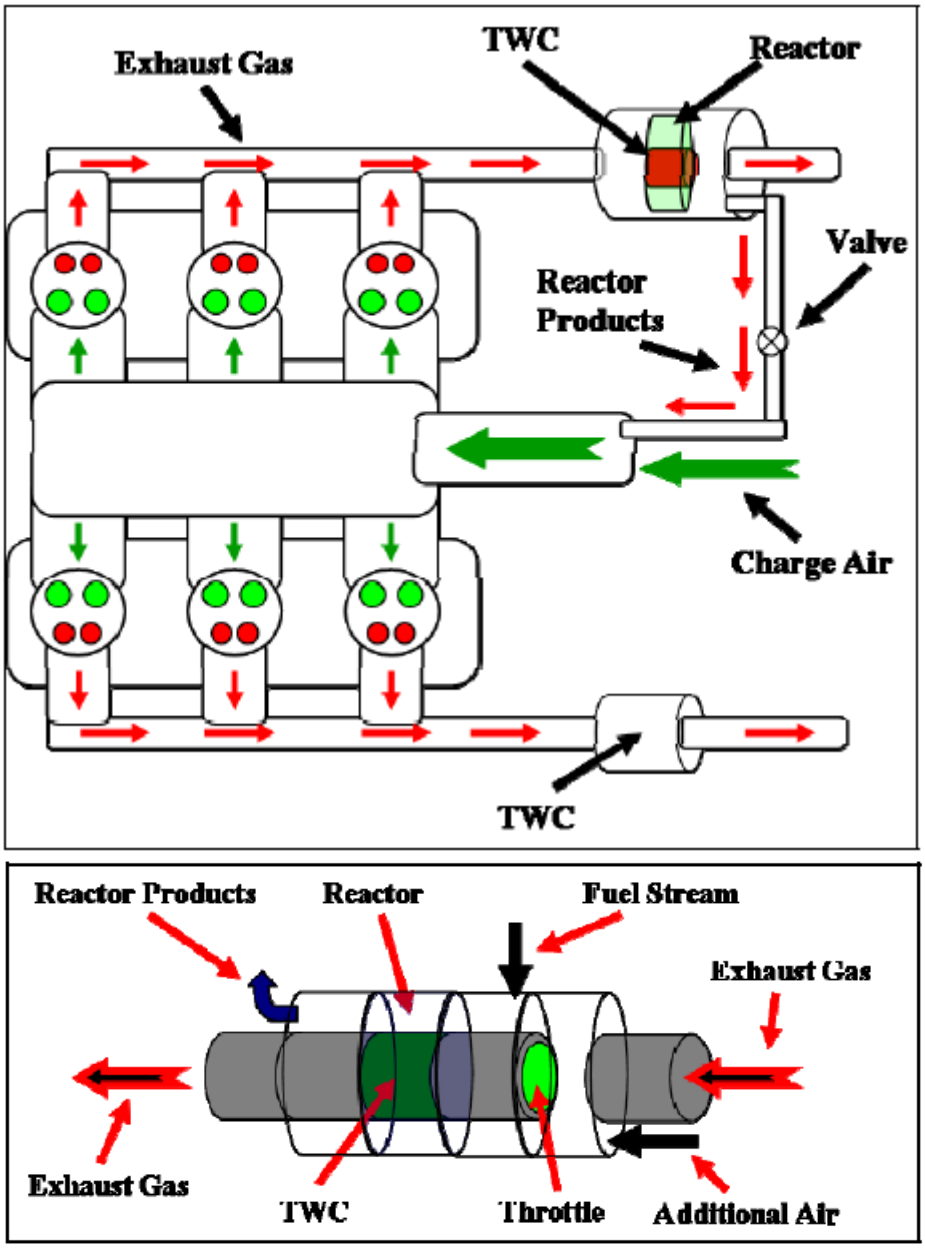

Figure 19: Sketch of on board fuel reforming structure (A) and reactor design outline (B) M. Ashur [35]

The details of the reactor design and performance optimisation have been described by M.Ashur in his PhD thesis [35]. In the present work only the effect of Reformed Exhaust Gas Recirculation (REGR) on HCCI engine performance will be discussed. As has been shown in Figure 19 (B) the exhaust gas enters the combined Three Way

Catalyst (TWC) and reactor container. Figure 19 (A) and (B) have shown the path of the gas in the system. When no reforming is required all gas passes through the TWC.

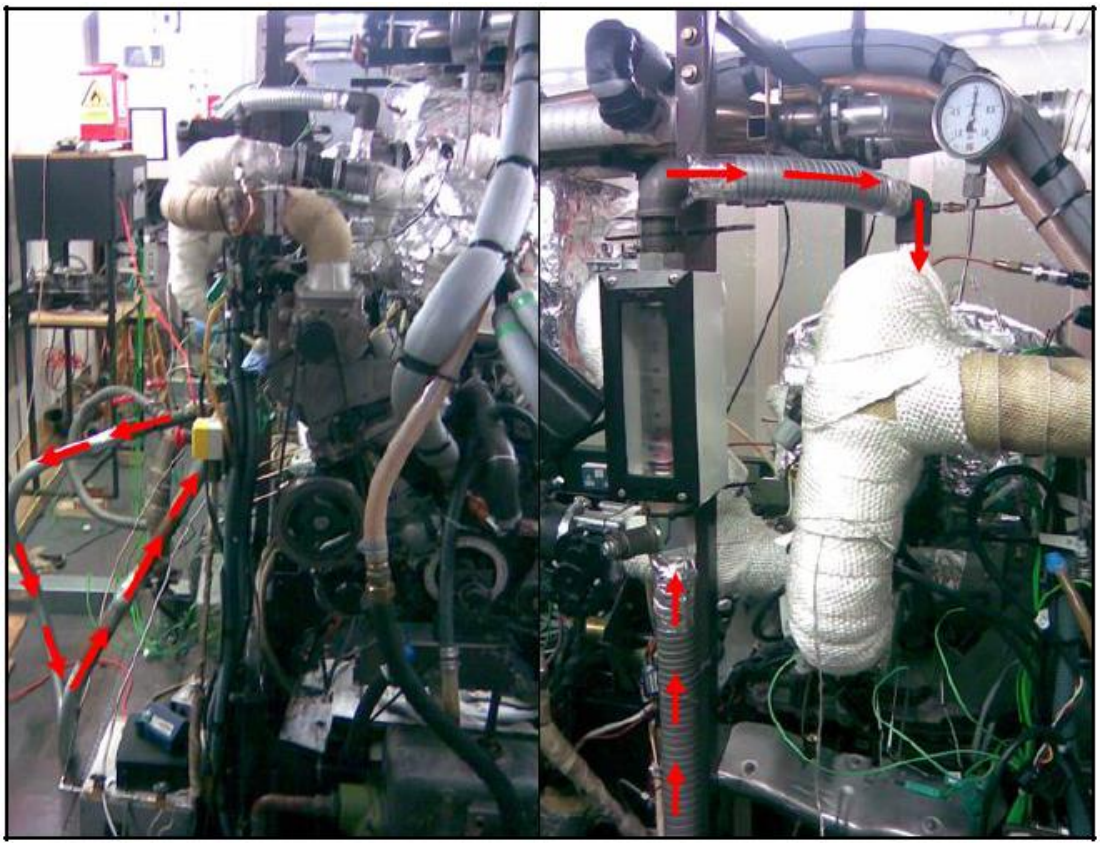

Figure 20: On-board fuel reforming as connected into thermal management system on the engine

When engine operating condition has reached the point that REGR has to be added, the control throttle can be adjusted to divert the required amount of exhaust gas into the reactor. Diverted fumes have to be mixed with a specific amount of the fuel stream in order to optimise reactor performance. In order to improve the fumes-fuel mixing process, the fuel stream has been injected via a number of circumferential holes. The prepared fuel-fumes mixture enters the reactor where reforming reactions occur. Reformer products (containing CO, CO2, H2 and UHC) have been collected on the other side of the reactor and are introduced into the engine inlet manifold. During tests which have been presented in this thesis the REGR has been additionally cooled before entering the inlet manifold. Cooling has been done by an increased length of pipe connecting the reactor with the inlet manifold: the pipe has not been insulated in

order to deliver a sufficient amount of heat transfer. The temperature of the REGR has been adjusted to match the charge air temperature. This effort has been exerted in order to separate the effect of REGR on engine performance from thermal effect on HCCI combustion. It is commonly known that by increasing charge temperature the low load limit can be reduced. Finally, the REGR has been passed through a flow meter in order to control the amount of REGR addition at 10%. The flow of the REGR as described above has been organised on the engine as shown in Figure 20.

3.4.6 SIMULINK Control Model

In order to control the engine, an in-house MATLAB / SIMULINK algorithm has been developed and employed in connection with a dSPACE system. The system is a computer controlled unit which enables users to control and record engine data. Kistler 6052A pressure transducers are fitted into the wall of the combustion chambers and measure in-cylinder pressures in all 6 cylinders with a 1 crank angle degree resolution. This frequency is dictated by the Baumer shaft encoder fitted into the engine shaft. Other parameters are measured with 100Hz which is the data sampling frequency of dSPACE system.

Recorded in-cylinder pressure data is used for on-line calculation of peak cylinder pressure, values of Net Mean Effective Pressure (NMEP), coefficient of variation of NMEP and rate of pressure rise. Calculated values can be instantly observed in dSPACE – Control Desk software.

Control of coolant and engine oil temperature is done through a PID controller implemented in the SIMULINK model. This controller generates a PWM signal which, depending on the temperature difference (requested and measured), triggers the relays. In turn, relays open and close the solenoid valves, adjusting the amount of

cooling water passing through the heat exchanger. All temperatures on the system are measured with K type thermocouples.

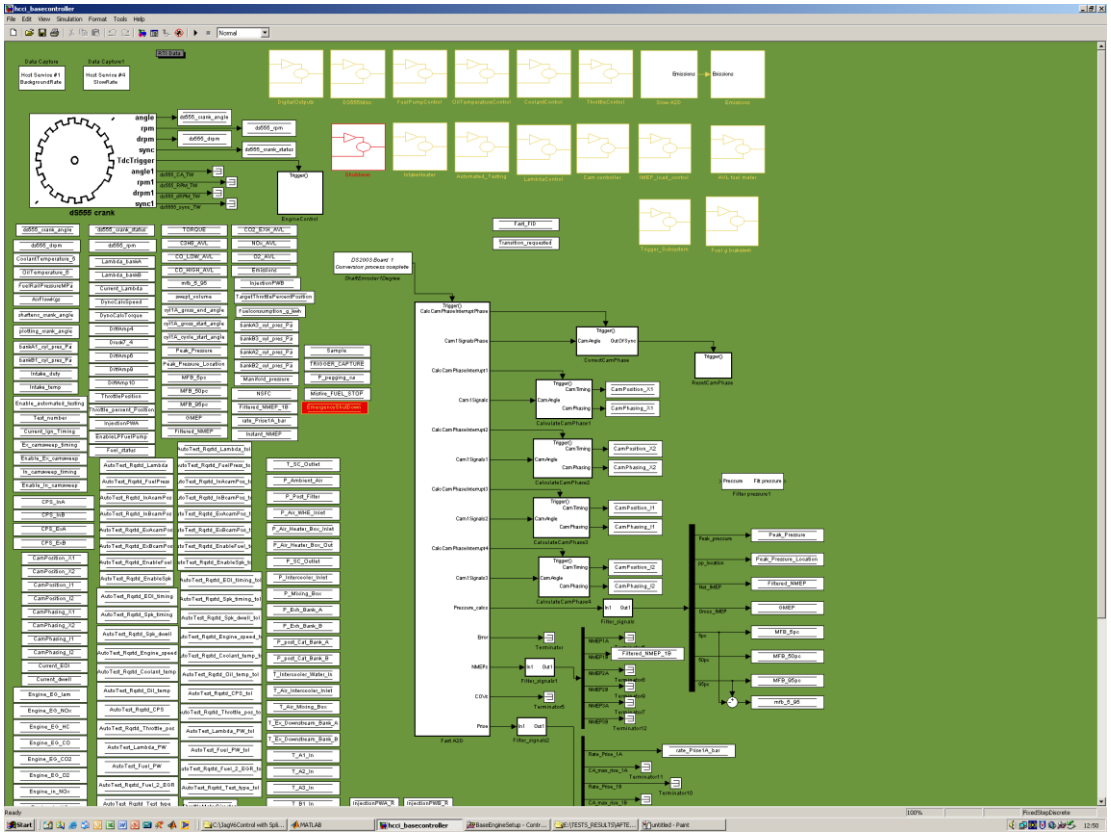

Figure 21: SIMULINK model for engine control

The amount of fuel injected is adjusted separately in each engine bank. For this purpose a closed loop lambda controller based on two wide range lambda sensors (one on each bank) was used. A single fuel injection strategy has been used with the injection timing set during the Negative Valve Overlap (NVO) period. This injection strategy allows the utilisation of the internal fuel reforming effect, which supports stable HCCI operation at low loads [51], [95]. Furthermore tests with split injection with different injection timing have been carried out by J Misztal [1]. The print screen of the SIMULINK model and Control Desk layouts are presented in Figure 21 and Figure 22. The development of the SIMULINK model and main Control Desk layout

was a joint effort of many people, however the first developers were Dr Andy Durrant and Dr Trevor Wilson.

The SIMULINK control model can be divided into four main parts:

- fast analogue inputs – record and process signals, e.g. in-cylinder pressures, cams sensor
- slow analogue inputs – record and process signals, e.g. all temperatures, pressures (other than in-cylinder), fuel level, engine speed and torque etc.
- digital outputs – on/off signals – trigger auxiliary equipment, e.g. low pressure fuel pump, coolant and oil temperature control, filling fuel balance
- fast digital outputs – used to generate the PWM signals for controlling throttles, cams position actuators etc.

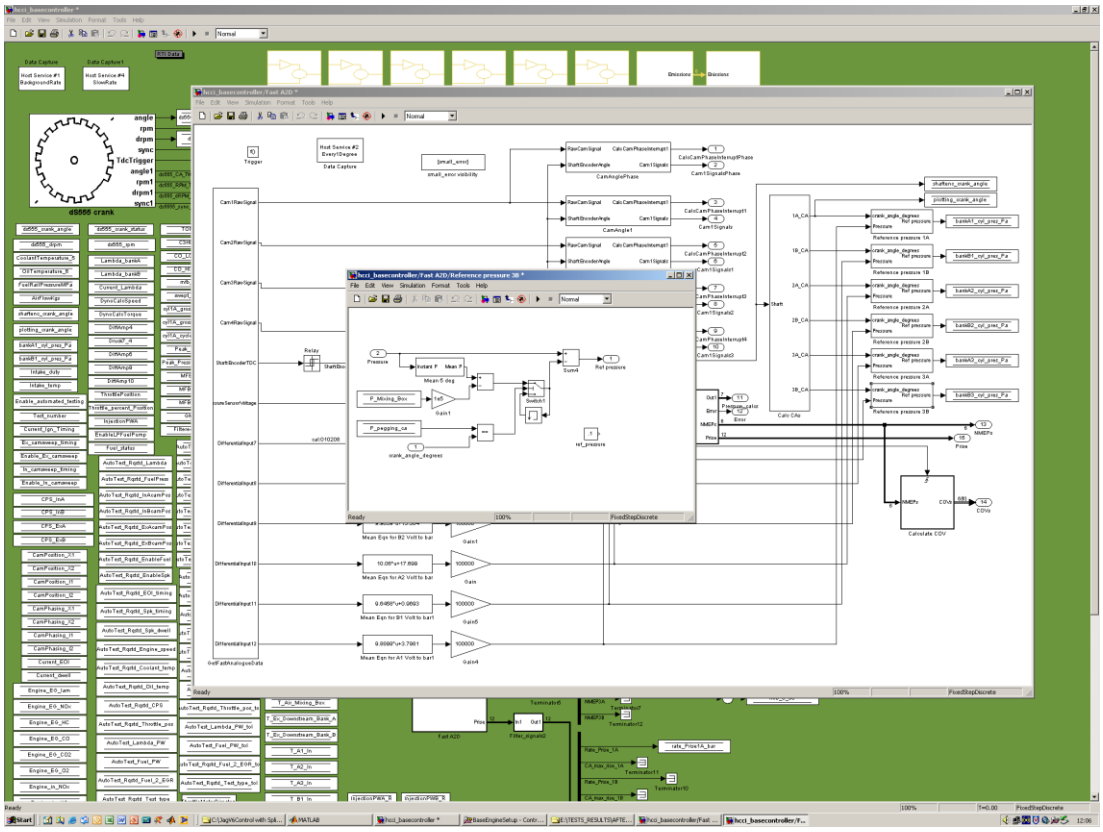

Figure 22: Control Desk panel – interface for controlling SIMULINK model

3.4.7 Test Cell Wiring

The heart of the control system is the wiring between the control PC, dSPACE, the interface boxes and the engine. The sketch of the wiring diagram is presented in Figure 23.

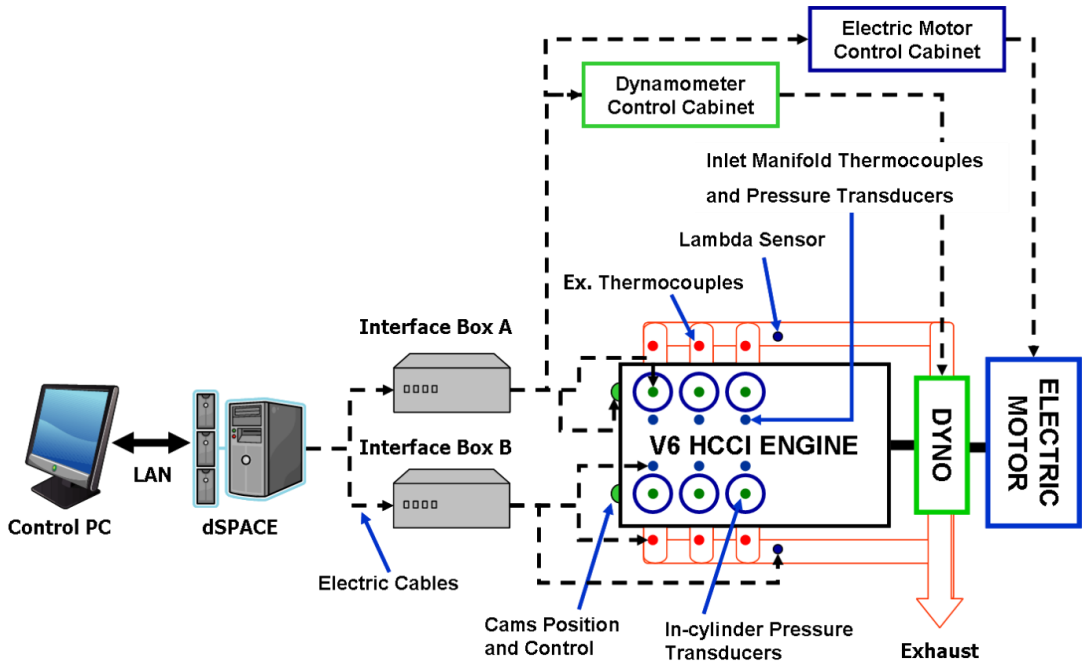

Figure 23: Sketch of wiring diagram

The control PC is connected with the dSPACE system through a LAN cable. The dSPACE is a modular system which in the existing configuration consists of:

- DS1005 PPC Board, a processor board which can give the real time calculation power to a modular system and can also provide the interface to the I/O boards and the host (control) PC.
- DS2003 Multi-Channel A/D Board – three of these boards digitising the analogue inputs signals with a total of 32 channels each.
- DS2003 Multi-Channel A/D Board – one of the 2003 boards is triggered by an external trigger (shaft encoder). This board digitises signals from cam sensors and in-cylinder pressure sensors. A maximum of 16 channels on this board can be used.

- DS2201 Multi I/O Board – this board has a wide range of features, however, in the existing configuration only four channels are used to generate PWM signals for throttle control.
- DS555 MPC555 Board – is a rapid prototyping board for the Motorola MRC555 processor. In the existing configuration it is responsible for injection and ignition control.
- DS4002 Timing and Digital I/O Board – features eight programmable timing I/O channels. In addition 32 general purpose digital I/O lines and two external interrupt lines are provided. The main task in the research engine is PWM signal generation for the VCT system control and the generation of TTL signals, which allows control of coolant valves, the fuel pump, cam profile switch (CPS) system and the charge air heaters.

The dSPACE system is connected by two interface boxes. Interface box "A" is responsible for processing in-cylinder pressure signals, cam position signals and other signals which control the engine and auxiliary systems. Interface box "B" is a place where all other sensors (thermocouples, pressure transducers in the inlet and exhaust manifold, lambda sensors, a humidity sensor, torque and engine speed readings etc) are connected and signals are conditioned for dSPACE board digitising. Figure 3.7-1 shows the most important sensors installed on the engine. All sensors are symmetric for both engine banks. The presented sketch does not include all installed sensors.

3.4.8 Fuel Consumption Measurements

At the core of the fuel measurement system shown in Figure 24 is an AVL fuel balancer. The amount of fuel consumed by the engine is measured by the mass of the fuel vessel. When the engine consumes the fuel the mass of the vessel decreases. By knowing the difference in mass between each time steps it is possible to calculate the

fuel consumption. The SIMULINK model calculates the mass of the fuel balance tank and with a 5 second time interval calculates the amount of fuel used by the engine. This process is fully automated and can be adjusted to suit the user's needs by adjusting the time interval during which mass reduction is calculated. The system automatically refills the tank when the fuel level drops below a set level; therefore, continuous engine operation is possible.

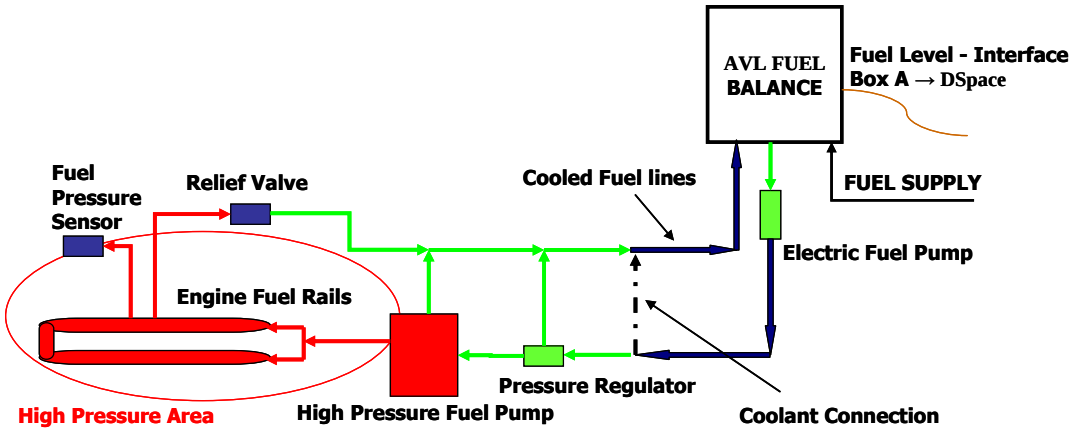

Figure 24: Sketch of fuel system on the research engine

3.4.9 Emission Measurements

Gas analysis includes measurement of carbon dioxide, carbon monoxide (NDIR – Non-Dispersive Infrared), hydrocarbons (FID – Flame Ionization Detector), oxygen (paramagnetic method) and NOx (chemiluminescence) emissions using an AVL CEB1 emission bench. The NOx analyzer has two separate ranges (2500ppm and 60ppm) for better accuracy when engine NOx emission is low.

Particulates measurements (PM) including size distribution have been carried out using a DMS500 Fast Particulate Spectrometer. A DMS system has been in use in a number of publications [97],[98]. Advantages of the DMS500 system are: flexible sampling and dilution options, fast time response, particles size range 5- 2500nm, data logging, and real time mass calculation. The operating principles are based on measurements of electrical mobility. Electrical mobility is a function of charge on the

particle and its aerodynamic drag. By knowing the electrical mobility the particle diameter can be calculated. Particles which are of low electrical mobility will travel further down the measuring column than highly mobile particles. Finally particles impinge upon one of a series of electrometer rings along the length of the column. These measure the electrical current from the arrival of charged particles, and thus their mobility. A schematic drawing of the measurement layout has been presented in Figure 25.

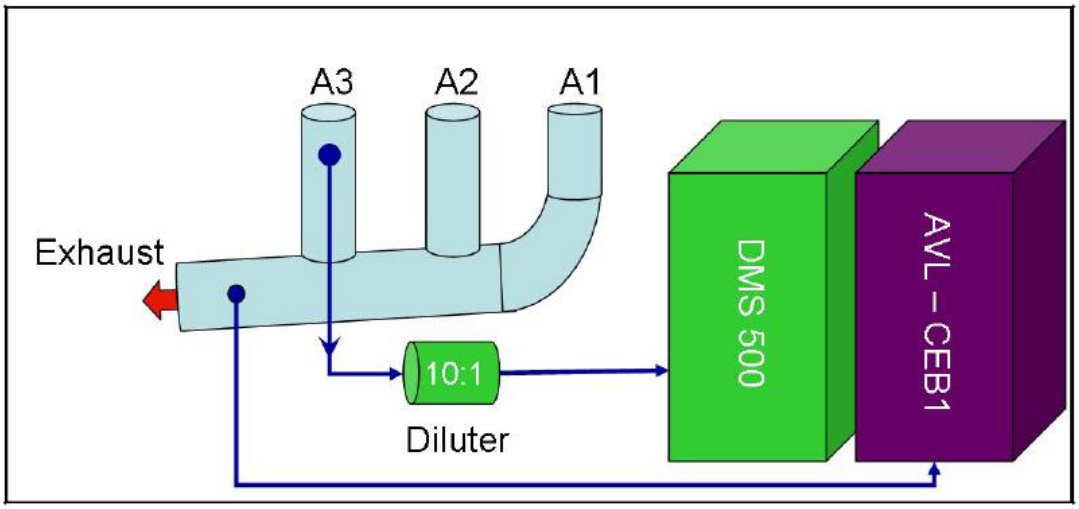

Figure 25: Sketch of emission measurements system

3.4.10 Procedures Used for Data Processing

The data processing procedure involves averaging over 100 consecutive pressure cycles (including pressures other than in-cylinder), temperatures, fuel consumption and other parameters. Parameters such as: NMEP, rate of pressure rise, COV of NMEP and fuel consumption are calculated in the SIMULINK model; only an averaged value is calculated during data processing. Parameters such as: mass fraction burnt, rate of heat release, maximum peak pressure, and maximum peak pressure location are calculated from recorded in-cylinder pressure data and used for further analysis. All data processing has been accomplished using MATLAB software. Since data is acquired with quite a large variation of ambient conditions, standardisation to

normal conditions has to be calculated. Methods and procedures used for data processing are described in subsequent sections.

3.4.11 In-Cylinder Pressure Sensors Referencing

One of the disadvantages of piezoelectric pressure transducers is their sensitivity to temperature. This sensitivity can cause the piezoelectric sensor reading to drift, therefore, the constant co-efficient has to be modified to re-calibrate the reading. One of the most popular ways of pressure referencing ("pegging") is based on the assumption that in-cylinder pressure is equal to inlet manifold pressure when the piston is at BDC. The SIMULINK block which calculates the coefficient for incylinder pressure is shown in Figure 26.

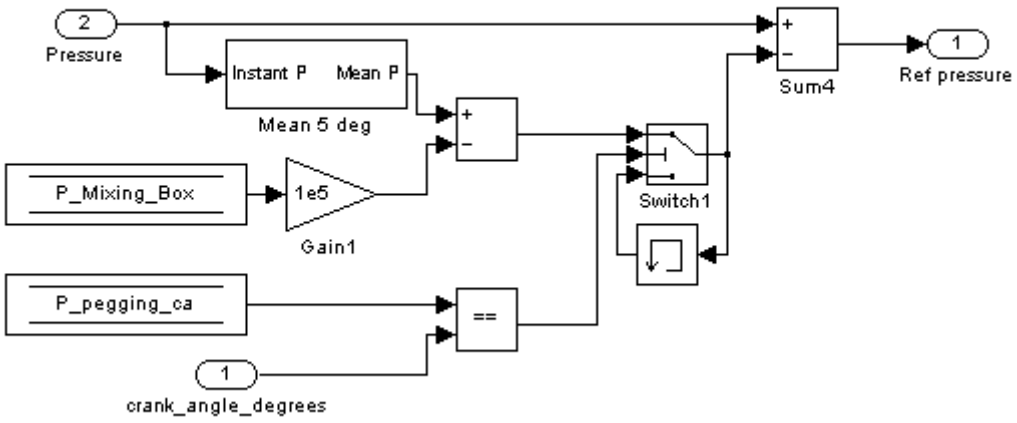

Figure 26: In-cylinder pressure referencing

When current crank angle is equal to specified crank angle ("P_pegging_ca" – 180º for the BDC) the coefficient is calculated as a difference between pressures in inlet manifold ("P_Mixing_Box") and in-cylinder pressure. The value of in-cylinder pressure is taken as an average for the last 5 CAD. The calculated coefficient is kept in memory until the next cycle induction at BDC. The final in-cylinder pressure is calculated as the difference between sensor readings and calculated coefficient. The procedure is the same for each cylinder.

3.4.12 Calculation of Specific Emission

The calculations of specific emissions are based on the directive 1999/96/EC of the European Parliament and of the Council of the European Union. This document describes the procedures and rules which should be applied when gaseous emissions from internal combustion engines are considered. The calculations include the dry to wet correction (AVL system measures only HC on wet base), NOx correction for humidity and temperature, calculation of the emission mass flow rates and finally calculation of the specific emissions. Equations used for emission conversion are as follows:

- dry to wet correction

$$conc(wet) = K_w \cdot conc(dry) \quad and, \quad K_w = (1 - F_{FH} \cdot \frac{\dot{m}_{fuel}}{\dot{m}_{air-dry}}) - K_{w2}$$

$$F_{FH} = \frac{1.969}{(1 + \frac{\dot{m}_{fuel}}{\dot{m}_{air-wet}})}; \quad K_{w2} = \frac{1.608 \cdot H_a}{1000 + (1.608 + H_a)}; \quad H_a = \frac{6.220 \cdot R_a \cdot p_a}{p_b - p_b \cdot R_a \cdot 10^{-2}}$$

$where:$

$H_a - g\ water\ per\ kg\ dry\ air$

$R_a - reletive\ humidity\ of\ \text{int}ake\ air, [\%]$

$p_a - saturation\ vapour\ pressure\ of\ the\ \text{int}ake\ air, [kPa]$

$p_b - total\ barometric\ pressure, [kPa]$

- NOx correction for humidity and temperature – due to NOx sensitivity to ambient temperature and humidity correction has to be made as

$$K_H = \frac{1}{1 + A \cdot (H_a - 10.71) + B \cdot (T_a - 298)} \quad and:$$

$$A = 0.309 \cdot \frac{\dot{m}_{fuel}}{\dot{m}_{air-dry}} - 0.0266; \quad B = -0.209 \cdot \frac{\dot{m}_{fuel}}{\dot{m}_{air-dry}} + 0.00954;$$

$where:$

$T_a - air\ temperature, \quad [K]$

- calculation of the emission mass flow rates – with the assumption that exhaust gas density is 1.293 kg/m3 at standard conditions (T=273K and p=101.3 kPa)

$$NO_{x-mass} = 0.001587 \cdot NO_{x-conc} \cdot K_H \cdot \dot{m}_{exhaust-wet}; \quad [g/h]$$
$$CO_{mass} = 0.000966 \cdot CO_{conc} \cdot K_H \cdot \dot{m}_{exhaust-wet}; \quad [g/h]$$
$$HC_{mass} = 0.000479 \cdot HC_{conc} \cdot K_H \cdot \dot{m}_{exhaust-wet}; \quad [g/h]$$

$$NO_{x-conc}, CO_{conc}, HC_{conc} - \textit{average concentrations (ppm) in the raw exhaust gas}$$

- calculation of the specific emissions

$$\overline{NO}_x = \frac{NO_{x-mass}}{P}; \qquad \overline{CO}_x = \frac{CO_{mass}}{P}; \qquad \overline{HC}_x = \frac{HC_{mass}}{P}$$

3.4.13 Calculation of the Mass Fraction Burnt

R. Stone[38] described the approach commonly used for burn rate analysis, originally devised by Rassweiler and Withrow. This technique is based on the assumption that in-cylinder pressure rise is due to two factors: pressure rise due to volume change and pressure rise due to combustion. Another assumption is made that pressure rise due to volume change can be modelled as a polytrophic process. Polytrophic exponent "k" can be calculated based on available in-cylinder pressure traces and cylinder volumes for each crank angle. Applying this assumption rise of in-cylinder pressure due to combustion can be calculated as follows:

$$\Delta p_c = p(\Theta+1) - p(\Theta) \cdot \left[\frac{V(\Theta)}{V(\Theta+1)}\right]^k; \qquad \textit{where:}$$

Δp_c – *pressure rise due to combustion*
$p(\Theta+1)$ – *in – cylinder pressure for crank angle* $i+1$
$p(\Theta)$ – *in – cylinder pressure for crank angle* i
$V(\Theta+1)$ – *cylinder volume for crank angle* $i+1$
$V(\Theta)$ – *cylinder volume for crank angle* i

Due to volume changes the pressure rise due to combustion is not directly proportional to the mass of fuel burned and has to be scaled, e.g. by the clearance volume at TDC. When pressure rise due to combustion reaches zero (after N crank angles) the end of combustion occurs. Assuming that scaled pressure rise due to combustion is proportional to the mass fraction burned, MFB will be:

$$MFB = \frac{\sum_{0}^{i} \Delta p_{c-scaled}}{\sum_{0}^{N} \Delta p_{c-scaled}}$$

3.4.14 Calculation of the Net Rate of Heat Release

R. Stone [38] described the approach used for the rate of heat release calculation. One of the first assumptions is that there is only one zone in the cylinder, which in turn leads to fully mixed reactants and products. Applying the 1st Law of Thermodynamics to the control volume and evaluating each term of that equation with support of semi-perfect gas behaviour, this assumption leads to the equation for net heat release:

$$\frac{dQ_n}{d\theta} = \frac{\gamma}{\gamma - 1} \cdot p \cdot \frac{dV}{d\theta} + \frac{1}{\gamma - 1} \cdot V \cdot \frac{dp}{d\theta}$$

The stated equation above can also be used for temperature calculations. Gas properties vary with temperature but due to relatively small variations between two consecutive crank angles, it is acceptable to use temperature from previous crank angles to calculate gas properties.

R. Stone [38] also proposed an empirical equation to calculate the internal energy "u" and gas constant "R". These equations were first proposed by Krieger and Borman. Internal energy is known as is the gas constant, therefore, the specific heat ratio $\gamma = c_p/c_v$ can be calculated.

$$u = K_1(T) - K_2(T)\cdot\phi; \quad [kJ/(kg\ of\ original\ air)] \quad where:$$

$$K_1(T) = 0.692\cdot T + 39.17\cdot 10^{-6}\cdot T^2 + 52.9\cdot 10^{-9}\cdot T^3 - 228.62\cdot 10^{-13}\cdot T^4 + \\ + 277.58\cdot 10^{17}\cdot T^5$$

$$K_2(T) = 3049.33 - 5.7\cdot 10^{-2}\cdot T - 9.5\cdot 10^{-5}\cdot T^2 + 21.53\cdot 10^{-9}\cdot T^3 - 200.26\cdot 10^{-14}\cdot T^4$$

$$with\ the\ equation\ for\ the\ gas\ const\ ant:$$

$$R = 0.287 + 0.020\cdot\phi; \quad [kJ/(kg\ of\ original\ air)K]$$

$$\phi - equivalence\ ratio$$

$$T - temperature\ [K]$$

The equations described above were applied to each of the 100 consecutive cycles during sampling and in the end the average rate of net heat release has been established. In our processing scripts if the temperature is above 1450K, the modification to the equations for dissociation have been implemented. The equations for this modification have not been presented but can easily be obtained from R. Stone [38].

3.4.15 Analysis of Uncertainties in Recorded Data

In this section aims to summarise any possibilities for measuring errors that may have occurred during data recording. For this purpose, a summary of manufacturers' accuracy reports with comments regarding specific phenomenon related to existing engine test cells are provided. This summary will include accuracy and error information for the following equipment (systems): dynamometer, fuel consumption system, pressure transducers and gaseous emissions equipment.

For the purpose of controlling the Froude EC38 eddy current dynamometer a DSG – Series 2000 Engine Test Bed Control System has been utilised. This system can control the dynamometer with set point time drift at 0.05% per month and a set point temperature coefficient of 0.01% per ºC. The control regulation is better than

±0.1% of the full range. The effect of mains voltage changes is negligible. The measurements of torque are provided by the strain load-cell and the speed is measured by magnetic pick-up and a 60 toothed wheel. The digital speed indicator has an accuracy of ±1 rev/min. The digital torque indicator has an accuracy of ±0.05%FSD (Full Scale Deflection).

Fuel consumption has been measured with the use of AVL 730 Dynamic Fuel Consumption Measuring Equipment. Following the AVL specification, the accuracy of the entire measuring system can be calculated as a sum of: fuel mass consumed (±0.12%), pendulum mass (±0.005%) and display resolution. Furthermore, the accuracy of the readings depends on the fuel mass consumed during measurement. The Simulink model settings lead to fuel consumption measurements of approximately 2.5 to 10g. This in connection which the specification of the vessel installed in the laboratory leads to the accuracy of within 0.8 to 2.3%.

The in-cylinder pressure measurements have been carried out with the Kistler 6052B pressure sensor coupled with a Kistler 5011B charge amplifier. The pressure sensor sensitivity has been given as approximately 20pC/bar. The linearity has been measured by the manufacturer to below ±0.4% FSO (Full Scale Output). Additionally, Kistler provides data on short term drift and load change drift, as measured on a test engine at 1500rpm and 9bar of NMEP. The short term drift has been measured to below ±0.5bar, when the load change drift has been measured at 1.5bar/s. The charge amplifier has a linearity error of below ±0.05% FS (Full Scale). Drift of below ±0.03pC/s at 25ºC has been measured due to MOSFET leakage current.

The gaseous emissions have been measured with an AVL CEB1 emissions bench. Three main parameters have been specified for this type of equipment: drift,

noise and linearity. All of those parameters have been specified to within ±1.0% of full scale.

Particulate matter measurements have been performed with CAMBUSTION DMS500 instrument. Manufacturer specifies that the instrument is certified for use if the particulate size and number are as follows: particulate size is within 5% of the standard in the region of 5 to 300nm; particulate size is within 10% of the standard for diameters above 300nm; particulate number concentration is within 10% of the standard. However, accuracy of measurements will not only depend on the accuracy of the instrument. Particulate measurement requires utmost attention as they will depend as well on the dilution condition. All measured values are averaged over a time of 100 engine cycles. This approach allows reduction of random errors to acceptable level. However, all the systematic errors will not be erased by this treatment.

3.5 Mathematical Model

The Thermal model is briefly presented in the following pages. The thermal management engine model components are listed together with the various mathematical relationships for the components used within the HCCI test rig. This allowed a deeper understanding into the behaviour and requirements of each individual component. The implementation of the physical problem is simplified together with the appropriate assumptions, in a lumped parameter fashion, and translated into Simulink on a component–by–component basis, forming a "library". The CHASE thermal model is based on two fundamental components:

1. The “Junction” or better described as a Control Volume component and
2. The “Resistance” or Connector component

These fundamental components can be adapted to create more specific subsystems such as:

1. Supercharger model
2. Intercooler model
3. Heat exchanger model
4. Fresh air throttle model and Heat regeneration throttle model
5. Valve models using incompressible fluid flow through an orifice
6. Valve models using compressible fluid flow through an orifice
7. HCCI combustion model

Each fundamental component was individually verified to ensure the correct response is obtained. Once verified, the fundamental components were combined into a full HCCI model and tested. This simplified model can now be elaborated to include higher order effects.

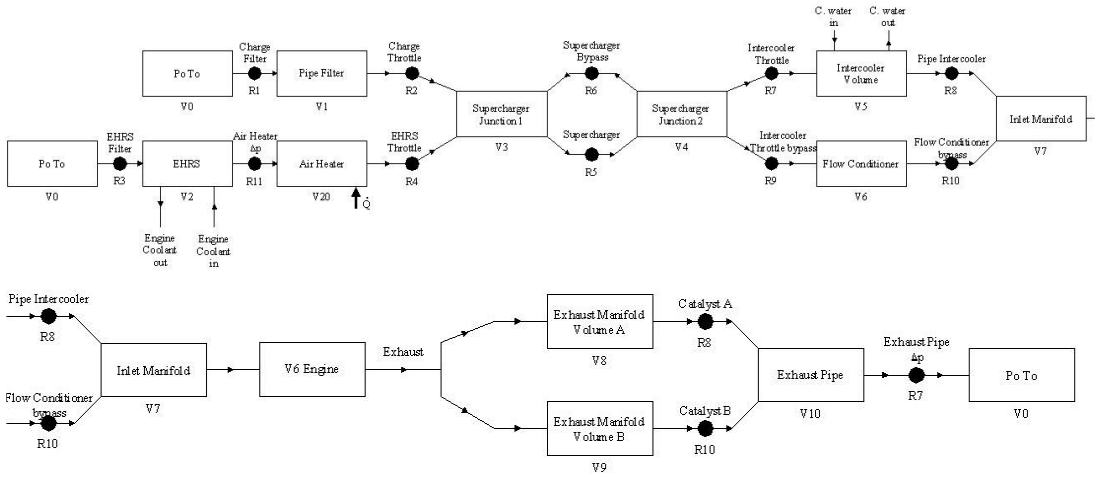

Figure 27: Thermal Management Model Layout

3.5.1 Model Solution

In order to extend the HCCI operation envelope using the Thermal Management system one needs to have the means to predict and control the behaviour and interactions of various system components aiming for maximum system efficiency. The modelling approach for the Thermal Management system presented in this document belongs to the category of "filling and emptying volumes" models. In filling and emptying models, the manifolds (or sections of piping) are represented by finite volumes where the mass of gas can increase or decrease with time. Each volume is treated as an open system control volume which contains gas at a uniform state. The volumes are connected by "resistance" components which are used to predict the mass flow across a restriction when a pressure drop is applied across it. A special case of resistance component is that of the supercharger where mass flow rates and temperature changes are related to pressure changes for any prescribed rotational speed. To solve the problem the energy and mass conservation equations are applied.

The ambient temperature and pressure provides the boundary conditions for the state of the gas in the control volume and through the various components this information is propagated towards the engine. The engine can provide information of the displaced volume, and by using the state of the gas (pressure and temperature) in

the inlet manifold, one can calculate and provide back to the control volume model (inlet manifold) the required mass flow state.

3.5.2 HCCI Control System Future Development

The simplified model described above allows for a deeper understanding into the dynamic behaviour of the system and help determining the control system requirements. As with most control system developments, it will be necessary to define precisely the control objective and operating envelope. Later, the system state variables, inputs and outputs necessary to achieve the control objective, have to be defined. Once completed, the required actuation can be investigated and modelled. The actuator models can then be included and evaluated using the simplified thermal model.

3.6 Filling and Emptying Modelling Method

It has already been mentioned that the modelling approach for the Thermal Management model can be described as "filling and emptying volumes". Each volume is treated as an open system control volume which contains gas at a uniform state. To solve the problem the energy and mass conservation equations are applied.

3.6.1 Junction (Control Volume)

The state of the gas in a control volume is determined by the mass conservation equation involving mass flows through the connected resistances and by an energy conservation equation, i.e. 1^{st} Law of Thermodynamics for open systems. Additionally ideal gas equation of state is used. Modelling of heat transfer to and from control volumes involves an essential and often the most uncertain part of a thermodynamic model, i.e. the overall heat transfer coefficient U [$Wm^{-2}K^{-1}$] describing the total thermal resistance in terms of heat transfer between the working

fluid and the environment. For this application the coefficient for each control volume was determined by accounting for conduction and convection resistances. The engine itself is a special case of a Control Volume and its model is discussed further on.

From the definition of 1st Law of Thermodynamics and during an irreversible process in a Control Volume, the energy change in a system is equal to the total heat supplied by the system minus the total work done by the system:

$$dQcv - dWcv = dE \qquad 1$$

Where dE is the total energy change of the elemental masses of which the system is composed. This means that the total energy change is the internal energy change including any kinetic and potential energy changes,

$$dE = dU + dke + dpe$$

However if one neglects the kinetic and potential energy change:

$$dQcv - dWcv = dU \qquad 2$$

The external work for an unsteady open system can be split into the net work done by the system on the environment and the net work done by the working fluid on the control volume surroundings:

$$dWx = dWcv + V dp_{fluid}$$

Thus rearranging

$$dWcv = dWx - V dp_{fluid} \qquad 3$$

Heat is a form of energy transfer by energy differential between system and environment. The external heat is the net heat supplied in the system by the environment minus the net heat rejected by the working fluid on the control volume surroundings:

$$dQx = dQcv - dUx_{fluid} \quad (4)$$

Thus substituting Equations (3) and (4) in Equation (2):

$$dU = dQx + dUx - dWx + V dp_{fluid}$$

Therefore the energy equation for an open thermodynamic system may be written as:

$$dU = dQx - dWx + dH_{fluid} \quad (5)$$

Where dH is the total enthalpy carried by the working fluid. Since one or more working fluids can enter/exit the control volume:

$$\frac{dU}{dt} = \frac{dQ}{dt} - \frac{dW}{dt} + \sum \frac{dH}{dt}$$

$$\frac{d(m.u)}{dt} = \dot{Q} - \dot{W} + \sum \dot{m}_{in} \cdot h_{in} - \sum \dot{m}_{out} \cdot h_{out} \quad (6)$$

$$RHS = \dot{Q} - \dot{W} + \sum \dot{m}_{in} \cdot c_p \cdot T_{in} - \sum \dot{m}_{out} \cdot c_p \cdot T_{out}$$

And since no work is carried out in the Control Volume ($\dot{W} = 0$ and V is constant except in the engine block)

$$RHS = \dot{Q} + \sum \dot{m}_{in} \cdot c_p \cdot T_{in} - \sum \dot{m}_{out} \cdot c_p \cdot T_{out} \quad (7)$$

At the left hand side of Equation (6)

$$LHS = \frac{d\left(m.u\right)}{dt} = \frac{d}{dt}\left(m \cdot c_v \cdot T\right) = m \cdot c_v \cdot \frac{dT}{dt} + c_v \cdot T \cdot \frac{dm}{dt}$$

Therefore

$$LHS = \frac{d\left(m.u\right)}{dt} = m \cdot c_v \cdot \frac{dT}{dt} + c_v \cdot T \cdot \frac{dm}{dt} \qquad 8$$

Where:

$u_{system} = (c_v T)_{control\ volume}$

$h_{system} = (c_p T)_{control\ volume}$

$$\frac{dm}{dt} = \sum \dot{m}_{in} - \sum \dot{m}_{out}$$

From Equation (8)

$$\frac{dT}{dt} = \frac{1}{m \cdot c_v}\left(\frac{d\left(m.u\right)}{dt} - c_v \cdot T \cdot \frac{dm}{dt}\right)$$

In addition the ideal gas equation is expressed as:

$$p \cdot V = m \cdot R \cdot T \qquad 9$$

From Equation (8) one can substitute with the ideal gas Equation (9) and rearrange

$$\frac{dT}{dt} = \frac{T \cdot R}{p \cdot V \cdot c_v}\left[\sum \dot{m}_{in} \cdot c_p \cdot T_{in} - \sum \dot{m}_{out} \cdot c_p \cdot T_{out} - c_v \cdot T \cdot \left(\sum \dot{m}_{in} - \sum \dot{m}_{out}\right) + \dot{Q}\right] \qquad 10$$

Equation (10) will calculate the rate of change of temperature in the Control Volume.

In order to calculate change of pressure in the Control Volume the ideal gas Equation (9) was differentiated:

$$\frac{dp}{dt} = \frac{R}{V}\left(\frac{dm}{dt}\cdot T + \frac{dT}{dt}\cdot m\right)$$

$$\frac{dp}{dt} = \frac{R}{V}\left[\left(\sum \dot{m}_{in} - \sum \dot{m}_{out}\right)\cdot T + \left(\frac{p\cdot V}{RT}\right)\cdot \frac{dT}{dt}\right] \qquad 11$$

Equation (11) will calculate the rate of change of pressure in the Control Volume. The state of the gas in the control volume can be determined by the energy and mass conservation equations coupled with information on the mass flow rates into and out of each volume, including heat flows (if any).

3.6.2 Resistance (Restriction – Δp in a pipe or reversible throttle)

A throttle body is a resistance in the system, and since air is treated as an ideal gas there is no temperature change across it, the throttle is treated to be reversible and adiabatic.

Compressible flow adiabatic Throttle

The throttle body is modelled using the equations for compressible fluid flow through an orifice, with choked flow for pressure ratios across the throttle lower than the critical value with no change of temperature and with values of discharge coefficients obtained from literature of typical throttle valves.

Therefore for pressure ratios across the throttle higher than the critical value the mass flow is given by Equation (12) where:

p_t : downstream absolute pressure
p_o : upstream absolute pressure

Unchoked Flow $\left(\frac{p_t}{p_o}\right) > \left(\frac{2}{\gamma+1}\right)^{\frac{\gamma}{\gamma\text{-}1}}$

$$\dot{m}_{thr} = \frac{C_D \cdot A_{thr} \cdot p_o}{\sqrt{R \cdot T_o}} \cdot \left(\frac{p_t}{p_o}\right)^{\frac{1}{\gamma}} \cdot \sqrt{\frac{2 \cdot \gamma}{\gamma - 1} \cdot \left[1 - \left(\frac{p_t}{p_o}\right)^{\frac{\gamma\text{-}1}{\gamma}}\right]} \qquad 12$$

For pressure ratios across the throttle lower than the critical value the mass flow is a function of the upstream pressure and is given by Equation (13):

Choked Flow $\left(\frac{p_t}{p_o}\right) \leq \left(\frac{2}{\gamma+1}\right)^{\frac{\gamma}{\gamma\text{-}1}}$

$$\dot{m}_{thr} = \frac{C_D \cdot A_{thr} \cdot p_o}{\sqrt{R \cdot T_o}} \cdot \sqrt{\gamma} \cdot \left(\frac{2}{\gamma+1}\right)^{\frac{\gamma+1}{2(\gamma\text{-}1)}} \qquad 13$$

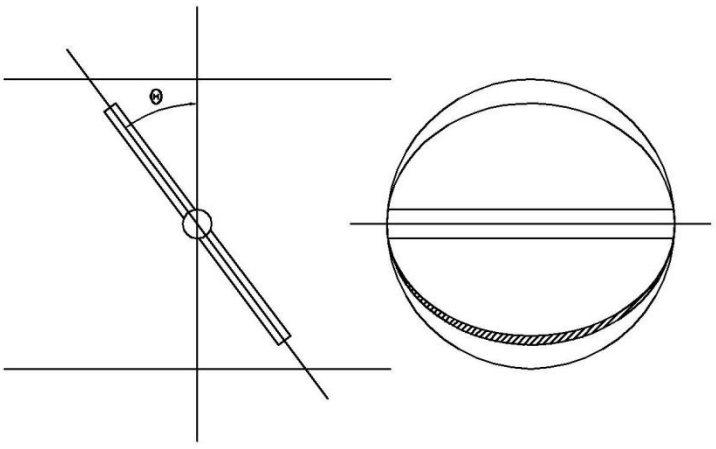

Figure 28: Throttle Angle

The throttle area is approximated by Equation (14):

$$A_{\text{throttle}} = \frac{\pi D^2}{4}\left(1 - \cos\theta\right) \qquad 14$$

Where:
θ = 0 fully closed
θ = 90 fully open

Head loss for turbulent flows

In order to minimise the complexity of the model, the pressure drop through some components was combined. Consecutively to do that effectively, the flow though the combined restrictions needs to be treated as incompressible so that the pressure loss coefficients can be combined easily and accordingly to the component configuration relations. Therefore assuming the fluid is incompressible, the head loss for turbulent flow can be calculated by the following equation:

$$\Delta p = \frac{\rho}{2} \cdot v^2 \cdot K \qquad 15$$

From Equation (15) one can substitute with the ideal gas Equation (9) and rearrange:

$$\Delta p = \frac{1}{2}\left(\frac{P_{in}}{R \cdot T_{in}}\right) \cdot \left(\frac{\dot{m} \cdot R \cdot T_{in}}{A_{in} \cdot P_{in}}\right)^2 \cdot K$$

Consequently:

$$\Delta p = \left(\frac{R \cdot T_{in}}{P_{in}}\right) \cdot \dot{m}^2 \left(\frac{1}{2} \cdot \frac{K}{A_{in}^2}\right)_{const} \qquad 16$$

Rearranging Equation (16)

$$\dot{m} = \sqrt{\frac{\Delta p \cdot P_{in}}{R \cdot T_{in} \cdot K_{turbulant}}} \qquad 17$$

Where:

$$K_{turbulant} = \left(\frac{1}{2} \cdot \frac{K}{A_{in}^2}\right) \qquad 18$$

Head loss for combined turbulent and laminar flows

Darcy's law is a phenomenologically derived constitutive equation that describes the flow of a fluid through a porous medium. The law was formulated by Henry Darcy based on the results of experiments (published 1856)[36] on the flow of water through beds of sand. Using Darcy's law and in order to model the directional loss, the linear and quadratic coefficients of the pressure drop through the intercooler are required. Therefore the head loss (irreversible pressure drop) in flow through various standard pipeline components is assumed to comply with a second degree polynomial related to mass flow:

$$\Delta P = A\dot{m}^2 + B\dot{m}$$

In order to relate this polynomial to the laws of fluid mechanics, it is assumed that pressure drop has a laminar component that relates to the first power of mass flow, as in Equation (16), whereas the turbulent component follows the mass flow in the second power, as in Equation (20).

Assuming the fluid is incompressible [37] p157, for a length of pipe “l” the laminar flow in a pipe can be expressed as:

$$q_v = \frac{\pi \cdot R^4}{8 \cdot \mu \cdot l} \cdot \Delta p \qquad 19$$

$$q_v = \frac{K_{\text{laminar}} \cdot \Delta p}{\mu}$$

$$\frac{\dot{m}}{\rho} = \frac{K_{\text{laminar}} \cdot \Delta p}{\mu}$$

The head loss for laminar flow can be calculated by the following equation:

$$\Delta p = \frac{\dot{m} \cdot \mu}{\rho \cdot K_{\text{laminar}}} \qquad 20$$

Where:

$$K_{\text{laminar}} = \frac{\pi \cdot R^4}{8 \cdot l} \qquad 21$$

3.6.3 Heat Exchanger and Intercooler

Heat exchanger

The Heat exchanger is modelled as a control volume. Heat flux is calculated using the effectiveness factor for a heat exchanger. A known heat exchanger performance is either measured or predicted by an external model thus the effectiveness factor can be calculated using Equation (25). In our case the temperature data were obtained using the suppliers predicted performance tables for the particular heat exchanger. Therefore according to the flowing temperatures and mass flow across the heat exchanger and using the effectiveness factor, the heat flux can be calculated using equation (26).

$$\varepsilon_{HE} = \frac{\dot{Q}_{HEactual}}{\dot{Q}_{HE\max}} \qquad \mathbf{22}$$

$$\dot{Q}_{HEactual} = C_{air} \cdot \left(T_{air\ out} - T_{air\ in} \right) \qquad 23$$

$$\dot{Q}_{HE\max} = C_{\min} \cdot \left(T_{exh\ in} - T_{air\ in} \right) \qquad 24$$

Where:

$$C_{\text{fluid}} = \dot{m}_{\text{fluid}} \cdot c_{p\ \text{fluid}}$$

Thus the effectiveness can be calculated by:

$$\varepsilon_{HE} = \frac{C_{air} \cdot \left(T_{air\,out} - T_{air\,in}\right)}{C_{\min} \cdot \left(T_{exh\,in} - T_{air\,in}\right)} \qquad 25$$

The heat transfer rate from the heat exchanger can be calculated by:

$$\dot{Q}_{HEactual} = \varepsilon_{HE} \cdot \dot{Q}_{HE\max}$$

$$\dot{Q}_{HEactual} = \varepsilon_{HE} \cdot C_{\min} \cdot \left(T_{exh\,in} - T_{air\,in}\right) \qquad 26$$

Rearranging Equation (23) the temperature out of the heat exchanger is:

$$T_{air\,out} = \frac{\dot{Q}_{HEactual}}{C_{air}} + T_{air\,in}$$

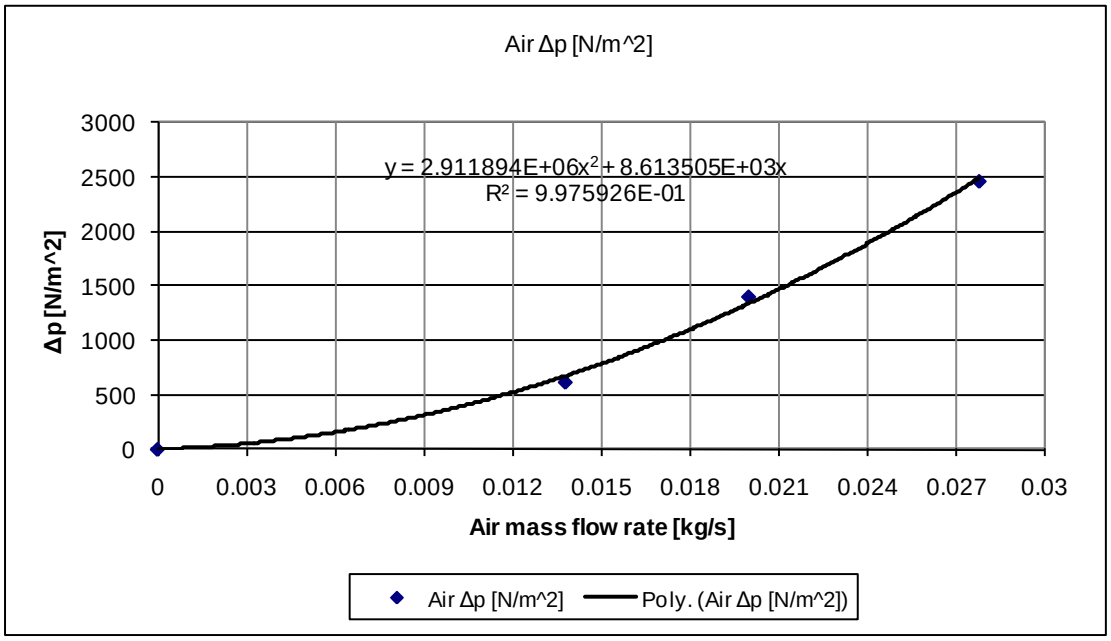

Figure 29: Pressure drop across the Heat exchanger

The pressure drop across the heat exchanger can be either measured or predicted by an external model. In this case the pressure data shown in Figure 29 were acquired using the suppliers predicted performance tables for the particular heat exchanger.

It has been observed that the head losses through various components comply to a second degree polynomial related to mass flow. In order to relate the polynomial with fluid dynamics low's, it is assumed that pressure drop has a turbulent component that follows the mass flow in the second power as in Equation (16) whereas the laminar component follows the mass flow in the first power as in Equation (20).

Intercooler

The intercooler is modelled similar to the heat exchanger model. The volume of the intercooler and associated pipes is lumped together so that this control volume will provide a faster solution. Heat flux is calculated using the effectiveness factor for an intercooler. A known intercooler performance is either measured or predicted by an external model thus the effectiveness factor can be calculated using Equation (30). In our case the temperature data were obtained by the known performance tables for the particular intercooler. Therefore according to the flowing temperatures and mass flow across the intercooler and using the effectiveness factor, the heat flux can be calculated using Equation (31).

$$\varepsilon_{INT} = \frac{\dot{Q}_{INTactual}}{\dot{Q}_{INT\max}} \quad 27$$

$$\dot{Q}_{INTactual} = C_{air} \cdot \left(T_{air\,in} - T_{air\,out} \right) \quad 28$$

$$\dot{Q}_{INT\max} = C_{\min} \cdot \left(T_{air\,in} - T_{cool\,in} \right) \quad 29$$

Where:

$$C_{\text{fluid}} = \dot{m}_{\text{fluid}} \cdot c_{p\ \text{fluid}}$$

Thus the effectiveness can be calculated by:

$$\varepsilon_{INT} = \frac{C_{air} \cdot \left(T_{air\ in} - T_{air\ out}\right)}{C_{\min} \cdot \left(T_{air\ in} - T_{cool\ in}\right)} \qquad 30$$

The heat transfer rate though the intercooler can be calculated by:

$$\dot{Q}_{INTactual} = \varepsilon_{INT} \cdot \dot{Q}_{INT\max}$$

$$\dot{Q}_{INTactual} = \varepsilon_{INT} \cdot C_{\min} \cdot \left(T_{air\ in} - T_{cool\ in}\right) \qquad 31$$

Rearranging Equation (28) the temperature out of the intercooler is:

$$T_{air\ out} = T_{air\ in} - \frac{\dot{Q}_{INTactual}}{C_{air}}$$

The pressure drop across the intercooler can be either measured or predicted by an external model. In our case the pressure data shown in Figure 30 were acquired by the known performance tables for the particular heat exchanger.

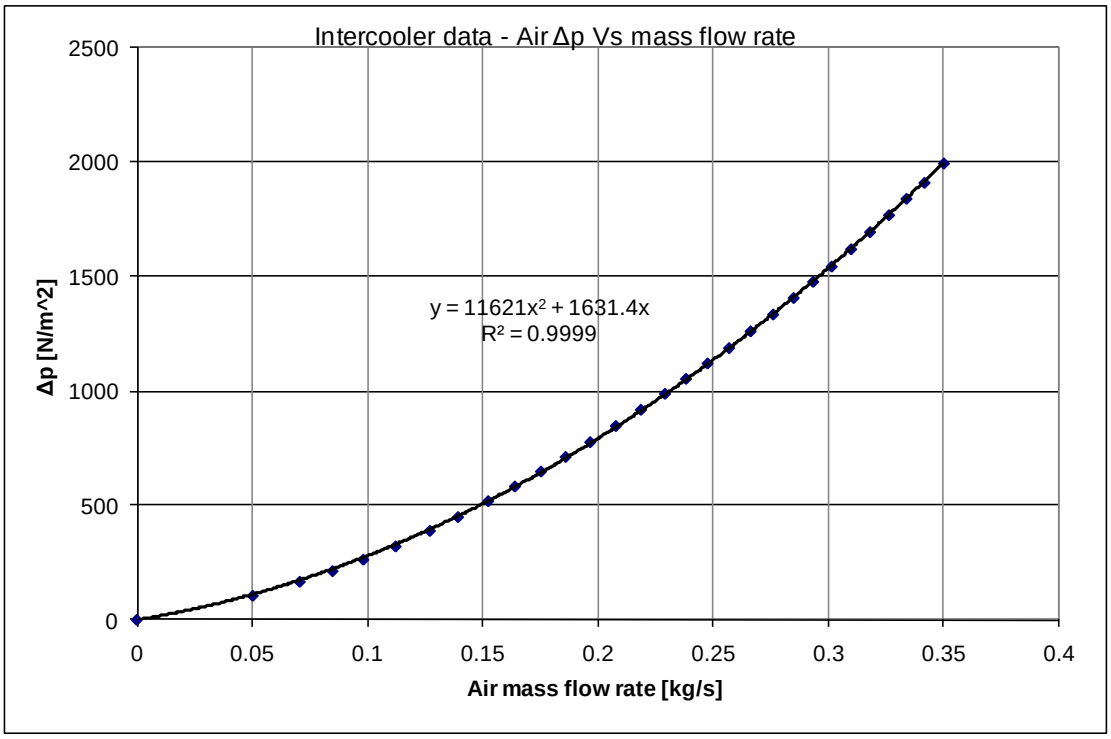

Figure 30: Pressure drop across the Intercooler

3.6.4 Supercharger Model

The implemented supercharger model uses supplier-provided mappings of isentropic efficiencies, pressure ratio, speed, temperature change and displaced volume relationships as summarised by the general function below.

$$\frac{\dot{m}_{sup}\sqrt{R\cdot T_{01}}}{p_{01}\cdot D^2}, n, \frac{\Delta T_o}{T_{01}} = f\left(\frac{N\cdot D}{\sqrt{R\cdot T_{01}}}, \frac{p_{02}}{p_{01}}, \frac{\dot{m}_{sup}}{\mu\cdot D}, \gamma\right)$$

These data is arranged in look-up tables. The performance characteristics of turbomachines and compressors can be illustrated using the following dimensionless parameters [43] p31-37 for compressor characteristics shown in Figure 31. The particular supercharger used is of a roots blower type, which the performance characteristics are very similar to Figure 31 on the right.

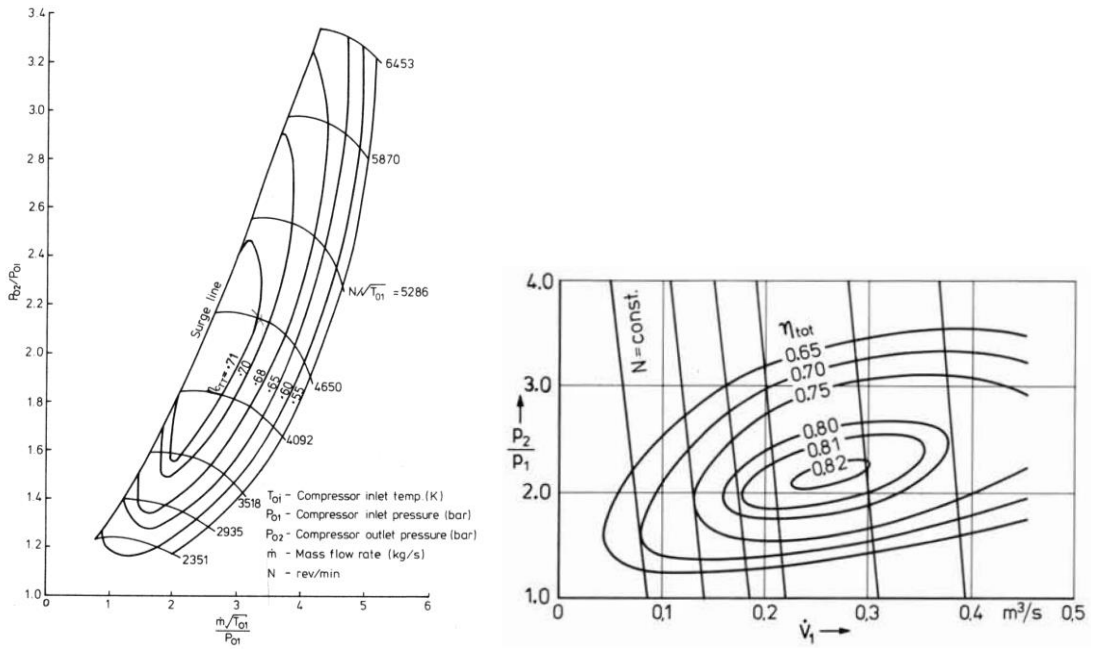

Figure 31: Compressor characteristics (Turbocharger left [43] p33) (Screw comp. right [7]p52)

In order to make the performance data independent of the inlet conditions (temperature and pressure) the following relations were applied:

$$\dot{m}_{\sup_{IC}} \cdot \frac{\sqrt{T_{IC}}}{p_{IC}} = \dot{m}_{\sup} \cdot \frac{\sqrt{T_i}}{p_i} \qquad 32$$

$$n_{icentropic_{IC}} = n_{icentropic} \qquad 33$$

$$\frac{N_{IC}}{\sqrt{T_{IC}}} = \frac{N_i}{\sqrt{T_i}} \qquad 34$$

$$\frac{\Delta T_{IC}}{T_{IC}} = \frac{\Delta T_i}{T_i} \qquad 35$$

$$\frac{\omega_{\sup_{IC}}}{\sqrt{T_{IC}}} = \frac{\omega_{\sup}}{\sqrt{T_i}} \qquad 36$$

To calculate the real displaced volume from the maps one can use Equation (32)

$$\frac{p_{IC}}{R \cdot T_{IC}} \cdot \frac{\dot{V}_{\sup_{IC}} \cdot \sqrt{T_{IC}}}{p_{IC}} = \frac{p_i}{R \cdot T_i} \cdot \frac{\dot{V}_{\sup} \cdot \sqrt{T_i}}{p_i}$$

therefore

$$\dot{V}_{\sup_{IC}} \cdot \frac{\sqrt{T_{IC}}}{R \cdot T_{IC}} = \dot{V}_{\sup} \cdot \frac{\sqrt{T_i}}{R \cdot T_i} \qquad 37$$

3.6.5 Engine Model

The control volume that is most complicated to describe analytically is that of a combustion cylinder. However, on first approach the engine is modelled as simply as possible while retaining the physical characteristics required by the CHASE Thermal management model.

The engine model used is based on the assumption that a HCCI operating cycle can be approximated by the Otto cycle. However, EGR must be taken into account in the cycle, as it is a fundamental factor in the HCCI operating mode. The proportion of EGR is provided in this model as an external input being the result of imposed valve events (timing and lift). The inlet manifold conditions are calculated by the CHASE thermal management model based on the air and enthalpy flow due to the various throttle positions, heat reservoirs in control volumes upstream and upstream boundary conditions. With the above information the engine model provides the mass flow rate values through the engine, conditions in the exhaust manifold and power output.

Compression – Expansion stroke with heat losses

To take into account heat losses during the compression and expansion strokes of the 4-stroke cycle one needs to investigate what happens thermodynamically to the gas. Therefore one can write the first law of thermodynamics for the process as:

$$\frac{dU}{dt} = \frac{dQ}{dt} - \frac{dW}{dt} \qquad 38$$

Where:

$$\frac{dU}{dt} = \mathrm{m} \cdot \mathrm{c_v} \cdot \frac{d\mathrm{T}}{dt}$$

$$\frac{dW}{dt} = \mathrm{p}\frac{d\mathrm{V}}{dt}$$

$$\frac{dQ}{dt} = \dot{\mathrm{Q}}_{\mathrm{loss}} = \mathrm{A}_{\text{combustion chamber}} \cdot \mathrm{h}\left(\mathrm{T}_{\text{cyl wall}} - \mathrm{T}_{\mathrm{gas}}\right)$$

Substituting the above relations to Equation (38):

$$\mathrm{m} \cdot \mathrm{c_v} \cdot \frac{d\mathrm{T}_{\mathrm{gas}}}{dt} = \mathrm{A}_{\text{combustion chamber}} \cdot \mathrm{h}\left(\mathrm{T}_{\text{cyl wall}} - \mathrm{T}_{\mathrm{gas}}\right) - \mathrm{p}\frac{d\mathrm{V}}{dt}$$

$$\mathrm{m} \cdot \mathrm{c_v} \cdot \frac{d\mathrm{T}_{\mathrm{gas}}}{dt} = \mathrm{A}_{\text{combustion chamber}} \cdot \mathrm{h}\left(\mathrm{T}_{\text{cyl wall}} - \mathrm{T}_{\mathrm{gas}}\right) - \frac{\mathrm{m} \cdot \mathrm{R} \cdot \mathrm{T}_{\mathrm{gas}}}{\mathrm{V}} \cdot \frac{d\mathrm{V}}{dt}$$

$$\frac{d\mathrm{T}_{\mathrm{gas}}}{dt} = \frac{\mathrm{A}_{\text{combustion chamber}} \cdot \mathrm{h}\left(\mathrm{T}_{\text{cyl wall}} - \mathrm{T}_{\mathrm{gas}}\right) - \frac{\mathrm{m} \cdot \mathrm{R} \cdot \mathrm{T}_{\mathrm{gas}}}{\mathrm{V}} \cdot \frac{d\mathrm{V}}{dt}}{\mathrm{m} \cdot \mathrm{c_v}} \qquad 39$$

Consequently Equation (39) cannot be solved analytically since the gas temperature (Tgas) cannot be eliminated. A numerical solution method was adapted in order to calculate the irreversible gas temperature during the compression and expansion

stroke due to heat loses. To calculate the cylinder heat transfer coefficient one can use the Woschni heat release correlation:

$$h=3.26\cdot B^{-0.2}\cdot p^{0.8}\cdot T^{-0.545}\cdot w^{0.8} \qquad 40$$

where: B[m], p[kpa], T[K], w[m/s]

Equation (40) can be rewritten as:

$$h=\frac{C_1\cdot\left(1\cdot e^{-3}\cdot p\right)^{0.8}}{B^{0.2}\cdot T^{0.545}}\cdot\left[C_2\cdot abs\left|c_{piston}\right|+C_3\cdot\frac{Vd\cdot T_1}{p_1\cdot V_1}\cdot\left(p_{ref}-p_{motored}\right)\right]^{0.8} \qquad 41$$

where: B[m], p[pa], T[K], V[m^3]

Woschni heat release constants:

C1=3.26;

C2=2.28; (C2=2.28 for compression, combustion & expansion phase, C2=6.18 for scavenging phase)

C3=3.24e-3; (C3=0 for compression & scavenging phase, C3=3.24e-3 for direct injection engines)

n=1.43; polytropic index

Since it is necessary for the Thermal management engine model to calculate the complete HCCI cycle with varying inlet conditions it is required to adjust the gas temperature during the adiabatic compression and expansion stroke with the irreversible case. Therefore by varying the initial conditions one can run the solution program to create two maps (one for each stroke) using different engine speed and inlet gas pressure and temperature. The solution program for the heat transfer calculations is included in in Appendix 6.

$$\Delta Tg_{2\text{compression}} = T_1 \cdot rc^{\gamma-1} - T_2 \quad 42$$

$$\Delta Tg_{4\text{expansion}} = \frac{T_3}{rc^{\gamma-1}} - T_4 \quad 43$$

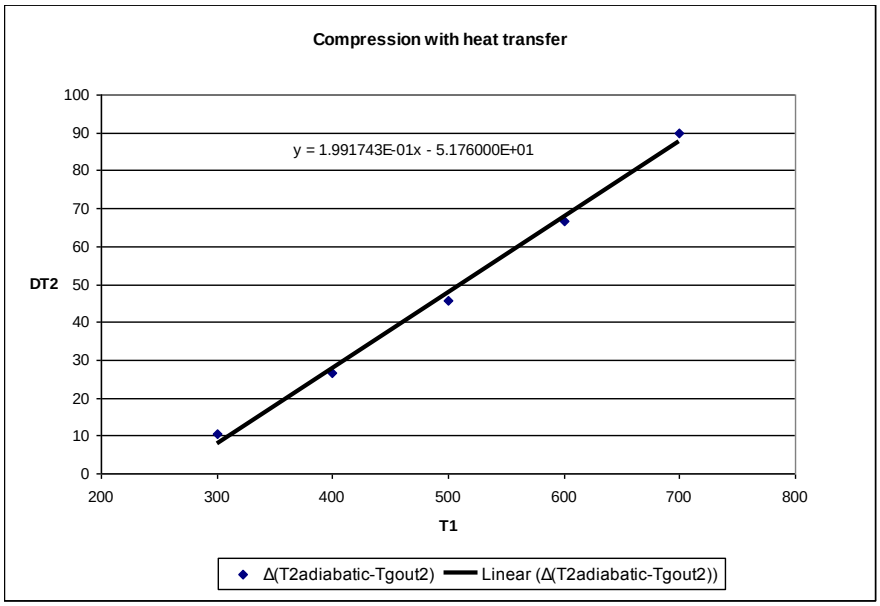

A)

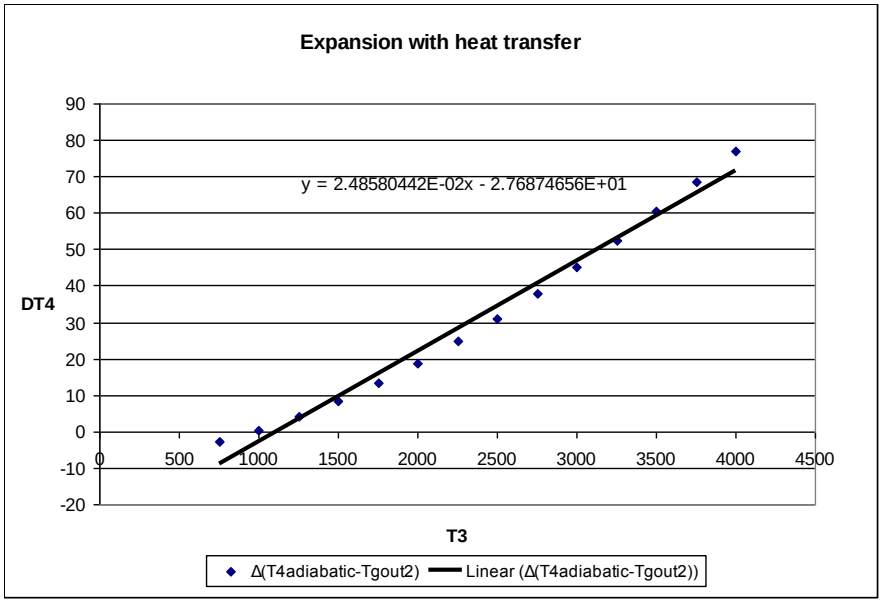

B)

Figure 32: ΔT gas with varying initial conditions (compression stroke A), (expansion stroke B)

Observing the results a linear relation can describe the difference of the gas temperature with less than 5% error.

$$\Delta Tg_{2\text{compression}} = \left(\mathrm{m}\cdot \mathrm{T}_1 + \mathrm{c}\right)$$

$$\Delta Tg_{2\text{compression}} = \left(\mathrm{Km}\cdot \mathrm{p}_1^{\,\mathrm{nm}}\cdot \mathrm{T}_1 - \mathrm{Kc}\cdot \mathrm{p}_1^{\,\mathrm{nc}}\right)$$

$$\mathrm{T}_2 = \mathrm{T}_1 \cdot \mathrm{rc}^{\gamma-1} - \Delta Tg_{2\text{compression}} \qquad 44$$

$$\Delta Tg_{4\text{expansion}} = \left(n\cdot \mathrm{T}_4 + d\right)$$

$$\Delta Tg_{4\text{expansion}} = \left(\mathrm{Km}\cdot \mathrm{p}_4^{\,\mathrm{nn}}\cdot \mathrm{T}_4 - \mathrm{Kc}\cdot \mathrm{p}_4^{\,\mathrm{nd}}\right)$$

$$\mathrm{T}_4 = \frac{\mathrm{T}_3}{\mathrm{rc}^{\gamma-1}} - \Delta Tg_{4\text{expansion}} \qquad 45$$

Assumed cycle for HCCI thermal management model

The following information is provided regarding the assumptions behind the engine model. The V6 HCCI engine performance can be modelled by a validated HCCI combustion model based on the Ricardo WAVE platform taking into account the gas dynamics in the engine system. The Ricardo WAVE model is presented in Section 3.8. Since the in-cylinder temperature data was available, the Ricardo WAVE model was used to tune the simplified engine model used for thermal management. Figure 33 and Figure 34 shows the typical pressure and temperature charts generated for a particular speed and valve timing in HCCI operation mode using the two models.

It is evident that the simplified model cannot not capture all the events that occur within the combustion chamber. From Figure 33 pressure prediction seems to have a better correlation although the peak pressure is not captured.

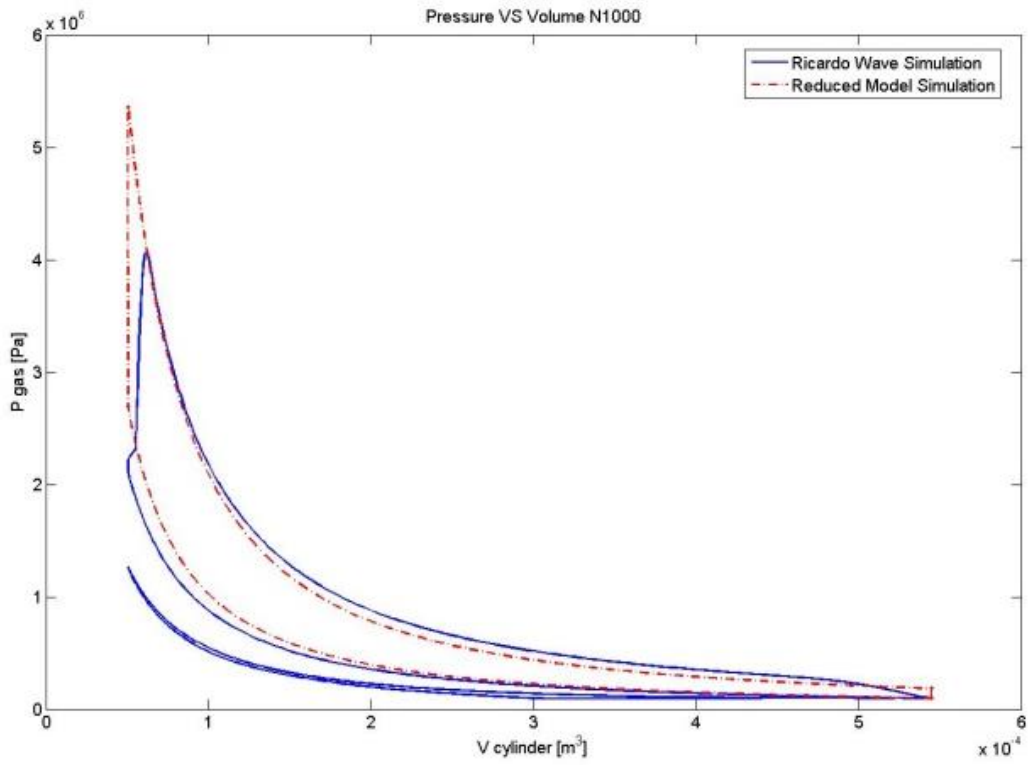

Figure 33: HCCI cycle PV diagram T.M. Mathematical model results compared with Ricardo Wave simulation

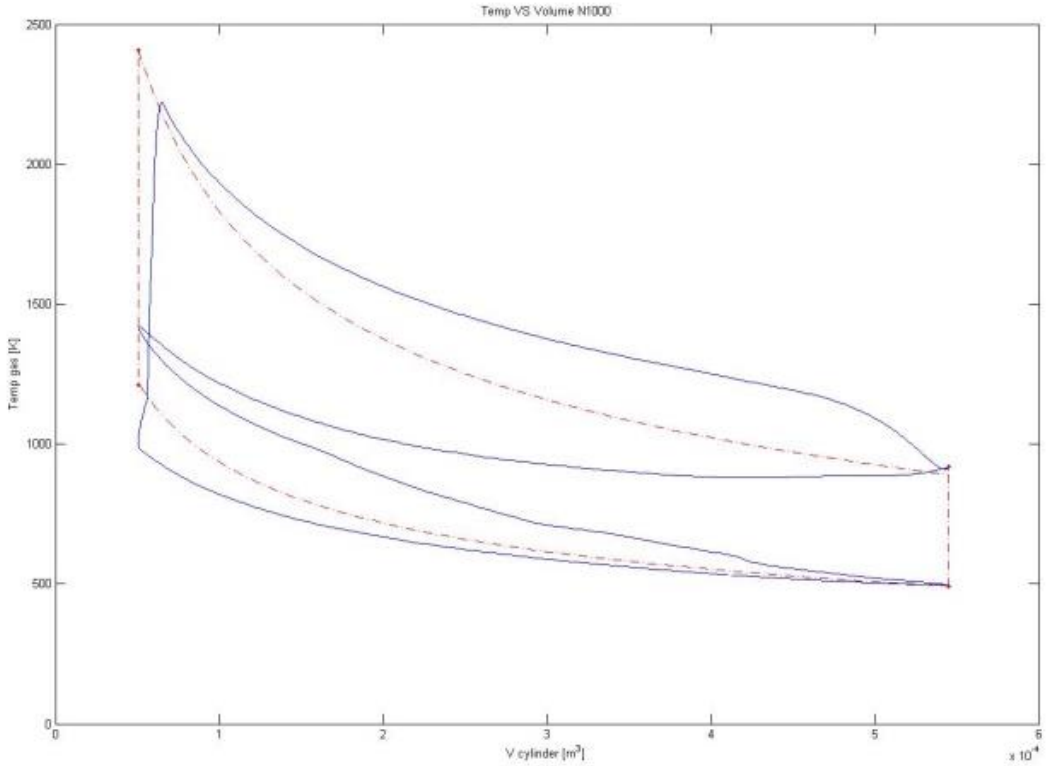

Figure 34: HCCI cycle TV diagram T.M. Mathematical model results compared with Ricardo Wave simulation

From Figure 34 the temperature prediction seems to be worse however the V6 HCCI Ricardo WAVE model has significant simplifications and limitations that are described in detailed in Section 3.8.2. Comparing the V6 HCCI Ricardo WAVE model with experimental data we experienced limitations with the Ricardo WAVE software in which the leakage amount though the gap between the cylinder and the piston is fixed. As a result of that the blow-by losses are under predicted and the pressure obtained from the model is higher. Another major Ricardo WAVE simplification is a zero dimensional cylinder model which produces difficulties in modeling of heat exchange and mixture compression processes. However in the absence of better temperature data the simplified model used simulated data from the Jaguar V6 HCCI engine Ricardo WAVE model.

In regards to the thermal management engine model, a fast model solution is desirable. To increase the model solution speed the detailed processes of negative valve overlap and the recompression stroke are neglected and the proportion of EGR is treated as an input to the engine model.

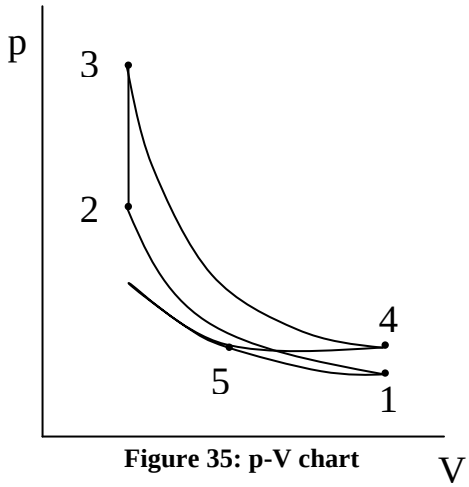

Figure 35: p-V chart

Referring to the p-V chart shown in Figure 35 during the recompression stroke the mass of exhaust gas is trapped in the cylinder after the exhaust valve has closed; and then the gas is compressed & expanded to the same cylinder volume. It is assumed for the purpose of this model that point 5 is timed to represent the

instant just after the inlet valve has opened and the trapped gas is about to be mixed with charge air at inlet manifold pressure.

Thus T_5 is the temperature of the exhaust gas trapped in the cylinder after EVC and after an assumed adiabatic compression/expansion during the NVO recompression, at the moment of IVO, assuming that it will expand at inlet manifold pressure. At the end of this process T_1 is as yet unknown because it depends upon inlet conditions, T_5 and the proportion of EGR.

At point 1 and point 5 the cylinder pressure will be the same as the inlet manifold.

$$p_1 = p_{im} \approx p_5$$

It can be proved that

$$T_1 = EGR \cdot T_5 + (1 - EGR) \cdot T_{Inlet\ Manifold} \qquad 46$$

$$m_{gas} = \frac{p_1}{RT_1} \cdot V_1 \text{ ; where } V_1 = \frac{rc \cdot Vd}{rc - 1}$$

$$m_{air} = (1 - EGR) \cdot m_{gas} \qquad 47$$

therefore

$$m_{air} = (1 - EGR) \cdot \frac{p_1}{RT_1} \cdot \frac{rc \cdot Vd}{rc - 1}$$

Compression stroke:

$$T_2 = T_1 \cdot rc^{\gamma - 1} - \Delta Tg_{2compression}$$

$$T_2 = T_1 \cdot rc^{\gamma - 1} - (Km \cdot p_1^{nm} \cdot T_1 - Kc \cdot p_1^{nc})$$

$$p_2 = \frac{m_{gas} \cdot R \cdot T_2}{V_2} = \frac{m_{gas} \cdot R \cdot T_2 \cdot (rc - 1)}{Vd}$$

Combustion:

$$Q_{comb} = m_f \cdot Q_{lcv} \cdot n_{thrc} \text{ ; where } Q_{comb} = m_{gas} \cdot c_v \cdot (T_3 - T_2)$$

$$Q_{comb} = \frac{m_{air} \cdot Q_{lcv} \cdot n_{thrc}}{AFR_{stoc} \cdot \lambda}$$

$$T_3 = \frac{Q_{comb}}{m_{gas} \cdot c_v} + T_2$$

$$p_3 = \frac{p_2 \cdot T_3}{T_2}$$

Expansion stroke:

$$T_4 = \frac{T_3}{rc^{\gamma-1}} - \Delta Tg_{4expansion}$$

$$T_4 = \frac{T_3}{rc^{\gamma-1}} - \left(Km \cdot p_4^{nn} \cdot T_4 - Kc \cdot p_4^{nd}\right)$$

$$p_4 = \frac{p_3}{rc^{\gamma}}$$

$$T_5 = T_4 \cdot \left(\frac{p_1}{p_4}\right)^{\frac{\gamma-1}{\gamma}} \quad 48$$

Combustion efficiency

The above equations describe the HCCI cycle however in order to describe the combustion process during the HCCI cycle it is required to separate the effects of incomplete combustion. Therefore the thermal conversion efficiency was introduced during the combustion stroke. Thermal conversion efficiency is defined in [33, p.85] and relates the actual work per cycle to the amount of chemical energy released in the combustion process. With the assumed HCCI cycle equations shown in the previous section it is possible to derive Equation (49) and the thermal conversion efficiency is noted here as "n_{thrc}". For a given engine speed, air to fuel ratio and valve timing the

average of internal EGR can be calculated, and with the average of measured temperatures before and after combustion one can calculate "n_{thrc}". However in cylinder temperature measurements before and after combustion were not available in our experimental setup. Therefore a validated HCCI engine model compiled in Ricardo WAVE was used instead. The Ricardo WAVE simulation results were applied to Equation (49) creating a lookup table for "n_{thrc}" and the results is shown as 3D dimensional surface in Figure 36.

Observing Figure 36 one can see there are two distinct peak regions for a particular set of engine speed and EGR where there is a significant temperature rise during combustion. Since the Ricardo WAVE model has significant simplifications and limitations such areas need to be approached with caution. It would have been desirable to obtain in cylinder temperature data in order to eliminate any uncertainties however such data were not available.

It is important to mention that Equation (49) represents the thermal conversion efficiency of a given engine, and this coefficient is valid only for that particular engine and its setup.

$$Q_{comb} = \frac{m_{air} \cdot Q_{lcv} \cdot n_{comb}}{AFR_{stoch} \cdot \lambda}$$

$$Q_{comb} = m_{gas} \cdot c_v \cdot (T_3 - T_2)$$

$$m_{air} = (1 - EGR) \cdot m_{gas}$$

$$\frac{m_{air} \cdot Q_{lcv} \cdot n_{thrc}}{AFR_{stoch} \cdot \lambda} = \frac{m_{air}}{(1 - EGR)} \cdot c_v \cdot (T_3 - T_2)$$

$$n_{thrc} = \frac{AFR_{stoch} \cdot \lambda \cdot c_v \cdot (T_3 - T_2)}{(1 - EGR) \cdot Q_{lcv}} \qquad 49$$

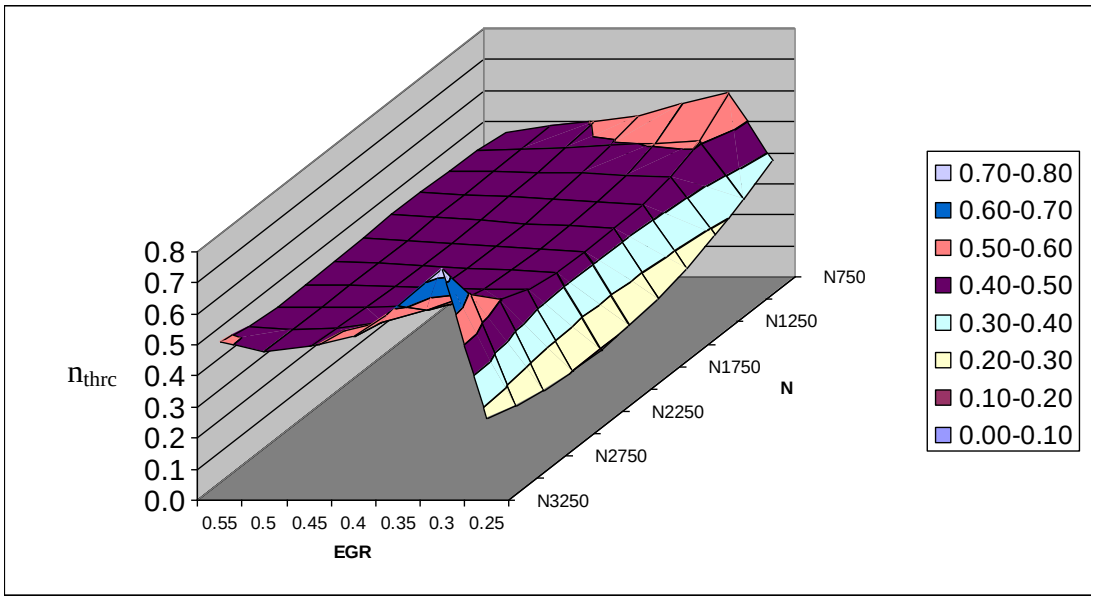

Figure 36: Thermal conversion efficiency map

Cycle solution program eliminating temperature T5

In order to create the engine mathematical model we rearranged the cycle equations obtained for the assumed cycle for HCCI using thermal management. Substituting all other known variables and solving Equation (48) for T_5 we obtained equation (50).

$$T5 = \left((EGR * (T5 - Tim) + Tim) * \left(\frac{(EGR * (T5 - Tim) + Tim)}{A + B - C} \right)^{\frac{1}{\gamma}} \right.$$

$$A = \left(\frac{rc^{-\gamma} * \left((1 - EGR) * ncomb * Qlhv * rc + AFR * cv\_air * \left(Kc * pim^{nc} * rc + \left(-Km * pim^{nm} * rc + rc^{\gamma} \right) * (EGR * T5 + Tim - EGR * Tim) \right) \right)}{AFR * cv\_air} \right) \qquad 50$$

$$B = Kd * \left(\frac{\left(pim * (1 - EGR) * ncomb * Qlhv * rc + AFR * cv\_air * \left(Kc * pim^{nc} * rc + \left(-Km * pim^{nm} * rc + rc^{\gamma} \right) * (EGR * T5 + Tim - EGR * Tim) \right) \right)}{\left(AFR * cv\_air * (EGR * (T5 - Tim) + Tim) \right)} \right)^{nd}$$

$$C = \frac{\left(Kn * (EGR * (T5 - Tim) + Tim) \right)}{pim * rc} * \left(\frac{pim * \left((1 - EGR) * ncomb * Qlhv * rc + AFR * cv\_air * \left(Kc * pim^{nc} * rc + \left(-Km * pim^{nm} * rc + rc^{\gamma} \right) * (EGR * T5 + Tim - EGR * Tim) \right) \right)}{\left(AFR * cv\_air * (EGR * (T5 - Tim) + Tim) \right)} \right)^{(1 + nn)}$$

From the simplification it was observed that the problem cannot be solved analytically since temperature T_5 cannot be eliminated, therefore the a numerical solution method was adapted in order to calculate the gas temperature during the end of compression and expansion strokes T_2 and T_4 from known values of T_1 and T_3. A set of variables are established for a particular cycle run and the program can solve Equation (50)

using the Newton Raphson method. The flowchart of the program is included in Appendix 4, whereas the cycle solution program is included in Appendix 5. For presentation purposes we rewrite equation (50) as a function based on the known variables into equation (51).

$T_5 = f(T_5, EGR, Tim, pim, Nengine, + const.)$ 51

For cross checking the solution of equation (50), we used Wolfram Mathematica to solve the Engine model equations for cycle efficiency, Power output and the derivative of T_5 that is needed to obtain a numerical solution using the Newton Raphson method.

Therefore cycle efficiency was calculated as an output in equation (52).

```
FullSimplify[Eff == 1 - (T4 - T1) / (T3 - T2)]
```

$$Eff + rc^{1-Y} == 1 \qquad 52$$

Power output was calculated as an output in equation (53)

```
FullSimplify[Power == mg * Cv * (T3 - T4 - (T2 - T1)) * N / 2]
```

$$Power == -\frac{Cv\,(-1+EGR)\,N\,ncomb\,Pim\,Qlcv\,rc^{1-Y}\,(-rc+rc^{Y})\,vd}{2\,AFR\,cv\,R\,(-1+rc)\,(EGR\,(T5-Tim)+Tim)} \qquad 53$$

The derivative of T_5 was calculated as an output in equation (54)

$$\partial_{T5}\left((EGR\,(T5-Tim)+Tim)\left(\frac{1}{1-\frac{(-1+EGR)\,ncomb\,Qlcv\,rc^{1-Y}}{AFR\,cv\,(EGR\,(T5-Tim)+Tim)}}\right)^{-1/Y}\right) \qquad 54$$

$$EGR\left(\frac{1}{1-\frac{(-1+EGR)\,ncomb\,Qlcv\,rc^{1-Y}}{AFR\,cv\,(EGR\,(T5-Tim)+Tim)}}\right)^{-1/Y} + \frac{(-1+EGR)\,EGR\,ncomb\,Qlcv\,rc^{1-Y}\left(\frac{1}{1-\frac{(-1+EGR)\,ncomb\,Qlcv\,rc^{1-Y}}{AFR\,cv\,(EGR\,(T5-Tim)+Tim)}}\right)^{1-\frac{1}{Y}}}{AFR\,cv\,(EGR\,(T5-Tim)+Tim)\,Y}$$

The thermal management model is based on this four-dimensional map and calculates all other temperatures in the cycle including temperature T_4, which is the temperature

at the exhaust runners and power output for a particular set of inlet manifold conditions during a particular time step. If any of the variables change, for example λ then the program using this map interpolates the solution based on this new set of variables. The relative air to fuel ratio can easily be calculated by the following formula:

$$\lambda = (\mathrm{AFR}_{\mathrm{actual}}/\mathrm{AFR}_{\mathrm{stoch}}) \qquad 55$$

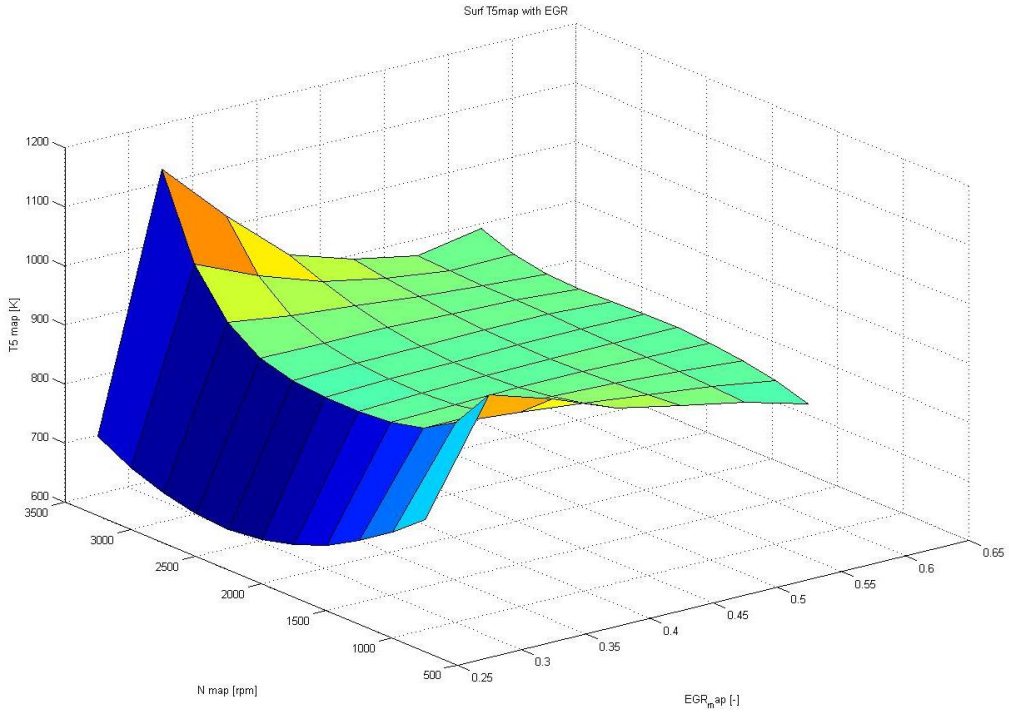

Figure 37: T5=f(N_{engine}, T_{im}, p_{im}, EGR)

While the surface map describes the cycle for one cylinder while calculating the engine mass flow in the Simulink model the total mass flow will be taken onto account. The cycle program will calculate the temperature T_5 based on the previously mentioned assumptions and equations. A multidimensional array describing T_5 can be created using the following engine operational boundary conditions. This array can be then used in the simplified engine model to close the mathematical loop and calculate the whole engine cycle.

The thermal management model is used mainly to test parameters for subsequent experimental setup and engine runs. Control of the air intake and boost pressure of the HCCI engine at The University of Birmingham using thermal management is conducted using the T.M. throttles. Positioning of the T.M. throttles to conduct tests remains a manual process and the operator has to manually change the position of these throttles using the SIMULINK Control Model. The alternative to the thermal management model was the validated HCCI engine model compiled in Ricardo WAVE and presented in Section 3.8. However the latter is not suitable for providing fast experimental parameters for testing as it has significantly longer simulation runs.

The thermal management model is believed to be adequate to capture the physics behind the air system of our engine test rig. This model was calibrated by the author from test data (Section 4.3) and has shown reasonable agreement and accuracy. Should the model need further improvement utilising combustion characteristics from experimental results would be necessary to model the inlet and exhaust ports by crank angle degree.

3.7 Mathematical Model Implementation – Realtime model

3.7.1 Solution Stability Problems

There were some problems which the solution of the model did not initialise. The problem was purely mathematical since in reality if there is no air flow across an orifice (or throttle) the pressure drop is zero ($\Delta p=0$) . However if we express this relation in a mathematical model if we divide a quantity with a zero pressure drop the solver cannot cope of the solution oscillations and the program crashes. In order to solve the problem the following modelling approach was taken.

In order to eliminate the mathematical instability we make sure that there is always a pressure loss across an orifice. This means when the model start, the orifice outlet pressure is the minimum number of the following instances:

1. either the orifice inlet pressure minus “eps” the smallest number that Matlab can compute.
2. or the orifice outlet pressure in the next iteration.

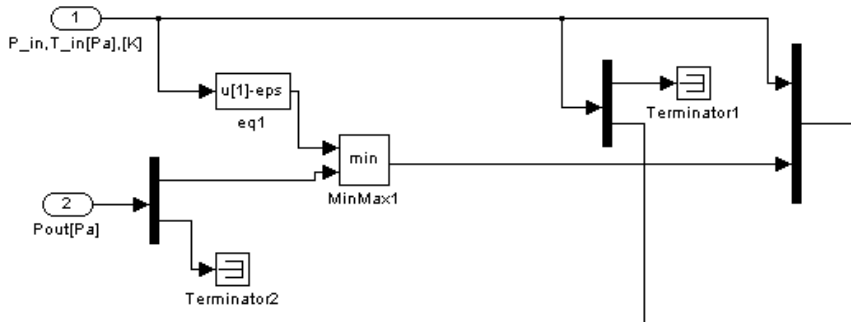

Figure 38: Method to calculate Δp avoiding divide by zero occurrence

This approach provides a fast model solution however the orifice is effectively modelled as a non return valve and throttle mass flows has to be monitored as the throttle orientation is highly important.

3.7.2 Backflow

Initially backflow through the various restrictions (orifice or throttle) was considered negligible and it was not taken into account. However during initial runs it has been noticed that considerable backflow occurs while the system is pressurised and the supercharger throttle bypass is suddenly opened. This is basically due to the size of the control volumes in the system. In order to accommodate to this effect the restriction and control volume models were updated.

Restriction model update

As it has been already explained the orifice shown in Figure 39 is effectively modelled as a non return valve. The new restriction model comprise two of these one way restriction orifices. Orifice A models the normal mass flow of air whereas the orifice (B) models the reverse mass flow of air with its inputs reversed. A simple (A)-(B) sum designates the mass flow though the orifice and the (-)ve sign is applied to the reversed mass flow. Last according to the sign of the mass flow the author ensured that the correct outlet temperature will be the output though the throttle. A bigger sketch of the restriction model sketch can be viewed in Appendix 9.

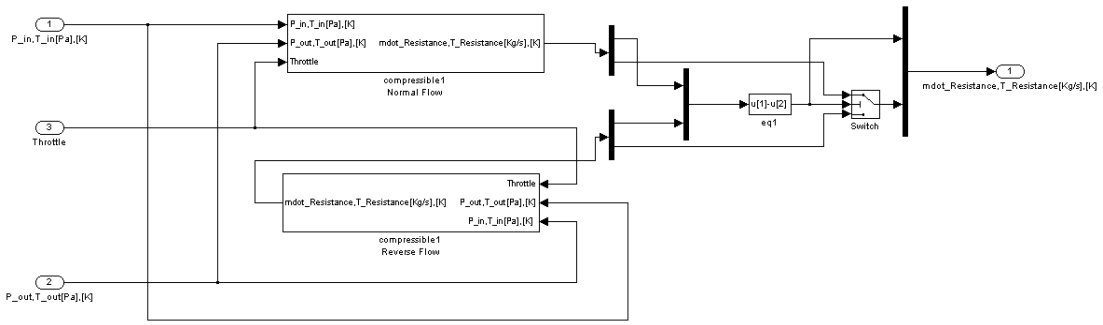

Figure 39: Restriction Model with backflow

Control Volume model update

The control volume model was updated to take into account backflow. It is assumed that the mass of air entering the CV has a nominal (+)ve sign flow where as mass out from the CV has a nominal(-)ve sign mass flow. If the sign changes this means that the flow has been reversed and the correct temperature needs to be assigned to the particular mass flow state.

Therefore the control volume model checks the inlet flows and convects the inlet temperature into the volume, whereas outlet flows convect the control volume temperature out of the control volume

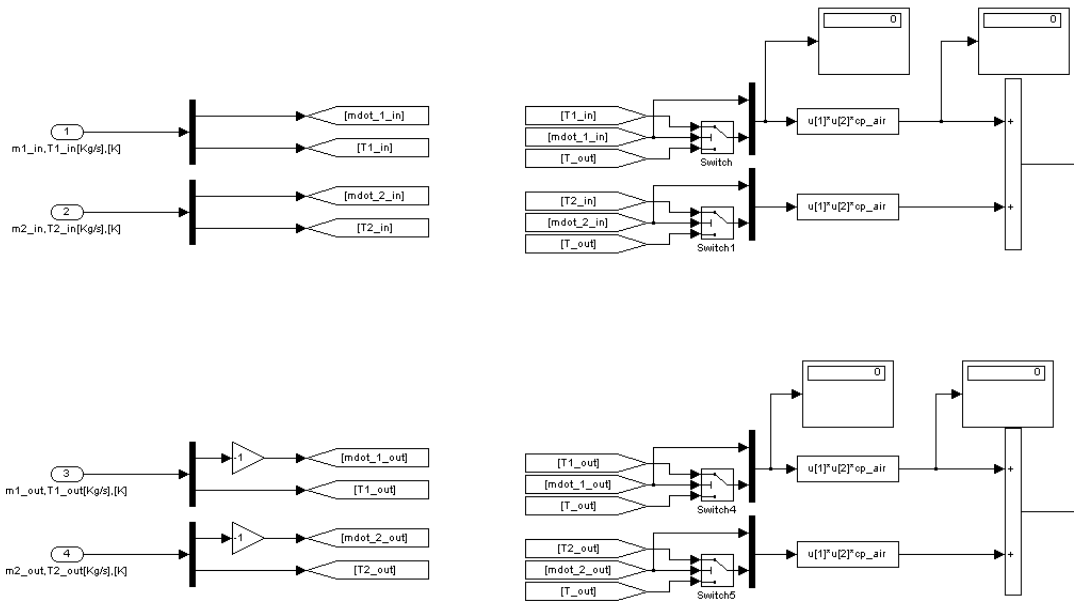

Figure 40: Control Volume Model with backflow

3.8 Ricardo WAVE Model

In this section the Ricardo WAVE Model is introduced and disused. In general modeling studies of HCCI engines with complex functionality can utilise vast amounts of resources. A commonly used method to model flow within the engine ducts and manifolds is to use 1-D flow commercial software. Unfortunately, to this day none of these software offer a suitable CAI combustion model and researchers usually develop their own cylinder and combustion models. The Ricardo WAVE model of the Jaguar V6 HCCI engine at The University of Birmingham comprise of an auto-ignition combustion model, which in turn can be used in conjunction with a 1D gas dynamics or 0D thermodynamics engine simulation code for HCCI engine cycle simulations. The combustion model consists of two parts – the first part predicts auto-ignition timing, based on the integral of the knock delay time, and the second part predicts the Heat Release Rate (HRR), based on the Watson correlation for Diesel engines. The equations for the HRR model were fitted with empirical coefficients derived from experimental results conducted at The University of Birmingham. The experimental data was measured under a number of engine operating conditions for different loads, speeds and equivalence ratios. The experiments were performed on a Jaguar V6 HCCI engine employing internal Exhaust Gas Residual (iEGR) trapping through Cam Profile Switching (CPS) and Variable Valve Timing (VVT) control.

The model features:

- Dimensions and geometry derived from the Thermal Management System Experimental System
- 3D Quasi modelling approach of inlet manifold and intercooler assembly.
- Initial and wall temperatures.

- Pressure loss, friction, discharge coefficients of all major parts (air filter, intercooler, catalysts, silencers) according to specifications sheets.
- An external combustion model that can perform both SI and HCCI combustion modes and transition between the two modes during one simulation case.

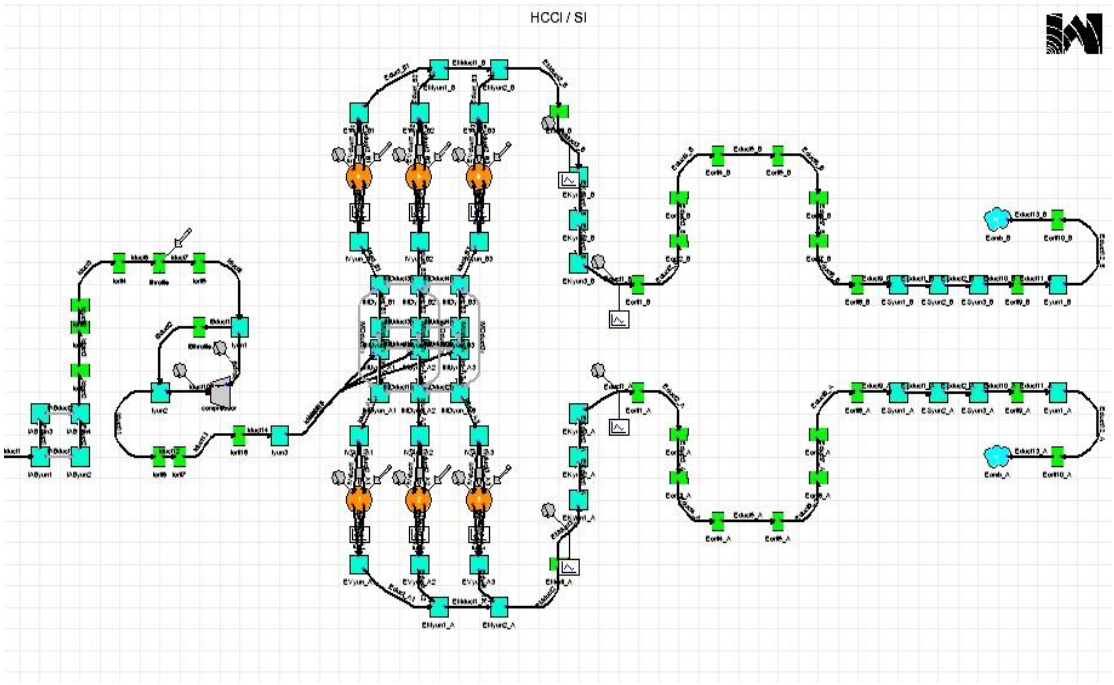

Figure 41: Ricardo WAVE HCCI– SI V6 engine model

3.8.1 Combustion model

The combustion model was written in FORTRAN and compiled as a Dynamic Link Library (DLL) file. The DLL file is linked with the Ricardo WAVE solver every integration time step. Linking period starts when inlet valve closes and finishes when MFB = 1 or until exhaust valve opens. For each time step Ricardo WAVE is exporting to combustion model variables such as crank angle, temperature, pressure and the model is exporting back to Ricardo WAVE MFB value and optionally ignition CA. The Heat release process and emissions analysis process takes place within the Ricardo WAVE solver.

The combustion model consists of two sub-models. The first is an Auto-Ignition Model and is responsible for calculating the ignition timing. The second is a Burn Profile Model responsible for calculating the Mass Fraction Burned (MFB) after ignition has occurred. Both sub-models are based on experimental results which are converted into exponential equations.

3.8.1.1 Auto-Ignition Model

The auto-ignition model consists of two parts. The first is calculating ignition delay time for various conditions for each time step. The second part accounts for pressure and temperature history inside the cylinder during the compression process. The main idea of the HCCI auto-ignition model originates from of the SI knock model. It can be assumed that for a homogeneous mixture the knock-integral should give a good foundation for HCCI. The first knock correlation was developed by Livengood and Wu [87]. It's based on the ignition delay correlation obtained from experiments on a rapid compression facility. The Arrhenius type relationship for the delay is described as follows:

$$\tau = A_A \cdot p^{-n} \cdot \exp\left(\frac{E_A}{R \cdot T}\right) \qquad 56$$

where: τ - local ignition time delay [ms]

E_A – activation energy

R – gas constant

A_A, n – constants

p – pressure [bar]

T – temperature [K]

The condition values are based on experimental results published by X.He, M.T. Donovan, B.T. Zigler [88]. The experiments were performed in a rapid compression

facility (RCF) for various iso-octane, oxygen, nitrogen, and argon mixtures. The experiments were conducted over a range of equivalence ratios (φ = 0.25 – 1), pressures (p = 5.12 – 23 atm), temperatures (T = 943 – 1027 K), and oxygen mole fractions (9 – 21 %). They discovered that ignition delay also depends on the equivalence ratio and the oxygen concentration. These parameters need to be included in the local ignition time delay equation (56). As a result they proposed equation (57)

$$\tau_{id} = 1.3 \cdot 10^{-4} \cdot p^{-1.05} \cdot \phi^{-0.77} \cdot \chi_{O_2}{}^{-1.41} \cdot \exp\left(\frac{33700}{R \cdot T}\right) \qquad 57$$

To account for pressure and temperature history inside the cylinder during the compression process the time integral in equation (58) is used:

$$\int_{t_{IVC}}^{t_{IVC}+\tau_{id}} \left(\frac{1}{\tau}\right) \cdot dt = 1 \qquad 58$$

where:

τ_{id} - total ignition delay time [s]

t_{IVC} – time of the inlet valve closure [s]

Because the value of local ignition delay time equation (56) reduces when the local temperature and pressure rise, the value of the integral in equation (58) increases parabolically as the piston approaches top dead centre (TDC). The time at which the value of the integral in equation (58) is equal to one is assumed to be the start of combustion.

3.8.1.2 Burn Profile Model

Experimental results with the use of a rapid compression facility (RCF) were published by X.He, M.T. Donovan, B.T. Zigler [88]

The biggest simplification of the auto-ignition model is a temperature threshold. It is very difficult to give accurate results for this approach, because the ignition delay

depends on many parameters. To predict an SI combustion burn profile, a Wiebe function is often applied, Lindstrom [89] however it is impossible to model accurate HCCI burn profiles using Wiebe functions because it predicts combustion as an S-shaped curve and it is difficult to predict the HCCI low temperature combustion (LTC) accurately. As result, accurate rate of pressure rise values for a wide range of engine conditions are required. HCCI often is associated with a two-stage heat-release process which demands the use of separate functions for each part. The first stage is a relatively slow low temperature combustion (LTC) led by straight-chain low octane number paraffin – N-heptane. This process is assumed to last between 1-10% MFB.

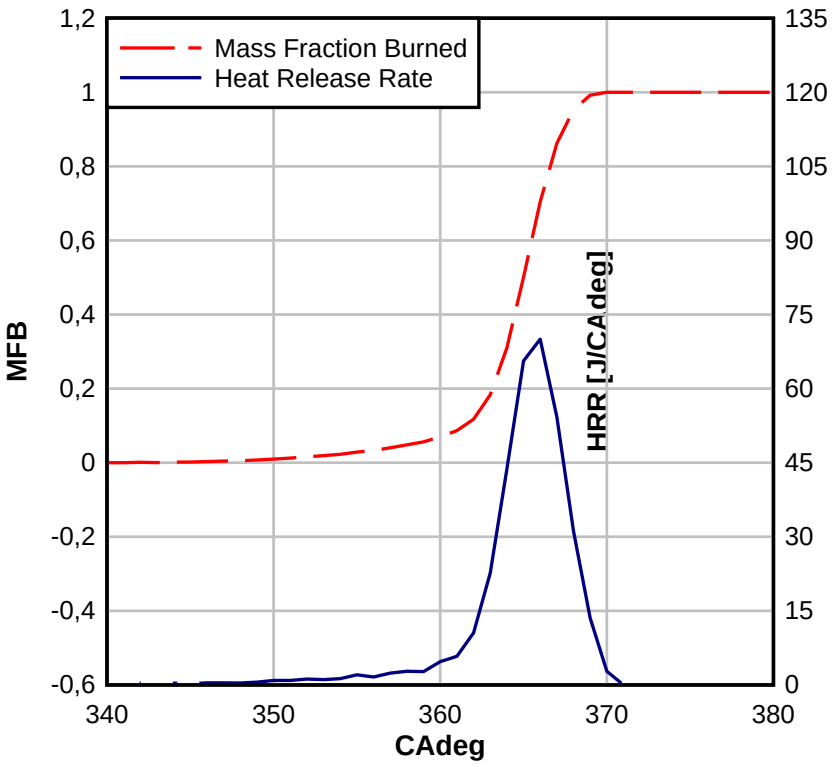

Figure 42: Typical Mass fraction burned curve and heat release rate from HCCI experiments

The second part is much faster, high temperature combustion (HTC). In this part two ingredients of gasoline: N-heptane and Iso-octane (branched-chain high octane number paraffin) combust until all the mixture is burned.

Figure 42 presents a MFB profile and HRR for one of our HCCI measured cases. It shows HCCI combustion can be split in a two-step process. Slow Low temperature combustion (LTC) process is visible from around 348 CAdeg and lasts until around 360 CAdeg. From 360 CAdeg and onwards a faster high temperature combustion (HTC) process is visible.

In [90] Qin used a simplified Watson's Diesel correlation [91] for HCCI MFB curve prediction. After omitting the Diesel diffusion burning phase the main combustion process – HTC (10%-100% MFB) could be described as:

$$MFB_{HTC} = 1 - \left(1 - \tau^{cp1}\right)^{cp2} \quad 59$$

$$\tau = \frac{\theta - \theta_{10\%MFB}}{\Delta\theta} \quad 60$$

$$\Delta\theta = l_1 + l_2 / speed^{1.5} - l_3 \cdot \log(EGR) \quad 61$$

where cp1 and cp2 are from correlations of engine parameters:

$$cp1^{-1} = e_1 - f_1 \cdot EGR - g_1 \cdot EGR^{1.5} \quad 62$$

$$cp2 = e_2 - f_2 / speed - g_2 \cdot EGR \quad 63$$

For the first stage of combustion – LTC (0%-10% MFB), the following correlation combining linear and exponential function was used:

$$MFB_{LTC} = A + B \cdot \exp\left(-\frac{\theta}{C}\right) \quad 64$$

where A, B and C are correlations of engine parameters.

$$\ln A = a_1 + b_1/speed^{1.5} + c_1/EGR^2 \quad 65$$

$$B = a_2 + b_2 \cdot speed^2 + c_2/EGR^2 \quad 66$$

$$C = a_3 + b_3 \cdot speed^{2.5} + c_3/EGR^3 \quad 67$$

where:

θ - local crank angle [deg]

$\theta_{10\%MFB}$ – crank angle where the 10% of mass fraction burned occurs [deg]

speed – engine speed [rpm]

EGR – fraction of exhaust gas residuals [kg/kg*100%]

λ - air/fuel ratio

a_1, a_2, a_3, b_1, b_2, b_3, c_1, c_2, c_3, e_1, e_2, f_1, f_2, g_1, g_2, l_1, l_2, l_3 – constants.

In Qin's publication [90] the proposed MFB equations was combined with the 1-D engine flow model and validated by experimental data. However this model was not fitted with different values of equivalence ratio, which seem to have a large effect on HCCI combustion. For the prediction of auto-ignition, a simplification for the temperature threshold was applied.

3.8.1.3 Developed Burn Profile Model

To follow the path outlined at the beginning of this section, a modified auto-ignition model and a modified burn profile model was used.

To predict auto-ignition, the local ignition time delay equation (57) was modified to account for the effect of the engine speed on the start of burning time, as shown by the modified Arhenius equation.

$$\tau = A_A \cdot \phi^{1.7} \cdot \chi_{O_2}{}^{-9.5} \cdot 1/speed^{13.1} \cdot \chi_{O_2}{}^{m \bullet speed} \cdot p^{-n} \cdot \exp\left(\frac{E_A}{R \cdot T}\right) \qquad 68$$

Two new terms, $\chi_{O_2}{}^{m \cdot speed}$ and $1/speed^{13.1}$, were added to the equation (68) which help the model capture a 'reversed trend' (ignition phase advances with increasing speed for low and medium engine speed and advances for high engine speed). The knock integral equation (58) remains unmodified.

For the prediction of burn profile, a modified Watson's Correlation for diesel engines was used. Burn equations (61), (62), (63), (65), (66), (67) were modified for achieving

better results for different air/fuel ratios and engine speeds. The natural logarithm was removed from equation (61). This helped to have accurate linear LTC burn phase prediction. Constant coefficients like λ and d_i have been added to the equations (65), (66), (67). This allowed the model to predict longer LTC burn phase for higher air/fuel ratios. The LTC (0-10% MFB) equations in its final forms are as follows:

$$MFB_{LTC} = A + B \cdot \exp\left(-\frac{\theta}{C}\right) \quad 69$$

$$\ln A = a_1 + b_1/speed^{1.5} + c_1/EGR^2 + d_1 \cdot \lambda \quad 70$$

$$B = a_2 + b_2/speed^2 + c_2/EGR^2 + d_2 \cdot \lambda \quad 71$$

$$C = a_3 + b_3/speed^{2.5} + c_3/EGR^3 + d_3 \cdot \lambda \quad 72$$

Constant coefficients like λ^i and $h_i \cdot speed$ have been added to the coefficient equations (61), (62), (63). This improvement allowed the model to predict slower, less "steep" HTC burn profile for higher air/fuel ratios. Additionally coefficients in equations (61), (62), (63), were adjusted to achieve better solution convergence and better accuracy. The final form of all equations for HTC burn phase (10-100% MFB) is as follows:

$$MFB_{HTC} = 1 - \left(1 - \tau^{cp1}\right)^{cp2} \quad 73$$

$$\tau = \frac{\theta - \theta_{10\%MFB}}{\Delta\theta} \quad 74$$

$$\Delta\theta = l_1 + l_2 / speed^{1.3} - l_3 / EGR^{2.2} - l_4 \cdot \lambda \quad 75$$

$$cp1 = e_1 - f_1 \cdot EGR^2 - g_1 \cdot \lambda^2 - h_1 \cdot speed \quad 76$$

$$cp2 = e_2 - f_2 \cdot EGR^2 - g_2 \cdot \lambda^3 - h_2 \cdot speed \quad 77$$

3.8.1.4 Developed Burn Profile Model fitting

The Ricardo WAVE model described earlier was fitted with coefficients based on the Jaguar V6 engine experiments. The engine is employing HCCI through negative valve overlap. The Cam Profile Switching (CPS) system allows the switching between two valve profiles – SI 9 mm maximum lift and HCCI 3 mm maximum lift. The load can be controlled by changing the valve timings in the range of 60 CAD allowed by the Variable Cam Timing (VCT) system for both the intake and exhaust cams, but the exhaust valve timing has the much bigger influence on the EGR amount and the load.

The model fitting process was based on 45 operating points for the achievable HCCI envelope over the range of engine speeds 1000-2900 rpm and two lambda values 1.0 and 1.2. Because the influence of the intake valve timing on the residual gas fraction (RGF) is much smaller than the exhaust valve timing, it was kept constant. The load was changed only through varying the exhaust valve timing. The knock limiting pressure rise rate was set to 6 bar/CAD. The EGR values for each point were taken from Ricardo WAVE simulation. Heat release analysis was done using Kreiger and Borman [92] method. A table with all the points and data used for the model fitting can be found in Appendix 7.

The following steps have been made to fit the correlative model:

- The burn profile model was fitted with the coefficients derived from experiments and modeling data.
- The Ricardo WAVE model was combined with an external combustion model written in FORTRAN to fit the knock-integral model with adequate coefficients. The combustion model was used for calculating the integral and MFB profiles. The target was to calibrate the integral in such way to achieve the best

convergence of the model in agreement with the experiment 50% MFB location data.

For fitting both models, an iterative methodology was used, which converged to the minimal sum of differences between calculated and measured values. As a result the MFB model should predict the pressure rise rate accurately, where the ignition model combined with the burn profile model should produce accurate 50% MFB locations which will help to define the low load boundary.

The final values of all constants used in Ricardo WAVE model are summarised in Table 8. A demonstration of the combustion model is presented in Figure 43.

Eq. 13 constants		Eqs. 16, 17, 18 constants						Eqs. 21, 22, 23 constants					
A_A	$2{,}96*10^{32}$	a_1	$-2{,}3*10^{-2}$	a_2	$2{,}474*10^{-2}$	a_3	8,49	l_1	15,98	e_1	1,356	e_2	1,305
m	$2{,}8*10^{-3}$	b_1	$-1{,}277*10^{-5}$	b_2	$-1{,}911*10^{-10}$	b_3	$-2{,}7*10^{-10}$	l_2	-12181	f_1	$-2{,}951*10^{-4}$	f_2	$-1{,}113*10^{-3}$
n	1,05	c_1	38	c_2	-25	c_3	$-2*10^{-5}$	l_3	77418	g_1	$-1{,}05*10^{-5}$	g_2	$-1{,}405*10^{-3}$
		d_1	$-1{,}727*10^{-3}$	d_2	$-2{,}727*10^{-4}$	d_3	-12	l_4	-6,82	h_1	$-2{,}96*10^{-4}$	h_2	$-1{,}377*10^{-4}$

Table 8: Calculated values of constants for the equations

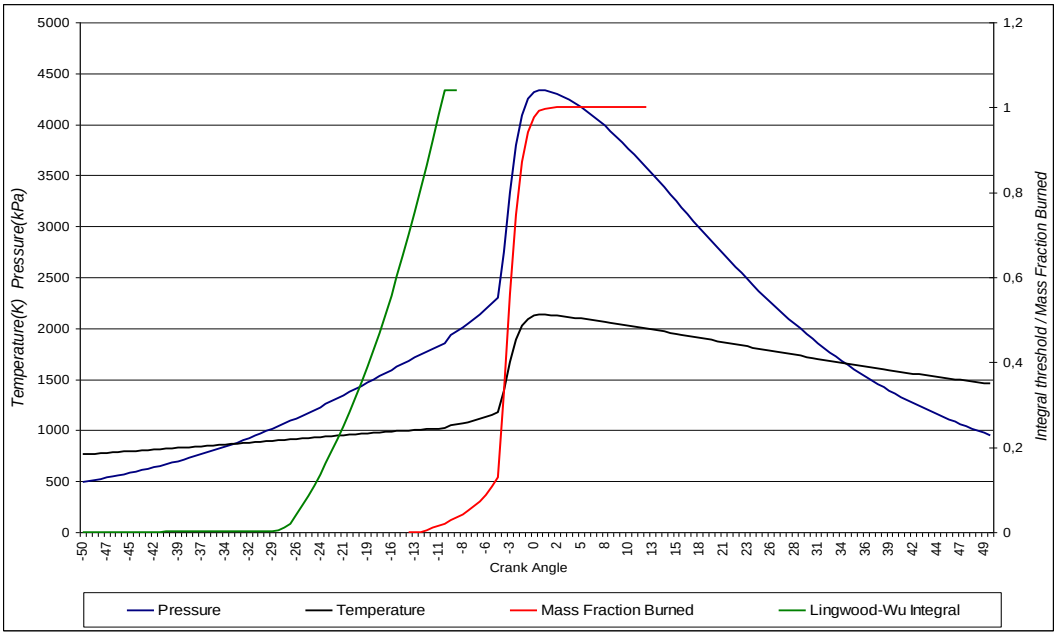

Figure 43: In-cylinder variables, time delay integral and MFB near the TDCC

3.8.2 Ricardo Wave Model Validation

Fitted correlations were used in the WAVE external combustion model and the calculations were performed for a different load and speed points in order to analyse fitting accuracy and obtain validation. For this purpose another set of experimental data was used.

The validation experiments were performed over the load/speed operating range of the V6 HCCI engine. The low load boundary is outlined by misfire as combustion is retarding with increasing amounts of EGR, and the high load boundary is limited by maximum pressure rise rate set for 6 bar/CAD. The load/speed sweeps were performed for three lambda values: 1.0, 1.2, 1.3. The maximum allowed engine speed was 2900 rpm so the experiments were run for speeds 1000-2900 rpm. Each sample is averaged over one hundred recorded cycles therefore the cycle to cycle variations are not considered here. Heat release analysis was done using Kreiger and Borman [92] method. The table with all points and data used for model validation can be found in Appendix 7.

Figure 44 shows the Residual Gas Fraction (RGF) obtained from the simulated results for various engine speeds. The inlet valve timing for all cases was kept constant. It can be noticed that there is a linear correlation between EGR and EVC for each engine speed. When exhaust valve timing is advanced, the amount of EGR decreases. This means that when the exhaust valve timing is changed we can assume that RGF will change proportionally.

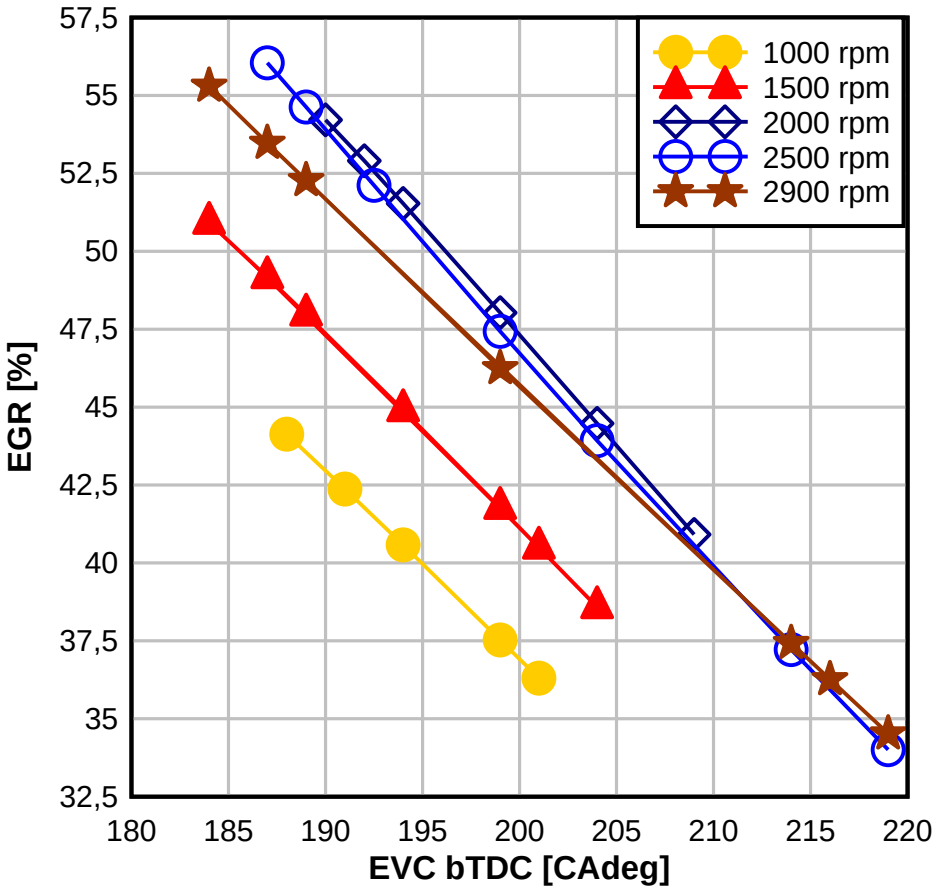

Figure 44: Amount of EGR for varied exhaust valve timing, inlet valve timing kept constant (Ricardo WAVE model)

The modeling and experimental data were compared in terms of load (Figure 45), 50% MFB location (Figure 46) and Rate Of Pressure Rise (ROPR) (Figure 47) difference. The operating envelopes in terms of engine load predicted by the model and measured in the experiment have been compared (Figure 48). A map showing the percentage difference of predicted load (NMEP) between the model and experiment is shown in Figure 45.

The model is over-predicting the engine load for the most advanced exhaust valve timings and for the higher engine speeds. The largest error observed is by approximately 0.5 bar (10%) and the average error is approximately by 0.23 bar (4%).

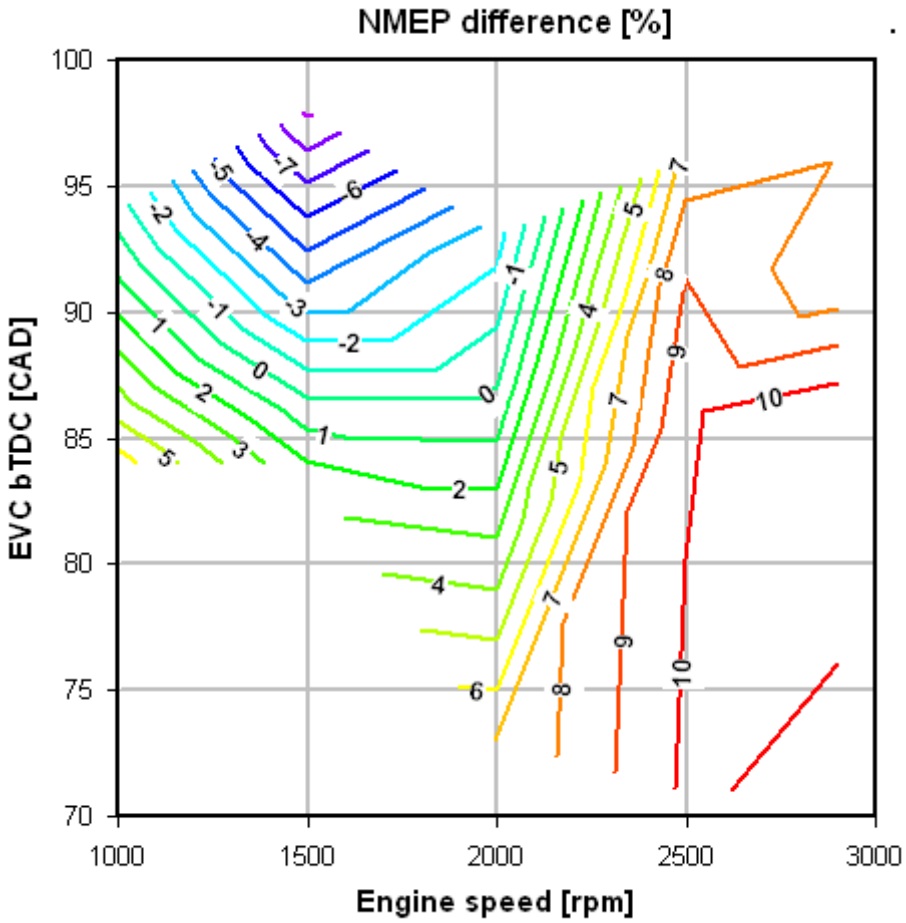

Figure 45: Map showing the difference of predicted load (NMEP) between the model and experiment (in %).

The differences in the load are probably caused by the engine cycle flow model itself and not necessarily by the combustion model. This could be a result of the cylinder blow-by loss calculation in the Ricardo WAVE model, which cannot be adjusted for the engine condition and it seems that the under-prediction is more evident at higher loads. It is clear that the MFB profiles for high loads are predicted more accurately.

The biggest error in the prediction of 50% MFB location (Figure 46) occurs at the higher engine speeds. The model is not able to fully follow the reversing speed trend mentioned earlier, however the error is acceptable. For medium engine speeds, the model is under-predicting the combustion phasing where on high speeds the

combustion phasing is over-predicted. The maximum individual error is 5.6 CAD and the average error is 1.83 CAD. All timings are arranged into a table in Appendix 7.

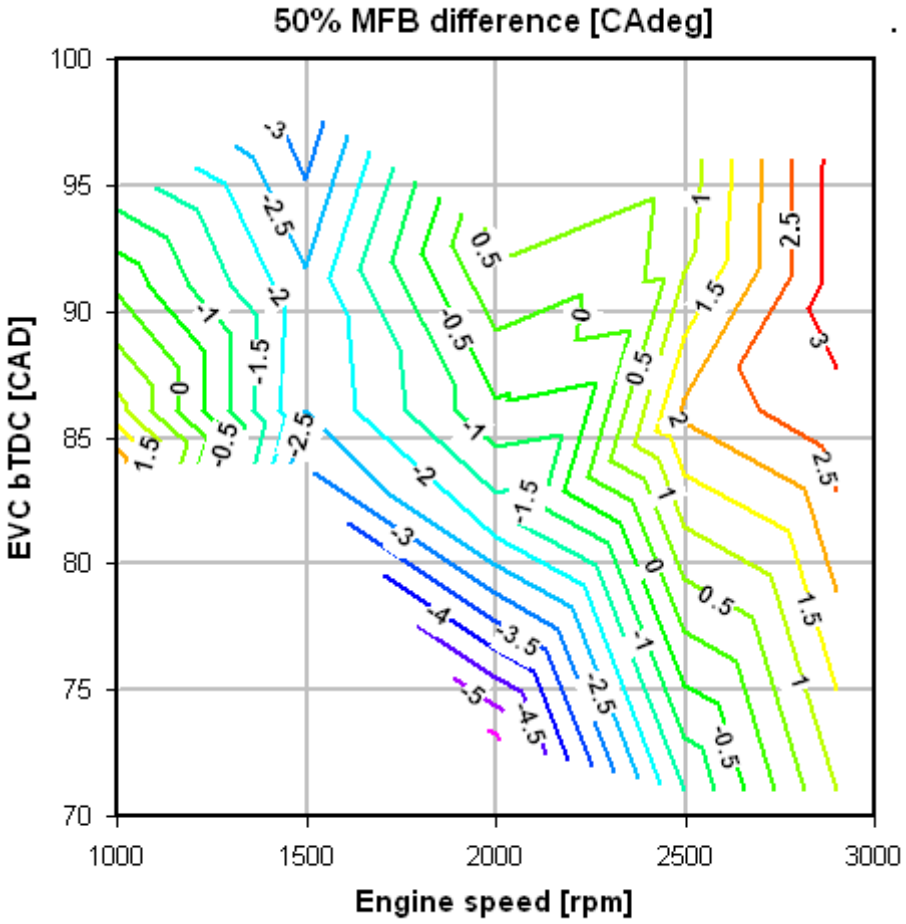

Figure 46: Map showing the difference of predicted 50% MFB location between the model and experiment: 50%MFB(model) – 50%MFB(experiment) [CAdeg]

Figure 47 compares the pressure rise rate and it can be seen that the biggest error is with the most advanced exhaust valve timing (by up to 1.2 bar/CAD – 40%). The average error is 0.5237 bar/CAD – 7.2 % The engine with advanced exhaust timing is for low load and thus the pressure rise rate is not a critical issue as for higher load conditions, implying that this error is acceptable.

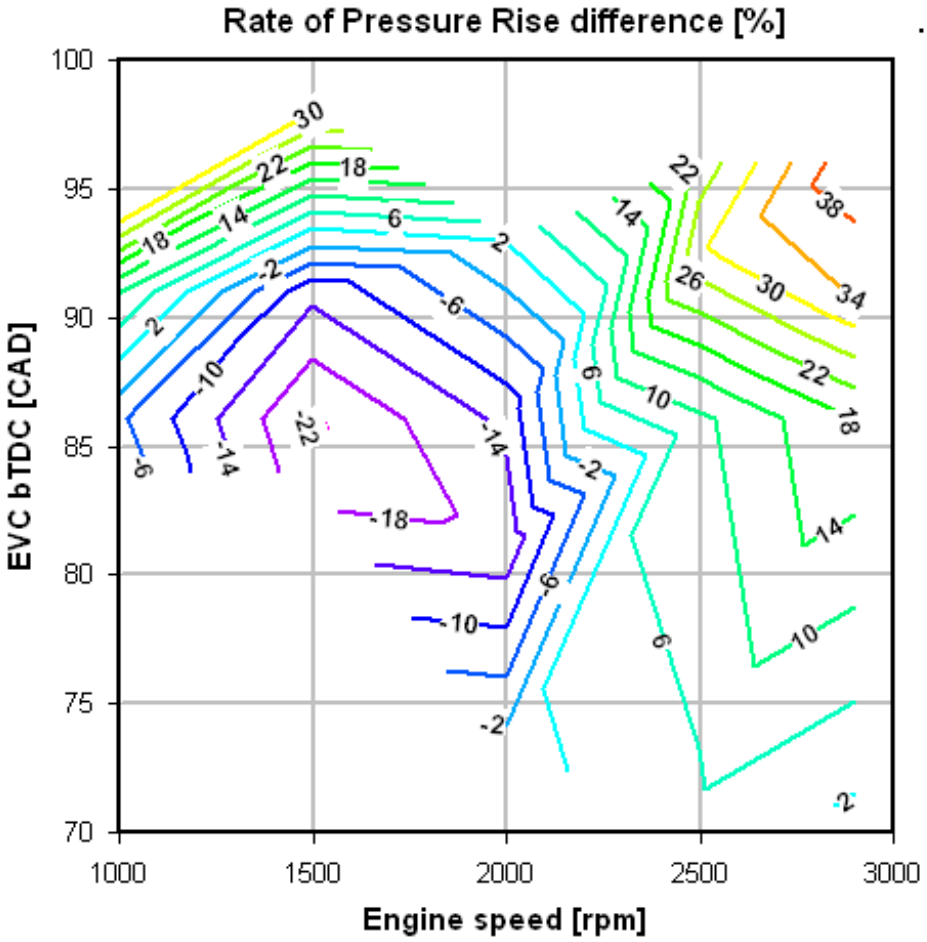

Figure 47: Map showing the difference of predicted ROPR between the model and experiment (in %).

Figure 48 presents the comparison of operating envelopes predicted by the model and measured in the experiment respectively. The high load boundary was found for a maximum pressure rise rate of 6 bar/CAD for both, the model and the experiment. The lower boundary is defined by the misfire limit. Misfire occurs when in-cylinder temperature and pressure history doesn't meet the ignition criteria.

The closer the conditions move towards misfire the more retarded the combustion timing becomes. Because of this phenomenon the 50% MFB location with the most retarded value where misfire didn't occur in experiment was chosen as a limit for the model.

The lowest load points for each speed were plotted on 50% MFB – speed graph and the curve which goes through these points was found. Additionally the engine speed was used in normalized form to avoid complex equations.

The low load boundary can be described by this two part correlation:

For speed < 1500rpm

$$50\%\,\mathrm{MFB}_{misfire} = \mathrm{m}_1 \cdot \mathrm{speed}'^2 - m_2 \cdot speed' + m_3 \left[CAd\ aTDCC\right] \quad (78)$$

$\mathrm{m}_1 = -38.4$
$\mathrm{m}_2 = 20.6$
$\mathrm{m}_3 = 12.25$

For speed >= 1500rpm

$$50\%\,\mathrm{MFB}_{misfire} = \mathrm{n}_1 \cdot \mathrm{speed}' - n_2 \left[CAd\ aTDCC\right] \quad (79)$$

$\mathrm{n}_1 = 3.016$
$\mathrm{n}_2 = 4.02$

Where

$$\mathrm{speed}' = \frac{engine\ speed[rpm]}{2000} \quad (80)$$

The engine model tends to over-predict load in the high range and the upper boundary is over-predicted by average value of 0.2 bar (NMEP) but the trend is predicted accurately. As for the lower boundary, the trend is also predicted well and the average discrepancy is around 0.21 bar (NMEP).

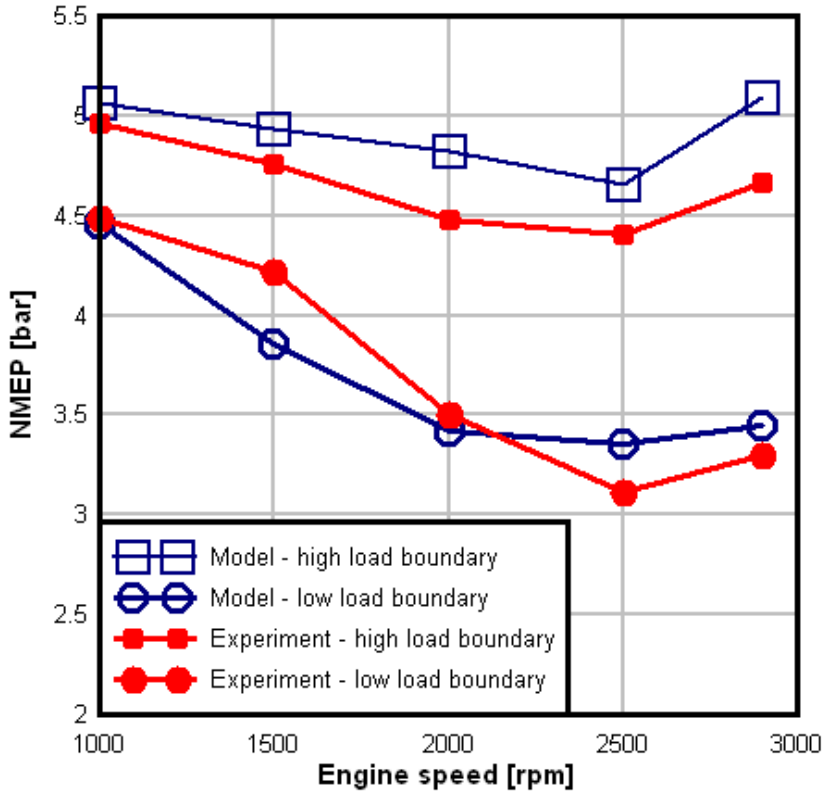

Figure 48: Engine and model operating envelope comparison

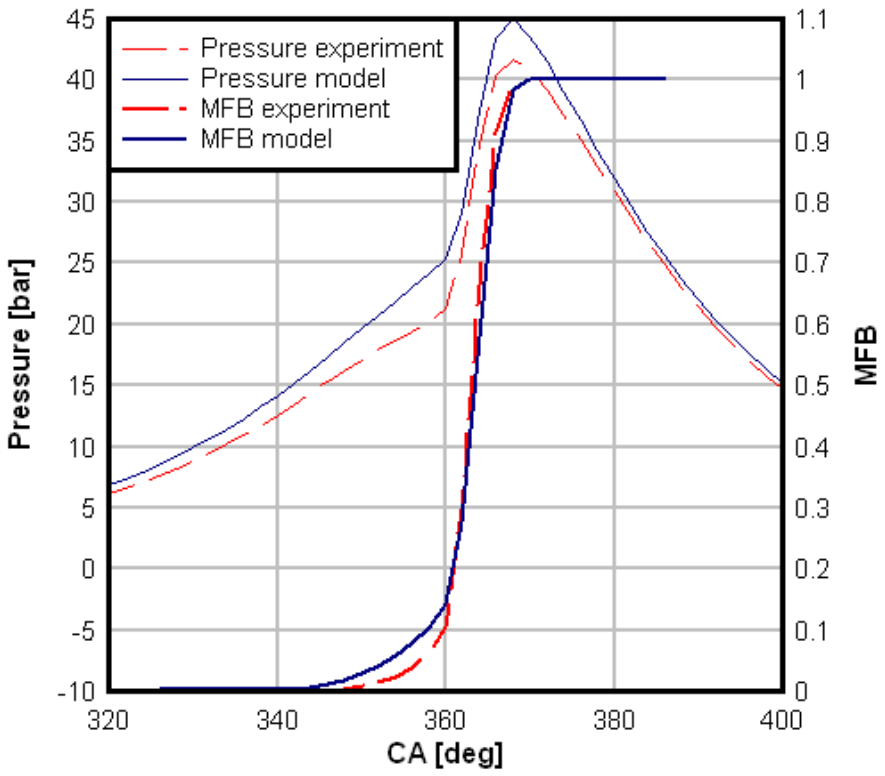

Figure 49: In-cylinder pressure trace and MFB profile comparison, 1500 rpm, 84 EVC bTDC, high load (4.76 bar NMEP), lambda=1.0

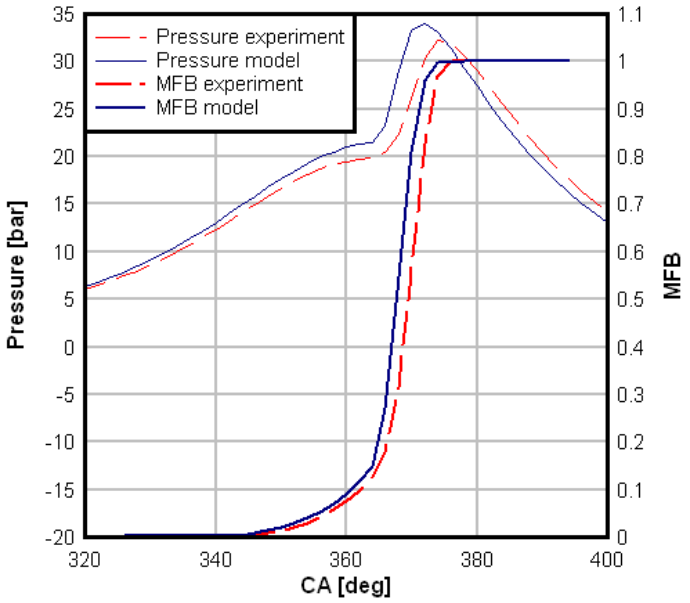

Figure 50: In-cylinder pressure trace and MFB profile comparison, 1500 rpm, 98 EVC bTDC, low load (4.22 bar NMEP), lambda=1.0

Experimental data was recorded for 100 cycles and then averaged over the recording period. For the low load cyclic variability was increasing. The Coefficient Of Variation (COV) for NMEP was kept under 5% at the low loads. Pressure traces in Figure 49 and Figure 50 for 2 different engine operating conditions show that there is good agreement for the MFB profiles obtained by modeling and experimental data, despite of the small discrepancies at the time of auto ignition and at maximum pressure positions. This is partly attributed to the limitation with Ricardo WAVE software in which the leakage amount though the gap between the cylinder and the piston is fixed. As a result of that the blow-by losses are under predicted for this engine and the pressure obtained from the model is higher. Another major Ricardo WAVE simplification is a zero dimensional cylinder model which produces difficulties in modeling of heat exchange and mixture compression processes. The difference is higher for the higher load condition in Figure 49 but it is less than 7% and thus is acceptable, although this contributed to the error in the upper load

boundary as shown in Figure 48. This problem should be less significant if the blow-by losses can be correctly calculated using a different engine simulation code.

Additional simulations and experiments have been performed to validate the model in different operating region than the region that the model was fitted on. Three operating points were chosen:

Naturally aspirated operation – high load (dp/dCA>6 bar)

Supercharged stoichiometric operation

Supercharged lean operation

Table 9 shows comparison of major parameters for these three operating points. The start of combustion is predicted by the model with a maximum 2.5 CAdeg error, which is an acceptable value. Combustion duration prediction shows an error of up to 1 CAdeg. Pressure rise rate is predicted accurately with some minor variations (+- 0.2 bar/CAdeg). Load is overestimated by the model for the high load case. This tendency could be seen in previous part of validation as well.

Engine speed [rpm]	Lambda	Boost pressure [bar]	IVO [CAdeg atdc]	EVC [CAdeg btdc]		5% MFB [CAdeg]	5% - 95% MFB [CAdeg]	Pressure Rise [dp/dCA]	IMEP [bar]
1500	1	0.2	95	91	experiment	363.4	15.6	5.52	5.32
					model	361.0	15.0	5.60	5.28
2500	1.3	0.2	65	91	experiment	356.6	13.8	4.27	4.59
					model	354.0	14.5	4.12	4.45
1000	1	0	65	84	experiment	363.9	12.2	7.28	4.96
					model	362.9	11.3	7.15	5.32

Table 9: Comparison of experimental and modeling results for three engine operating points.

3.8.3 Summary: Ricardo Wave Model

The in-cylinder pressure data was analysed and the heat release rate was calculated for various cases. The two most important parameters which define HCCI combustion are the 50% MFB location and the maximum rate of in-cylinder pressure rise. For

high loads the pressure rise rate defines the limit of HCCI operation, whereas for low loads the 50% MFB location can be used to identify misfires which outline the lower load boundary. There is a tendency for the pressure rise rate to increase and for the combustion to advance when the engine load is increased. For lower loads the combustion process is becoming longer and the timing of 50% MFB is retarded.

For an HCCI engine exhaust valve timing is the most important load control variable as it affects the EGR amount significantly.

It was found that the location of 50% Mass Fraction Burned (MFB) and the peak rate of pressure rise can be chosen as the key parameters charactering the HCCI combustion in engine simulations. The fitted combustion model was then implemented into the V6 engine Ricardo WAVE model and validation of its predictive calculations was obtained using a different set of experimental data. The results show that the predicted 50% MFB position is within an average error of 1.84 crank angle degrees (CAdeg) and the predicted peak rate of pressure rise is within an average error of 0.53 bar/CAdeg (7.2%).

Chapter 4. Experimental Results

4.1 Extending the HCCI Map

The engine was run in HCCI mode using the thermal management system as means of stabilisation of ambient conditions in order to have repetitive HCCI test results and control of the air intake of the engine operating in HCCI mode. The cases shown in Table 10 describe the engine and Thermal Management system configuration for the obtained HCCI boundary of the averaged NMEP values for all engine cylinders. The abbreviations used in this text to describe the engine setup in each case are as follows:

Abbreviations		
NP:	Normal Air path	
NP-C:	Normal Air path with cooling	
HP:	Heated Air path	
HP-H:	Heated Air path with Heating	
EOI:	End of injection before TDC combustion	
BP:	Boost Pressure [bar]	
Cases for HCCI Boundary		
Case	Engine Setup	NMEP [MPa]
1	N=1000-HP-H λ=1.0 EOI250	0.507
2	N=1000-HP-H λ=1.0 EOI350	
3	N=1000-HP-H λ=1.2 EOI350 BP=0.1 bar	0.421
4	N=1500-NP-C λ=1.0 EOI250	0.582
5	N=1500-HP-H λ=1.0 EOI250	
6	N=1500-HP-H λ=1.3 EOI350	0.378
7	N=2500-NP-C λ=1.3 EOI350 BP=0.2 bar	0.603
8	N=2500-NP-C λ=1.2 EOI350	0.331
9	N=2500-NP λ=1.2 EOI350	

Table 10: Abbreviations and Cases for HCCI Boundary

The requirements for HCCI operation was that any cylinder at any one instant would need to have dP/dCA values less than 6 [bar/CA]. This value was provided by the engine manufacturer and was the absolute maximum we could safely operate the

engine. To obtain stable HCCI it was possible to change the induced gas temperature and pressure, quantity of re-induced exhaust gas (EGR) by altering the inlet and exhaust valve timing, injection timing and lastly the air to fuel ratio.

No other additional method (such as the use of spark-assisted mode) was used to help sustain the HCCI mode of operation. For some cases similar NMEP values were obtained in one or more cases at a particular engine speed. The best configuration was determined after implementing the HCCI control strategy. Figure 51 shows the improved operational map for HCCI mode for the Jaguar 3.0 litre V6 HCCI engine using the Thermal Management system.

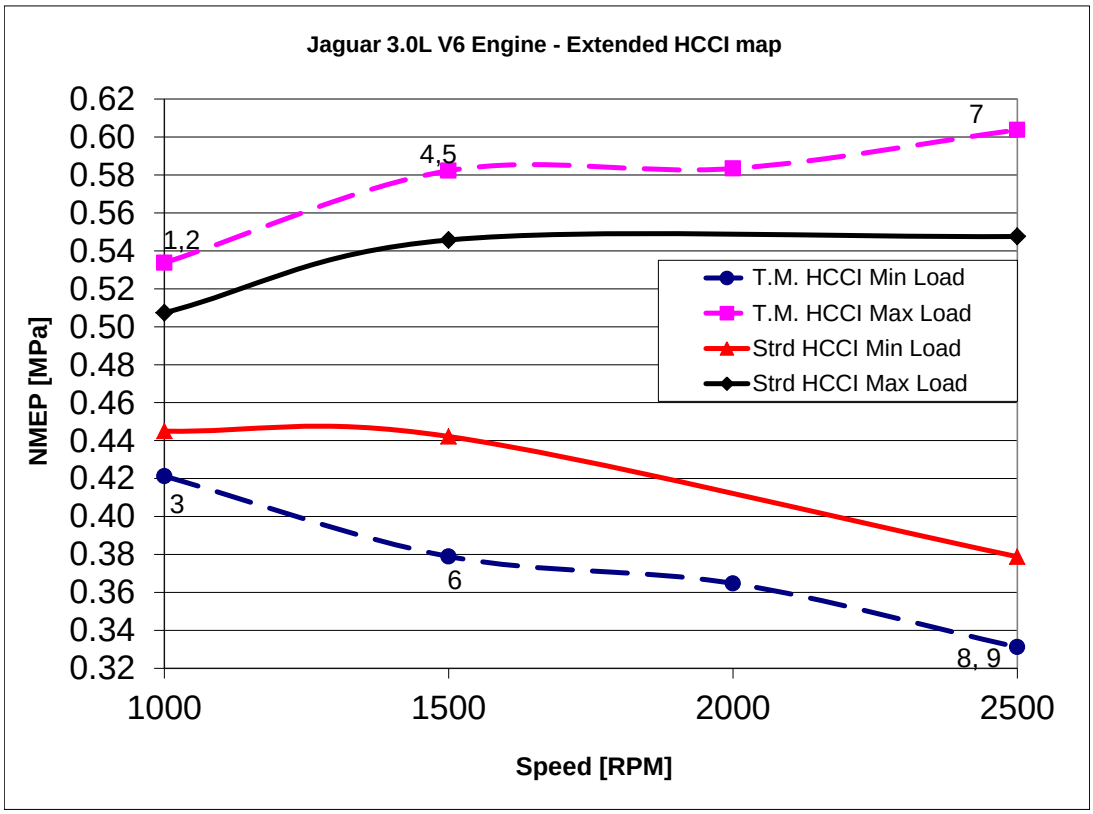

Figure 51: Extended HCCI Map showing boundary cases (from Table 10)

4.2 HCCI Control Strategy

One of the project objectives is to reduce HCCI emissions and in particular NOx and HC. Each condition was investigated individually and the best configuration is presented below. The cases shown in Figure 52 to Figure 55 are taken from Table 10.

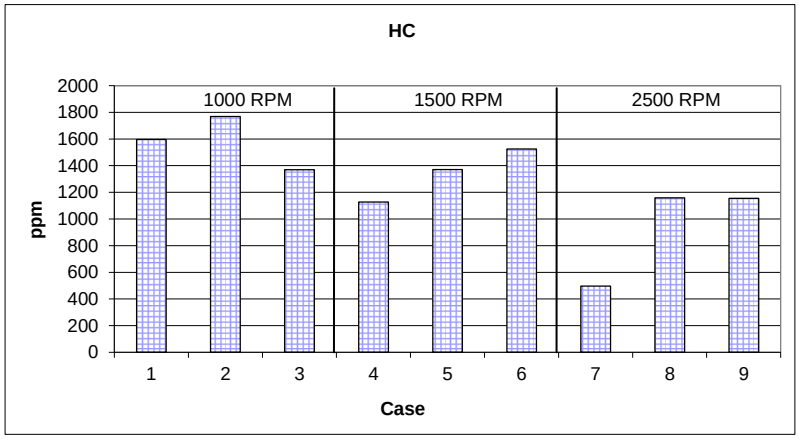

Figure 52: HC for Extended HCCI Map, Case 1 to 9

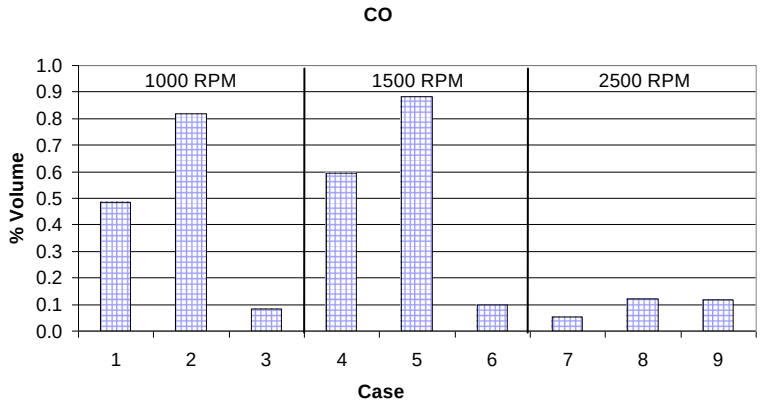

Figure 53: CO for Extended HCCI Map, Case 1 to 9

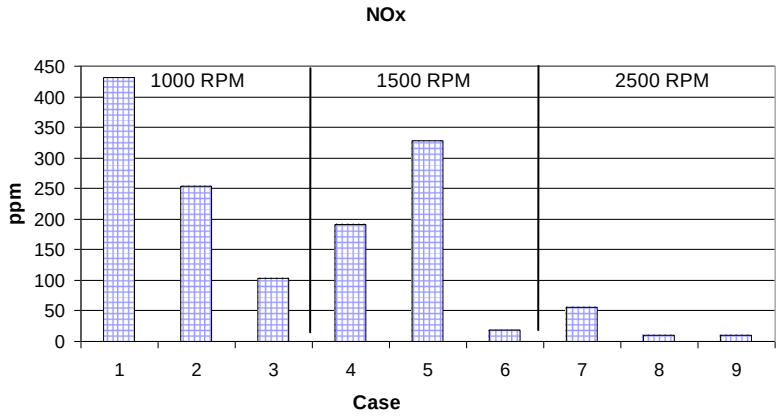

Figure 54: NOx for Extended HCCI Map, Case 1 to 9

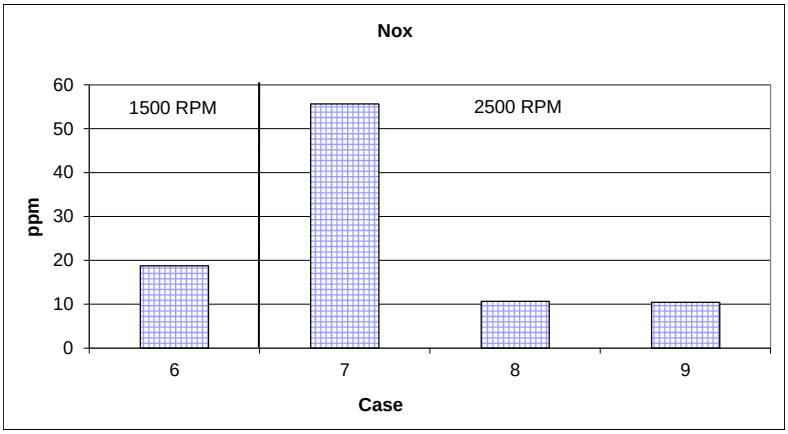

Figure 55: NOx for Extended HCCI Map, Case 6 to 9

4.2.1 1000 RPM

At the higher boundary there were two cases that achieved similar NMEP values. From Figure 51 and Figure 54 the results show that using earlier injection as in Case 2 one can achieve the highest NMEP and the lowest NOx emissions. At lower boundary one can achieve the lowest extension for HCCI using the configuration such as in Case 3.

4.2.2 1500 RPM

At 1500 RPM one using the T.M. system can achieve the most significant extension of the HCCI map at the lower boundary. At higher boundary there were two cases that achieved similar NMEP values. From Figure 51 and Figure 54 the results show that lowering the charge air temperature and using boosting as in Case 4 it is possible to achieve the highest NMEP and the lowest NOx and HC emissions.

4.2.3 2500 RPM

At the lower boundary there were two cases that achieved similar NMEP values. Both cases run lean and observing Figure 52 to Figure 55 we can see similar emission data revealing that both cases could be potentially used.

4.3 Comparison of Experimental and Modelled Data

In order to validate the system model two arbitrary sample points were chosen at different engine speeds and loads from test data, as shown in Table 11. The results from this data is included in Appendix 10.

230707_1000-HP-H_Lamda10_EOI350	Pre Validation Case A
230707_1000-HP-H_Lamda10_EOI350	Validation Case A
270707_1500-HP-H_Lamda13_EOI350	Validation Case B
250707_2500-HP-H_Lamda10_EOI350_BP01	Validation Case C
190707_1500-HP-H_Lambda10_EOI350	Validation Case D
270707_15-HP-H_Lamda13_EOI350	Validation Case E

Table 11: Realtime Model Validation Cases

Figure 56 shows the experimental layout and model representation for the HCCI engine and all auxiliary components.

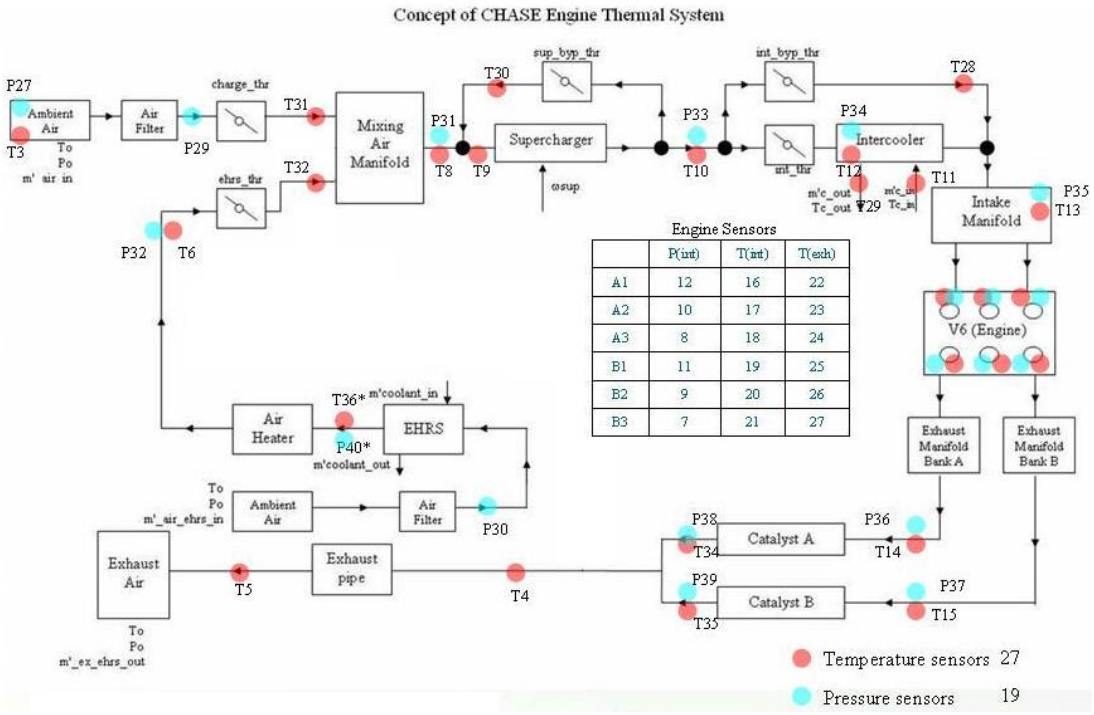

Figure 56: Model representation of the experimental layout

Model Validation Results

The following data show the measured and predicted pressure and temperature values in the system. Calibration of model required some adjustment to heat transfer

coefficient for heat losses in different control volume components. Figure 57 shows the results before calibration for Case A whereas Figure 58 shows the results after calibration for Case A. The engine inlet and exhaust data are presented as averaged values for all cylinders, whereas the rest of the data are measured at various points along the system as shown in the system layout in Figure 56.

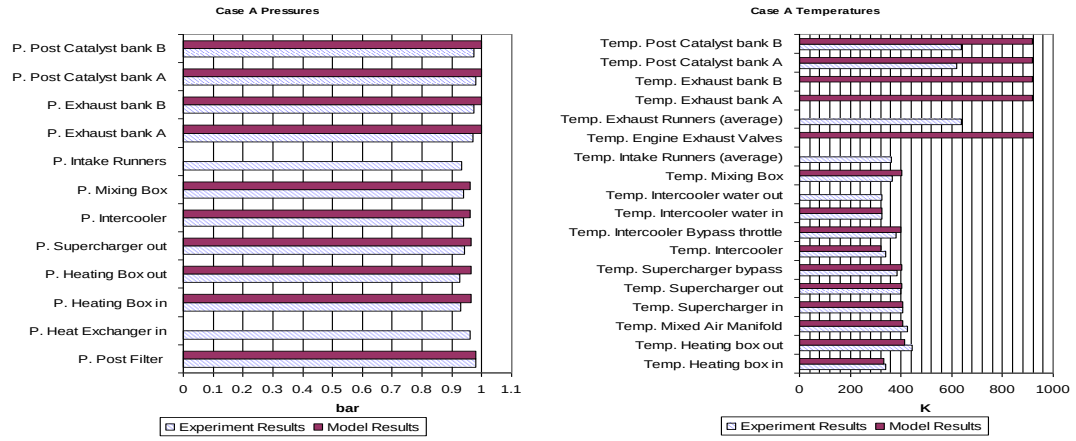

Figure 57: Model Fitting raw data Case A

A gain factor to the UA value for each control volume component was applied to the model in order to adjust the data and match the experimental results.

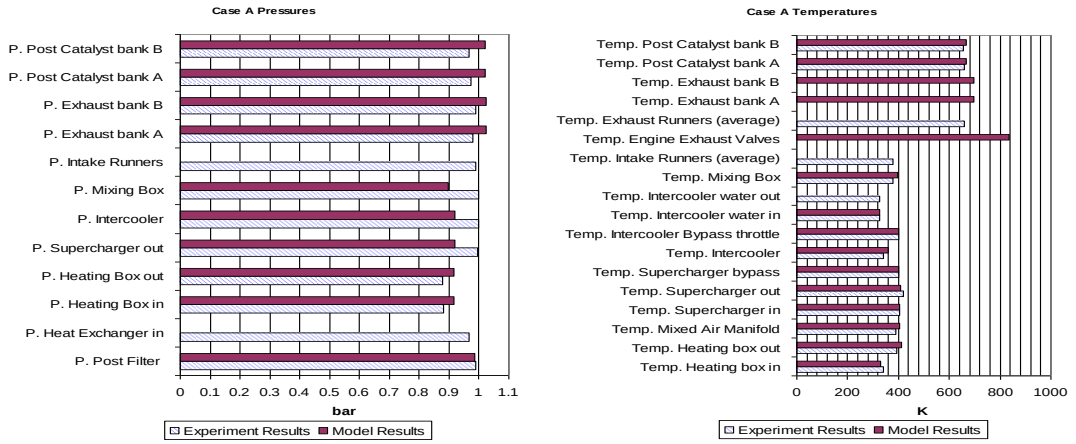

Figure 58:Calibrated Model Case A data

From Figure 58 it is clear that adjusting the heat loses in the system has enabled a good correlation between the experimental data and model prediction with minimal error both in pressure and temperature estimation.

Validation of the model is performed by applying the model calibrated for Case A to Cases B and C listed in Table 11. The validation results – experimental and predicted pressure and temperature values at various points in the system are presented in Figure 57 to Figure 60. Looking at the engine exhaust temperatures one can observe that on Figure 57 there are some differences between the modelled and experimental values. It should be noted that because of the model configuration (the volume of the exhaust pipe and heat losses though the exhaust runners) the measured exhaust temperatures points are not the same with the predicted temperature points of the engine model. Therefore an adjustment has been made to the model in order to calculate the correct exhaust temperatures which the effect can be seen from Figure 58, through Figure 60.

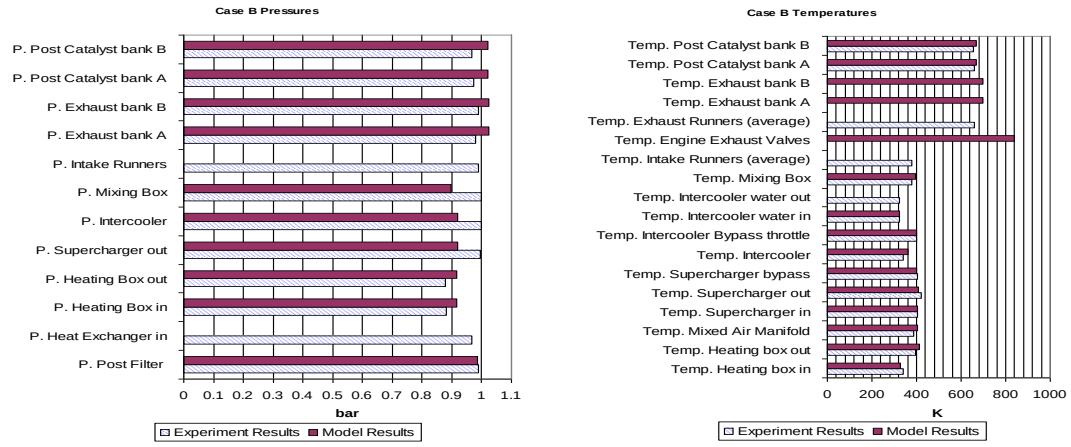

Figure 59: Validation Case B data

Figure 61 shows the averaged net mean effective pressure for all cylinders across all cases. Comparing the predicted and measured NMEP for the same condition one can see that the model is slightly over predicting the value of IMEP. This inaccuracy is one of the major challenges with the HCCI engine thermal management model as it lacks a combustion model because of its simplicity.

Overviewing the results one can see that there is good correlation between the experimental data and the model pressure and temperature predictions with

minimal error. Figure 61 shows the Net Mean Effective Pressure (NMEP) data from all the cases in Table 11 whereas Table 12 shows the difference of NMEP of simulated data from experiments. The results show that the simplified model shows partial compliance with experimental engine results.

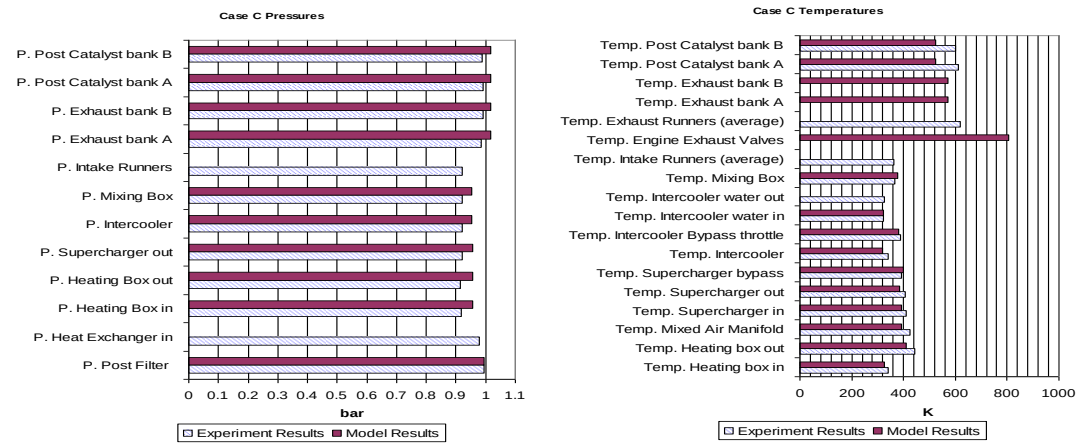

Figure 60: Validation Case C data

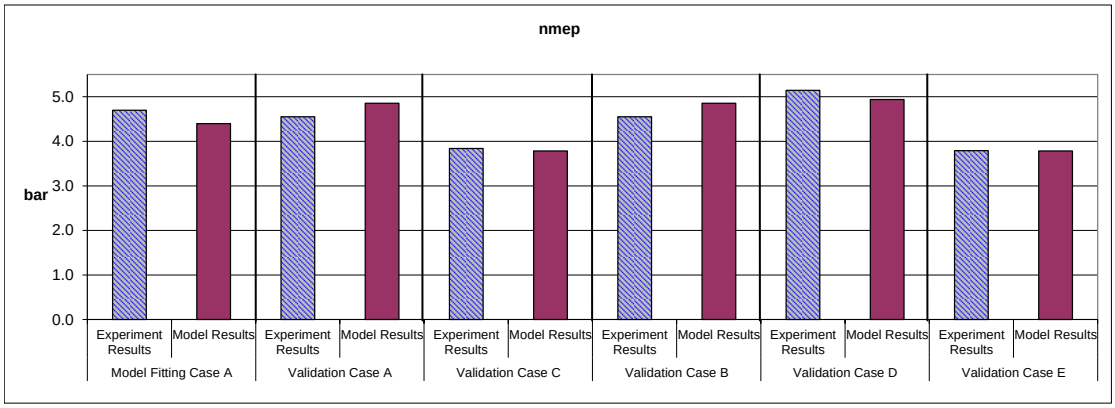

Figure 61: Net mean effective pressure data

nmep - difference from experimental data		
Validation Case A	-0.3 bar	-6.66 %
Validation Case B	-0.3 bar	-6.66 %
Validation Case C	0.06 bar	1.47 %
Validation Case D	0.21 bar	4.03 %
Validation Case E	0.01 bar	0.15 %
Abs. average error	0.23 bar	

Table 12: Net mean effective pressure data comparison

To further improve the engine model accuracy, the thermal conversion efficiency data near the HCCI boundary would need further adjustment using the real engine data. At

the moment the temperature data used to calibrate the realtime combustion model are interpolated from a validated Ricardo WAVE HCCI engine model simulation results. Because of this there is great uncertainty running the empirical engine model near the HCCI boundary and the only way to further fine-tune this model is to use experimental data obtained at that region.

4.4 Demonstrating the Thermal Management Model

At the experimental rig is possible to measure the temperatures in the inlet and exhaust port runners but there are no means to measure/log the temperatures during the HCCI cycle.

Case	Engine Setup
1	N=1500-HP-H λ=1.0 EOI350
2	N=1500-HP-H λ=1.0 EOI250
3	N=1500-HP-H λ=1.0 EOI250
4	N=1500-NP-C λ=1.0 EOI350
5	N=1500-NP-C λ=1.3 EOI350 BP=0.2 bar
6	N=2500-NP λ=1.2 EOI350
7	N=2500-NP-C λ=1.0 EOI350
8	N=2500-NP-C λ=1.2 EOI350
9	N=2500-HPλ=1.0 EOI350
10	N=2500-HP-H λ=1.0 EOI350
11	N=2500-HP-H λ=1.2 EOI350

Table 13: Cases for T.M. Demonstration

In order to visualise the effect of heating the charge air and the effectiveness of the heating system one can use the simulation model. Figure 62 shows the calculated in-cylinder temperature at the beginning of compression for the upper boundary for Cases 1 to 5 and Figure 63 the equivalent in-cylinder temperature calculated for the lower boundary for Case 6 to 11 shown in Table 13.

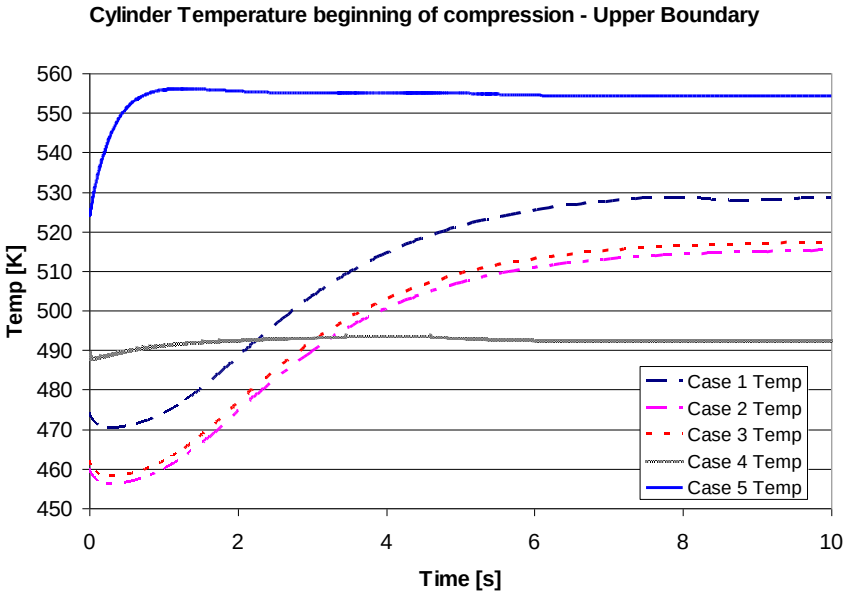

Figure 62: Cylinder temperature at beginning of compression – cases 1 to 5 upper boundary

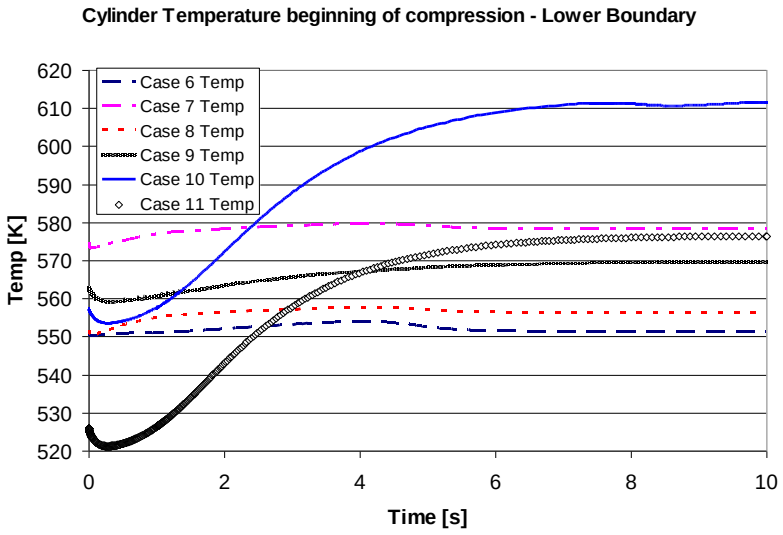

Figure 63: Cylinder temperatures at beginning of compression – cases 11 to 16 lower boundary

It can be concluded that by using the heaters the thermal system provides approximately 55K temperature differential whereas using the intercooler and supercharging one can obtain approximately 30K temperature differential in this configuration. The calculated temperatures can be used for positioning the T.M throttles, predicting the engine or boundary conditions for further and detailed modelling investigations such as CFD computations.

4.5 The Effect of Thermal Management on HCCI operation

4.5.1 Heating

Using heated inlet air resulted in advanced combustion. The decrease of the lower operational boundary can clearly be seen in Figure 51 especially at 1500 RPM; at other speeds this difference effect on load is significantly smaller. However, due to the heater's path there was 0.1 bar pressure drop in the inlet air flow which introduces partial throttling to the heated line path. It was also observed that possibly due to this pressure drop low dP/dCA values were obtained which resulted in a smooth and relatively silent HCCI operation.

4.5.2 Throttling

Using throttling one can achieve lower loads and the engine at some conditions runs very quietly in HCCI mode. It is possible to run HCCI up to 0.2 bar under-pressure in the inlet manifold after which the engine becomes unstable. It is believed that the lower loads are achieved partially due to heating the inlet air and partially due to throttling even if this might increase pumping losses. Furthermore, the supercharger was used to increase the inlet manifold pressure eliminating the 0.1 bar pressure drop and therefore yielding 1 bar absolute pressure in the inlet manifold. Using only the effect of heating for HCCI it was possible to obtain lower loads for the same valve timings.

Load Case		Max Load NMEP [MPa]	Min Load NMEP [MPa]
Case A	N=1000-NP λ=1.0 EOI350	0.507	0.445
Case B	N=1000-HP-H λ=1.0 EOI350	0.531	0.445
Case C	N=1000-HP-H λ=1.0 EOI350 BP=0.1 bar	0.486	0.449
Case D	N=1000-HP-H λ=1.2 EOI350	0.487	0.435
Case E	N=1000-HP-H λ=1.2 EOI350 BP=0.1 bar	0.442	0. 421
Case F	N=1000-HP-H λ=1.0 EOI250	0.533	0.468

Table 14: Effect of Thermal Management and Control for HCCI

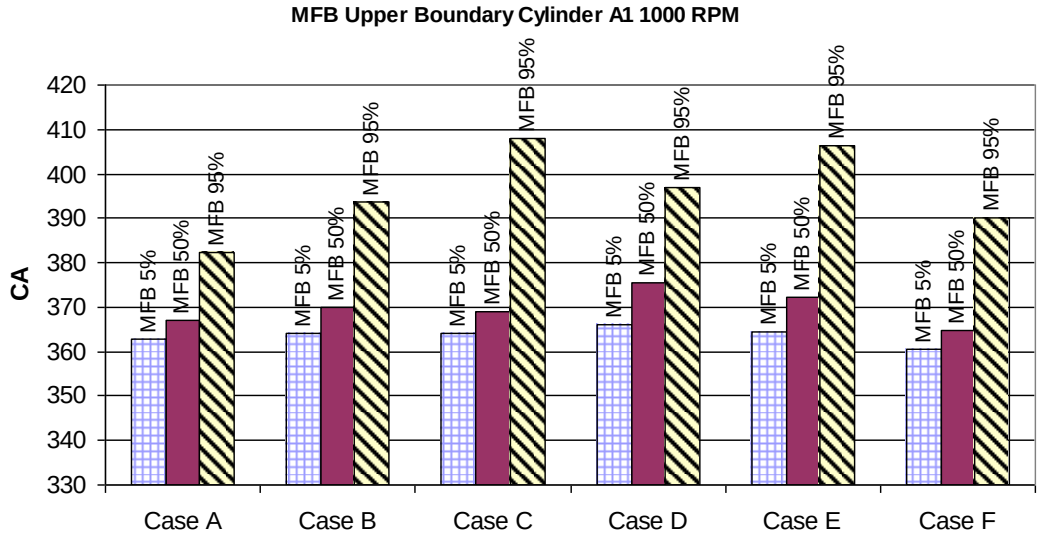

Figure 64: Mass Fraction Burned - Upper Boundary

Comparing the results of tests with different end of injection timing for both upper and lower boundary (Case B end of injection at 250 CA and Case F end of injection at 250 CA shown in Table 14) it seems that for end of injection at 350 CA it was possible to slow the combustion process. Furthermore when heating is maintained and injection timing is advanced to 250 CA NMEP is increased.

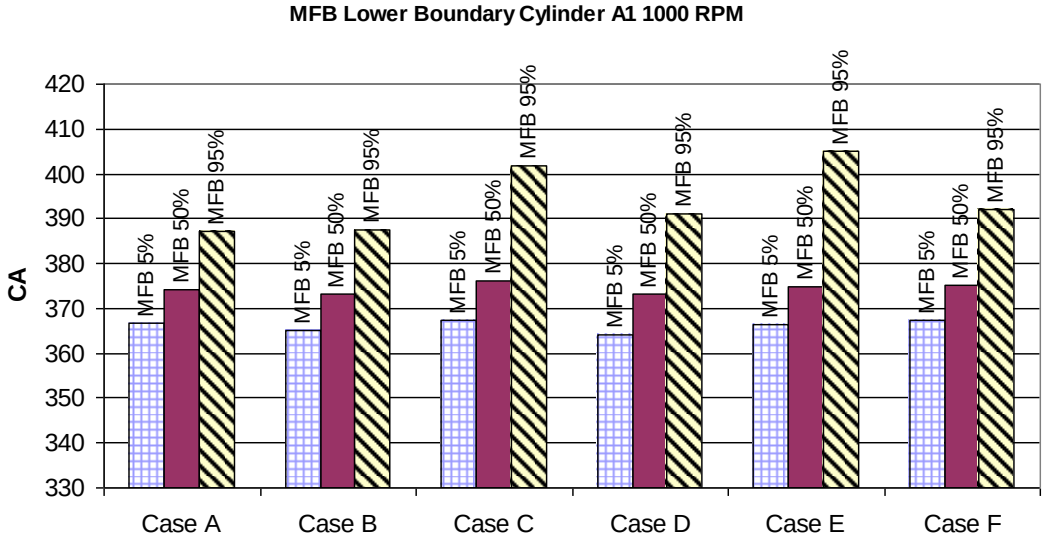

Figure 65: Mass Fraction Burned - Lower Boundary

Investigating the effect of varying λ (Case B λ=1 and Case D λ=1.2 shown in Table 14) reveals that there are two significant observations. Firstly the engine does not

work in HCCI mode with λ less than 0.95. Secondly comparing Case A (normal air path λ=1) and Case C (heated path λ = 1.0 and compensating for the throttling effect with boosting) it is shown that for the same valve timings, it is possible to achieve lower loads by heating the charge air.

4.5.3 Boosting and Cooling

For 2500 RPM higher loads with similar emissions were achieved. For 1500 RPM the engine was generally unstable. For these tests there wasn't enough time to complete the investigation to our satisfaction, and the author believes the intercooler was run at too low temperatures and there was not enough energy to initiate auto-ignition. Therefore for further future work if one we wants to thoroughly investigate the effect of cooling a next set of experiments is required for 1500 RPM.

Chapter 5. CFD Investigation

Computational Fluid Dynamics (CFD) is an established and continuously developing field of Fluid Dynamics. Computational methods are getting more and more significant in the aerodynamic design as the computational efforts are increasing. The main purpose of CFD is to reduce the costs of design as a number of variations of the individual product of design can be simulated in order to find the best configuration possible. Mathematical modelling of the phenomenon of fluid flow reduces the costs of design drastically because no manufacturing and therefore no material costs are needed for the test of different variations. There are several different methods of solutions for flow patterns, distributions of flow variables. Very sophisticated methods had been developed for external flow with heat transfer that can be applied in this problem. Usually most of the uncertainties with CFD arise from the way turbulence is modelled. Therefore the appropriate choice of turbulence model needs to suit the application. We are fortunate in this case because there is extensive literature for turbulence modelling and also there is technical support from the software provider if more information is needed. Usually validation with measurements is required when approaching a project for the first time in order to confirm the modelling results. If the model used reports similar results with experiments then this model can be used for further modelling studies.

In this research project has used CFD to study the computed flow field, thermal system performance, thermal energy distribution and heat flux flow in the proposed T.M. system. This was required as components of the T.M. system did not perform as expected. The CFD study was not the core scope of this work however one cannot present CFD results without adequate knowledge on the subject. Thus an introduction

into CFD methods is presented in Appendix 2. The remaining of this chapter will discuss the CFD T.M. model setup and results.

5.1 Settings of CFD Tool, ANSYS CFX for T.M. simulation

5.1.1 Computational Grid

The geometry for the Thermal |Management System (Figure 5) was generated using Solidworks and then imported to ANSYS Workbench, a common platform for all ANSYS products that can be used to import or create model geometry, mesh, and perform FEA, CFD or other simulations. By using ANSYS Workbench, the complex 3D computational grid was meshed using unstructured mesh pattern. Usually the thickness of the boundary layer is small comparing to the other sizes in the computational domain, so a fine grid in the regions of high velocity and pressure gradients, near the boundary layer was created. The computational power of the machine limits the maximum number of cells that can be used and it is hard to create a very fine grid on the wall surfaces with a known limitation for the number of cells. Because of the complexity of the 3D model and the very fine mesh required, and since this is a scientific research, special treatment of the grid was made in order to achieve the maximum number of "good" cells that give good boundary conditions for the turbulence model - see [40]. The number of total cells used is roughly the same for all the configurations since the same approach and same division of the grid was followed. The total number of elements is of the range of 1,205,000 elements. Out of those very few had an inclination thus giving a false reading for the environment around them. From Figure 66 the y^+ values are generally $1 < y^+ < 50$ which is within the expected range however because of localised high gas speeds the values for y^+ can reach 100. As it has been explained in Appendix 2 Section 7.6.7, y^+ is a function of

the Reynolds number thus the maximum value of y^+ is problem dependant especially for high speed flows.

In detail a typical mesh for the Thermal |Management System comprises of:

Global Number of Nodes: 361173

Global Number of Elements: 1205621

Total Number of Tetrahedrons: 1013181

Total Number of Prisms: 5212

Total Number of Hexahedrons: 130414

Total Number of Pyramids: 56814

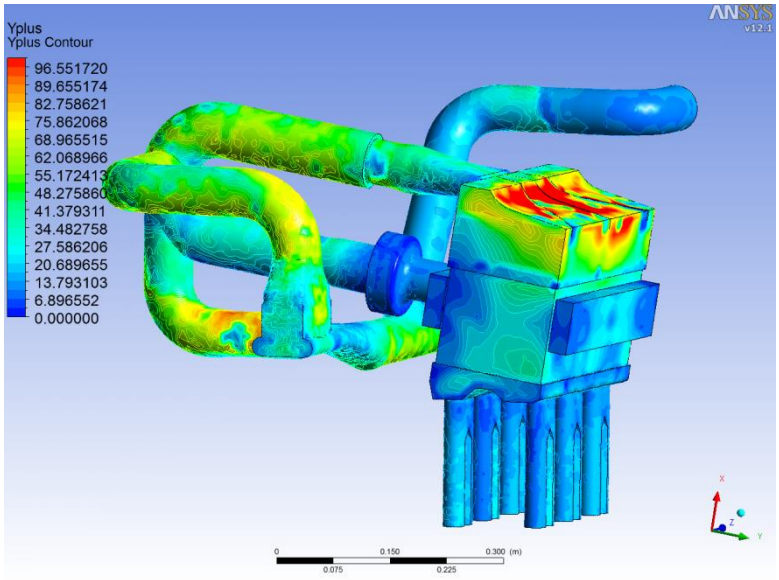

Figure 66: Case 8 – Typical y^+ values for T.M. CFD Simulations

5.1.2 Model Setup

Boundary Conditions

The boundary conditions were defined in ANSYS CFX pre-processor.

The inlet boundary condition: is an Inlet Mass Flow boundary condition where the mass flow magnitude is measured and the direction is known. In the present case the direction of the mass flow is normal to the inlet boundary, and the velocity distribution is uniform. The turbulent intensity is also given by the values of the

turbulent kinetic energy and that of the dissipation of it. Turbulence Intensity is set to typical values 5% for the flow as we have no other data.

Wall boundary condition: The walls boundary is considered as a wall function with the default wall functions options for the SST $k-\omega$ model applied. Heat loss is accounted by using an appropriate Heat Transfer Coefficient on all wall surfaces and a constant air temperature on the far field which is measured experimentally.

Outflow boundary condition: Pressure outlet is used as outlet boundary condition. The average value of pressure, temperature, turbulence quantities on the outlet surface is set to a constant averaged measured value; the direction of flow through the surface is extrapolated from the interior of the domain. Reversed flow is acceptable through this surface because the average values are already given during the boundary condition setup phase.

Interior Boundary Condition: The default for the remaining cells and surface in the domain is automatically set to fluid boundary condition the value of which is set from the solver program ANSYS CFX. In our case the fluid used was air modelled as an ideal gas with constant density $\rho_{air} = 1.225\left[kg/m^3\right]$ with the normal conditions of operating Pressure of 101325Pa and Temperature of 300K. As the medium is handled as incompressible, no material equations were needed

Turbulence models

The Shear-Stress Transport (SST) $k-\omega$ Model was used because of the robust and accurate formulation of the $k-\omega$ model in the near-wall region with the free-stream independence of the $k-\varepsilon$ model in the far field.

Differencing Scheme setup

The only choice was the Second Order Upwind Scheme. It was applied for Momentum, Turbulent kinetic energy, and Dissipation of turbulent kinetic energy equations.

Energy Equation

A heat transfer model is used to predict the temperature throughout the flow. Heat transfer by conduction, convection, turbulent mixing and viscous work are included. The Thermal Energy model was used and models the transport of enthalpy throughout the fluid domain. It differs from the Total Energy model in that the effects of mean flow kinetic energy are not included. It consequently reproduces the same results as the Total Energy model when kinetic energy effects are negligible. The Total Energy model should be used for gas flows where the Mach number exceeds 0.2, and high speed liquid flows where viscous heating effects arise in the boundary layer, where kinetic energy effects do become significant.

Intercooler model setup

The pressure loss through the heat exchanger is modelled using Darcy's law, a phenomenologically derived constitutive equation that describes the flow of a fluid through a porous medium. In order to model the directional loss, the linear and quadratic coefficients of the pressure drop through the intercooler are required. Therefore supplier’s performance tables for the particular intercooler were rearranged and a second degree polynomial relating the pressure loss data against gas velocity through the intercooler core was formed (Figure 67).

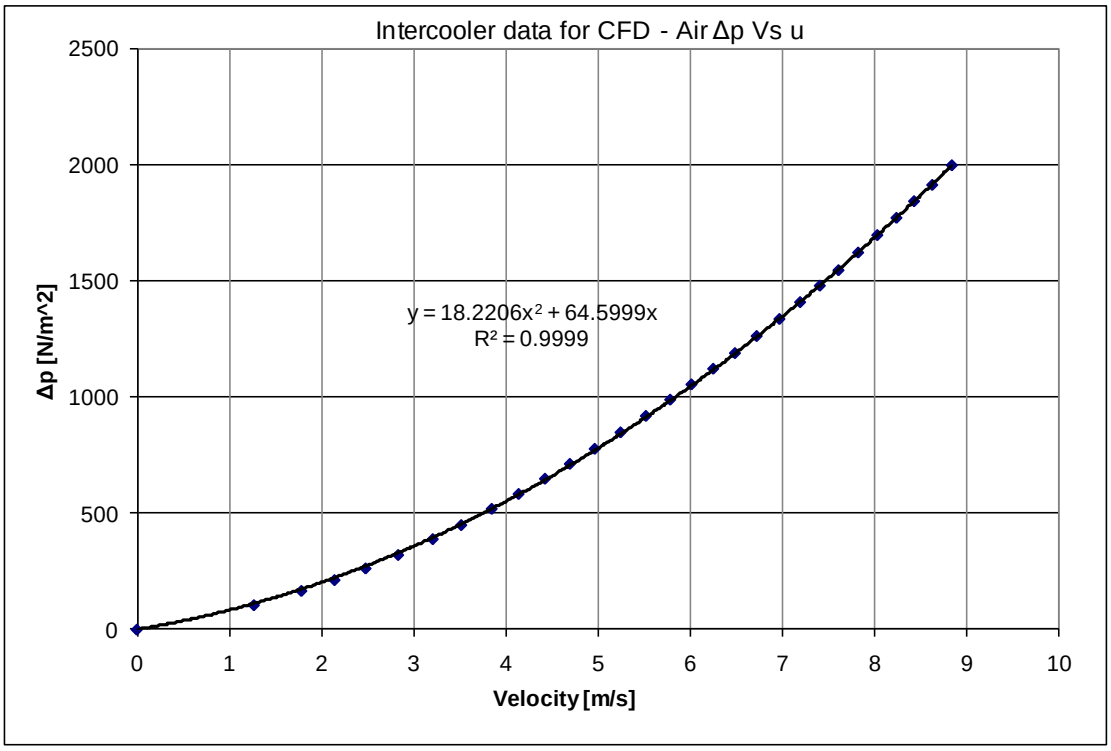

Figure 67: Pressure loss data through the intercooler

Last the heat rejected/added to the CFD simulation is modelled as an energy source term added directly to the energy equation through the entire intercooler domain. A multiplication coefficient was used for the directional loss in the transverse direction for the linear and quadratic coefficients. This would ensure that the intercooler model would represent the restrictive flow and the associated pressure drop through the intercooler fins. Heat flux is calculated in a similar manner as described in Section 3.6.3 using the effectiveness factor for a heat exchanger/intercooler.

Supercharger model setup

The supercharger is modelled as a directional momentum source added directly to the momentum equation. The momentum source is defined as a pressure rise divided by the length of the supercharger subdomain in the streamwise direction. The limitation to this approach is that the flow field accuracy of the supercharger is not implicitly modelled. The supercharger characteristic for each engine speed (Table 15)

is obtained from Section 3.6.4. The state of the fluid at the supercharger inlet is known therefore an expression for the corrected volume flowrate at the supercharger inlet can be easily compiled using Equation 37. For each modelled case the supercharger is spinning at a constant speed therefore the pressure ratio can be expressed a 1-dimensional array as a function of corrected volume flowrate at the supercharger inlet. Therefore the pressure at the supercharger exit is simply the pressure ratio multiplied by the pressure at the supercharger inlet.

Engine speed [Rpm]	**Pr [-]**					
	1	1.2	1.4	1.6	1.8	2
	Corrected volume inlet flow *sqrt (Tic) / R*Tic					
1000	3.928E-06	3.198E-06	2.474E-06	2.170E-06	1.922E-06	1.847E-06
1250	4.884E-06	4.166E-06	3.516E-06	3.205E-06	2.951E-06	2.838E-06
1500	5.841E-06	5.134E-06	4.558E-06	4.241E-06	3.980E-06	3.828E-06
1875	7.275E-06	6.586E-06	6.122E-06	5.794E-06	5.523E-06	5.314E-06
2000	7.758E-06	7.094E-06	6.643E-06	6.320E-06	6.043E-06	5.838E-06
2500	9.689E-06	9.129E-06	8.728E-06	8.423E-06	8.123E-06	7.937E-06

Table 15: Supercharger performance data

Throttles setup

The throttle modelling is an important part of the Thermal Management System. However since the CFD investigation aims to simulate the system at steady state and compare against measured values, the throttles are set at the measured angle for each case and the CFD model is uniformly meshed. Therefore the throttles are simply part of the wall boundary.

5.1.3 Cases Run using ANSYS CFX

The cases simulated using ANSYS CFX are the cases shown in Table 10 that describe the engine and Thermal Management system configuration for the obtained HCCI boundary. In the next section the results and evaluation of the computed flow field, thermal system performance and thermal energy distribution and heat flux flow in the proposed system is presented.

5.2 CFD Model Results

Figure 68 to Figure 72 shown in the next section are the temperature streamlines of the fluid flow for the cases shown in Table 16 (Case 1 to 5) and Table 18 (Case 6 to 9). A streamline visualises the path of a fluid particle starting from the inlet boundary condition until it reaches the outlet boundary of the fluid domain. Figure 73 to Figure 77 shown in the next section are the wall temperature of the fluid domain for the cases shown in Table 16 (Case 1 to 5) and Table 18 (Case 6 to 9). These plots show the wall temperature and indicate heat path through the fluid domain.

From data analysis shown in Table 17 and Table 19 the maximum error of simulated data from experimental temperature data measurements is 16.84 % whereas the minimum is -1.12%. Within the same tables the maximum error of simulated data from experimental pressure data measurements is 11.99 % whereas the minimum is 1.15%. Again from the same tables if one compares the variance of the data for each case, for example in Case 1 the CFD temperature deviation from the average value is 0.98°C then the local data variance is 1.18%. The same values for the experimental data for the same case is 1.58°C and 1.79% respectively. The general trend is that if the maximum error is high then the variance within the data is high, which means that for that particular case the CFD simulation has a deficiency in capturing what actually happens in the real case.

Comparing the pressure and temperature in the inlet runners, the averaged values for the variables obtained by CFD is comparable with the averaged experimental measurements. From analysis on the outputs between the experimental measurements and the CFD results, the deviation of the experimental measurements for temperature at the exit of the inlet runners is smaller compared to the deviation of the CFD results at the same location; the maximum deviation for experimental values is 4.54% where

as for the CFD results this is 10.3%. The deviation of the experimental measurements for pressure at the exit of the inlet runners is larger compared to the deviation of the CFD results; the maximum deviation for experimental values is 21.68% where as for the CFD results this is 0.11%.

From the above observations one can suggest that a highly turbulent flow pattern exist at the mixing box / inlet runners as fluctuations of pressure and temperature are expected between measurements for each bank. The temperature measurements fluctuate between each bank however the fluctuation range is relatively similar. If however the heated path with heating is used (HPH) to deliver the induction air, one cannot observe a clear pattern for the path of gas that is consistent for all tested cases, thus not able to indicate if a port receives repeatedly lower temperatures compared to the other ports. Furthermore for the cases that the gas has to bypass the intercooler, the vertical disc in the heated path is designed to act as a flow straightener, but unfortunately it also introduces a significant pressure drop through the intercooler bypass path. As result some hot gas will leak though the intercooler throttle, then cool down while it passes though the intercooler then mix with the hot gas and exit the domain reducing the thermal efficiency of the system. If air is only allowed to pass through the intercooler, one can observe a clear and consistent pattern for the path of gas that is true for all cases involving the air passing through the intercooler. However in these cases the temperature deviation between measurements is small thus one can claim that the air is uniformly cooled and delivered to all ports.

An investigation of the total heat lost in the CFD models (Table 16 to Table 18), reveals that approximately 25% of the heat is lost through the mixing box, approximately 25% of the heat is lost though the engine and approximately 50% of the total heat lost is though the pipework regardless how the thermal management

system was used or the engine operating conditions. The long ducting was necessary because of the physical mismatch of the available components and the excessive heat lost through the ductwork was compensated by using 3 [kW] electric heating to heat the air additionally to the exhaust gas heat recuperation system.

The relatively large volume of the mixing box and the assorting pipework increase the heat transfer between charge air, engine parts and the environment; this is more evident for low gas speeds specifically for Cases 1 to 3 (Table 16). From the experimental measurements it has been observed that with either heating or cooling of the charge air using the T.M. system, and in order to achieve better performance from the engine, the charge air flow rate through the system must be relatively high (roughly above 24g/s). This was confirmed by the CFD results as the highest total heat loss for the investigated cases was during Cases 1 to 3 (Table 16 and Table 18). Therefore using the current thermal management system if the flow rate is not kept high enough the increase of heat transfer with the environment will significantly reduce the minimum (and maximum) achievable temperature of the system.

This indicates a need for a more compact thermal management system that will reduce the heat losses to the minimum. The time lag with this inlet temperature control system depends upon the following, a) the time lag in the various throttle valves, b) the time lag in accelerating the air in the piping and c) the time distance between a mixing point and the cylinders.

During heating mode the temperature of the air in the hot path up until the mixing point does not change significantly thus enough thermal inertia is provided to the system to overcome any heat losses and supply almost constant hot air temperature at flow transients. However the hot and cold air mixing especially near the supercharger junctions is more turbulent and depends on the supercharger speed

and the supercharger bypass throttle position, thus the wall temperature near the supercharger and adjacent ducts is expected to vary significantly between the different operating conditions. (Figure 73 to Figure 77).

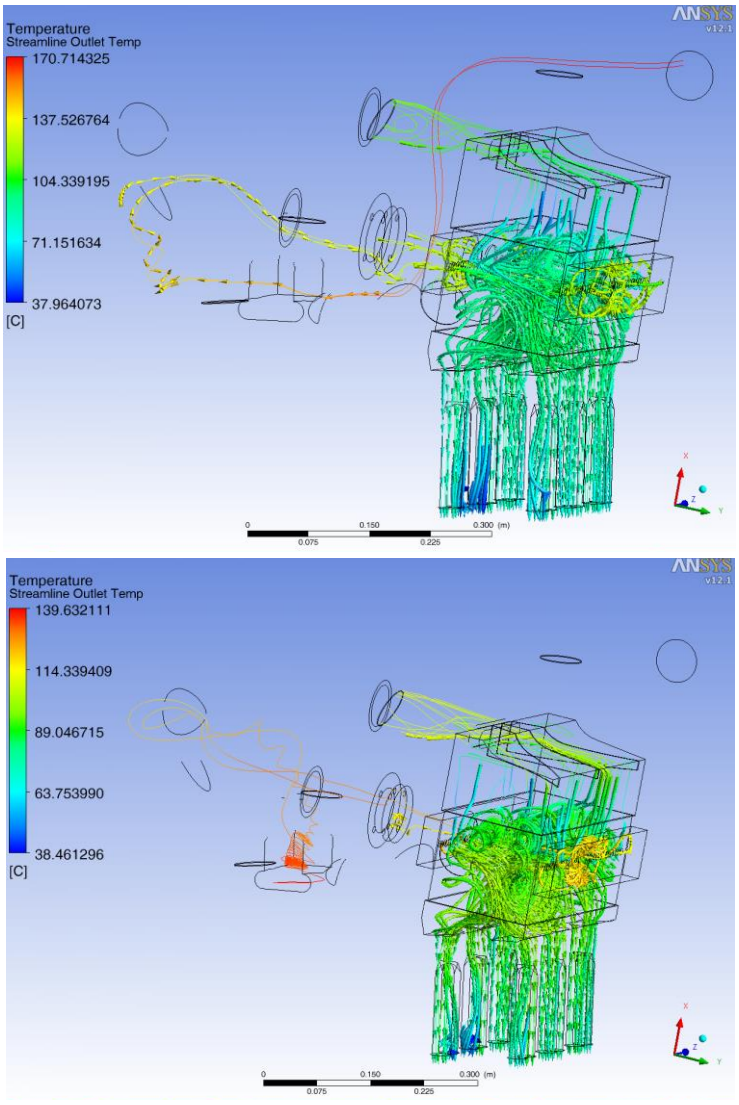

Figure 68: Temp. streamlines - A) Case 1 - 1000[RPM] - HPH, B) Case 2- 1000[RPM] - HPH

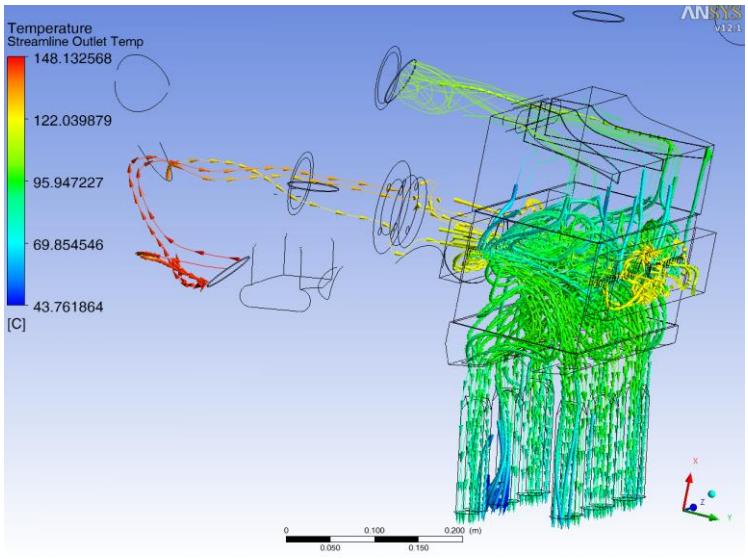

Figure 69: Temp. streamlines - Case 3 - 1000[RPM] - HPH - BP 0.2[bar]

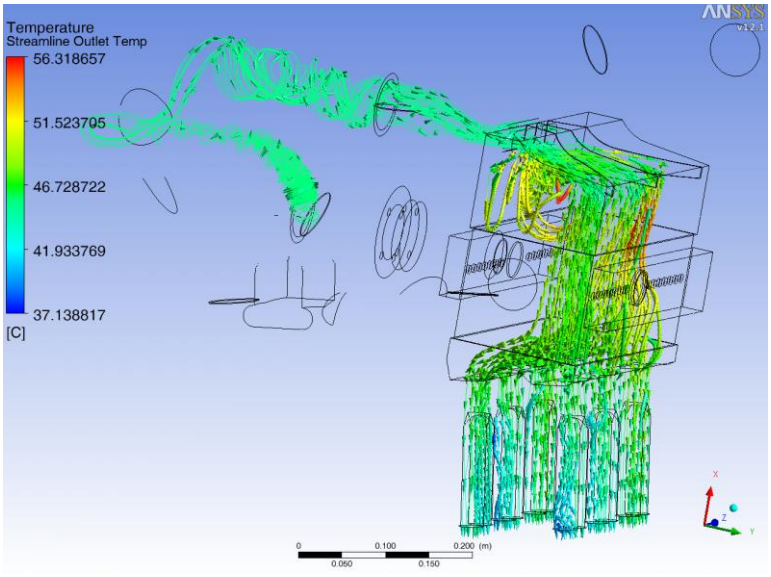

A)

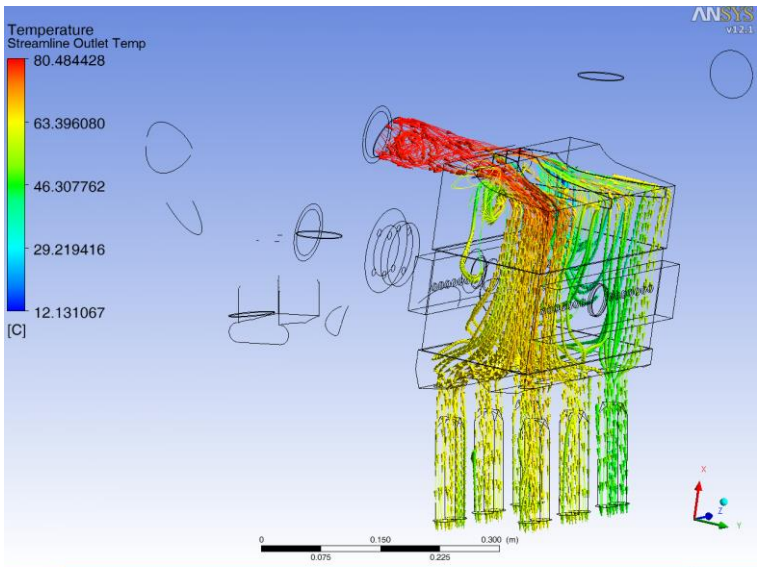

B)

Figure 70: Temp. streamlines - A) Case 4 - 1500[RPM] - NPC, B) Case 5 - 1500[RPM] – HPH

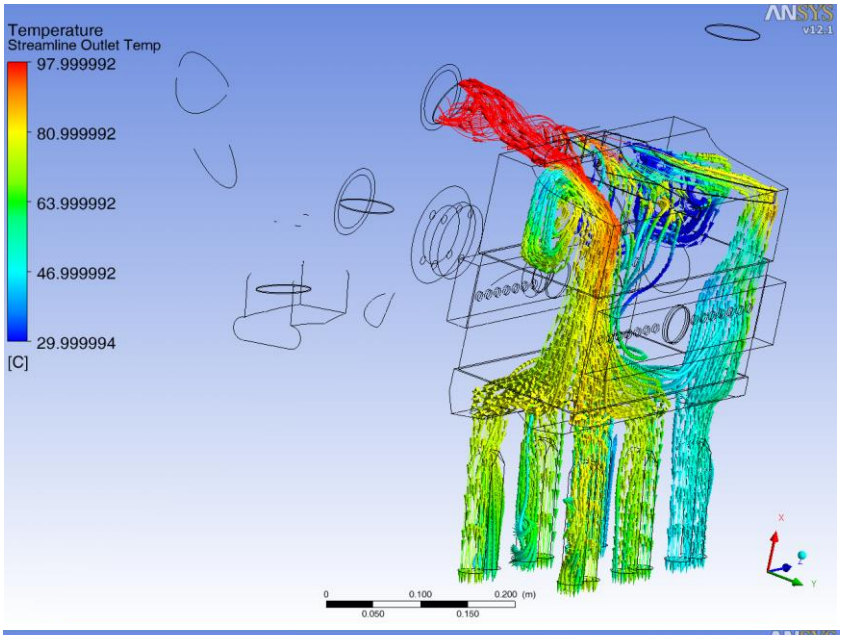

A)

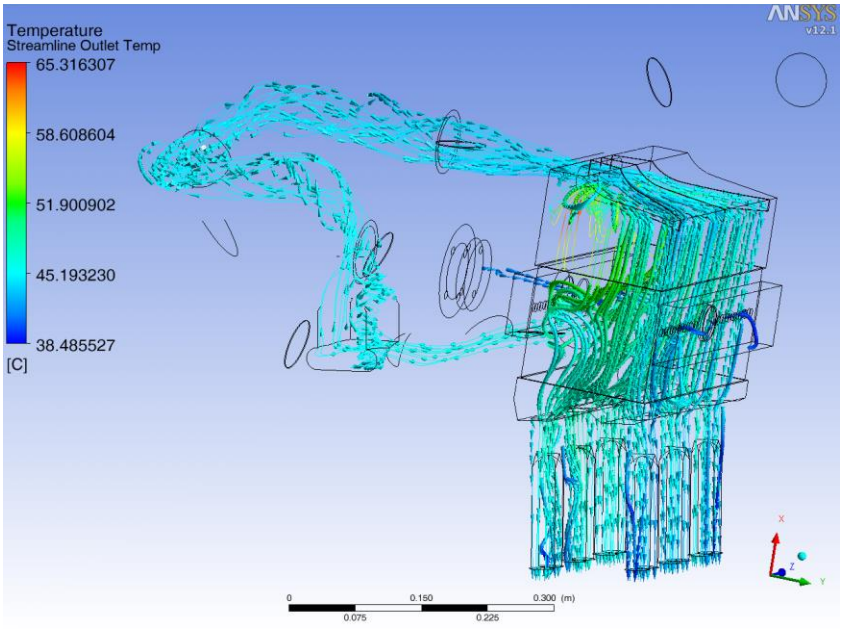

B)

Figure 71: Temp. streamlines - A) Case 6 - 1500[RPM] - HPH, B) Case 7 - 2500[RPM] - NPC - BP 0.2[bar]

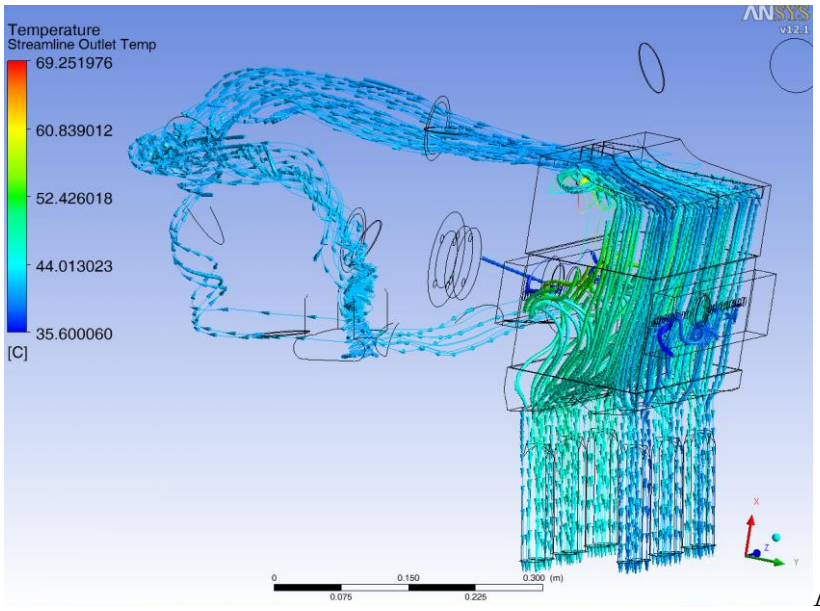

A)

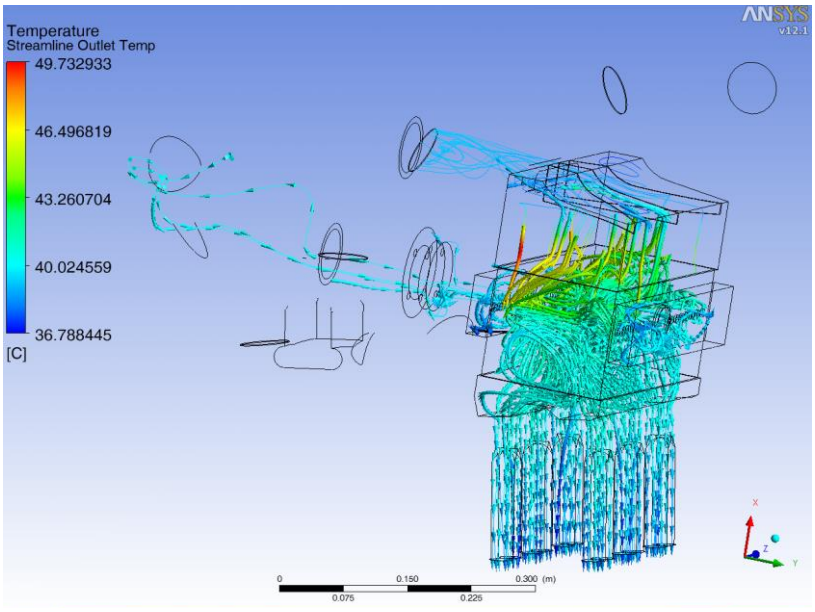

B)

Figure 72: Temp. streamlines - A) Case 8 - 2500[RPM] - NPC, B) Case 9 - 2500[RPM] - NP

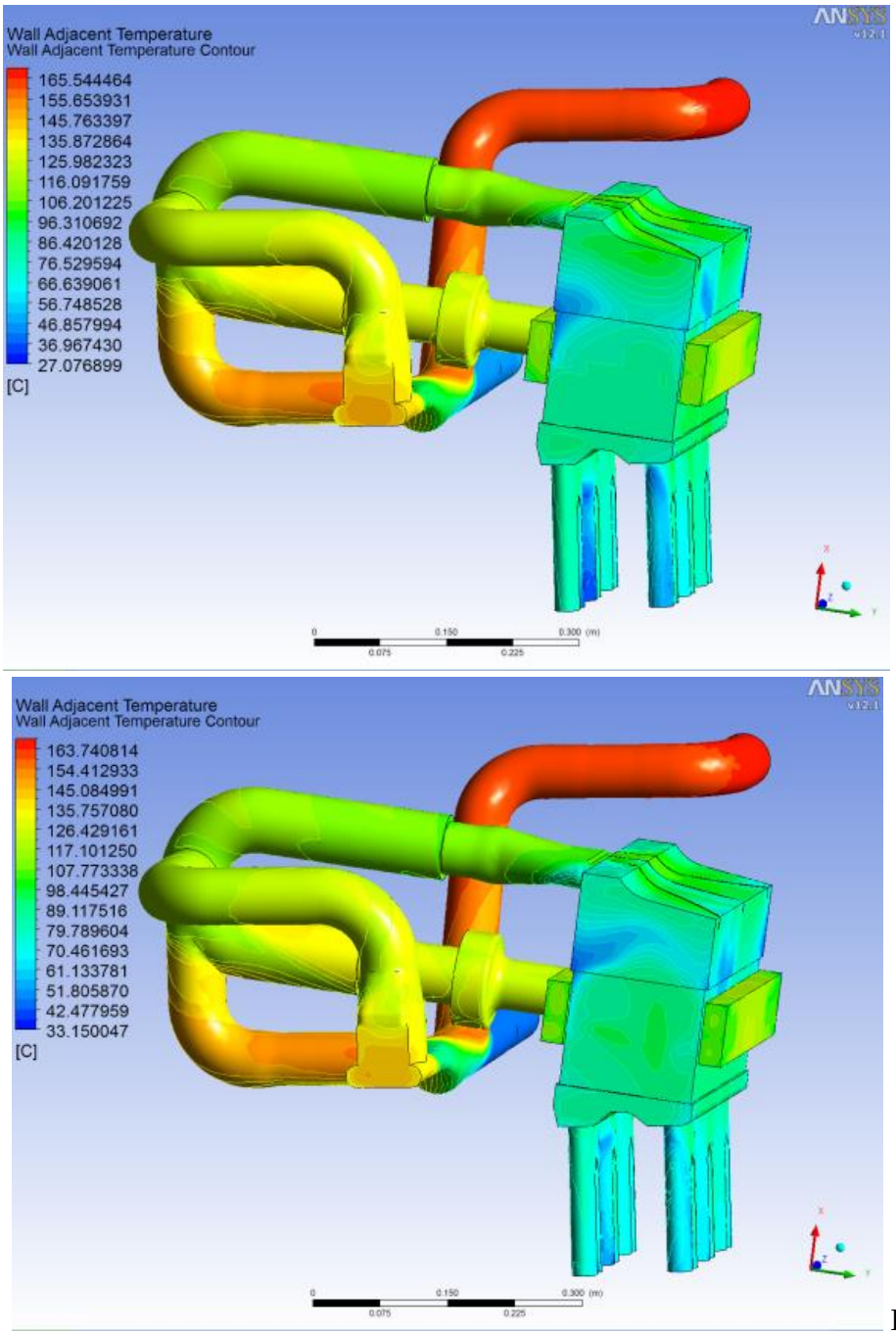

A)

B)

Figure 73: Wall Temp. - A) Case 1 - 1000[RPM] - HPH, B) Case 2- 1000[RPM] – HPH

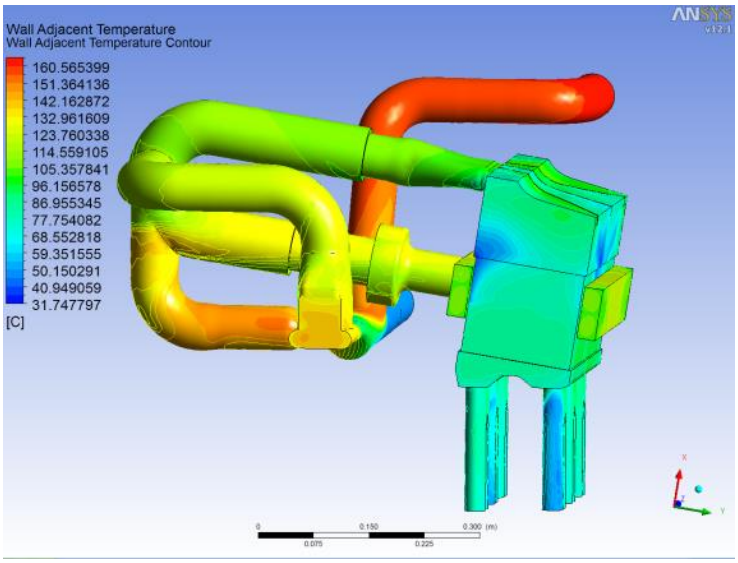

Figure 74: Wall Temp.- Case 3 - 1000[RPM] - HPH - BP 0.2[bar]

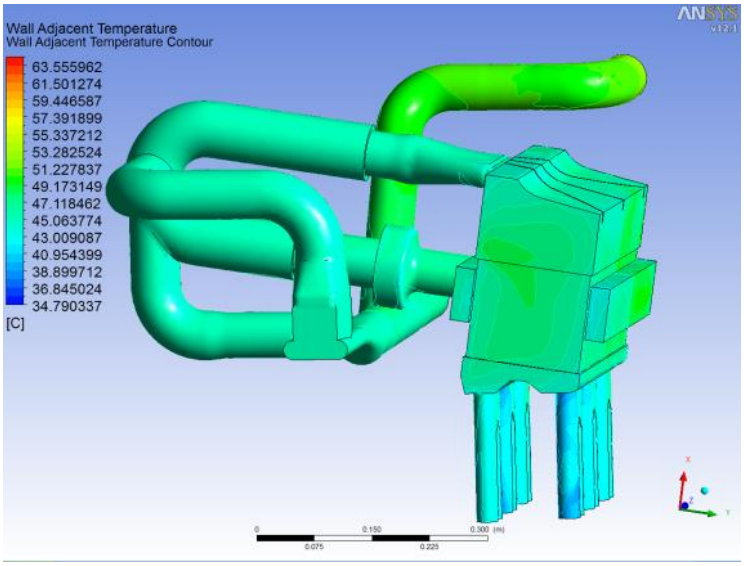

A)

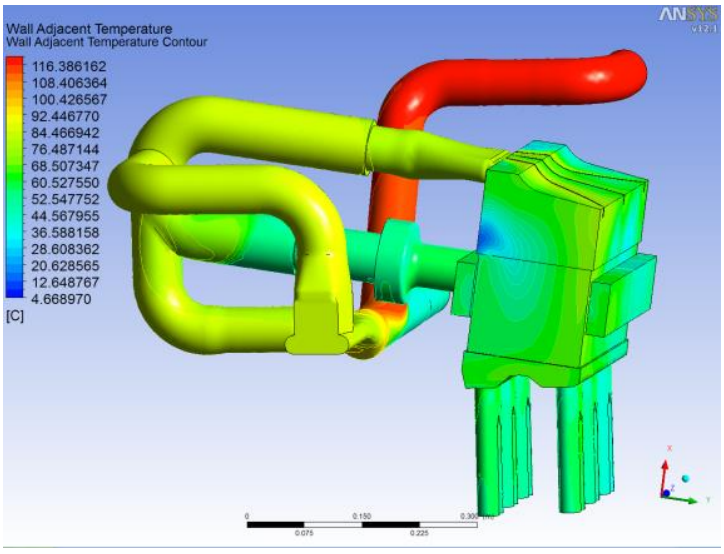

B)

Figure 75: Wall Temp - A) Case 4 - 1500[RPM] - NPC, B) Case 5 - 1500[RPM] - HPH

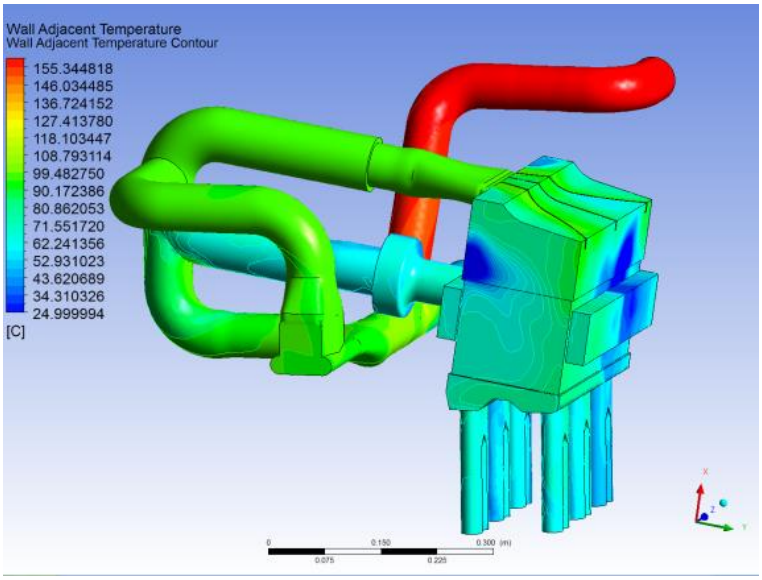

A)

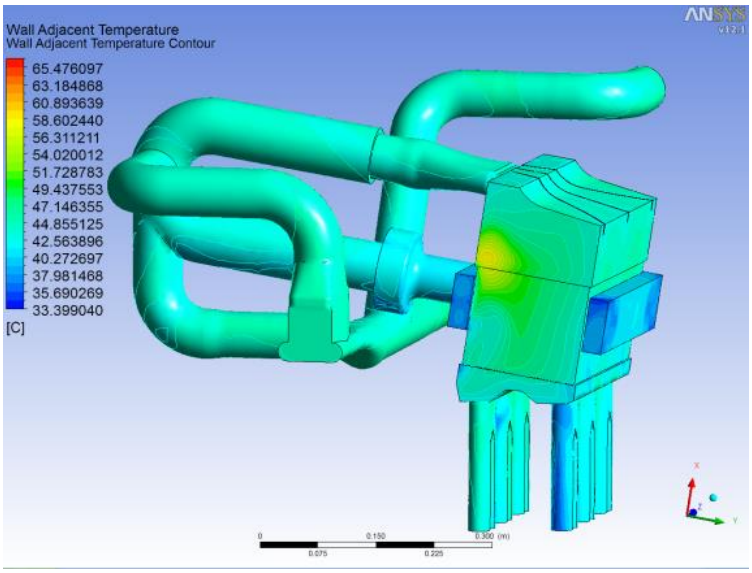

B)

Figure 76: Wall Temp - A) Case 6 - 1500[RPM] - HPH, B) Case 7 - 2500[RPM] - NPC - BP 0.2[bar]

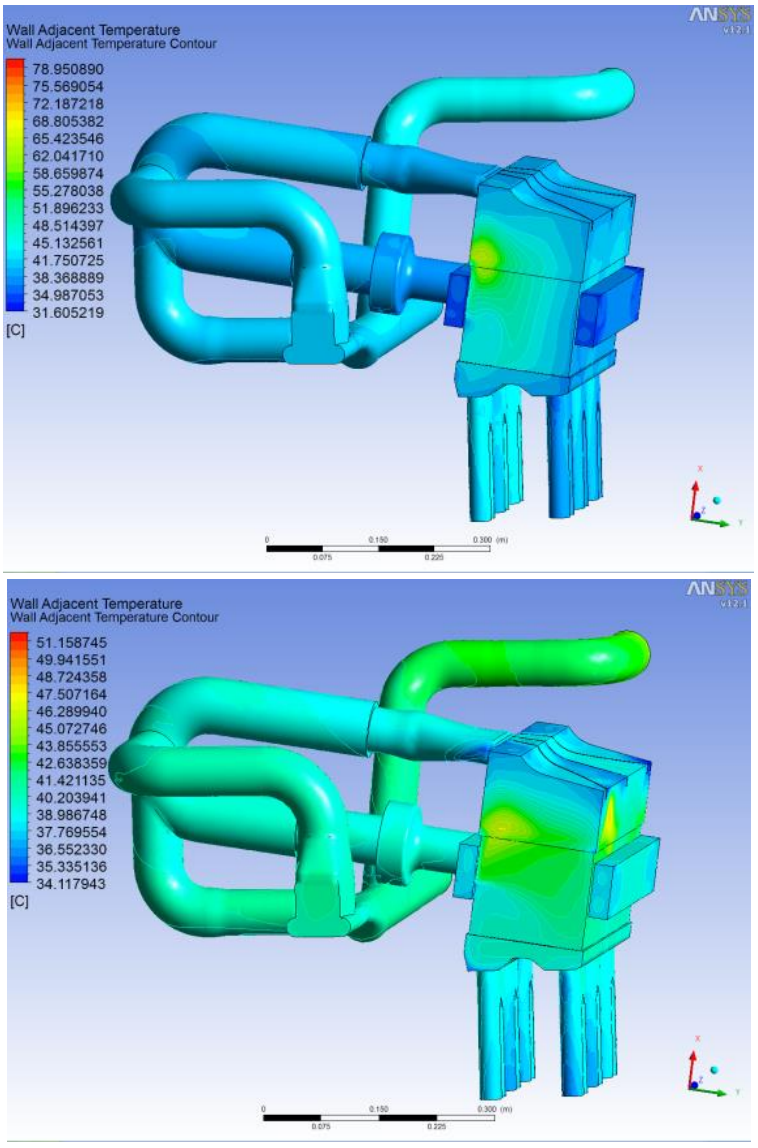

A)

B)

Figure 77: Wall Temp - A) Case 8 - 2500[RPM] - NPC, B) Case 9 - 2500[RPM] – NP

	Case1		Case2		Case3		Case4		Case5	
Cold Massflow In [kg s^-1]	2.575E-03	4.192E-04	2.455E-03	3.921E-04	2.634E-03	4.550E-04	2.272E-02	2.564E-02	2.814E-03	4.541E-04
Hot Massflow In [kg s^-1]	1.503E-02	1.719E-02	1.424E-02	1.630E-02	1.517E-02	1.735E-02	3.575E-03	5.493E-04	1.965E-02	2.185E-02
Total Massflow In [kg s^-1]	1.761E-02	1.669E-02	1.670E-02	1.780E-02	1.781E-02	2.619E-02	2.630E-02	2.230E-02	2.246E-02	2.035E-02
Total Massflow Out [kg s^-1]	-1.761E-02	0.000E+00	-1.669E-02	0.000E+00	-1.780E-02	0.000E+00	-2.619E-02	0.000E+00	-2.230E-02	0.000E+00
Cold Temperature In [C]	47.72	47.75	46.85	46.88	50.17	50.21	46.47	46.47	45.39	45.42
Hot Temperature In [C]	170.60	170.71	168.60	168.63	165.30	165.38	52.59	52.62	120.50	120.49
A1 Temperature Out [C]	85.00	85.82	83.58	86.23	83.89	89.51	43.43	41.24	67.20	74.71
A2 Temperature Out [C]	83.61	90.90	81.08	89.37	83.12	92.82	43.39	44.01	56.63	76.02
A3 Temperature Out [C]	83.91	88.02	80.16	87.54	83.20	93.02	45.12	41.11	68.65	76.71
B1 Temperature Out [C]	82.19	88.01	80.26	88.14	80.10	92.27	43.80	43.95	68.78	77.26
B2 Temperature Out [C]	83.76	89.41	81.77	88.76	81.57	92.96	43.43	42.64	65.56	76.44
B3 Temperature Out [C]	82.24	87.48	79.02	87.19	81.53	92.75	45.11	41.23	65.56	77.30
Cold Pressure In [Pa]	-3183.00	-3183	-2706	-2705	-2349	-2348	-1752	-1724	-1291	-1290
Hot Pressure In [Pa]	-3194.00		-2716		-2360		-1725		-1310	
A1 Gauge Pressure Out [Pa]	-8802.00	-8425	-7814	-7332	-3974	-3236	-3119	-2493	-10632	-9663
A2 Gauge Pressure Out [Pa]	-8799.00	-9510	-7811	-8311	-3971	-4254	-3111	-3625	-10631	-10696
A3 Gauge Pressure Out [Pa]	-8800.00	-8747	-7812	-7919	-3972	-3811	-3113	-3379	-10631	-10407
B1 Gauge Pressure Out [Pa]	-8805.00	-8791	-7817	-7951	-3976	-3898	-3121	-3377	-10634	-10308
B2 Gauge Pressure Out [Pa]	-8807.00	-8720	-7818	-7926	-3979	-3817	-3115	-3249	-10633	-10314
B3 Gauge Pressure Out [Pa]	-8800.00	-9228	-7812	-8576	-3973	-4297	-3113	-3713	-10631	-10941
Mixing Box Heat Loss [W]	-224.70		-216		-220		-76		-110	
Engine Heat Loss [W]	-224.10		-221		-230		-76		-129	
pipe Heat Loss [W]	-586.60		-566		-568		-114		-375	
Total Heat Loss [W]	-1035.00		-1003		-1019		-266		-614	
Mixing Box Heat Flux [W/m^2]	-446.00		-430		-438		-151		-218	
Engine Heat Flux [W/m^2]	-1270.00		-1252		-1304		-432		-731	
Pipe Heat Flux [W/m^2]	-841.50		-811		-815		-164		-538	

Table 16: Results for Case 1 to Case 5

	Case1		Case2		Case3		Case4		Case5	
	CFD	Experiment	CFD	Experiment	CFD	Experiment	CFD	Experiment	CFD	Experiment
Numerical Average for Temperature Out [C]	83.45	88.27	80.98	87.87	82.24	92.22	44.05	42.36	65.40	76.41
Deviation of measurements from average value	0.98	1.58	1.44	1.03	1.29	1.24	0.77	1.25	4.13	0.88
Local data variance	1.18%	1.79%	1.78%	1.17%	1.57%	1.34%	1.74%	2.96%	6.31%	1.15%
Difference from Experiments	5.78 %		8.52 %		12.14 %		-3.83 %		16.84 %	
Numerical Average for Gauge Pressure Out [Pa]	-8802	-8903	-7814	-8003	-3974	-3885	-3115	-3306	-10632	-10388
Deviation of measurements from average value	2.91	358.92	2.65	385.00	2.67	350.79	3.54	396.32	1.15	395.48
Local data variance	0.03%	4.03%	0.03%	4.81%	0.07%	9.03%	0.11%	11.99%	0.01%	3.81%
Difference from Experiments	1.15 %		2.41 %		-2.23 %		6.12 %		-2.29 %	

Table 17: Result data analysis - Case 1 to Case 5

	Case6		Case7		Case8		Case9	
Cold Massflow In [kg s^-1]	3.546E-03	4.498E-04	2.676E-02	3.047E-02	1.862E-02	2.108E-02	1.862E-02	2.106E-02
Hot Massflow In [kg s^-1]	1.685E-02	1.990E-02	4.382E-03	6.751E-04	3.036E-03	5.817E-04	3.044E-03	6.022E-04
Total Massflow In [kg s^-1]	2.040E-02	3.114E-02	3.114E-02	2.166E-02	2.166E-02	2.166E-02	2.166E-02	0.000E+00
Total Massflow Out [kg s^-1]	-2.035E-02	0.000E+00	-3.114E-02	0.000E+00	-2.166E-02	0.000E+00	-2.166E-02	0.000E+00
Cold Temperature In [C]	47.48	47.51	46.27	46.28	41.81	41.81	41.54	41.54
Hot Temperature In [C]	168.40	168.43	46.15	46.16	46.08	46.10	44.18	44.21
A1 Temperature Out [C]	91.31	87.43	42.86	42.74	40.12	43.28	38.73	41.67
A2 Temperature Out [C]	83.80	90.17	43.49	45.05	40.83	46.57	38.34	44.95
A3 Temperature Out [C]	66.41	89.46	43.47	43.03	40.95	43.26	38.31	41.38
B1 Temperature Out [C]	88.49	90.93	44.61	44.13	43.12	47.92	38.58	47.12
B2 Temperature Out [C]	86.17	90.18	45.60	43.79	43.94	44.39	38.64	42.89
B3 Temperature Out [C]	75.99	90.09	44.98	43.31	43.72	44.28	38.28	43.24
Cold Pressure In [Pa]	-2214.00	-2213	-1583	-1544	-1216	-1198	-1203	-1185
Hot Pressure In [Pa]	-2228.00		-1545		-1198		-1185	
A1 Gauge Pressure Out [Pa]	-10770.00	-8874	15260	17291	-2278	-1856	-2347	-1674
A2 Gauge Pressure Out [Pa]	-10770.00	-10036	15266	17052	-2277	-1798	-2349	-1812
A3 Gauge Pressure Out [Pa]	-10770.00	-9317	15262	17065	-2277	-2811	-2347	-2597
B1 Gauge Pressure Out [Pa]	-10770.00	-9270	15252	17515	-2278	-2251	-2350	-2645
B2 Gauge Pressure Out [Pa]	-10770.00	-9401	15254	16831	-2278	-2004	-2349	-2365
B3 Gauge Pressure Out [Pa]	-10770.00	-9978	15267	15930	-2277	-3131	-2349	-3192
Mixing Box Heat Loss [W]	-154.10		-47		-35		-34	
Engine Heat Loss [W]	-149.70		-71		-55		-42	
pipe Heat Loss [W]	-545.10		-83		-60		-58	
Total Heat Loss [W]	-848.90		-201		-149		-134	
Mixing Box Heat Flux [W/m^2]	-305.80		-94		-70		-68	
Engine Heat Flux [W/m^2]	-848.40		-400		-309		-236	
Pipe Heat Flux [W/m^2]	-782.00		-119		-85		-83	

Table 18: Results for - Case 6 to Case 9

	Case6		Case7		Case8		Case9	
	CFD	Experiment	CFD	Experiment	CFD	Experiment	CFD	Experiment
Numerical Average for Temperature Out [C]	82.03	89.71	44.17	43.67	42.11	44.95	38.48	43.54
Deviation of measurements from average value	8.45	1.11	0.96	0.77	1.52	1.72	0.18	1.98
Local data variance	10.30%	1.23%	2.18%	1.76%	3.61%	3.84%	0.46%	4.54%
Difference from Experiments	9.36 %		-1.12 %		6.73 %		13.15 %	
Numerical Average for Gauge Pressure Out [Pa]	-10770	-9479	15260	16948	-2278	-2308	-2349	-2381
Deviation of measurements from average value	0.00	408.55	5.61	502.17	0.50	498.37	1.12	516.05
Local data variance	0.00%	4.31%	0.04%	2.96%	0.02%	21.59%	0.05%	21.68%
Difference from Experiments	-11.99 %		11.06 %		1.36 %		1.38 %	

Table 19: Result data analysis - Case 6 to Case 9

5.3 Summary

In this chapter the computed flow field and thermal system performance has been presented. It has been confirmed that the averaged values for the variables obtained by CFD is comparable with the averaged experimental measurements.

If the heated path with heating is used (HPH) to deliver the induction air, one cannot observe a clear pattern for the path of gas that is consistent for all tested cases, thus not able to indicate if a port receives repeatedly lower temperatures compared to the other ports.

For the cases that the gas has to bypass the intercooler, the vertical disc in the heated path introduces a significant pressure drop through the intercooler bypass path. As result some hot gas will leak though the intercooler throttle, cool down while it passes though the intercooler then mixed with the hot gas and exit the domain reducing the thermal efficiency of the system.

If air is only allowed to pass through the intercooler, one can observe a clear and consistent pattern for the path of gas that is true for all cases involving the air passing through the intercooler. And because the temperature deviation between these measurements is small enough one can claim that the air is uniformly cooled and delivered to all ports.

An investigation of the total heat lost in the CFD models, reveals that approximately 25% of the heat is lost through the mixing box, approximately 25% of the heat is lost though the engine and approximately 50% of the total heat lost is though the pipework regardless how the thermal management system was used or the engine operating conditions.

Finally it has been observed that with either heating or cooling the charge air using the T.M. system, and in order to achieve better performance from the engine, the charge air flow rate through the system must be relatively high (roughly above 24g/s). If the flow rate is not kept high enough the increase of heat transfer with the environment at low gas speeds will significantly reduce the minimum (and maximum)

achievable temperature of the system. This indicates a need for a more compact thermal management system that will reduce the heat losses to the minimum.

Chapter 6. Analysis – Thermal Management System as a tool for HCCI Window Expansion and Emission Comparison

By nature HCCI combustion is very sensitive to charge temperature. One of the ways of adjusting the temperature of the charge is by varying the temperature of the inlet air. The thermal management (T.M.) system has been designed to support relatively fast responses to a requested inlet air temperature change. For a better understanding and optimisation of the T.M. system, a Simulink model has been developed and the mixing flows have been examined. The effect of the T.M. system on HCCI operation based on experimental results is being discussed in this chapter.

6.1 T.M. HCCI Window Expansion

Figure 78 presents the impact of the T.M. system on the lowest and the highest achievable load. It is possible to observe that with use of the T.M. system both limits can be expanded. Expanding HCCI range upwards has been achieved mainly through boosting with a cooling of charge air. Expansion downwards has been a combination of more than one factor, including: heating of inlet air, increasing air-to-fuel ratio, and the throttling effect of the T.M. system (the throttling effect of the T.M. system has been described elsewhere). From Figure 79 it is possible to observe that apart from 1000rpm in both load ranges (the highest and the lowest), applying T.M. (expanding the operating window) has not caused an emissions penalty. Furthermore there is an improvement in all presented components. This improvement has been achieved mainly due to increased air-to-fuel ratio at the low load (NMEP) boundary. In addition to increased air-to-fuel ratio on the high load boundary, cooling of inlet air has been applied. Therefore in-cylinder temperature has been reduced and emissions suppressed. When the engine was operated at 1000rpm, HCCI combustion has a

smaller operating range and more combustion variations were observed. Increased emissions, then, at low engine speed appear to have been due to increased combustion variations.

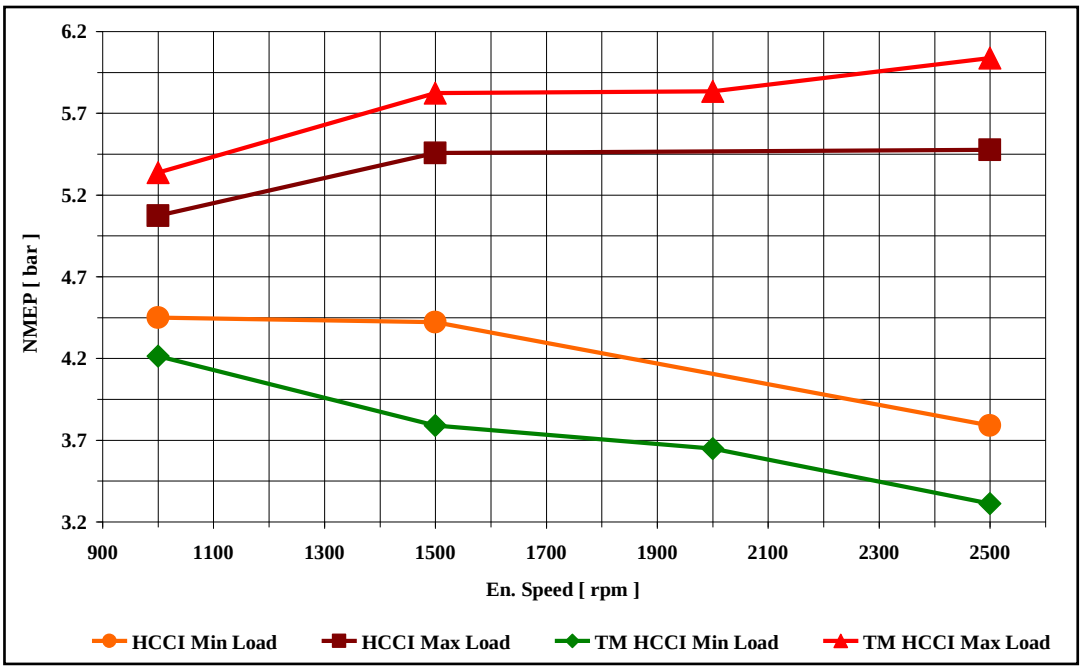

Figure 78: HCCI window expansion due to T.M. system

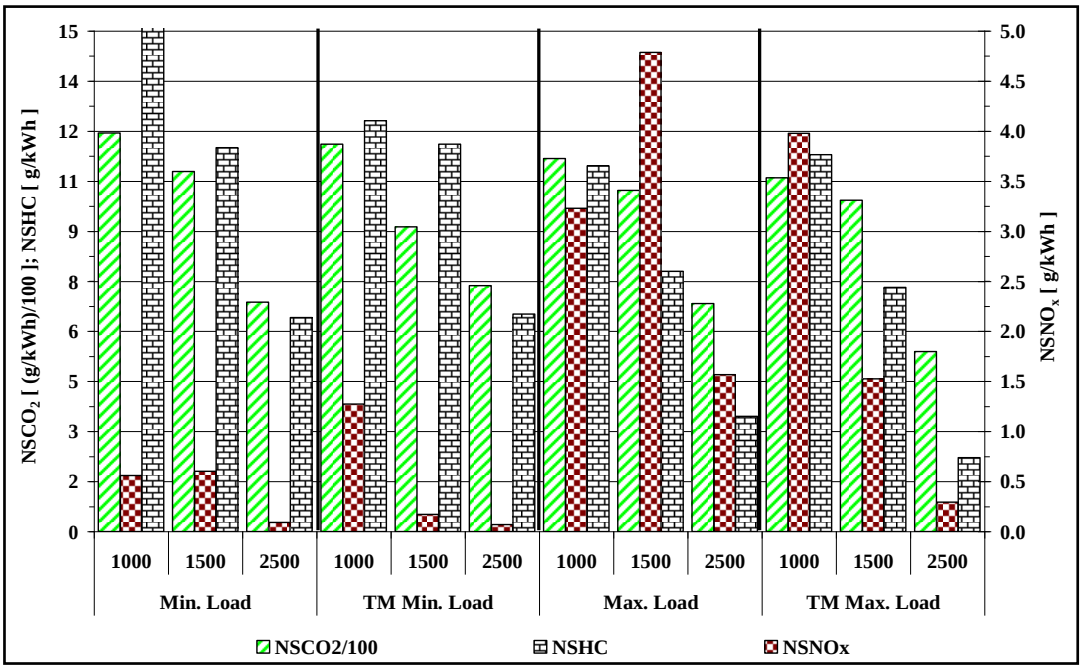

Figure 79: Gaseous emissions comparison with and without T.M. system

6.2 Charge Air Heating Impact on HCCI with Set Valve Timing

An interesting observation has been made during the data analysis when inlet air was heated. The case description is marked in Figure 80 as 35(or 25) H(or HH) where: the first number describes the end of injection for example 35 stands for 350 ºbTDCc and 25 stands for 250ºbTDCc; letter H stands for "hot" air path, where as HH for "hot" air path with heating.

As shown in Figure 80, heating of inlet air increased achievable NMEP for fixed valve timing at low and high engine speeds. However, BMEP has shown a different trend at higher speeds.

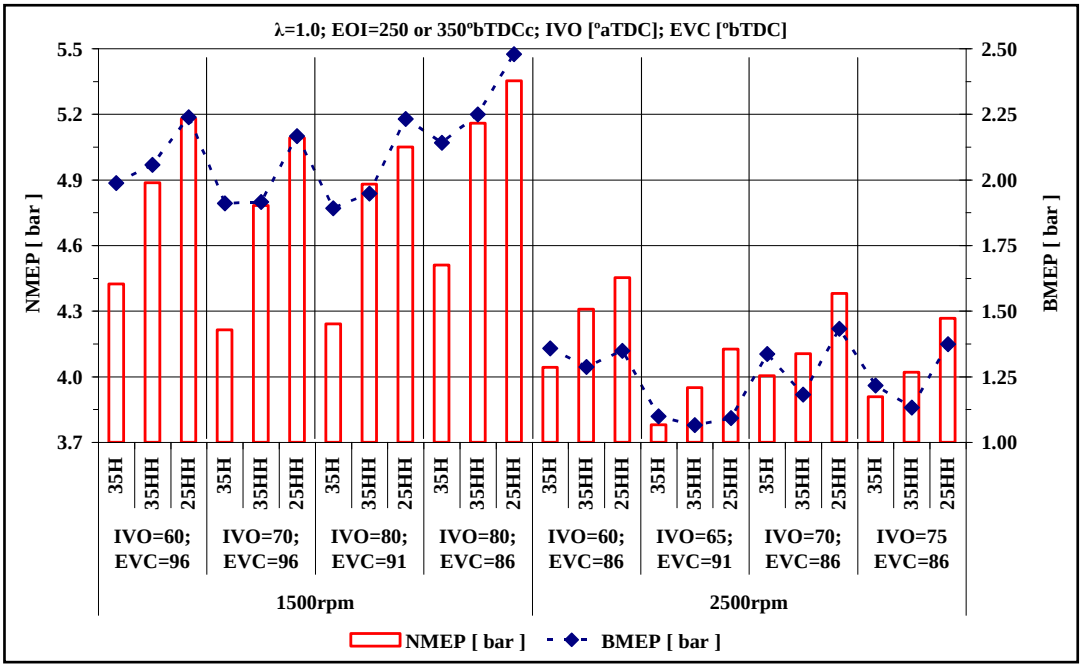

Figure 80: Effect of inlet air heating and injection timing on achieved load for fixed valve timing; 25(35) – EOI respectively 250 or 350ºbTDCc, H – "hot" air path, HH – "hot" air path with heating

As a supplement to Figure 80, Table 20 has been made. One must be remember that in the T.M. system due to the additional ducting and heating components used in the path of the air flow, there would be an unavoidable throttling effect on the "hot" air path (0.1 bar under-pressure in the inlet manifold).

Figure 80 and Table 20 present three cases for two engine speeds. Firstly, air is not heated but is passing through a "hot" part of the inlet manifold (the case marked as 35H in Figure 80); secondly, heating is applied and inlet air temperature has risen (the case marked as 35HH). In both of these cases the injection timing has been set at 350ºbTDCc. Finally, as a third case, heating has continued to increase the inlet air temperature while the injection timing was retarded to 250ºbTDCc (the case marked as 25HH).

En. Speed	CASE	NMEP	BMEP	dP/ca	IVO	EVC	Air Flow	Torque	Tin	Tex	NSNOx	NSHC	$\eta_{vol.}$	$\eta_{comb.}$	$\eta_{th.\ conv.}$
		bar	bar	bar/deg.	ºaTDC	ºbTDC	kg/s	Nm	ºC	ºC	g/kWh	g/kWh	%	%	%
1500	35H-15	4.42	1.99	2.32	60	96	0.0191	47.0	77	390	0.33	8.5	47.7	92.9	23.0
	35HH-15	4.89	2.06	2.54	60	96	0.0180	48.6	89	373	0.26	7.4	45.2	91.9	23.2
	25HH-15	5.18	2.24	1.95	60	96	0.0186	52.9	93	381	0.20	7.6	46.3	91.9	25.5
2500	35H-25	3.78	1.10	1.39	65	91	0.0208	26.0	78	375	0.10	5.7	31.0	92.6	16.9
	35HH-25	3.95	1.06	1.53	65	91	0.0205	25.2	104	368	0.09	5.1	30.6	91.7	17.9
	25HH-25	4.13	1.09	1.16	65	92	0.0205	25.8	111	384	0.08	5.3	31.2	87.4	18.6

Table 20: Detailed samples specification for T.M. tests with fixed valve timing; 35(25) – EOI respectively 250 or 350ºbTDCc, H – "hot" air path, HH – "hot" air path with heating

As mentioned earlier, from Figure 80 it can be observed that when heating has been applied the NMEP as well as the BMEP had increased. This behaviour was not expected as with increasing inlet air temperature the air density has decreased; therefore less air (by mass) has been inducted (Table 20). This trend is clearly visible at 1500rpm, but, when engine speed was increased to 2500rpm the results show a slightly different picture. The NMEP has kept the same trend as at lower engine speed; however, the BMEP has reduced when heating was applied. From Figure 80 and Table 20 it has been possible to calculate that the increase in NMEP at 1500rpm is approximately 0.5 to 0.6bar; when at 2500 it does not exceed 0.2bar. R. Stone[38] has described the effect of increased friction losses with increasing engine speed. This in turn explains the change in trend for BMEP between 1500 and 2500rpm. As mentioned earlier, the increase in NMEP at 2500rpm has been relatively small and

therefore has not been able to make up to the increased friction losses; thus BMEP at higher engine speed has been lower (when heating is applied). In order to explain why NMEP has increased when heating had been applied Figure 81 for 1500rpm and Figure 82 for 2500rpm was created.

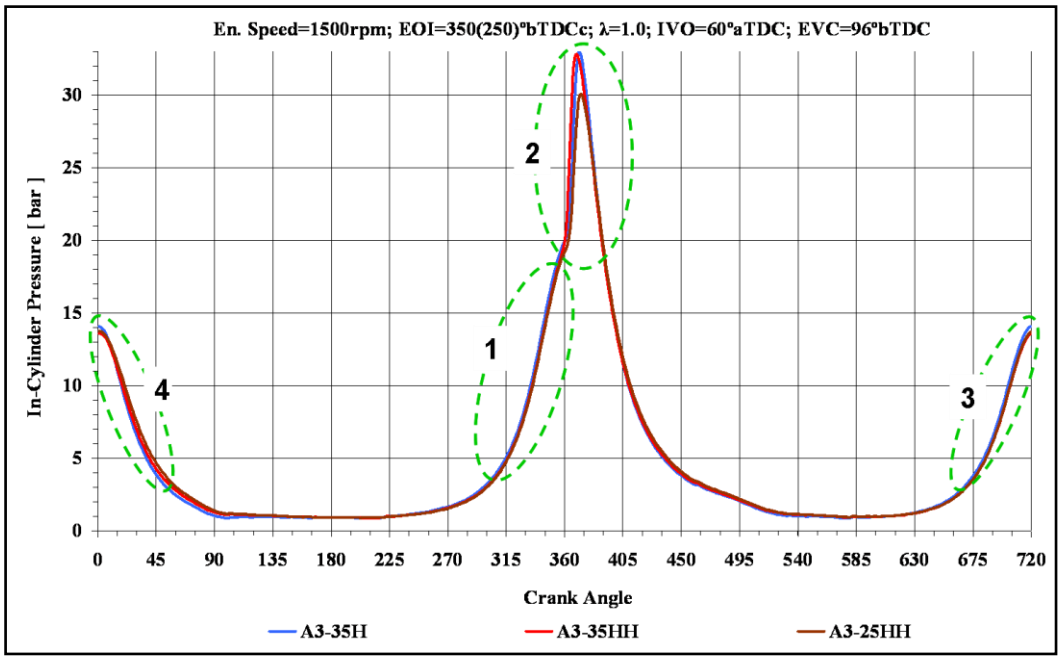

A)

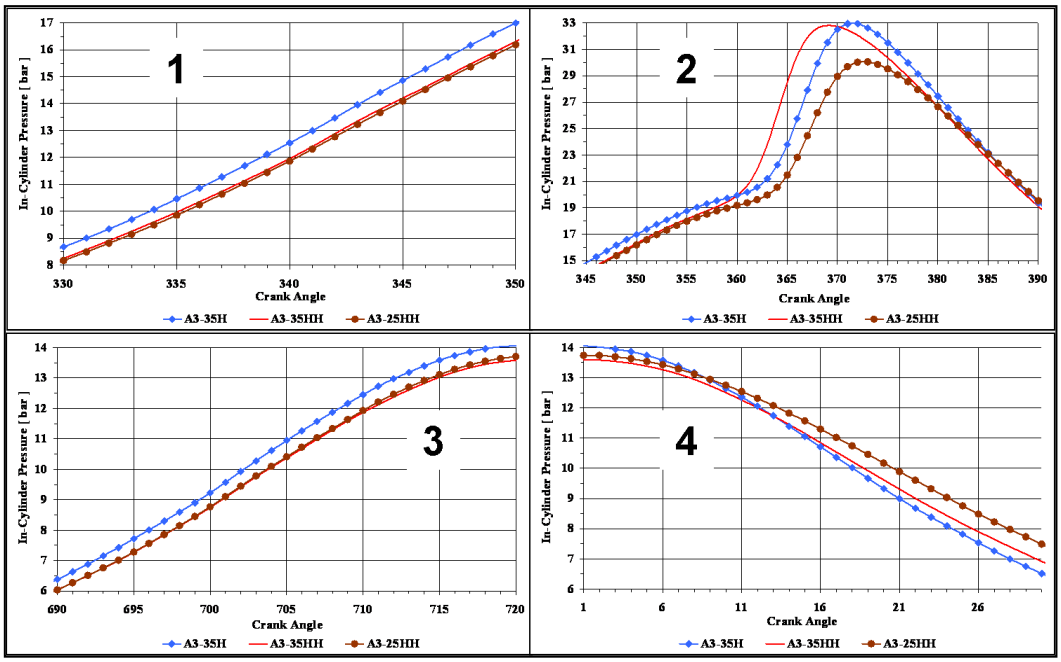

B)

Figure 81: In-cylinder pressure trace for T.M. test with fixed valve timing at 1500rpm.

If one examines Figure 81 it is visible that since the case without heating (35H-15) has a higher mass flow 0.019kg/s compared to 0.018kg/s for the case with heating

(35HH-15 - Table 20), more energy has to be delivered in order to compress the in-cylinder mixture. In both compression strokes (before combustion and during NVO) in-cylinder pressure for the case at 35H-15 is higher than for the case at 35HH-15 or 25HH-15. At the same time, when the expansion side of the NVO part of the cycle is observed less energy has been recovered for the case at 35H-15 than for other two. In addition, when the net heat released during the cycle has been calculated it becomes clear that the increased inlet air temperature reduces the heat exchange between the charge mixture and the environment.

When no heating has been applied the net heat released during the cycle (as calculated for cylinder A3) has reached 1.4kJ. When the temperature of inlet air was increased, the amount of heat released was higher and reached 1.57kJ (despite a lower fuel quantity being injected). Furthermore, when heating is maintained and injection timing was retarded to 250ºbTDCc the amount of heat released during the cycle reached 1.6kJ.

When engine speed was increased to 2500rpm (Figure 82) some changes to the described process occur. The mass flow rate between the sample without heating (35H-25) and with heating (35HH-25) has lowered slightly. Therefore the in-cylinder pressure for all three cases during compression (before combustion and during NVO) is almost the same. This leads to the conclusion that the increase in NMEP is mainly due to improved thermal conditions and reduced heat dissipation. The small change in air flow rate at higher engine speed is probably due to the lower volumetric efficiency (Table 20) and the increased role of gas compressibility effects at higher engine speeds. Similar to the case at lower engine speed more heat has been released during combustion when heating is applied.

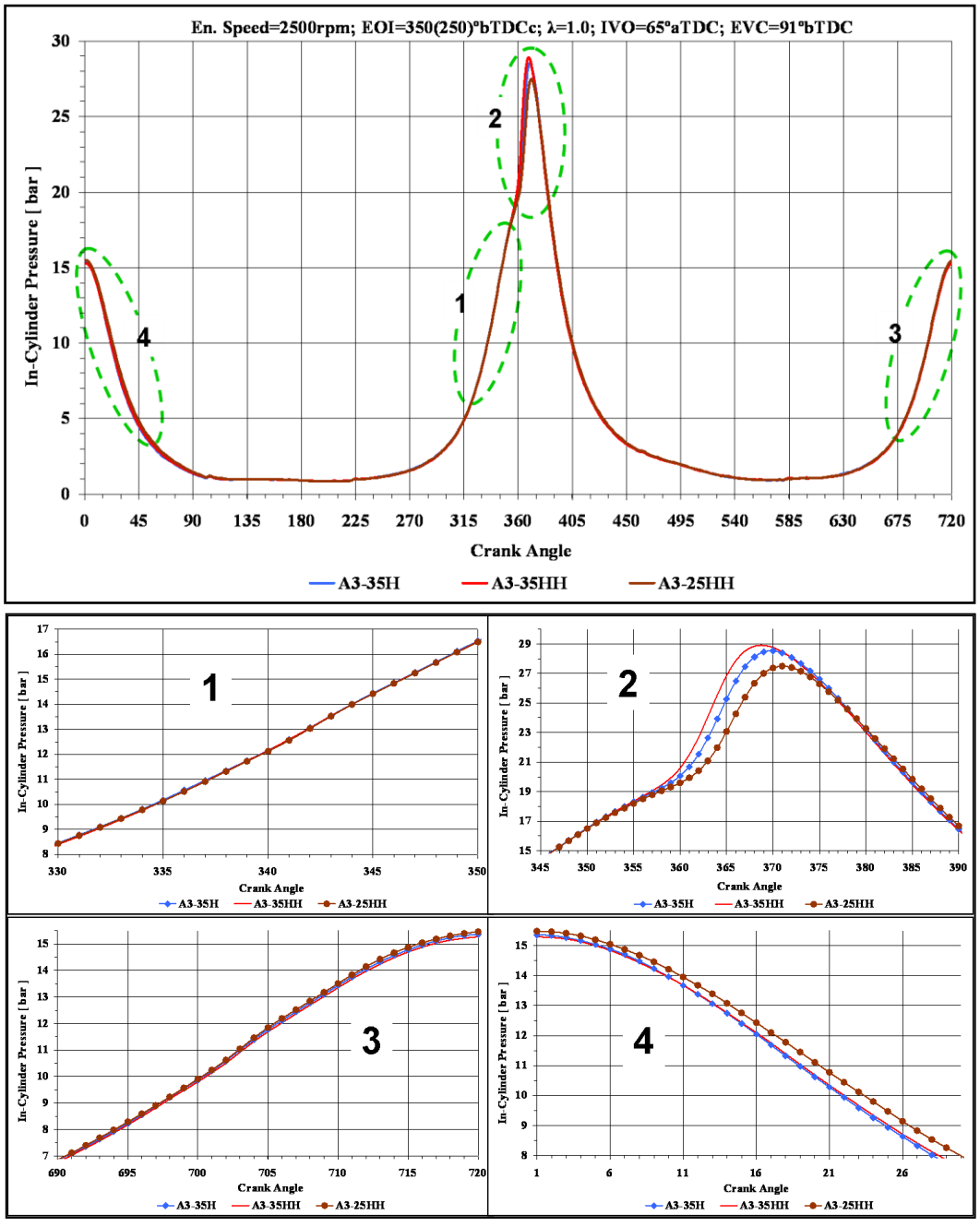

Figure 82: In-cylinder pressure trace for T.M. test with fixed valve timing at 2500rpm.

However, at higher speeds the differences between with heating and without heating are much smaller than the cases at lower engine speeds. When no heating is applied (case 35H-25) the net heat released during the cycle was 1.6kJ; when heating has been applied it reached 1.7kJ. The further improvement has been achieved by retarding injection timing to 250°bTDCc, which in turn increased the amount of heat released during combustion to 1.74kJ. In addition it is worth noting that with an

increasing engine air flow rate, the efficiency of the T.M. system increases. This is due to less heat being dissipated into the environment; therefore, a higher inlet air temperature can be achieved. At 2500rpm the air flow rate increased to about 0.0015kg/s, which in turn increased the achievable inlet air temperature by about 10ºC.

If we have a closer look at gaseous emission results (Table 20) it is shown that NO_x emissions have been reduced by the induction of a warmer charge of air. NO_x emissions have been reduced even further when injection timing has been retarded to 250ºbTDCc. Firstly it is expected that NO_x emissions have been reduced due to the improved mixture homogeneity as the higher inlet air temperature improved the fuel evaporation process (due to higher in-cylinder temperature during NVO). Secondly, combustion in-cylinder temperature has been reduced which in turn suppresses NO_x emissions. These two effects also explain the HC emissions. When heating was applied the mixture homogeneity improves, therefore NSHC emissions was lower. When injection timing was retarded the mixture homogeneity was reduced and the lower in-cylinder temperature (during combustion) had a dominant effect, causing higher HC emissions. Furthermore an examination of the thermal conversion efficiency has been made. It seems that the optimal point from the thermal conversion efficiency is to operate HCCI with heating and injection at around IV MOP (in the presented cases 250ºbTDCc). At both engine speeds thermal efficiency is calculated to be the highest for the case with heating and injection timing set at 250ºbTDCc.

Finally, increased inlet air temperature has advanced the start of combustion (as defined by $MFB_{10\%}$). At 1500rpm this effect is more visible and for the sample marked as 35HH-15 the start of combustion is advanced by 1.9CA (compared with sample 35H-15). At 2500rpm this effect was smaller and the advance in the start of

combustion has reached only 0.9º for sample 35HH-25 compared with sample 35H-25. Moreover heating of inlet air does not reduce combustion duration (as defined by $MFB_{10\text{-}90\%}$). At 1500rpm the combustion duration for the sample with heating (35HH-15) was longer than without (35H-15). When no heating was applied combustion lasts for 12.3º, but when inlet air temperature was increased the combustion duration increased to 13.8º. Increasing engine speed to 2500rpm has lead to diminishing this effect and in both cases combustion lasts for 10.5º.

6.3 Charge Air Cooling Impact on HCCI with Set Valve Timing

Figure 78 presents the trend between NMEP and BMEP and the combustion details in Table 20. The data is divided into two engine speed groups, within which a number of valve timings have been selected in order to show the impact of charge air cooling and injection timing on HCCI operation. Three main cases are considered within the single valve timing set up. The case description is marked in Figure 83 as 35(or 25) B(or C) - 15(or 25) where: the first number describes the end of injection for example 35 stands for 350 ºbTDCc and 25 stands for 250ºbTDCc; letter B stands for "Base" case (HCCI operation without the additional charge air treatment) and C stands for "Cooled" cases (charge air passed through the intercooler with the coolant water temperature fixed at 30ºC); finally the last number describes the engine speed divided by 100. The flow rate of intercooler coolant water has been fixed at about $40l/\min$. The inlet valve timing shown in Figure 83 has been given in "ºaTDC" for inlet valve opening and in "ºbTDC" for exhaust valve closing. The air-to-fuel ratio has been kept at stoichiometric through all tests.

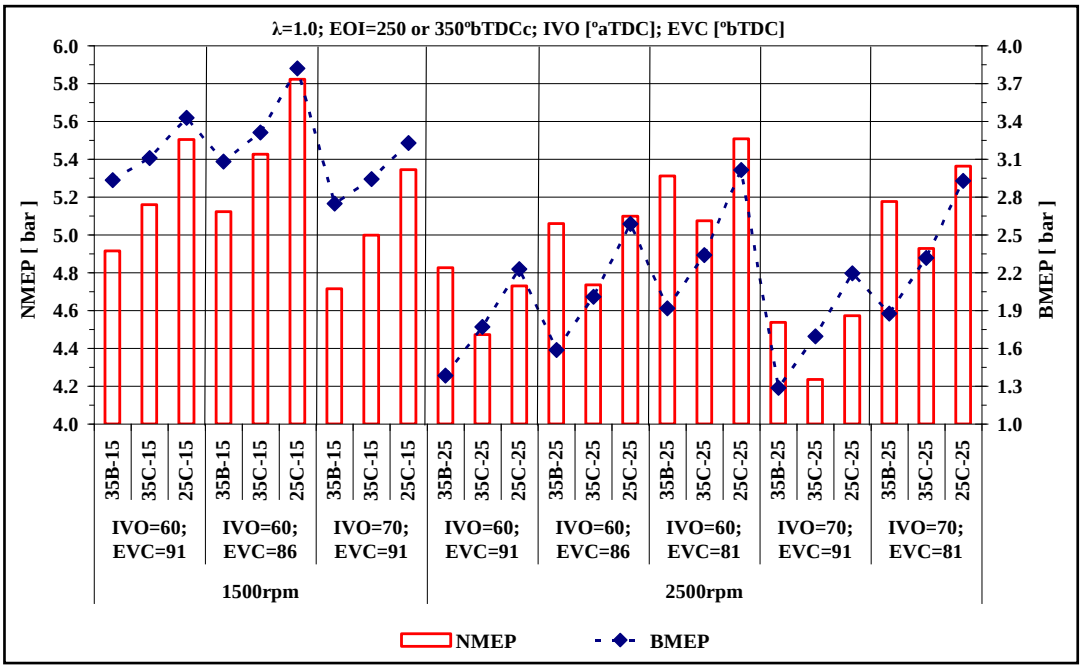

Figure 83: Effect of inlet air cooling and injection timing on NMEP-BMEP correlation for HCCI operation; 35(25) – EOI respectively 250 or 350ºbTDCc, B – base (normal) operation, C – charge air cooling

When Figure 83 is examined, it can be observed that at 1500rpm there is a clear trend between NMEP-BMEP and charge air temperature. When inlet air temperature has been lowered both parameters have increased. However, if one examines the 2500rpm data it can be seen that BMEP has been increasing when inlet air temperature has been reduced as well as when injection timing has been retarded. At the same time unexpectedly NMEP was in most of the cases slightly lower when air has been cooled to rise again when injection has been retarded. An attempt to explain this behaviour is put forward in the following sections.

En. Speed	CASE	NMEP	BMEP	dP/ca	IVO	EVC	Air Flow	Torque	Tin	Tex	NSNOx	NSHC	$\eta_{vol.}$	$\eta_{comb.}$	$\eta_{th.\ conv.}$
		bar	bar	bar/deg.	ºaTDC	ºbTDC	kg/s	Nm	ºC	ºC	g/kWh	g/kWh	%	%	%
1500	35B-15	4.92	2.93	5.19	60	91	0.0238	69.3	57	411	1.35	8.0	58.4	91.1	32.3
	35C-15	5.16	3.11	4.99	60	91	0.0234	73.5	46	412	1.10	6.1	57.3	94.2	28.2
	25C-15	5.50	3.43	2.51	60	91	0.0247	81.0	45	446	0.76	6.8	60.6	93.2	31.9
2500	35B-25	4.83	1.38	3.12	60	91	0.0232	32.7	73	411	0.21	4.2	34.4	---	---
	35C-25	4.47	1.77	2.84	60	91	0.0240	41.8	53	421	0.21	3.6	35.4	96.4	24.7
	25C-25	4.73	2.23	2.71	60	91	0.0252	52.7	57	443	0.25	3.7	36.7	97.0	26.6

Table 21: Detailed test specification for selected valve timing to compare effect of charge air cooling on HCCI operation

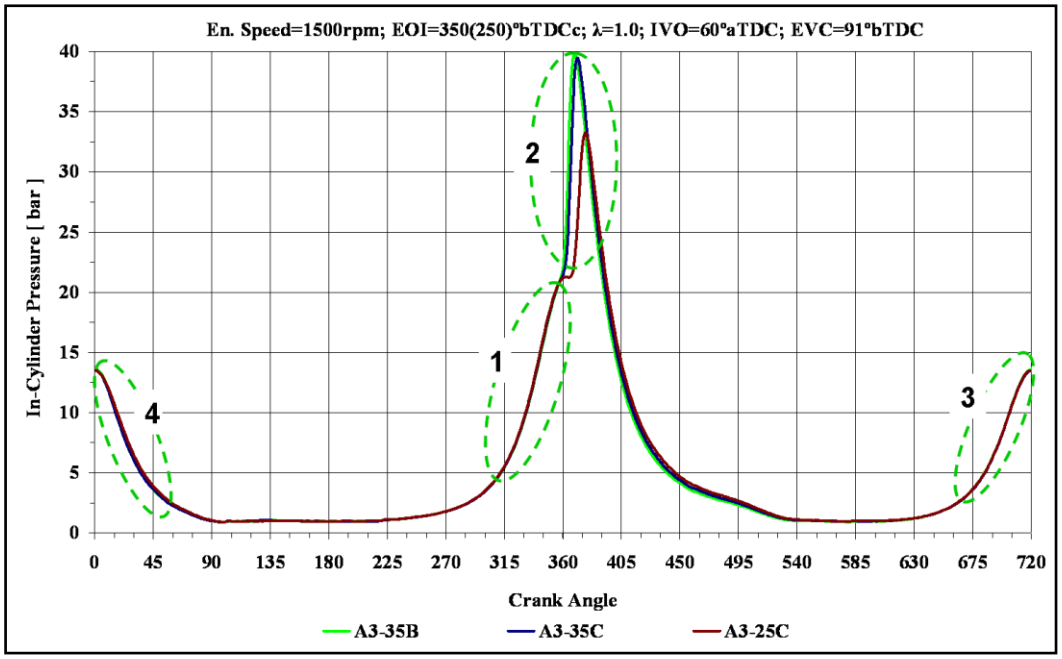

A)

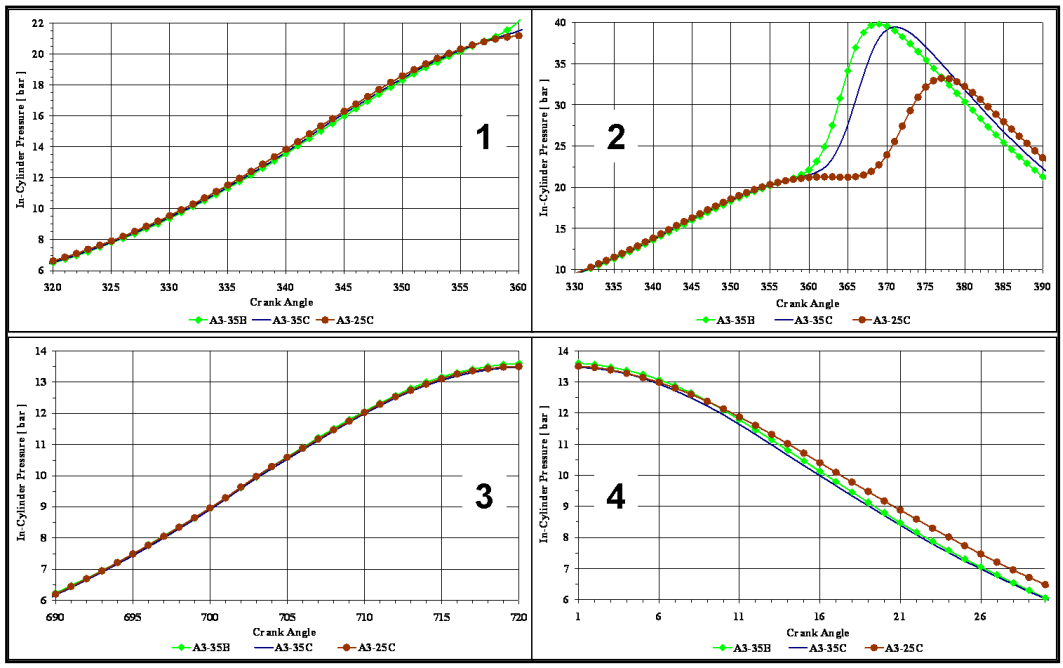

B)

Figure 84: Effect of charge air cooling on in-cylinder pressure at 1500rpm

Figure 84 presents the in-cylinder pressure for cases described in detail in Table 21. From Table 21 it is possible to observe that when cooling has been applied (case 35C-15) the mass flow of fresh air has been almost the same as for the case without cooling (35B-15). However, after observing the injector's pulse width it was shown that cold inlet air requires more fuel to be injected in order to keep the air-to-fuel ratio

constant. The pulse width has increased by about 5% (54μs) from 1078μs due to the cold inlet air. This in turn suggests that more fresh air has been introduced. This discrepancy can be explained by small changes in the ambient temperature (about 5ºC); therefore air density has changed slightly and caused misleading measurements of air flow. The injectors pulse width is a more accurate indicator in this case as all parameters related to injection have been fixed. On the other hand the increase in fresh air has not been significant as one can observe in Figure 84B. The in-cylinder pressure for all three cases at 1500rpm does not show any changes during both compression strokes (before combustion and during NVO - Figure 84B-1 and Figure 84B-3 respectively).

From Figure 84 it can be concluded that cooling of charge air has affected combustion phasing considerably. Reducing inlet temperature by about 10ºC has retarded the start of combustion ($MFB_{10\%}$ point) by 2º (from 2.4º to 4.3º, for cases 35B-15 and 35C-15 respectively). Furthermore combustion duration ($MFB_{10\text{-}90\%}$) has increased marginally from 6.5 to 7º. The cooling of inlet air might be useful only at the upper boundary of HCCI. Therefore, one more parameter is very important – the rate of pressure rise. HCCI combustion is already limited due to the high rate of pressure rise, which makes it important to reduce this parameter. Unfortunately, in Table 21 it has been proven that both the cooling of charge air and the retarding of injection timing lead to an increased rate of pressure rise. The counteraction against this increase may include increasing the air-to-fuel ratio or advancing exhaust valve timing.

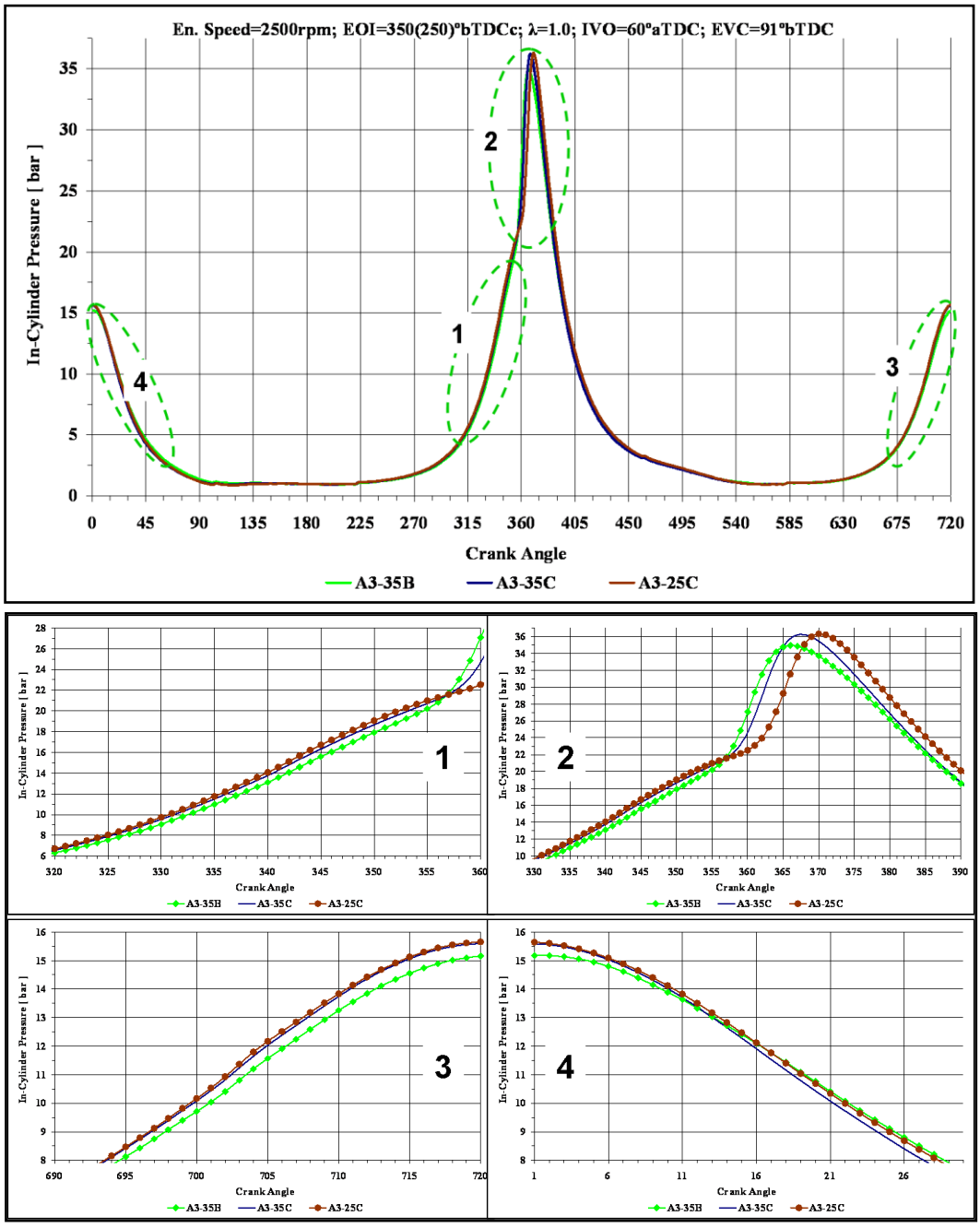

Figure 85: Effect of charge air cooling on in-cylinder pressure at 2500rpm

Figure 85 and Figure 86 are an attempt to explain the relationship between NMEP and BMEP at 2500rpm. From Figure 85 and Table 21 it is clear that when cooling has been applied the NMEP has dropped by about 0.3 to 0.4bar but BMEP has risen by about a similar value. When SI engines are considered, one of the factors important for optimal (the highest) torque output is a minimum ignition timing advance (MBT). Discussion regarding this parameter has been conducted by R. Stone [38] and J. B.

Heywood [5]. It has been concluded that there is always an optimum point that supports the highest torque. Either advancing or retarding the ignition point will lower the torque output. R. Stone [38] performed a simulation from which it was clear that retarded ignition has a much greater impact on BMEP output than advanced ignition. It has been shown as well that shifting from the optimal MBT point affects the maximum in-cylinder pressure and its location, however, the effect on work output (NMEP) is much less visible. Despite the obvious differences between SI and HCCI combustion it is still valid that the location of peak cylinder pressure and the maximum cylinder pressure will correlate to maximum torque and further to BMEP. It has been reasoned then, that the main factor responsible for low BMEP at base (reference) condition (sample 35-B-25) has been early auto-ignition. It is possible to observe in Figure 85B-1 that in-cylinder pressure has significantly increased before the TDC of combustion. This in turn increased the work required to overcome high in-cylinder pressure and reduced torque output (and BMEP).

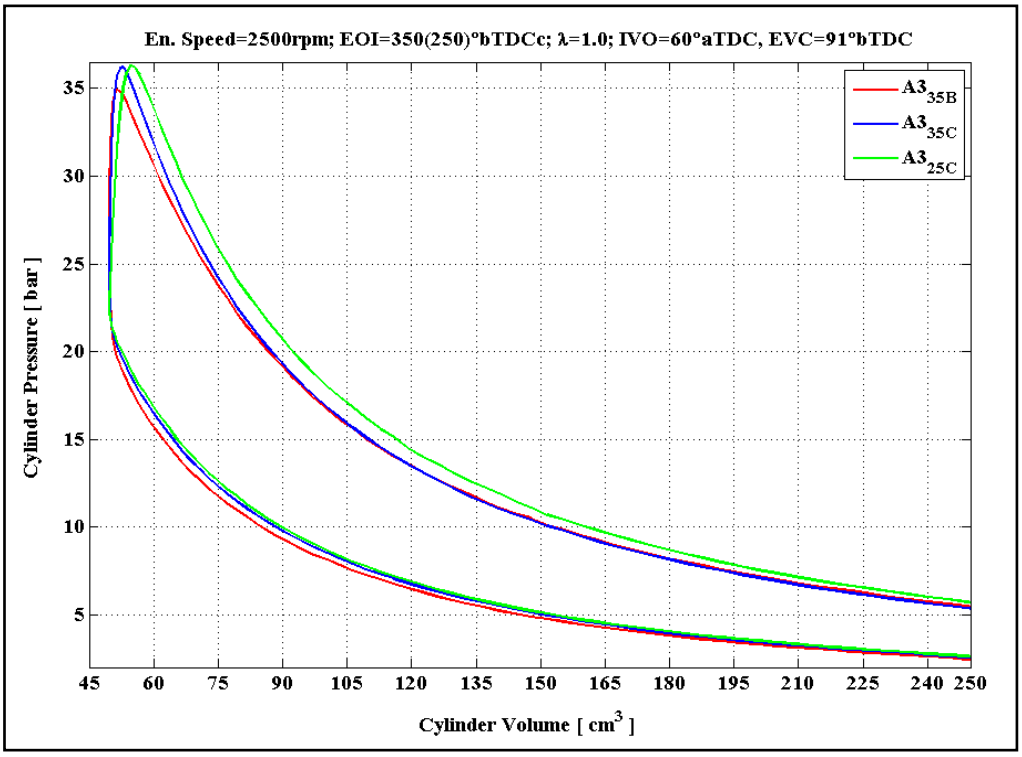

Figure 86: Pressure-Volume diagram for charge air cooling at 2500rpm

In Figure 85B-1 it is visible that in-cylinder pressure has risen significantly before TDC. However, if data has been plotted on a p-V chart it becomes clear that the differences between the normal (base) and a cooled case are very small. This in turn explains the difference between NMEP and BMEP. Figure 86 does not show the whole pressure curves: the recompression part of the HCCI cycle has been neglected. When a closer look at the start of combustion and combustion duration has been taken, it is revealed that the cooling of charge air has retarded the start of combustion. The point of $MFB_{10\%}$ has been retarded from 1.3ºbTDCc (case 35B-25) to 0.3ºaTDCc (case 35C-25). When injection timing has been retarded (with cooling of charge air) from 350ºbTDCc to 250ºbTDCc (case 25C-25), the start of combustion has been retarded even further to 3.2ºaTDCc. At the same time combustion duration has been reduced from 9º (case 35B-25) to 7.1º (case 35C-25) and 7.4º (case 25-C-25). It is reasoned that this effect is mainly due to higher exhaust temperature when inlet air cooling has been applied. The exhaust temperature has risen from 411ºC at base case to 421-443ºC at cooled cases.

Gaseous emissions have been presented in Table 21. It is possible to observe that a different trend in emissions has been achieved for low engine speed (1500rpm) than for high engine speed (2500rpm). At low engine speed either cooling of inlet air or a combination of cooling and retarding of the ignition timing has led to lower $NSNO_x$ emissions. Moreover NSHC emissions have been lowered when cooling has been applied, but have increased slightly when injection is retarded. UHC emissions have followed the same trend when engine speed is increased. However, due to generally lower emission levels, emission differences become lower. The $NSNO_x$ emissions trend changes at higher speed. $NSNO_x$ emissions have been at the same level with a small increase when cooling has been combined with retarded injection. It is expected

that very low emissions of $NSNO_x$ at higher engine speed was the reason for the trend change. It is reasoned that relatively high NSHC emissions for both "base" samples (35B-15 and 35B-25) is due to early combustion phasing, therefore the main part of combustion has taken place in a narrow space when the piston is close to TDC. $NSNO_x$ reduction at 1500rpm has been mainly due to lower in-cylinder temperature. At 2500rpm in-cylinder temperature for samples with air cooling (35C-25) and combined cooling and retarded combustion (25C-25) have been higher but combustion duration has been shorter. Therefore it is expected that these two factors counteract resulting in the specified emissions.

As it has been described elsewhere, a part of the thermal management system is a mixing box. This design solution does not seem to be the most effective as its large volume increased the heat transfer between charge air and engine parts (and the environment). In both cases (heating and cooling) of inlet air, it has been observed that in order to achieve better T.M. system performance the flow rate through the system must be relatively high (briefly above 24g/s). If flow rate is not kept high enough the heat transfer reduces the minimum (and maximum) achievable temperature significantly.

6.4 Summary

The effect of charge air temperature on HCCI performance has been considered in this chapter. It has been proven that by varying inlet air temperature one can either increase the maximum load or further reduce the minimum achievable load therefore expanding the operating envelope for a gasoline multi-cylinder V6 engine running in HCCI mode. Special care has to be exerted while cooling the charge air, as the appropriate amount of energy for auto-ignition has to be delivered to initiate HCCI combustion. This in turn requires the advancing of the exhaust valve timing to supply

enough hot exhaust gas and it requires a reduction in the operating valve timing range. However, by reducing inlet air temperature the maximum achievable load for HCCI combustion increases by about 0.3bar (of NMEP) through a variety of engine speeds.

Applying inlet air heating used to be one of the most popular ways of achieving HCCI combustion. During the presented test its impact on the lowest achievable load seems to be somehow reduced. It is possible to reduce the achieved load by using heating alone but the reduction is not that significant. In order to expand the low HCCI boundary even further, inlet air heating has been combined with throttling of inlet air. By applying both of these techniques the lowest achievable load during HCCI combustion was increased ranging from 0.25 to 0.5bar (of NMEP) increase from the baseline depending on engine speed. Unfortunately, this approach is accompanied with the penalty of higher fuel consumption.

Finally, it has been shown that by applying thermal management on both load regimes (the lowest and the highest) an improvement in both $NSNO_x$ and NSHC emissions has been achieved.

Chapter 7. Conclusions

To control the dynamic operation in HCCI mode the conditions that induce combustion have been dynamically controlled by changing the compression ratio, induced gas temperature and pressure, quantity and temperature of re-induced exhaust gas (EGR), injection strategy. In the preceding sections it has been proven that a means of control of HCCI operation in a multi-cylinder engine can be performed by using Thermal Management. The most important findings by this research will be summarised in this chapter. Some suggestions for future work will also be presented.

7.1 Summary of Presented Findings

Chapter 4: A mathematical model describing the Thermal Management system of the Jaguar V6 HCCI engine at The University of Birmingham has been developed. The mathematical model was tuned using a combination of simulated results from a validated Ricardo WAVE HCCI engine model and experimental data. The model was verified using experimental data. With this mathematical model one can predict the behaviour of the installed Thermal Management system enabling the use of Thermal Management to extend the HCCI operating envelope and investigation of the various configurations in the HCCI operating region.

The system model can run in real time and can easily be implemented for a forward predicting control strategy. In addition this model is used for predicting the boundary conditions for further and detailed modelling investigations such as in CFD computations.

The upper HCCI operating range can be increased by using an intercooler and supercharging whereas the lower HCCI operating boundary can be extended using the

combined effect of heating and throttling. Furthermore an HCCI control strategy has been proposed aiming to reduce NOx and HC emissions.

Chapter 5: CFD Investigation – In this chapter the computed flow field and thermal system performance has been presented. It has been confirmed that the averaged values for the variables obtained by CFD is comparable with the averaged experimental measurements.

If one implements a thermal management system as the one presented in this thesis in order to control HCCI and the heated path with heating is used (HPH) to deliver the induction air, one cannot observe a clear pattern for the path of gas that is consistent for all tested cases, thus not able to indicate if a port receives repeatedly lower temperatures compared to the other ports.

For the cases that the gas has to bypass the intercooler, the vertical disc in the heated path introduces a significant pressure drop through the intercooler bypass path. As result some hot gas will leak though the intercooler throttle, cool down while it passes though the intercooler then mixed with the hot gas and exit the domain reducing the thermal efficiency of the system.

If air is only allowed to pass through the intercooler, one can observe a clear and consistent pattern for the path of gas that is true for all cases involving the air passing through the intercooler. And because the temperature deviation between these measurements is small enough one can claim that the air is uniformly cooled and delivered to all ports.

An investigation of the total heat lost in the CFD models, reveals that approximately 25% of the heat is lost through the mixing box, approximately 25% of the heat is lost though the engine and approximately 50% of the total heat lost is

though the pipework regardless how the thermal management system was used or the engine operating conditions.

Finally it has been observed that with either heating or cooling the charge air using the T.M. system, and in order to achieve better performance from the engine, the charge air flow rate through the system must be relatively high (roughly above 24g/s). If the flow rate is not kept high enough the increase of heat transfer with the environment at low gas speeds will significantly reduce the minimum (and maximum) achievable temperature of the system. This indicates a need for a more compact thermal management system that will reduce the heat losses to the minimum.

Chapter 6: Analysis – Thermal Management System as a tool for HCCI Window Expansion and Emission Comparison – The effect of charge air temperature on HCCI performance has been considered in this chapter. It has been proven that by varying inlet air temperature one can either increase the maximum load or further reduce the minimum achievable load therefore expanding the operating envelope for a gasoline multi-cylinder V6 engine running in HCCI mode. Special care has to be exerted while the cooling the charge air as the appropriate amount of energy for auto-ignition has to be delivered. This in turn requires the advancing of the exhaust valve timing to supply enough hot exhaust gas and it requires a reduction in the operating valve timing range. However, by reducing the inlet air temperature the maximum achievable load for HCCI combustion increased by about 0.3bar (of NMEP) through a variety of engine speeds.

Applying inlet air heating used to be one of the most popular ways of achieving HCCI combustion. During the presented test its impact on the lowest achievable load seems to be somehow reduced. It is possible to reduce achieved load but the reduction is not significant. In order to expand the low HCCI boundary even further, inlet air

heating has been combined with throttling of inlet air. By applying both of these techniques the lowest achievable load during HCCI combustion was increased by 0.25 (of NMEP) from the baseline at 1000rpm and by 0.5bar (of NMEP) from the baseline at 1500rpm. Unfortunately, this approach is accompanied with the penalty of higher fuel consumption.

Finally, it has been shown that by applying thermal management on both load regimes (the lowest and the highest) an improvement in both $NSNO_x$ and NSHC emissions has been achieved.

7.2 Future Work Suggestions

While performing the experimental work utilising the Thermal Management System and trying to expand the operating envelope, for 2500 RPM we generally achieved higher loads with relatively similar emission results. However for 1500 RPM the engine was generally unstable. For these tests there wasn't enough time to complete the investigation to our satisfaction, and the author believes the intercooler was run at too low temperatures and there was not enough energy to initiate auto-ignition. Therefore for further future work if one wants to thoroughly investigate the effect of cooling a next set of experiments is required for 1500 RPM.

References

[1] Jacek Waldemar Misztal, 'Study of Homogeneous Charge Compression Ignition (HCCI) combustion and emission characteristics in a multi-cylinder engine', A thesis submitted to The University of Birmingham for the degree of DOCTOR OF PHILOSOPHY; School of Mechanical Engineering, The University of Birmingham, December 2008.

[2] Yap Min Yi, Daniel Francis, ' Homogeneous Charge Compression Ignition Load Range Extension and Control Issues with Residual Gas Trapping ', A thesis submitted to The University of Birmingham for the degree of DOCTOR OF PHILOSOPHY; School of Mechanical Engineering, The University of Birmingham, April 2005.

[3] EU Emission Standards for Passenger Cars, www.dieselnet.com/standards/eu/ld.php 19July 2010.

[4] Jari Hyvönen, 'The performance of a Multi Cylinder HCCI Engine using Variable Compression Ratio and Fast Thermal Management ', A thesis submitted to Lund Institute of Technology for the degree of DOCTOR OF PHILOSOPHY; Department of Energy Sciences, Division of Combustion Engines, 2005.

[5] Heywood, J, Internal Combustion Engine Fundamentals, - London,. Mcraw-Hill, 1988

[6] M. Stockinger, H. Schäpertöns, P. Kuhlmann: "Versuche an einem gemischansugenden Verbrennungsmotor mit Selbstzündning", MTZ Motortechnische Zeitschrift 53 (1992) 2 pp 80-85

[7] K.Zinner: Supercharging of Internal Combustion Engines, Berlin; Heidelberg, New York, Springer-Verlag, 1978

[8] Christensen, M., Hultqvist, A. and Johansson, B. "Demonstrating the Multi Fuel Capability of a Homogeneous Charge Compression Ignition Engine with Variable Compression Ratio", SAE Transactions, Journal of Engines, vol. 108, SAE Technical Paper, 1999-01-3679

[9] Christensen, M., Johansson, B., "Influence of Mixture Quality on Homogeneous Charge Compression Ignition", SAE Technical Paper, 982454.

[10] Persson, H, Agrell,M, Olsson, J-O, Johansson, B: "The Effect of Intake Temperature on HCCI Operation Using Negative Valve Overlap", SAE Technical Paper, 2004-01-0944

[11] Hyvönen, J., Haraldsson, G., Tunestål, P, Johansson, "HCCI Closed-Loop Combustion Control Using Fast Thermal Management", SAE Technical Paper, 2004- 01-0943.

[12] Hyvönen, J., Haraldsson, G. and Johansson, B. Supercharging HCCI to Extend the Operating Range in a Multi-Cylinder VCR-HCCI Engine, 2003-01-3214

[13] J. Olsson, P. Tunestal, B. Johansson, ‘Closed-Loop Control of an HCCI Engine’, SAE Technical Paper, 2001-01-1031

[14] Hyvönen, J., Haraldsson, G. and Johansson, B. - Balancing Cylinder-to-Cylinder Variations in a Multi-Cylinder VCR-HCCI Engine, SAE Technical Paper, 2004-01-1897

[15] Zhao. F, Asmus T., Assanis D., Dec J., Eng J. and Najt P., "Homogeneous charge compression ignition engines - key research and development issues", SAE International, PT-94, ISBN 0-7680-1123-X

[16] Flowers, D. et al, "HCCI in a CFR Engine: Experiments and detailed Kinetic Modelling” SAE Technical Paper, 2000-01-0328

[17] Stanglmaier, R.H., Roberts, C.E, "Homogeneous charge compression ignition (HCCI): Benefits, compromises, and future engine applications, " SAE Technical Paper, 1999-01-3682

[18] Thring, R. H., "Homogeneous Charge Compression Ignition (HCCI) engines", SAE Technical Paper, 892068

[19] M. Sjöberg, L. Edling, T. Eliassen, L. Magnusson, H. Angström, 'GDI HCCI:Effect of Injection Timing and Air Swirl on Fuel Stratification, Combustion and Emissions Formation', SAE Technical Paper, 2002-01-0106

[20] Onishi, S., Jo, S. H. Shoda, K., Jo, P.D., Kato, S., atoshi, "Active Thermo-Atmosphere Combustion (ATAC) - a new combustion process for internal combustion engines", SAE Technical Paper, 790501

[21] M. Sjöberg, J. E. Dec, 'Combined Effects of Fuel-Type and Engine Speed on Intake Temperature Requirements and Completeness of Bulk-Gas Reactions for HCCI Combustion', SAE Technical Paper, 2003-01-3173

[22] Jeff Allen and Don Law, “Variable Valve Actuated Controlled Auto-Ignition: Speed Load Maps and Strategic Regimes of Operation", SAE Technical Paper, 2002-01-0422

[23] Li, J., Zhao, H, Ladommatos and Ma, T., "Research and Development of Controlled Auto-Ignition (CAI) Combustion in a 4-Stroke Multi-Cylinder Gasoline Engine, SAE Technical Paper, 2001-01-3608

[24] Yang, J. , Todd and Kenney, T., "Development of a Gasoline Engine System using HCCI technology – The Concept and Results", SAE Technical Paper, 2002-01-2832

[25] Hongming Xu, Andrew W., Huiyu F., et al "Operating characteristics of a homogeneous charge compression ignition engine with cam profile switching - Simulation study", SAE Technical Paper, 2003-01-1859

[26] Hongming Xu, Michael Liu, et al "Modelling of HCCI Engines: Comparison of Single-zone, Multi-zone and Test Data", SAE Technical Paper, 2005-01-2123

[27] Hongming Xu, Huiyu Fu, Huw Williams and Ian Shilling, "Modelling Study of Combustion and Gas Exchange in a HCCI (CAI) Engine" SAE Technical Paper, 2002-01-0114

[28] D. Yap, A. Megaritis, M. L. Wyszynski, and Hongming Xu, "Residual Gas Trapping for Natural Gas HCCI", SAE Technical Paper, 2004-01-1973

[29] .D Yap, A. Megaritis, M. L. Wyszynski, and Hongming Xu, "Applying boosting to gasoline HCCI operation with residual gas trapping" SAE Technical Paper, 2005-01-2121

[30] D. Yap, A. Megaritis, S. Peucheret M. L. Wyszynski, and Hongming Xu, "Effect of Hydrogen Addition on Natural Gas HCCI Combustion", SAE Technical Paper, 2004-01-1972

[31] .D Yap, A. Megaritis, M. L. Wyszynski, and Hongming Xu, "Effect of inlet valve timing on boosted gasoline HCCI with residual gas trapping", SAE Technical Paper, 2005-01-2136

[32] Hongming Xu, Simon Rudolph, Zhi Liu, et al "An Investigation into the Operating Mode Transitions of a Homogeneous Charge Compression Ignition Engine Using EGR Trapping" SAE Technical Paper, 2004-01-1911

[33] Guzzella, L. Introduction to modelling and control of internal combustion engine systems - Berlin; New York, NY : Springer, 2004

[34] Miller, Donald S. (Donald Stuart), Internal flow systems. – Cranfield, BHRA Fluid Engineering, 1978

[35] Mukhtar M. Ashur, 'Exhaust Gas Reforming of Gasoline Using an Integrated Fuel Reformer and TWC with Fluidic Valve for Exhaust Flow Management for HCCI Engine', A thesis submitted to The University of Birmingham for the degree of DOCTOR OF PHILOSOPHY; School of Mechanical Engineering, The University of Birmingham, June 2008.

[36] Henry Darcy, *Les Fontaines Publiques de la Ville de Dijon* ("The Public Fountains of the Town of Dijon"), Dalmont, Paris (1856).

[37] Massey, B. S., Bernard Stanford Mechanics of fluids / Bernard Massey . - 7th ed . - Cheltenham : Stanley Thornes, 1998

[38] R. Stone, 'Introduction to Internal Combustion Engines (Third Edition), MACMILLAN PRESS LTD

[39] Lakshinarayana Budgur, Fluid Dynamics and Heat Transfer of Turbomachinery, John Wiley & Sons Inc (1996). p. (10-42), (70-78), (358-371), (745-749).

[40] ANSYS CFX 12.0 manual

[41] SCHLICHTING, H. "Boundary Layer Theory", McGraw-Hill, 1979.

[42] ANSYS FLUENT 12 Theory Guide, Section 4.12 Near-Wall Treatments for Wall-Bounded Turbulent Flows

[43] Watson, N. Turbocharging the internal combustion engine / N. Watson, the late M.S. Janota . - London : Macmillan, 1982

[44] Kiencke, U. Automotive control systems / Uwe Kiencke, Lars Nielsen . - Berlin; London : Springer, 2000

[45] G. Shibata, K. Oyama, T. Urushihara, T. Nakano, 'The Effect of Fuel Properties on Low and High Temperature Heat Release and Resulting Performance of an HCCI Engine', SAE Technical Paper, 2004-01-0553.

[46] G. Shibata, K. Oyama, T. Urushihara, T. Nakano, 'Correlation of Low Temperature Heat Release with Fuel Composition and HCCI Engine Combustion', SAE Technical Paper, 2005-01-0138.

[47] G. Shibata, T. Urushihara, 'The Interaction between Fuel Chemicals and HCCI Combustion Characteristics under Heated Intake Air Conditions', SAE Technical Paper, 2006-01-0207.

[48] N. Milovanovic, D. Blundell, R. Pearson, J. Turner, R. Chen, 'Enlarging the Operational Range of a Gasoline HCCI Engine By Controlling the Coolant Temperature', SAE Technical Paper, 2005-01-0157

[49] J. E. Dec, M. Sjöberg, 'A Parametric Study of HCCI Combustion – the Sources of Emissions at Low Loads and the Effects of GDI Fuel Injection', SAE Technical Paper, 2003-01-0752

[50] Nieberding R-G, 'The Knocking Syndrome - Its Cure and Its Potential', SAE Technical Paper, 982483

[51] Urushihara T., Hiraya K., Kakuhou A., Itoh T., 'Expansion of HCCI Operating Region by the Combination of Direct Fuel Injection, Negative Valve Overlap and Internal Fuel Reformation', SAE Technical Paper, 2003-01-0749.

[52] J. Martinez-Frias, S. M. Aceves, D. Flowers, J. R. Smith, R. Dibble, 'HCCI Engine Control by Thermal Management', SAE Technical Paper, 2000-01-2869.

[53] Marriott Craig D., Reitz Rolf D Experimental Investigation of Direct Injection Gasoline for Premixed Compression-Ignited Combustion-Phasing Control, SAE Technical Paper, 2002-01-0418

[54] T. Aroonsrisopon, D. Foster, T. Morikawa, M. Iida, 'Comparison of HCCI Operating Ranges for Combinations of Intake Temperature, Engine Speed and Fuel Composition', SAE Technical Paper, 2002-01-1924.

[55] M. Iida, T. Aroonsrisopon, M. Hayashi, D. Foster, J. Martin, 'The Effect of Intake Air Temperature, Compression Ratio and Coolant Temperature on the Start of Heat Release in an HCCI (Homogeneous Charge Compression Ignition) Engine', SAE Technical Paper, 2001-01-1880

[56] U. Wagner, R. Anca, A. Velji, U. Spicher, 'An Experimental Study of Homogeneous Charge Compression Ignition (HCCI) with Various Compression Ratios, Intake Air Temperatures and Fuels with Port and Direct Fuel Injection', SAE Technical Paper, 2003-01-2293

[57] H. Persson, M. Agrell, J. Olsson, B. Johansson, H. Ström, 'The Effect of Intake Temperature on HCCI Operation Using Negative Valve Overlap', SAE Technical Paper, 2004-01-0944

[58] M. Sjöberg, J. E. Dec, 'An Investigation of the Relationship between Measured Intake Temperature, Bdc Temperature and Combustion Phasing for Premixed and DI HCCI Engines', SAE Technical Paper, 2004-01-1900

[59] J. Chang, Z. Filipi, D. Assanis, T-W. Kuo, P. Najt, R. Rask, 'Characterizing the Thermal Sensitivity of a Gasoline Homogeneous Charge Compression Ignition Engine with Measurements of Instantaneous Wall Temperature and Heat Flux', International Journal of Engine Research (DOI: 10.1243/146808705X30558), Vol. 6, 2005

[60] M. Morgan, W. Cheng, T. Kenney, J. Yang, 'Effect of Air Temperature and Humidity on Gasoline HCCI Operating in the Negative-Valve-Overlap Mode', SAE Technical Paper, 2007-01-0221.

[61] J. Hyvönen, G. Haraldsson, B. Johansson, 'Operating Range in a Multi Cylinder HCCI Engine Using Variable Compression Ratio', SAE Technical Paper, 2003-01-1829 (JSAE - 20030178).

[62] S. M. Aceves, D. L. Flowers, F. Espinosa-Loza, J. Martinez-Frias, J. E. Dec, M. Sjöberg, R. W. Dibble, R. P. Hessel, 'Spatial Analysis of Emissions Sources for HCCI Combustion at Low Loads Using a Multi-Zone Model', SAE Technical Paper, 2004-01-1910

[63] G. Haraldsson, P. Tunestål, B. Johansson, J. Hyvönen, 'HCCI Combustion Phasing in a Multi Cylinder Engine Using Variable Compression Ratio', SAE Technical Paper, 2002-01-2858

[64] M. Christensen, B. Johansson, 'Supercharged Homogeneous Charge Compression Ignition (HCCI) with Exhaust Gas Recirculation and Pilot Fuel', 2000 International Spring Fuels And Lubricants Meeting & Exposition, Paris, France; SAE Technical Paper, 2000-01-1835

[65] J-O. Olsson, P. Tunestål, B. Johansson, 'Boosting for High Load HCCI', SAE Technical Paper, 2004-01-0940

[66] J-O. Olsson, P. Tunestål, G. Haraldsson, B. Johansson, 'A Turbo Charged Dual Fuel HCCI Engine', SAE Technical Paper, 2001-01-1896

[67] M. Christensen, B. Johansson, A. Hultqvist, 'The Effect of Piston Topland Geometry on Emissions of Unburned Hydrocarbons from a Homogeneous Charge Compression Ignition (HCCI) Engine', SAE Technical Paper, 2001-01-1893

[68] K. Hatamura, 'A Study on HCCI(Homogeneous Charge Compression Ignition) Gasoline Engine Supercharged by Exhaust Blow Down Pressure', SAE Technical Paper, 2007-01-1873 (JSAE, 20077130)

[69] M. Canakci, 'An Experimental Study for the Effects of Boost Pressure on the Performance and Exhaust Emissions of a DI-HCCI Gasoline Engine', Fuel (DOI:10.1016 /j.fuel.2007.08.002), Fuel 87,1503–1514, 2008

[70] J. E. Dec, M. L. Davisson, M. Sjöberg, R. N. Leif, W. Hwang, 'Detailed HCCI Exhaust Speciation and the Sources of Hydrocarbon and Oxygenated Hydrocarbon Emissions', SAE Technical Paper, 2008-01-0053

[71] U. Elghawi, J. Misztal, A. Tsolakis, M.L. Wyszynski, H.M Xu, J. Qiao, 'GC-MS Speciation and Quantification of 1,3 Butadiene and Other C1-C6 Hydrocarbons in SI / HCCI V6 Engine Exhaust', SAE Technical Paper, 2008-01-0012

[72] A. Bhave, M. Kraft, L. Montorsi, F. Mauss, 'Sources of CO Emissions in an HCCI Engine: A Numerical Analysis', Combustion and Flame (DOI:10.1016/j.combustflame. 2005.10.015), 144, 634–637, 2006.

[73] M. Sjöberg, J. E. Dec, 'An Investigation into Lowest Acceptable Combustion Temperatures for Hydrocarbon Fuels in HCCI Engines', Proceedings of the Combustion Institute (DOI:10.1016/j.proci.2004.08.132) ,30 (2719–2726), 2005.

[74] J. W. Girard, R. W. Dibble, D. L. Flowers, S. M. Aceves, 'An Investigation of the Effect of Fuel-Air Mixedness on the Emissions from an HCCI Engine', SAE Technical Paper, 2002-01-1758

[75] E. Kaiser, M. Matti Maricq, N. Xu, J. Yang, 'Detailed Hydrocarbon Species and Particulate Emissions from a HCCI Engines as a Function of Air-Fuel Ratio', SAE Technical Paper, 2005-01-3749

[76] D. Kawano, H. Naito, H. Suzuki, H. Ishii, S. Hori, Y. Goto, M. Odaka, 'Effects of Fuel Properties on Combustion and Exhaust Emissions of Homogeneous Charge Compression Ignition (HCCI) Engine', SAE Technical Paper, 2004-01-1966

[77] D. S. Kim, C. S. Lee, 'Improved Emission Characteristics of HCCI Engine by Various Premixed Fuels and Cooled EGR', Fuel (DOI:10.1016/j.fuel.2005.08.041),85, 695–704, 2006.

[78] M. C. Mulenga, D. S-K. Ting, G. T. Reader, M. Zheng, 'The Potential for Reducing CO and NOx Emissions from an HCCI Engine Using H2O2 Addition', SAE Technical Paper, 2003-01-3204

[79] P. Price, R. Stone, J. Misztal, H. Xu, M. Wyszynski, T. Wilson, J. Qiao, 'Particulate Emissions from Gasoline Homogeneous Charge Compression Ignition Engine', SAE Technical Paper, 2007-01-0209

[80] M. L. Wyszynski, T. Megaritis, R. S. Lehrle, 'Hydrogen from Exhaust Gas Fuel Reforming: Greener, Leaner and Smoother Engines', Presentation in H2Net Meeting.

[81] Jones, M., and Wyszynski, M., Exhaust gas reforming of hydrocarbon fuels, SAE Technical Paper, 931096, 1993

[82] Jamal, Y., and Wyszynski, M.,L. (1994), On-board generation of hydrogen-rich gaseous fuel – a review, International Journal of Hydrogen Energy, 1994, Vol. 19, No. 7,557-572

[83] J. P. Kopasz, L. E. Miller, D. V. Applegate, 'Effects of Multicomponent Fuels, Fuel Additives and Fuel Impurities on Fuel Reforming', SAE Technical Paper, 2003-01-2254

[84] J. P. Kopasz, S. Ahmed, M. Krumpelt, P. Devlin, 'Challenges in Reforming Gasoline: All Components Are Not Created Equal', SAE Technical Paper, 2001-01-1915

[85] Yap, D., Peucheret, S., Megaritis, A., Wyszynski, M., and Xu, H., (2006), Natural gas HCCI engine operation with exhaust gas fuel reforming, International Journal of Hydrogen Energy, Vol.31, pp.587-595, 2006.

[86] Potrzebowski A., Misztal J., et al (2009), Proceedings of the Institution of Mechanical Engineers, Part D - Journal of Automobile Engineering – 2009 – Potrzebowski - 1207-21, doi 10.124309544070JAUTO1005

[87] J. C. Livengood, P. C. Wu. “Correlation of Autoignition Phenomena in Internal Combustion Engines and Rapid Compression Machines”. Pages 347–356. Fifth Symposium (International) on Combustion, 1955.

[88] X. He, M.T. Donovan, B.T. Zigler, T.R. Palmer, S.M. Walton, M.L. Wooldridge, A. Atreya. “An experimental and modeling study of iso-octane ignition delay times under homogeneous charge compression ignition conditions” Combustion and Flame 142 (2005) 266-275

[89] Lindstrom F., Angstrom H. E., Kalghatgi G., Moller C. E. “An Empirical SI Combustion Model Using Laminar Burning Velocity Correlations”, SAE Paper 2005-01-2106, 2005

[90] 2. Jing Qin, Hui Xie, Yan Zhang, “A combustion Heat Release Correlation for CAI Combustion Simulation in 4-Stroke Gasoline Engines” SAE 2005-01-0183

[91] N. Watson, A.D. Piley, M. Marzouk “A Combustion Correlation for Diesel Engine Simulation”, SAE Paper 800029, 1980

[92] Krieger R. B. “The Computation of Apparent Heat Release for Internal Combustion Engines”, ASME publication 6370 A, 1967

[93] Ricardo WAVE documentation.

[94] Hua Zhao, 'HCCI and CAI Engines for the Automotive Industry', Woodhead
Publishing.

[95] G. Gnanam, M. Johnson, A. Sobiesiak, G. Reader, 'HCCI Combustion with Internal Fuel Reforming, Varied Levels of EGR and Charge Preheat – a Computational Study', SAE, 2005-01-0140.

[97] B. P. Pundir, R. Kumar, 'Combustion and Smoke Emission Studies on a Hydrogen Fuel Supplemented DI Diesel Engine', SAE, 2007-01-0055.

[98] S. Sassaki, Y. Tonegawa, T. Nakajima, 'Potential of Nanoparticle Formation by Vehicles', SAE, 2006-01-0622.

Appendix 1

7.3 Derivation of equations for Filling and Emptying Modelling Method Engine Model

7.4 Derivation 1

The definition of EGR states that EGR is the proportion of the mass of exhaust gases over the mass of charge air.

$$EGR = \frac{m_{egr}}{m_{gas}} \tag{81}$$

Thus after the valve events are completed in the cylinder chamber the mass of charge air can be described as:

$$m_{gas} = m_{egr} + m_{air} \tag{82}$$

$$m_{gas} = EGR \cdot m_{gas} + m_{air}$$

$$m_{air} = (1 - EGR) \cdot m_{gas} \tag{83}$$

7.5 Derivation 2

After the valve events we can describe with an energy balance the difference in energy between exhaust gas and fresh air assuming that the exhaust gas in the cylinder is homogeneous and has relative similar properties with ambient air.

$$m_{gas} \cdot c_v \cdot T_1 = m_{egr} \cdot c_v \cdot T_5 + m_{air} \cdot c_v \cdot T_{im} \tag{84}$$

$$m_{gas} \cdot T_1 = EGR \cdot m_{gas} \cdot T_5 + (1 - EGR) \cdot m_{gas} \cdot T_{im}$$

$$T_1 = EGR \cdot T_5 + (1 - EGR) \cdot T_{im} \tag{85}$$

Appendix 2

7.6 Introduction to CFD

7.6.1 Computation Methods

For most CFD solvers the fluid is assumed to be a continuum. This way of approach ignores the molecular structure of the given fluid and introduces new variables as velocity, pressure and temperature. On molecular level these variables cannot be applied. So the mentioned way of approach defines that a fluid volume element must have a size large enough for being capable of defining temperature, and pressure. Velocity is then only a higher order of magnitude of the motion of this minimal size volume element on which the motion of the molecules is modelled. The governing equations of the motion of fluids are based on this hypothesis. For taking viscous effects into account we need to process the simultaneous solution of the non-linear second order differential equations of Motion and the differential equation of Continuity. These are non-linear methods. The main part of the CFD codes are solving for these mentioned equations, so the domain of interest must be discretized into small volume elements and the governing equations are integrated through these elements in the whole domain. Several methods came to exist for the solution of the mentioned equations. Below are the three procedures:

a) Finite Difference

b) Finite Volume and

c) Finite Element methods.

Finite Difference method was the first method that was applied for flow pattern simulations. The procedure of this method solves for the discretized differential form of the governing equations in the computational domain using node points and the

distances between the neighbouring nodes. By this way the velocity and pressure values can be obtained in every node.

Finite Volume method solves for the integral form of the governing equations of flow and divides the domain into volume elements. The velocity and the pressure values are then computed and usually located in the middle point of each volume element. For its robustness, low memory needs and conservativeness this method is used in most of the present CFD codes.

Finite Element method uses the theory of weighted residuals for the solution of the governing equations. The velocity and pressure values will be located on the vertices of the elements that were obtained after discretization of the domain. The method of Finite Elements is not widely used in Fluid Dynamics because of its high amount of memory consumption. However, the grid generation techniques of this method is adapted by Finite Volume methods because its ability for meshing very complex geometries

ANSYS CFX uses an element-based finite volume method. All the solution variables and fluid properties are stored at the element nodes. Each node is surrounded by a set of surfaces that define the control volume. Gauss' Divergence Theorem is applied to convert the volume integrals involving divergence and gradient operators. to surface integrals, in such a way that the relevant quantity (mass, momentum, energy, etc.) is conserved in a discrete form for each control volume. The volume integrals represent source or accumulation terms, and the surface integrals represent the summation of the fluxes. A semi-Finite Element approach using the shape function method that depends on the element used to create the mesh, is used to calculate various geometric quantities, including integration point coordinates and surface area vectors.

Other CFD solvers implement the Lattice Boltzmann method instead of solving the Navier Stokes equations. Using this method the discrete Boltzmann transport equation is solved to simulate the flow of a Newtonian fluid using collision models. The Boltzmann equation describes the statistical distribution of one particle in a controlled volume and can be used to study how a gas or fluid transports physical quantities such as heat and momentum, and thus to derive transport properties such as viscosity, and thermal conductivity. By simulating streaming and collision processes across a finite number of particles, these particle interactions can demonstrate a microcosm of viscous flow behaviour applicable across the whole flow field. However the weakness of this approach is it is inherently transient thus it is not suitable to perform steady state simulations.

It is beyond the scope of this report to scrutinise the numerical methods that CFD solvers use to perform computations. Therefore the basic governing equations and how they were applied using ANSYS CFX will be described next. The turbulence models and the applied near wall treatments will also be detailed. The discretization process and how ANSYS CFX computes the solution will not be described. If more detailed description is needed , the reader can refer to [39] p.32-34 or [40].

7.6.2 Continuity Equation

The continuity equation expresses the conservation of mass, and is written in the following form:

$$\frac{\partial \rho}{\partial t} + \frac{\partial}{\partial x_j}\left(\rho u_j\right) = S_m \qquad 86$$

Where ρ [kg/m^3] is the density of the fluid, the subscript j (=1,2,3) denotes the direction considering as follows: x_1=x, x_2=y, x_3=z; u_j [m/s] is the component of the

velocity in the direction of x_j, and S_m is a source of mass that can be added by a discrete second phase in two phase flows. In the present case, the value of S_m is zero.

7.6.3 The Equation of Motion

This equation expresses the conservation of momentum in the domain of interest. In general in ANSYS CFX, it takes the following form:

$$\frac{\partial}{\partial t}(\rho u_i) + \frac{\partial}{\partial x_j}(\rho u_i u_j) = -\frac{\partial p}{\partial x_i} + \frac{\partial \tau_{ij}}{\partial x_j} + \rho g_i + F_i \qquad 87$$

where p[Pa] is the static pressure, τ_{ij} [Pa] is the stress tensor due to viscosity, g_i [m/s^2] is the component of the gravitational acceleration vector in the direction of x_i. The subscript i denotes the direction which the component equation is written. F_i [N/m^3] denotes external body forces in the direction of x_i. F_i can arise from a discrete disperse secondary phase and it can also be a virtual force in a relative frame of reference, or it occurs at porous media and user defined sources.

The stress tensor τ_{ij} is given by the following equation:

$$\tau_{ij} = \left[\mu\left(\frac{\partial u_i}{\partial x_j} + \frac{\partial u_j}{\partial x_i}\right)\right] - \frac{2}{3}\mu\frac{\partial u_l}{\partial x_l}\delta_{ij} \qquad 88$$

where μ [kg/ms] is the molecular viscosity of the fluid and the second term in the expression above expresses the effect of bulk viscosity that occurs at dilatation of a fluid volume.

7.6.4 Energy Equation

ANSYS CFX solves the energy equation in the following form

$$\frac{\partial}{\partial t}(\rho E) + \nabla\left(\vec{u}(\rho E + p)\right) = \nabla\cdot\left(k_{eff}\nabla T - \sum_j h_i \vec{J}_j + \left(\tau_{ij}\cdot\vec{u}\right)\right) + S_h \qquad 89$$

where k_{eff} is the effective conductivity ($k + k_t$ where k_t is the turbulent thermal conductivity, defined according to the turbulence model being used), and $\vec{J}_j$ is the diffusion flux of species j. The first three terms on the right-hand side of Equation (59) represent energy transfer due to conduction, species diffusion, and viscous dissipation, respectively. S_h includes the heat of chemical reaction, and any other volumetric heat sources one might define. In the present case, the value of S_h is zero.

In Equation (59)

$$E = h - \frac{p}{\rho} + \frac{u^2}{2} \qquad 90$$

where sensible enthalpy h is defined for ideal gases as

$$h = \sum_j Y_j h_j \qquad 91$$

and for incompressible flows as

$$h = \sum_j Y_j h_j + \frac{p}{\rho} \qquad 92$$

Equation (61) and (62) is the mass fraction of species j where

$$h_j = \int_{Tref}^{T} c_{pj} dT \qquad 93$$

There are simplifications to Equation (59) where pressure work and kinetic energy terms are negligible for example for incompressible or low speed flows. However the different variations of the energy equation will not be presented here; for further information the reader is referred to [40].

7.6.5 Basic Concepts of Turbulent Flows

Most engineering flows are turbulent, with laminar and transitional regions occurring near the leading edge of a surface. Turbulence influences the aerodynamic

and thermodynamic performance and therefore its consideration is critical to any analysis. A brief introduction of the subject is provided in this section.

Turbulence is characterized by irregular or random fluctuations of the velocity field. These fluctuations mix transported quantities such as momentum, energy, and species concentration, and cause the transported quantities to fluctuate as well. It often originates as instability of high-Reynolds-number laminar flow which results in a transition to turbulence. Turbulence is a very complex phenomenon to measure and analyze. Because of its random variation in space and time, much analysis relies on statistical approaches because they are computationally expensive to simulate directly in practical engineering calculations. Instead, the instantaneous (exact) governing equations can be time-averaged, ensemble-averaged, or otherwise manipulated to remove the small scales, resulting in a modified set of equations that are computationally less expensive to solve. However, the modified equations contain additional unknown variables, and turbulence models are needed to determine these variables in terms of known quantities which is then fed back into the modified equations. The additional terms which appear in these equations must be modelled, and therefore the problem of including turbulence in the formulation is often referred to as the closure problem. Statistical approaches vary from very rough (often purely empirical) models to highly sophisticated (often impractical for the up to date technology) models.

Turbulence, in addition to being random and irregular, is three-dimensional. Velocity fluctuations exist in all directions, even if the mean (time average) flow is one- or two-dimensional. Turbulence is diffusive and dissipative. Diffusion gives rise to rapid mixing and increase the rate of momentum, heat, and mass transfer. Dissipation is characterized by deformation work associated with velocity

fluctuations, and it increases the internal energy of the fluid at the expense of the kinetic energy in the mean flow and the turbulence.

There are several books and reviews on the subject of turbulent flow. A good description can be found in [39]. An attempt is made below to classify the turbulent flows encountered:

a) Homogeneous or nonhomogeneous
b) Isotropic or nonisotropic
c) Steady or unsteady mean flow
d) Incompressible (M < 0.3) or compressible (M> 0.3); subsonic (M < 1), transonic (M = 1), supersonic (M > 1)
e) Two-dimensional mean flow (i.e cascade rotor, stator applications in turbo-machinery) and three-dimensional mean flow
f) Internal or external flows
g) Simple strain or extra strain with curvature, rotation, buoyancy effects
h) Free shear flows (cascade wake, rotor wake, tip leakage, jet)
i) Wall bounded shear flows (cascade and rotor blade boundary layer, annulus wall and hub wall boundary layers, ducts boundary layer separation, throttles, valves etc.)

The technique used in solving the turbulent flow equations and the model or equations employed for representing turbulence depends on the type of flow listed. Most classifications are obvious, but some need extensive investigation.

7.6.6 Turbulence Modelling

As mentioned in previous section, CFD solvers solve the Reynolds Averaged Navier Stokes (RANS) and Continuity Equations. Modelling provides the closure equations and fluctuation terms in these equations. For taking viscous effects into

account these model equations need to be processed simultaneously with the solution of the non-linear second order differential equations of Motion and the differential equation of Continuity. These are non-linear methods however there are some simplifications on the governing equations of flow for most of the cases.

The closure techniques, more known as turbulent models, can be classified as follows:

a) Zero-Equation or Algebraic Eddy Viscosity Models. These models employ an algebraic form for the turbulent stresses
b) One-Equation Models. These models employ an additional PDE (Proportional Differential Equation) for a turbulence velocity scale.
c) Two-Equation Models. These models employ one PDE for a turbulence length scale and one PDE for a turbulence velocity scale.
d) Reynolds Stress Models. (RSM) These models employ several (usually seven) PDE's for all of the components of the turbulence stress tensor.
e) Large Eddy Simulation (LES) model. LES is an approach which solves for large-scale fluctuating motions and uses "sub-grid" scale turbulence models for the small-scale motion. The equations for this method are usually filtered over the grid size of the computational cells. All scales smaller than the resolution of the mesh are modelled and all scales larger than the cells are computed. This approach is several orders of magnitude more computationally expensive than a RANS simulation and is therefore not generally used in industrial flow simulations. It is most appropriate for free shear flows, as the length scales near the solid walls are usually very small and require small cells even for the LES method.
f) Detached Eddy Simulation (DES) model. A hybrid approach, which combines features of classical RANS formulations with elements of Large Eddy

Simulations (LES) methods. The concept has been termed Detached Eddy Simulation (DES) and is based on the idea of covering the boundary layer by a RANS model and switching the model to a LES mode in detached regions. Ideally, DES would predict the separation line from the underlying RANS model.

g) Direct Numerical Simulation. The time-dependent (3D) structure is resolved through a numerical solution of time-dependent Navier Stokes equations

The first two models invoke the concept proposed by Boussinesq (1877) - see [39] p.35. In this concept, turbulent stresses in the mean momentum equation are assumed to be proportional to the mean rate of strain where the constant is called "eddy" viscosity, is a special function of the mean velocity field. The physical idea behind this concept is explained in Tennekes and Lumley (1972) - see [39] p.35. The stresses in laminar flows arise as a result of random molecular motion, which is conceptually similar to turbulent fluctuations. The resemblance between these two motions is somewhat superficial. Nevertheless, it is assumed that the transfer of momentum and heat by molecular motion is similar to that induced by turbulent fluctuations. The concept of "eddy viscosity" is phenomenological and has no mathematical basis. It should be emphasized that molecular viscosity is a property of fluid and that turbulence is a property of flow. Therefore, the eddy viscosity is likely to be a function of the flow properties (e.g., mean velocity) and may also be a tensorial quantity in a three-dimensional flow -see [39] p. 35.

Brief descriptions on the turbulence models available in ANSYS CFX will be given with some information regarding their applications. It is beyond the scope of this work to discuss specialised models such as the LES and DES. If more details are

required the reader can seek more information in [40] ANSYS CFX - Solver Theory Guide, Turbulence and Wall Function Theory or - [39] p.34-42.

ANSYS CFX provides the following choices of turbulence models:

a) Laminar Model
b) Zero Equation model
c) One-Equation Models - Spalart-Allmaras model
d) Two-Equation Models.
    - $k-\varepsilon$ models
        - Standard $k-\varepsilon$ model
        - RNG - Renormalization-group $k-\varepsilon$ model
        - EARSM - Realizable $k-\varepsilon$ model
    - $k-\omega$ models
        - Standard $k-\omega$ model
        - Shear-stress transport (SST) $k-\omega$ model
e) Reynolds stress model (RSM)
f) Large Eddy Simulation (LES) model
g) Detached Eddy Simulation (DES) model

Choosing a Turbulence Model for CFD

It is an unfortunate that no single turbulence model is universally accepted as being superior for all classes of problems. The choice of turbulence model will depend on considerations such as the physics included in the flow, the established practice for a specific class of problem, the level of accuracy required, the available computational resources, and the amount of time available for the simulation. To make the most appropriate choice of model for an application, it is needed to understand the capabilities and limitations of the various options [40] ANSYS CFX - Solver Theory Guide, Turbulence and Wall Function Theory

The purpose of this section is to give an overview of the models used and the issues related to choose the turbulence models as provided in ANSYS CFX manual. If more information is needed [39] p. (34-42) can be used as reference for more detailed descriptions on turbulence models and [40] ANSYS CFX manual describes all the mathematical models used by CFD tool ANSYS CFX.

The computational effort and cost in terms of CPU time and memory of the individual models is very important factor. As computer memory and speed continue to increase, utilization of the models such as LES, DES and Direct Numerical Simulation (DNS) models will become more common. However it is impossible to state which model is best for a specific application. All the possible turbulence model capabilities and limitations need to be considered. Some general guidelines are presented in [40] ANSYS CFX manual to help choosing an appropriate turbulence model for the application modelled.

Zero Equation Models

A constant turbulent eddy viscosity is calculated for the entire flow domain from the mean velocity and a geometric length scale by using an empirical formula. Because no additional transport equations are solved, these models are referred to as ‘zero equation' models.

One Equation Models

Algebraic eddy viscosity models are based on the mixing length concept – see [39] p.35. In algebraic eddy viscosity models, an algebraic expression for the mixing length, 1, is provided for closure where 1 is termed the mixing length and it represents the local large-scale motion in a turbulent flow. Several groups have developed algebraic eddy viscosity models. One of the most widely used models for the

engineering calculation of boundary layers is the Spalart-Allmaras Model. This model is a vorticity based production model. It solves a modelled transport equation for the kinematic eddy viscosity. In this one-equation model, it is not necessary to calculate a length scale related to the local shear layer thickness. This model was designed specifically for aerospace applications involving wall-bounded flows and has been shown to give good results for boundary layers subjected to adverse pressure gradients. In its original form, the Spalart-Allmaras model is a low Reynolds number model, requiring the viscous affected region of the boundary layer to be properly resolved. In ANSYS CFX the model has been modified so it uses wall functions, where the mesh is too coarse for the resolution of boundary layer. Furthermore, the near-wall gradients of the transported variable in the model are much smaller than the gradients of the transported variables in the $k-\varepsilon$ or $k-\omega$ models. This might make the model less sensitive to numerical error when non-layered meshes are used near walls. On a cautionary note, however, the Spalart-Allmaras model is still relatively new, and no claim is made regarding its suitability to all types of complex engineering flows. For instance, it cannot be relied on to predict the decay of homogeneous, isotropic turbulence. But it is given from the software manufacturer an approximation formula to calculate Turbulence Intensity which is:

$$Turb.Int = \frac{\bar{v}}{\left(\sqrt{\frac{3}{2}} \cdot v_{average} \cdot l\right)} \qquad 94$$

where

$l = 0.007 \cdot d_{hydraulic}$ and $\bar{v}$ = Modified Turbulence Viscosity

Furthermore, one-equation models are often criticized for their inability to rapidly accommodate changes in length scale, such as might be necessary when the flow

changes abruptly from a wall-bounded to a free shear flow. What follows is the two equation models supported by CFD tool ANSYS CFX.

Two-Equation Models - $k-\varepsilon$ and $k-\omega$ Models

In the algebraic eddy viscosity model, local equilibrium of the turbulence is assumed, and the eddy viscosity is assumed to be scalar (the same in all directions), mainly dependent on the mean velocity field. The characteristics of the turbulence field itself never enter into this formulation. The two-equation model is intended to rectify this situation by relating the eddy viscosity to some gross local properties of turbulence. These are intended for application in situations where turbulence is not in equilibrium. The most widely used model in this category is the Jones - Launder $k-\varepsilon$ model (1972, 1973) - see [39] p.37. The Wilcox - Rubesin $k-\omega$ model (1980), which has been specifically developed for boundary layer flows with large pressure gradients, is also used by many investigators. There is considerable similarity (in physical concept) between these two models, so briefly both is presented

The two-equation model employs equations governing dynamics or gross properties of turbulence, and it relates them to eddy viscosity. This concept introduces additional physics (local values of k and ε) in the formulation and has been very successful in computing two-dimensional flows.

An equation for the kinetic energy of turbulence (k) can be derived from the Navier Stokes equation for velocity where an additional transport equation for dissipation (ε) is needed to close these equations. This is derived from the Navier Stokes equation through manipulation - see [39] p. 38-39.

The Standard $k-\varepsilon$ Model

The simplest "complete models" of turbulence are two-equation models which the solution of two separate transport equations allows the turbulent velocity and length scales to be independently determined. The standard $k-\varepsilon$ model in ANSYS CFX falls within this class of turbulence model and has become the workhorse of practical engineering flow calculations in the time since it was proposed by Jones - Launder $k-\varepsilon$ model (1972, 1973) - see [39] p. 37. Robustness, economy, and reasonable accuracy for a wide range of turbulent flows explain its popularity in industrial flow and heat transfer simulations. It is a semi-empirical model, and the derivation of the model equations relies on phenomenological considerations and empiricism. As the strengths and weaknesses of the standard $k-\varepsilon$ model have become known, improvements have been made to the model to improve its performance. Two of these variants are available in ANSYS CFX, the RNG $k-\varepsilon$ model and the realizable $k-\varepsilon$ model

The RNG $k-\varepsilon$ Model

The RNG $k-\varepsilon$ model was derived using a rigorous statistical technique (called renormalization group theory). It is similar in form to the standard $k-\varepsilon$ model, but includes the following refinements:

- The RNG model has an additional term in its dissipation (ε) equation that significantly improves the accuracy for rapidly strained flows.
- The effect of swirl on turbulence is included in the RNG model, enhancing accuracy for swirling flows.
- The RNG theory provides an analytical formula for turbulent Prandtl numbers, while the standard $k-\varepsilon$ model uses user-specified, constant values.

- While the standard $k-\varepsilon$ model is a high-Reynolds-number model, the RNG theory provides an analytically-derived differential formula for effective viscosity that accounts for low-Reynolds-number effects. Effective use of this feature does, however, depend on an appropriate treatment of the near-wall region. These features make the RNG $k-\varepsilon$ model more accurate and reliable for a wider class of flows than the standard $k-\varepsilon$ model.

Explicit Algebraic Reynolds Stress Model (EARSM)

The Explicit Algebraic Reynolds Stress Model (EARSM) or as it is also known as the Realizable $k-\varepsilon$ model is a relatively recent development and differs from the standard $k-\varepsilon$ model in two important ways:

- The realizable $k-\varepsilon$ model contains a new formulation for the turbulent viscosity.
- A new transport equation for the dissipation rate (ε), has been derived from an exact equation for the transport of the mean-square vorticity fluctuation.

The term "realizable" means that the model satisfies certain mathematical constraints on the Reynolds stresses, consistent with the physics of turbulent flows. Neither the standard $k-\varepsilon$ model nor the RNG $k-\varepsilon$ model is realizable. An immediate benefit of the realizable $k-\varepsilon$ model is that it more accurately predicts the spreading rate of both planar and round jets. It is also likely to provide superior performance for flows involving rotation, boundary layers under strong adverse pressure gradients, separation, and recirculation. Both the realizable and RNG $k-\varepsilon$ models have shown substantial improvements over the standard $k-\varepsilon$ model where the flow features include strong streamline curvature, vortices, and rotation. Since the model is still

relatively new, it is not clear in exactly which instances the realizable $k-\varepsilon$ model consistently outperforms the RNG model. However, initial studies have shown that the realizable model provides the best performance of all the $k-\varepsilon$ model versions for several validations of separated flows and flows with complex secondary flow features. One limitation of the realizable $k-\varepsilon$ model is that it produces non-physical turbulent viscosities in situations when the computational domain contains both rotating and stationary fluid zones (e.g., multiple reference frames, rotating sliding meshes). This is due to the fact that the realizable $k-\varepsilon$ model includes the effects of mean rotation in the definition of the turbulent viscosity. This extra rotation effect has been tested by the software manufacturer on single rotating reference frame systems and showed superior behaviour over the standard $k-\varepsilon$ model. However, due to the nature of this modification, its application to multiple reference frame systems should be taken with some caution. - see [40] for information about how to include or exclude this term from the model.

The Standard $k-\omega$ Model

The standard $k-\omega$ model in ANSYS CFX is based on the Wilcox $k-\omega$ model - see [37] p.37, which incorporates modifications for low-Reynolds-number effects, compressibility, and shear flow spreading. The Wilcox model predicts free shear flow spreading rates that are in close agreement with measurements for far wakes, mixing layers, and plane, round, and radial jets, and is thus applicable to wall-bounded flows and free shear flows.

$\omega = \frac{\varepsilon}{k}$ where (k) is Turbulent Kinetic Energy.

A variation of the standard $k-\omega$ model called the SST $k-\omega$ model is also available in ANSYS CFX, and is described next.

The Shear-Stress Transport (SST) $k-\omega$ Model

The Shear-Stress Transport (SST) $k-\omega$ model was developed by Menter - see [40] to effectively blend the robust and accurate formulation of the $k-\omega$ model in the near-wall region with the free-stream independence of the $k-\varepsilon$ model in the far field. To achieve this, the $k-\varepsilon$ model is converted into a $k-\omega$ formulation. The SST $k-\omega$ model is similar to the standard $k-\omega$ model, but includes the following refinements:

- The standard $k-\omega$ model and the transformed $k-\varepsilon$ model are both multiplied by a blending function and both models are added together. The blending function is designed to be one in the near-wall region, which activates the standard $k-\omega$ model, and zero away from the surface, which activates the transformed $k-\varepsilon$ model.
- The SST model incorporates a damped cross-diffusion derivative term in the (ω) equation.
- The definition of the turbulent viscosity is modified to account for the transport of the turbulent shear stress.
- The modelling constants are different. These features make the SST $k-\omega$ model more accurate and reliable for a wider class of flows (e.g., adverse pressure gradient flows, airfoils, transonic shock waves) than the standard $k-\omega$ model.

Reynolds Stresses Models (RSM)

In flows where the turbulent transport or non-equilibrium effects are important, the eddy-viscosity assumption is no longer valid and results of eddy-viscosity models might be inaccurate. Algebraic Reynolds stress (EARSM) models solve algebraic equations for the Reynolds stresses, whereas differential Reynolds Stress Models

solve differential transport equations for the individual components of the Reynolds stress tensor and the dissipation rate. These models do not use the eddy viscosity hypothesis, avoiding isotropic viscosity assumption of other models. The standard Reynolds Stress model in ANSYS CFX is based on the ε - equation where as ANSYS CFX provides two additional Reynolds Stress - ω models; the Omega Reynolds Stress and Baseline (BSL) Reynolds Stress models. The advantage of the ω -equation is that it allows for a more accurate near wall treatment with an automatic switch from a wall function to a low-Reynolds number formulation based on the grid spacing. Reynolds Stress or Second Moment Closure (SMC) models naturally include the effects of streamline curvature, sudden changes in the strain rate, secondary flows or buoyancy compared to turbulence models using the eddy-viscosity approximation. Hence RSM models are characterized by a higher degree of universality; the penalty for this flexibility is a high degree of complexity in the resulting mathematical system. The increased number of transport equations leads to reduced numerical robustness, requires increased computational effort and often prevents their usage in complex flows because they are tougher to converge due to close coupling of equations. Theoretically, Reynolds Stress models are more suited to complex flows, however, practice shows that Reynolds Stress models often prove inferior to two-equation models.

Turbulence model Summary

One transport equation models

Models such as Spalart-Allmaras are recommended for boundary layers subjected to adverse pressure gradients. Single transport equation models solve directly for a modified turbulent viscosity. Designed specifically for aerospace applications involving wall-bounded flows on a fine, near-wall mesh. ANSYS CFX's

implementation allows use of coarser meshes and there is option to include strain rate in k production term improving the predictions of vortical flow. They are computationally economical for large meshes however performs poorly for 3D flows, free shear flows, flows with strong separation. Suitable for mildly complex (quasi-2D) external/internal flows and boundary layer flows under pressure gradient (e.g. airfoils, wings, airplane fuselage, missiles, ship hulls).

Two transport equation models

Standard $k-\varepsilon$ is the baseline two transport equation model solving for k and ε. Coefficients are empirically derived; valid for fully turbulent flows only. Options to account for viscous heating, buoyancy, and compressibility are shared with other k-ε models. It is Robust and widely used despite the known limitations of the model. Performs poorly for complex flows involving severe ∇p, separation, strong streamline curvature. Suitable for initial iterations, initial screening of alternative designs, and parametric studies.

Standard $k-\omega$ is a two transport equation model solving for k and ω, the specific dissipation rate (ε/k) based on Wilcox (1998). The model demonstrates superior performance for wall bounded and low-Re flows. Shows potential for predicting flow transition. Options are available to account for transitional, free shear, and compressible flows. Superior performance for wall-bounded boundary layer, free shear, and low Re flows. Suitable for complex boundary layer flows under adverse pressure gradient and separation (external aerodynamics and turbo-machinery). Can be used for transitional flows (though tends to predict early transition). Separation is typically predicted to be excessive and early.

SST $k-\omega$ A variant of the standard $k-\omega$ model. Combines the original Wilcox model (1988) for use near walls and standard $k-\varepsilon$ model away from walls using a

blending function. Also limits turbulent viscosity to guarantee that $\tau_t \sim k$. The transition and shearing options borrowed from the standard $k-\omega$. No compressibility option. Similar benefits as the standard $k-\omega$. Dependency on wall distance makes this less suitable for free shear flows.

7.6.7 Near-Wall Treatment for Turbulent Flows

Overview for mesh near wall treatment

Turbulent flows are significantly affected by the presence of the wall boundary. Firstly there is the no-slip condition that must be satisfied in the flows and the boundary layer has the greatest gradients in velocity so it is the main generation place of turbulence. Very close to the wall, viscous damping reduces the tangential velocity fluctuations, while kinematic blocking reduces the normal fluctuations. Toward the outer part of the near-wall region, the large velocity gradients produce high turbulent kinetic energy. It is then obvious that the flow near the walls plays a key role for turbulent flows as the formed boundary layer will affect heat transfer. It is a very sensitive point of turbulence modelling because of its significant influence on the turbulence field even in the inside of the domain far away from the walls.

Usually the thickness of the boundary layer is small comparing to the other sizes in the computational domain, so a fine grid for the direct resolution of the boundary layer would be needed. The computational limitations restricts the maximum number of cells one can use in a model and it is hard to create a very fine grid on every single wall surface boundaries. There are preprocessors that support the boundary layer closure by providing an automated Boundary Layer mesh. This approach is called “near-wall modelling” and can be used for relative simple geometries as pipes, ducts, and other simple shaped bodies. Automatic boundary layer mesh creating will work well for certain cases but is difficult to use in complex geometries where defeaturing

and user input is required. In cases, where the direct resolution of the boundary layer is not possible, special near-wall treatments are needed to give good boundary conditions for the turbulence models. These treatments must be applied very carefully because the whole flow field depends on the generated turbulence in the boundary layer. Using special treatments at the walls, it reduces the number of necessary cells near the wall. In this case the theory of the boundary layers [41] is used to preserve the basic physical background without the complete solution for turbulence parameters in the boundary layer directly. The validity of wall functions depends on the distance normal from the wall. Figure 87 represents the applicable wall functions in the function of the dimensionless wall distance y^+, which is, in the present picture in logarithmic scale. y^+ is used to compare the location of the first node P away from a wall.

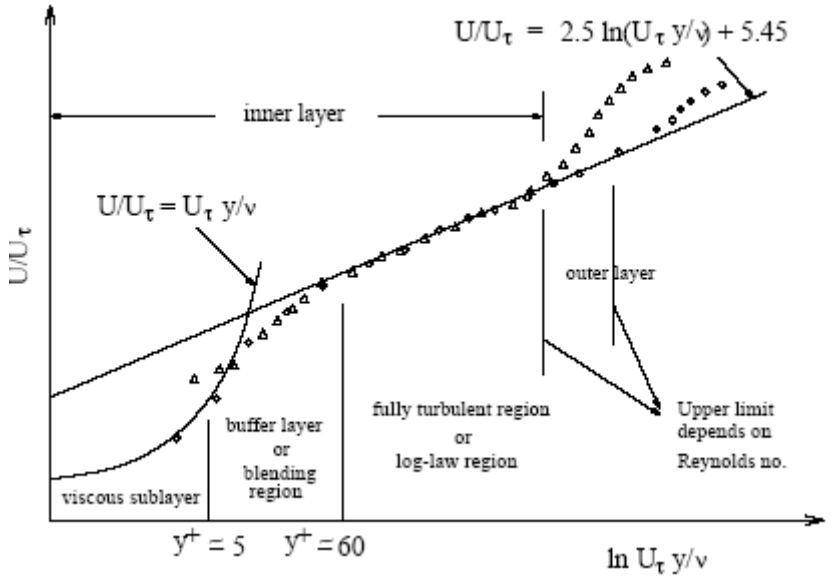

Figure 87: Subdivisions of the Near-Wall region [42]

The wall functions have only been developed for planar surfaces and are not valid for faces with high curvature. They are also not valid for flows with separations on the walls and with reattachments. The wall functions are exact solutions of the boundary layer equations that are the simplified versions of the Navier-Stokes equations [41]

and these solutions do not involve separation. Separation phenomenon can only be handled by solving the Navier-Stokes equations in the whole boundary layer from the outer region until the wall. There are modifications of the wall functions in ANSYS CFX and these wall functions are sensitized to the adverse pressure gradients and give better turbulence properties in case of separation and reattachment. From the integral parameters of the flow, it can be estimated, how large the error is, when the turbulence parameters are computed by using wall functions as boundary conditions. Wall functions are definitely not applicable in simulations where the processes inside the boundary layer are highly important, and the choice on modelling turbulence by RANS, RMS or higher complexity methods leys upon the modeller. Obviously higher turbulence complexity will have a direct effect on increasing the accuracy of the model however this will also increase run times and in most of these cases a "good" boundary layer mesh is often difficult to create.

Standard Wall Functions

In earlier versions of ANSYS CFX, the wall functions were based on the proposal of Launder and Spalding [42] and for equilibrium boundary layers these functions were the same as in [41]:

$$U^* = \frac{1}{\kappa}\ln(Ey^*) \qquad 95$$

where

$$U^* = \frac{U_P C_\mu^{1/4} k_P^{1/2}}{\tau_w/\rho} \qquad 96$$

$$y^* = \frac{\rho C_\mu^{1/4} k_P^{1/2} y_P}{\mu} \qquad 97$$

and:

κ	=	von Karman's constant (0.419)
E	=	empirical constant (9.81)
U_P	=	mean velocity of the fluid at node P
k_P	=	turbulent kinetic energy at node P
y_P	=	distance from node P to the wall
μ	=	dynamic viscosity of the fluid

For the standard wall functions the logarithmic law is valid, if y*>30~60. The log-law is applied when y*>11,06. For the case of y*<11,06, the laminar stress-strain relationship is used:

$$U^* = y^* \qquad 98$$

In the previous equations the quantities U* and y* were used rather than U^+ and y^+ as it can be seen in [41]. In equilibrium boundary layers, where the flow is governed by only wall shear stress (such as the case of flat plate) the previously indicated quantities are one the same. However in the case of adverse pressure gradients a different indication needs to be introduced for handling the non-equilibrium wall functions. One of the major drawbacks of the wall-function approach is that the predictions depend on the location of the point nearest to the wall and are sensitive to the near-wall meshing; refining the mesh does not necessarily give a unique solution of increasing accuracy.

Scalable Wall Functions

The problem of inconsistencies in the wall-function, in the case of fine meshes, can be overcome with the use of the Scalable Wall Function formulation. It can be applied on arbitrarily fine meshes and allows the user to perform a consistent mesh refinement independent of the Reynolds number of the application. The basic idea behind the scalable wall-function approach is to limit the y* value used in the logarithmic

formulation by a lower value of. 11.06 which is the intersection between the logarithmic and the linear near wall profile. The computed y* value is therefore not allowed to fall below this limit. Therefore, all mesh points are outside the viscous sublayer and all fine mesh inconsistencies are avoided. While the wall-functions presented above allow for a consistent mesh refinement, they are based on physical assumptions which are problematic, especially in flows at low Reynolds numbers. The $k-\omega$ model of Wilcox has the advantage that an analytical expression is known for ω in the viscous sublayer, which can be exploited to achieve this goal. To overcome this problem a formulation was devised which automatically switch from wall-functions to a low-*Re* near wall formulation as the mesh is more refined. the use The automatic near-wall treatment to take advantage of the additional effects in the viscous sublayer is incorporated into many models including the SST $k-\omega$ model [40] ANSYS CFX manual.

7.7 CFD – limitations & Application

7.7.1 Problems and Limitations of CFD Tools

Computational modelling provides engineers the opportunity to get detailed information about an investigated situations. Also wind tunnels provide high amount of information for design but in both, CFD and wind tunnels measurements errors can be found. The probes used for measurement and also the evaluation processes have inherent errors and these errors are already highly analyzed and most of them can be corrected through the evaluation process. In CFD simulations a new type of error has arise, that is called Numerical Error and depends mainly on the discretization method and the mesh that is used. This sort of error is a typical property of the numerical solution of differential equations and is due to the finite discretization of the

infinitesimal differences. Improving the CFD codes that are based on the continuum theory can be achieved with the increase of computer abilities towards the infinity.

7.7.2 CFD in the Present- Industrial Applications

Still nowadays the continuum based theory is in use for a wide range of applications. Almost all of the CFD codes commercially use Finite Volume method for the solution for Reynolds Averaged Navier Stokes (RANS) equations simultaneously with the equation of continuity. Therefore the effects of turbulence must be modelled as mentioned in previous section. There is no general purpose turbulence model in the commercial CFD packages yet, and all of the turbulence models are problem oriented. For industrial use in most cases the present turbulence models are well applicable and the software systems are being developed directly for industry.

There are a lot of organisations that create multipurpose software for modelling problems in Fluid Dynamics. In these software a wide range of models can be found for turbulence, discrete phase, combustion, cavitation, evaporation, boiling, solidification, melting etc. Using these software packages, engineers can involve plenty of phenomena into their calculations.

Software systems are becoming more and easy to use. Usually a software package consists of the following parts:

- Geometry definition and grid generation
- The preprocessor section is the process and specification of the boundary conditions.
- In the Solver section the governing equations of flow are solved.
- In the postprocessor section takes place the evaluation process, i.e. here can be seen the results of the calculations done by the solver.

The geometry structures used in the industry are sometimes very complex so some packages offer a CAD based software, with which 3D solid modelling of the geometry of the given problem can be done, that eases the specification of the problem.

Appendix 3

Flowchart of subroutine used to calculate a map of values for the temperature of trapped exhaust gas.

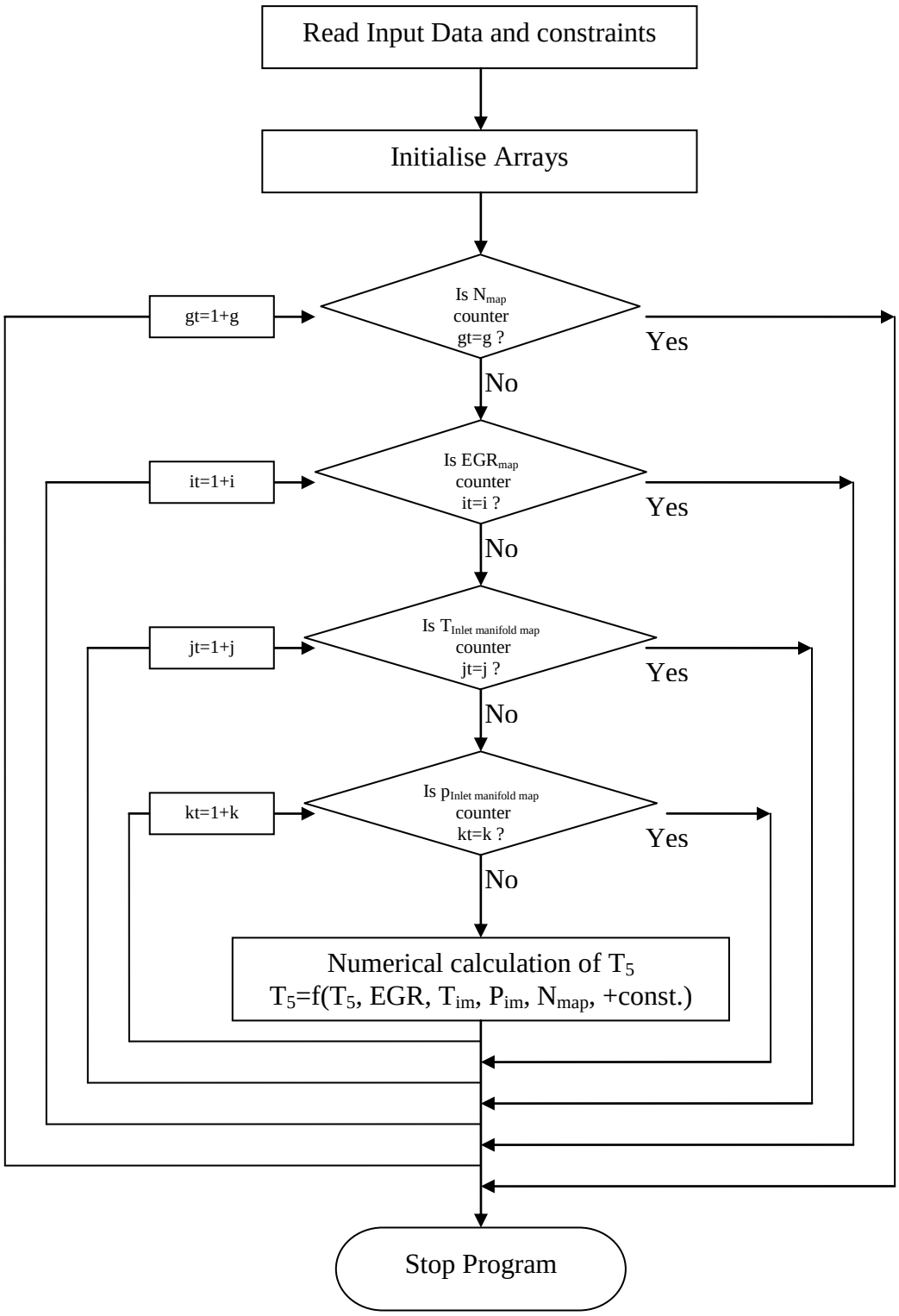

Appendix 4

T_5 Temperature calculation

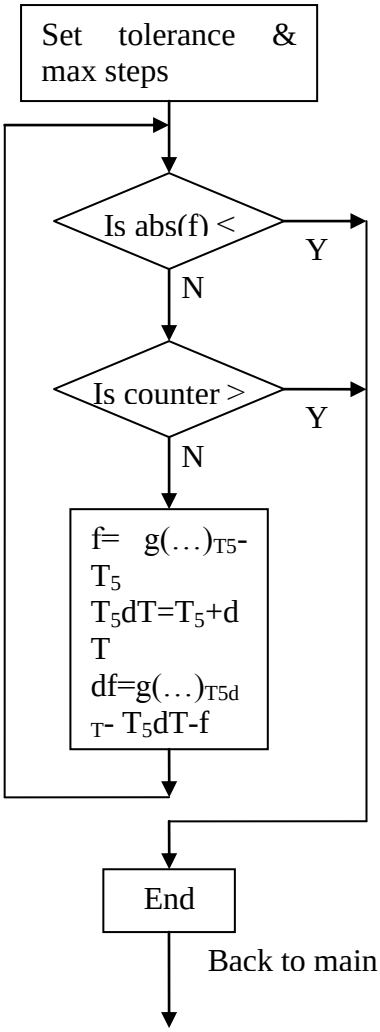

Where:

$$g(T5)= \left(\left(EGR * \left(T5 - Tim\right) + Tim\right) * \left(\frac{\left(EGR * \left(T5 - Tim\right) + Tim\right)}{A + B - C} \right)^{-\frac{1}{\gamma}} \right.$$

$$A= \left(\frac{rc^{-\gamma} * \left((1 - EGR) * ncomb * Qlhv * rc + AFR * cv\_air * \left(Kc * pim^{nc} * rc + \left(-Km * pim^{nm} * rc + rc^{\gamma}\right) * \left(EGR * T5 + Tim - EGR * Tim\right)\right)\right)}{AFR * cv\_air} \right)$$

$$B=Kd * \left(\frac{\left(pim * \left(1 - EGR\right) * ncomb * Qlhv * rc + AFR * cv\_air * \left(Kc * pim^{nc} * rc + \left(-Km * pim^{nm} * rc + rc^{\gamma}\right) * \left(EGR * T5 + Tim - EGR * Tim\right)\right)\right)}{\left(AFR * cv\_air * \left(EGR * \left(T5 - Tim\right) + Tim\right)\right)} \right)^{nd}$$

$$C= \frac{\left(Kn * \left(EGR * \left(T5 - Tim\right) + Tim\right)\right)}{pim * rc} *$$

$$\left(\frac{pim * \left((1 - EGR) * ncomb * Qlhv * rc + AFR * cv\_air * \left(Kc * pim^{nc} * rc + \left(-Km * pim^{nm} * rc + rc^{\gamma}\right) * \left(EGR * T5 + Tim - EGR * Tim\right)\right)\right)}{\left(AFR * cv\_air * \left(EGR * \left(T5 - Tim\right) + Tim\right)\right)} \right)^{(1 + nn)}$$

Appendix 5

Engine Cycle solution program

```
%***REMOVE THE GREEN FIELDS after I finish with Heat Transfer programming****
clear;          %these commands exist on the load_data file
clc;            %these commands exist on the load_data file

Tc=400; %engine cylinder wall temperature
N_map=[750:250:3250];
EGR_map=[0.25:0.05:0.55];
Tim_map=[300:200:700];
pim_map=[0.5e5:0.5e5:2.5e5];

dT=0.1;

gamma_air=1.4; %these values exist on the load_data file
cv_air=728;    %these values exist on the load_data file

L=138.1e-3;
%rc=11.2;
rc=10.8;
bore=89e-3;
stroke=79.5e-3;
a=stroke/2;
cyl=6;

%ncomb=0.9;
%ncomb=0.38;
EGR_ncomb_Map;

Qlhv=43.3e6;
AFR=14.66;

Acrown = pi*bore^2/4;
Apiston = Acrown^1.3;
Achamber = Acrown^1.4;

% REMINDER DO NOT MIX THESE VOLUMES WITH THE CONTROL VOLUMES IN THE SIMULINK MODEL
Vd=Acrown*stroke;
V_cyl_point_1=rc*Vd/(rc-1);
V_cyl_point_2=V_cyl_point_1/rc;
Vc=V_cyl_point_2;

gt=length(N_map);
it=length(EGR_map);
jt=length(Tim_map);
kt=length(pim_map);
%T5map=ones(size(N_map));
T5map=ones(gt,it,jt,kt);

for g=1:gt
    N=N_map(g);

    compression_expansion_parameters;

    % start to find the T5 zero for each i,j,k
    for k=1:kt
        for j=1:jt
            for i=1:it
            %EGR=EGR_map;
            %Tim=Tim_map;
            EGR=EGR_map(i);
            Tim=Tim_map(j);
            pim=pim_map(k);
            ncomb=ncomb_map(i,g);
            T5=1500;

            f = ( ((EGR .* ((T5 - Tim)) + Tim)) .* ((((EGR .* ((T5 - Tim)) +
Tim))./((((1./(AFR .* cv_air)) .* ((1./rc.^(gamma_air) .* (((1 - EGR) .* ncomb .* Qlhv
.* rc + AFR .* cv_air .* ((Kc .* pim.^nc .* rc + ((-Km .* pim.^nm .* rc +
rc.^gamma_air)) .* ((EGR .* T5 + Tim - EGR .* Tim)))))))) + Kd .* ((((pim .* (((1 -
EGR) .* ncomb .* Qlhv .* rc + AFR .* cv_air .* ((Kc .* pim.^nc .* rc + ((-Km .*
```

```
pim.^nm .* rc + rc.^gamma_air)) .* ((EGR .* T5 + Tim - EGR .* Tim))))))))./((AFR .*
cv_air .* ((EGR .* ((T5 - Tim)) + Tim)))))).^nd - ((1./(pim .* rc)) .*((Kn .* ((EGR .*
((T5 - Tim)) + Tim)) .* ((((pim .* (((1 - EGR) .* ncomb .* Qlhv .* rc + AFR .* cv_air
.* ((Kc .* pim.^nc .* rc + ((-Km .* pim.^nm .* rc + rc.^gamma_air)) .* ((EGR .* T5 +
Tim - EGR .* Tim)))))))) ./ ((AFR .* cv_air .* ((EGR .* ((T5 - Tim)) + Tim)))))).^(1 +
nn))))))))).^(-1 ./ gamma_air)) -T5;
            tol=0.005;
            counter=0;
            while (abs(f)>tol) && (counter<100) %loop to find the correct T5 for each
point of the map using my inputs
                T5dT=T5+dT;

                df = ( ( ((EGR .* ((T5 - Tim)) + Tim)) .* ((((EGR .* ((T5 - Tim)) +
Tim))./((((1./(AFR .* cv_air)) .* ((1./rc.^(gamma_air) .* (((1 - EGR) .* ncomb .* Qlhv
.* rc + AFR .* cv_air .* ((Kc .* pim.^nc .* rc + ((-Km .* pim.^nm .* rc +
rc.^gamma_air)) .* ((EGR .* T5 + Tim - EGR .* Tim)))))))) + Kd .* ((((pim .* (((1 -
EGR) .* ncomb .* Qlhv .* rc + AFR .* cv_air .* ((Kc .* pim.^nc .* rc + ((-Km .*
pim.^nm .* rc + rc.^gamma_air)) .* ((EGR .* T5 + Tim - EGR .* Tim)))))))).*((AFR .*
cv_air .* ((EGR .* ((T5 - Tim)) + Tim)))))).^nd - ((1./(pim .* rc)) .*((Kn .* ((EGR .*
((T5 - Tim)) + Tim)) .* ((((pim .* (((1 - EGR) .* ncomb .* Qlhv .* rc + AFR .* cv_air
.* ((Kc .* pim.^nc .* rc + ((-Km .* pim.^nm .* rc + rc.^gamma_air)) .* ((EGR .* T5 +
Tim - EGR .* Tim)))))))) ./ ((AFR .* cv_air .* ((EGR .* ((T5 - Tim)) + Tim)))))).^(1 +
nn))))))))).^(-1 ./ gamma_air)) -T5dT-f)./dT; %df(xo)
                K=f ./ df;      %f(xo)/df(xo)
                T5=T5-K;    %x1=x0-f(xo)/df(xo)
                counter=counter+1;
                f = ( ((EGR .* ((T5 - Tim)) + Tim)) .* ((((EGR .* ((T5 - Tim)) +
Tim))./((((1./(AFR .* cv_air)) .* ((1./rc.^(gamma_air) .* (((1 - EGR) .* ncomb .* Qlhv
.* rc + AFR .* cv_air .* ((Kc .* pim.^nc .* rc + ((-Km .* pim.^nm .* rc +
rc.^gamma_air)) .* ((EGR .* T5 + Tim - EGR .* Tim)))))))) + Kd .* ((((pim .* (((1 -
EGR) .* ncomb .* Qlhv .* rc + AFR .* cv_air .* ((Kc .* pim.^nc .* rc + ((-Km .*
pim.^nm .* rc + rc.^gamma_air)) .* ((EGR .* T5 + Tim - EGR .* Tim)))))))).*((AFR .*
cv_air .* ((EGR .* ((T5 - Tim)) + Tim)))))).^nd - ((1./(pim .* rc)) .*((Kn .* ((EGR .*
((T5 - Tim)) + Tim)) .* ((((pim .* (((1 - EGR) .* ncomb .* Qlhv .* rc + AFR .* cv_air
.* ((Kc .* pim.^nc .* rc + ((-Km .* pim.^nm .* rc + rc.^gamma_air)) .* ((EGR .* T5 +
Tim - EGR .* Tim)))))))) ./ ((AFR .* cv_air .* ((EGR .* ((T5 - Tim)) + Tim)))))).^(1 +
nn))))))))).^(-1 ./ gamma_air)) -T5;
            end

            T5map(g,i,j,k)=T5;

            end
        end
    end
end
```

Appendix 6

Heat transfer Calculation

```
clear;                    %these commands exist on the load_data file
clc;                      %these commands exist on the load_data file

R_air=287;                %these values exist on the load_data file
cp_air=1015;              %these values exist on the load_data file
cv_air=cp_air-R_air;      %these values exist on the load_data file
gamma_air=cp_air/cv_air; %these values exist on the load_data file
%p1=1e5;
%T1=490;

No=1000;
Tc=400; %engine cylinder wall temperature
dto=0.001;
t_mapo=[0.06:dto:0.09];
T3_map=[750:250:4000];
N_map=[500:500:3500];
p3_map=[1e6:1e6:10e6];

L=138.1e-3;
%rc=11.2;
rc=10.8;
bore=89e-3;
stroke=79.5e-3;
a=stroke/2;
cyl=6;

Acrown = pi*bore^2/4;
Apiston = Acrown^1.3;
Achamber = Acrown^1.4;

% REMINDER DO NOT MIX THESE VOLUMES WITH THE CONTROL VOLUMES IN THE SIMULINK MODEL
Vd=Acrown*stroke;
V1=rc*Vd/(rc-1);
V2=V1/rc;
Vc=V2;
V3=V2;
V4=V1;

Tge1=ones (size(t_mapo));
Tge2=ones (size(t_mapo));
Tge3=ones (size(t_mapo));
Tge4=ones (size(t_mapo));

pge1=ones (size(t_mapo));
pge2=ones (size(t_mapo));
pge3=ones (size(t_mapo));
pge4=ones (size(t_mapo));


ilm=length(T3_map);
jlm=length(p3_map);
klm=length(N_map);

Nplot=ones(ilm,jlm,klm);
p3plot=ones(ilm,jlm,klm);
T3plot=ones(ilm,jlm,klm);
V4plot=ones(ilm,jlm,klm);
V3plot=ones(ilm,jlm,klm);

Tgout1=ones(ilm,jlm,klm);
Tgout2=ones(ilm,jlm,klm);
Tgout3=ones(ilm,jlm,klm);
Tgout4=ones(ilm,jlm,klm);

pout1=ones(ilm,jlm,klm);
pout2=ones(ilm,jlm,klm);
pout3=ones(ilm,jlm,klm);
pout4=ones(ilm,jlm,klm);
```

```
for il=1:ilm
    T3=T3_map(il);

for jl=1:jlm
    p3=p3_map(jl);

for kl=1:klm
    N=N_map(kl);

    dt=dto*No/N;
    t_map=t_mapo*No/N;


    % start to find the f(x,y)
    m=p3.*V3/(R_air.*T3);
    omega = 2*pi*N/60;
    theta = omega.*t_map;
    s_t = a*cos(theta)+sqrt(L^2 - a^2*sin(theta).^2);
    u_t =( -a*omega.*sin(theta)-( a^2*omega*cos(theta).*sin(theta) ./ sqrt(L^2 -
a^2.*sin(theta).^2)));
    Awall_t = pi*bore.*(L + a - s_t);
    A_t = Apiston + Achamber + Awall_t;
    V_t = Vc + Acrown.*(L + a - s_t);
    dV_dt = -Acrown.*(u_t);
    dV2_dt = (a*Acrown*omega.*sin(theta).*(1+ a.*cos(theta)./sqrt(L^2 -
a^2.*sin(theta).^2) ));



    %IC for Euler 1 is for compression with heat transfer, 3 is adiabatic
    %the hc and df array is not needed to be created since its direcly calculated in
the loop

    Tge1(1)=T3;
    Tge2(1)=Tge1(1);
    Tge3(1)=Tge1(1);
    Tge4(1)=Tge1(1);


    %Woschni heat release constants
    C1=3.26;
    C2=2.28;    %C2=2.28 for compression, combustion & expansion phase C2=6.18 for
scaverging phase,
    C3=3.24e-3; %C3=0 for compression & scaverging phase, C3=3.24e-3 for direct
injection engines
    %n=1.34; reccomeded by Watson Janota Book
    n=1.43;

    %Honhenberg heat release constants
    K1=130;
    K2=1.4;

    %Modified Woschni heat release constants
    Z1=4; %scale
    ICH_t= Vc/Achamber + (L + a - s_t);

    % iterate
    im=length(t_map);
    for i=1:im-1
        %solve with Euler
        %Adiabatic compression
        hce1_t(i) = 0;
        dfe1(i)=( ( ( hce1_t(i) .* A_t(i) .* (Tc-Tge1(i))) -
(m*R_air.*Tge1(i).*dV_dt(i)./V_t(i) ) ) /(cv_air*m) );

        Tgen1=Tge1(i)+dfe1(i)*dt;
        pgen1=m*R_air.*Tgen1/V_t(i);
        Tge1(i+1)=Tgen1;
        pge1(i+1)=pgen1;

        %Woschni
        hce2_t(i) = (  C1.*bore^-0.2 .* ((m*R_air.*Tge2(i)./(( V_t(i)).*1e3)).^0.8) ./
Tge2(i).^0.545 .*(  C2.*abs(u_t(i)) + C3.*( (V_t(i).*T3./(p3*V3)) .* (
(m*R_air.*Tge2(i)./V_t(i)) - (p3.*(V3./V_t(i))^n) ) ) ).^0.8  );
        dfe2(i)=( ( ( hce2_t(i) .* A_t(i) .* (Tc-Tge2(i))) -
(m*R_air.*Tge2(i).*dV_dt(i)./V_t(i) ) ) /(cv_air*m) );
```

```
        Tgen2=Tge2(i)+dfe2(i)*dt;
        pgen2=m*R_air.*Tgen2/V_t(i);
        Tge2(i+1)=Tgen2;
        pge2(i+1)=pgen2;

        %Honhenberg (from Watson book)
        hce3_t(i) = (K1.* (m*R_air/1e5.*Tge3(i)./V_t(i)).^0.8./Vd^0.06 ./ Tge3(i).^0.4
.*(abs(u_t(i))+K2).^0.8);
        dfe3(i)=( ( ( hce3_t(i) .* A_t(i) .* (Tc-Tge3(i))) -
(m*R_air.*Tge3(i).*dV_dt(i)./V_t(i) ) ) /(cv_air*m) );

        Tgen3=Tge3(i)+dfe3(i)*dt;
        pgen3=m*R_air.*Tgen3/V_t(i);
        Tge3(i+1)=Tgen3;
        pge3(i+1)=pgen3;

        %Modified Woschni
        hce4_t(i) = (  Z1.*ICH_t(i)^-0.2 .* ((m*R_air.*Tge4(i)./((
V_t(i)).*1e3)).^0.8) ./ Tge4(i).^0.73 .*(  C2.*abs(u_t(i)) + C3./6.*(
(V_t(i).*T3./(p3*V3)) .* ( (m*R_air.*Tge4(i)./V_t(i)) - (p3.*(V3./V_t(i))^n) ) )
).^0.8  );
        dfe4(i)=( ( ( hce4_t(i) .* A_t(i) .* (Tc-Tge4(i))) -
(m*R_air.*Tge4(i).*dV_dt(i)./V_t(i) ) ) /(cv_air*m) );

        Tgen4=Tge4(i)+dfe4(i)*dt;
        pgen4=m*R_air.*Tgen4/V_t(i);
        Tge4(i+1)=Tgen4;
        pge4(i+1)=pgen4;


    end


    Nplot(il,jl,kl)=N;
    p3plot(il,jl,kl)=p3;
    T3plot(il,jl,kl)=T3;
    V3plot(il,jl,kl)=V_t(1);
    V4plot(il,jl,kl)=V_t(im);

    Tgout1(il,jl,kl)=Tge1(im);
    Tgout2(il,jl,kl)=Tge2(im);
    Tgout3(il,jl,kl)=Tge3(im);
    Tgout4(il,jl,kl)=Tge4(im);

    pout1(il,jl,kl)=pge1(im);
    pout2(il,jl,kl)=pge2(im);
    pout3(il,jl,kl)=pge3(im);
    pout4(il,jl,kl)=pge4(im);


end
end
end

rp1=pout1./p3plot;
%rp1=p3plot./pout1;
npol1=log(rp1)./-log(rc);

rp2=pout2./p3plot;
%rp2=p3plot./pout2;
npol2=log(rp2)./-log(rc);

rp3=pout3./p3plot;
%rp3=p3plot./pout3;
npol3=log(rp3)./-log(rc);

rp4=pout4./p3plot;
%rp3=p3plot./pout3;
npol1=log(rp1)./-log(rc);
```

Appendix 7

Set of experimental data used for Ricardo Wave model fitting.

Number	Engine speed [rpm]	λ	IVO [CAdeg atdc]	EVC [CAdeg btdc]	5% MFB [CAdeg]	50% MFB [CAdeg]	95% MFB [CAdeg]	Pressure Rise [dp/dCA]	NMEP [bar]
1	1000	1.0	65.0	93.8	364.8	376.8	384.3	2.72	4.49
2	1000	1.0	65.0	86.0	364.4	372.0	377.8	6.57	4.89
3	1000	1.0	65.0	84.0	363.9	370.6	377.1	7.28	4.96
4	1000	1.0	75.1	78.8	364.2	371.3	376.7	7.26	5.07
5	1000	1.2	65.0	80.8	363.3	370.9	376.8	3.04	4.47
6	1000	1.2	65.0	85.9	363.8	374.8	382.4	1.64	4.12
7	1500	1.0	65.0	97.4	362.0	372.3	379.6	2.35	4.22
8	1500	1.0	65.0	95.9	362.0	371.3	378.6	2.91	4.34
9	1500	1.0	65.0	86.1	361.1	367.7	373.8	6.43	4.69
10	1500	1.0	65.0	83.8	360.8	367.5	372.7	6.92	4.76
11	1500	1.0	85.1	76.0	363.6	372.3	378.8	6.15	4.93
12	1500	1.3	65.0	81.0	362.1	372.9	381.4	2.32	4.19
13	1500	1.3	65.0	86.1	361.5	372.6	380.4	1.85	3.89
14	1500	1.3	65.0	76.1	361.2	373.8	381.2	2.75	4.41
15	1500	1.3	65.0	71.0	363.1	376.4	384.5	2.47	4.70
16	2000	1.0	85.1	90.9	359.6	368.6	379.6	2.99	3.61
17	2000	1.0	85.1	86.0	359.6	367.5	378.8	3.99	3.89
18	2000	1.0	85.1	81.0	359.4	367.6	378.3	4.95	4.12
19	2000	1.0	85.1	76.1	360.0	368.7	378.1	5.45	4.34
20	2000	1.0	95.1	65.8	364.3	375.6	385.9	5.76	4.77
21	2000	1.3	65.0	83.2	360.1	369.4	378.5	2.72	3.68
22	2000	1.3	65.0	81.0	360.6	369.5	379.3	2.91	3.82
23	2000	1.3	65.0	76.1	361.5	370.7	380.2	3.29	4.10
24	2000	1.3	65.0	70.9	362.4	372.7	381.3	3.18	4.36
25	2500	1.0	65.0	95.8	359.7	368.6	378.8	2.27	3.29
26	2500	1.0	65.0	90.7	359.8	367.3	376.7	3.07	3.55
27	2500	1.0	65.0	80.9	359.4	365.1	374.9	5.33	3.99
28	2500	1.0	75.1	92.6	358.5	368.7	380.2	2.21	3.31
29	2500	1.0	75.0	76.0	358.6	365.7	373.9	5.66	4.12
30	2500	1.0	75.0	71.0	359.5	367.1	372.4	6.39	4.41
31	2500	1.0	85.2	80.9	358.5	367.3	377.8	3.47	3.79
32	2500	1.0	85.1	66.0	362.2	373.6	391.1	5.72	4.64
33	2500	1.2	57.8	75.9	360.5	368.5	375.3	3.28	3.97
34	2500	1.2	57.9	66.0	361.6	371.4	376.5	4.71	4.57
35	2500	1.2	65.0	76.1	360.6	368.4	376.8	3.28	3.98
36	2500	1.2	65.0	65.9	361.8	372.2	378.0	4.57	4.62
37	2500	1.2	75.0	76.8	360.6	368.9	378.4	2.76	3.87
38	2500	1.2	75.0	61.0	363.2	376.3	384.2	4.16	4.86
39	2900	1.0	65.0	96.0	360.2	368.1	377.9	2.05	3.56
40	2900	1.0	65.0	90.9	355.7	367.1	375.7	2.51	3.79
41	2900	1.0	58.4	95.9	359.8	368.3	377.8	1.86	3.30
42	2900	1.0	58.4	91.0	359.8	367.6	375.5	2.47	3.58
43	2900	1.0	58.2	86.2	360.0	367.2	374.8	3.26	3.81
44	2900	1.0	58.2	76.1	359.7	368.0	372.8	4.89	4.39
45	2900	1.0	65.2	95.9	360.0	368.6	378.6	1.73	3.37

Set of experimental and modeling data used for Ricardo Wave model validation.

Engine speed [rpm]	λ	IVO [CAdeg atdc]	EVC [CAdeg btdc]		5% MFB [CAdeg]	50% MFB [CAdeg]	95% MFB [CAdeg]	5% - 95% MFB [CAdeg]	Pressure Rise [dp/dCA]	NMEP [bar]
1000	1	65	94	experiment	364.8	376.8	384.3	19.5	2.72	4.49
				model	364.8	375.8	384.1	19.3	4.02	4.46
1500	1	65	98	experiment	362.0	372.3	379.6	17.6	2.35	4.22
				model	358.9	368.9	377.4	18.5	3.39	3.86
2000	1	85	93	experiment	359.4	369.1	380.8	21.4	2.65	3.51
				model	359.3	369.8	380.1	20.8	2.71	3.42
2500	1	75	96	experiment	358.8	370.0	384.1	25.3	1.78	3.11
				model	359.7	370.7	382.9	23.2	2.52	3.36
2900	1	58.5	96	experiment	359.8	368.3	377.8	18.0	1.86	3.30
				model	363.5	371.5	383.3	19.8	3.16	3.58
1000	1	65	91	experiment	364.5	374.9	381.3	16.7	4.17	4.65
				model	363.8	374.8	380.1	16.3	4.65	4.71
1500	1	65	91	experiment	361.0	368.9	376.3	15.3	4.88	4.52
				model	358.0	366.5	374.0	16.0	4.32	4.35
2000	1	85	86	experiment	359.6	367.5	378.8	19.2	3.99	3.89
				model	359.4	366.9	377.4	18.0	3.53	3.90
2500	1	75	92.5	experiment	358.5	368.7	380.2	21.7	2.21	3.31
				model	359.5	369.5	380.0	20.5	2.89	3.63
2900	1	58.5	91	experiment	359.8	367.6	375.5	15.7	2.47	3.58
				model	363.8	370.8	380.0	16.2	3.77	3.86
1000	1	65	86	experiment	364.4	372.0	377.8	13.4	6.57	4.89
				model	366.2	373.2	380.2	14.0	6.25	5.13
1500	1	65	86	experiment	361.1	367.7	373.8	12.7	6.43	4.69
				model	358.2	365.2	371.6	13.4	5.25	4.71
2000	1	85	81	experiment	359.4	367.6	378.3	18.9	4.95	4.12
				model	357.6	365.6	375.0	17.4	4.25	4.25
2500	1	75	86	experiment	359.5	365.5	376.5	17.0	3.32	3.59
				model	361.1	367.6	378.0	16.9	3.65	3.98
2900	1	58.5	86	experiment	360.0	367.2	374.8	14.8	3.26	3.81
				model	363.1	370.1	379.1	16.0	3.98	4.27
1000	1	65	84	experiment	363.9	370.6	377.1	13.2	7.28	4.96
				model	366.4	372.9	380.4	14.0	7.05	5.30
1500	1	65	84	experiment	360.8	367.5	372.7	12.0	6.92	4.76
				model	358.2	364.6	371.7	13.5	5.72	4.86
2000	1	85	73	experiment	360.5	369.0	376.0	15.5	5.97	4.48
				model	355.4	363.4	370.4	15.0	5.99	4.82
2500	1	75	71	experiment	359.5	367.1	372.4	12.8	6.39	4.41
				model	357.6	365.6	372.4	14.8	6.76	4.91
2900	1	58.5	71	experiment	361.0	369.1	373.2	12.2	5.87	4.67
				model	362.3	370.1	375.3	13.0	5.96	5.16

Appendix 8

Thermal Management Mathematical Model Layout

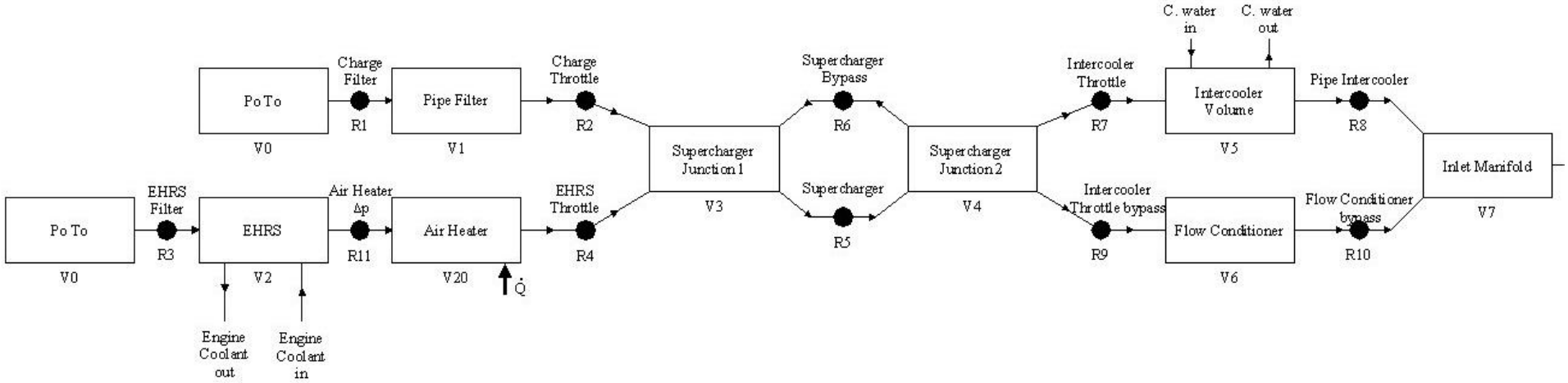

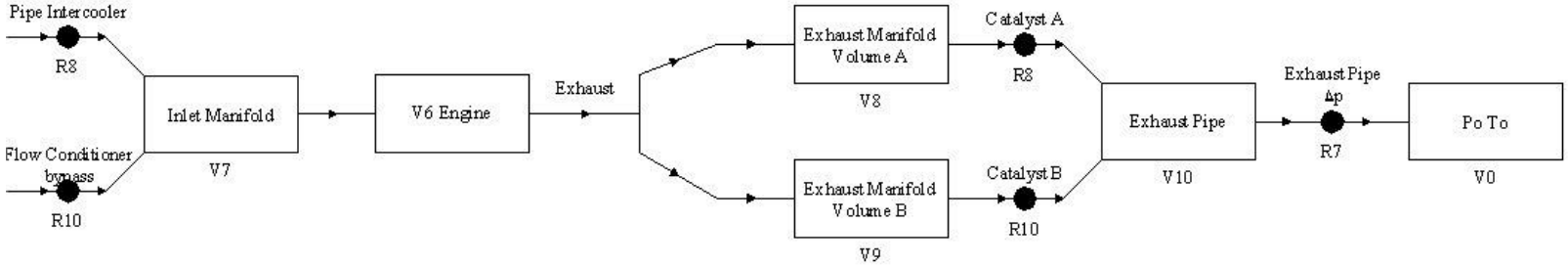
Pipe Intercooler
R8
Flow Conditioner bypass
R10
Inlet Manifold
V7
V6 Engine
Exhaust
Exhaust Manifold Volume A
V8
Exhaust Manifold Volume B
V9
Catalyst A
R8
Catalyst B
R10
Exhaust Pipe
V10
Exhaust Pipe Δp
R7
Po To
V0

Appendix 9

Restriction Model with backflow

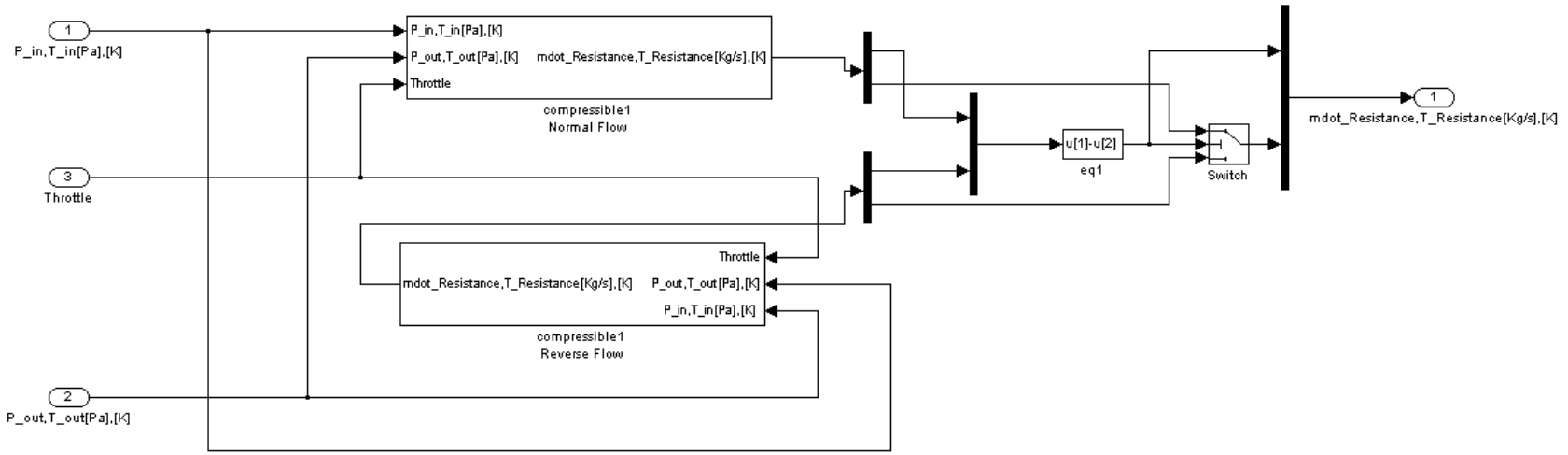

Appendix 10

Realtime Model Validation Case results

	230707_1000-HP-H_Lamda10_EOI350		230707_1000-HP-H_Lamda10_EOI350		270707_1500-HP-H_Lamda13_EOI350		250707_2500-HP-H_Lamda10_EOI350_BP01		190707_1500-HP-H_Lambda10_EOI350		270707_15-HP-H_Lamda13_EOI350	
	Model Fitting Case A		Validation Case A		Validation Case C		Validation Case B		Validation Case D		Validation Case E	
	Experiment Results	Model Results	Experiment Results	Model Results	Experiment Results	Model Results	Experiment Results	Model Results	Experiment Results	Model Results	Experiment Results	Model Results
Temperature Ambient Air [K]	320.568526	320.568526	323.811893	323.811893	319.596867	319.596867	323.811893	323.811893	326.444373	326.444373	320.655755	320.655755
Pressure Ambient Air [bar]	0.97946574	0.97946574	0.98603353	0.98603353	0.99494695	0.99494695	0.98603353	0.98603353	0.99513824	0.99513824	0.99111759	0.99111759
Speed [RPM]	1014.1409	1014.1409	2526.2417	2500	1519.1853	1519.1853	2526.2417	2500	1519.9741	1519.9741	1519.0174	1519.0174
Lambda	0.99335593	0.99335593	0.997749035	0.997749035	1.3037917	1.3037917	0.997749035	0.997749035	1.00021015	1.00021015	1.3021712	1.3021712
Charge Air throttle [deg]	2.87857143	2	2.92142853	2	2.85000003	2	2.92142853	2	2.14285716	2	2.85000003	2
Supercharger Bypass throttle [deg]	83.7020601	83	19.1592801	19.5	83.4027849	80	19.1592801	19.5	83.3801931	88	83.5349076	88
Intercooler throttle [deg]	2.66958189	2	2.41540227	2	2.41428321	2	2.41540227	2	2.45483064	2	2.54219796	2
Intercooler Bypass throttle [deg]	84.137679	88	83.7456642	88	83.8294245	88	83.7456642	88	83.747799	88	83.9573856	88
						0						
Normal Path mass flow [kg/s]	0.000390687	0.0001019	0.000554097	0.0002	0.000386922	0.00015	0.000554097	0.0002	0.000524125	0.00015	0.00015	0.00015
Heated Path mass flow [kg/s]	0.014633325	0.007	0.022258322	0.03189	0.0175	0.0175	0.022258322	0.03189	0.019611794	0.0175	0.0175	0.0175
EGR (calculated)	0.490634109	0.45	0.546082467	0.2823	0.4	0.4	0.546082467	0.2823	0.47937547	0.4	0.4	0.4
	[bar]	[bar]	[bar]	[bar]	[bar]	[bar]	[bar]	[bar]	[bar]	[bar]	[bar]	[bar]
nmep	4.6968335		4.55081075		3.840570417		4.55081075		5.14410225		3.789509017	
		4.398		4.854		3.784		4.854		4.937		3.784
	[bar]	[bar]	[bar]	[bar]	[bar]	[bar]	[bar]	[bar]	[bar]	[bar]	[bar]	[bar]
P. Post Filter	0.98057557	0.9795	0.98839813	0.9863	0.99562915	0.9949	0.98839813	0.9863	0.99934553	0.9951	0.9949	0.9949
P. Heat Exchanger in	0.95974456		0.96765246		0.97801317		0.96765246		0.97770676		0	
P. Heating Box in	0.9287973	0.9628	0.8821214	0.9161	0.91881335	0.9562	0.8821214	0.9161	0.91810212	0.9558	0.9562	0.9562
P. Heating Box out	0.92458195	0.9628	0.87748879	0.9153	0.91467934	0.9559	0.87748879	0.9153	0.91366768	0.9555	0.9559	0.9559
P. Supercharger out	0.94091449	0.9627	0.99551418	0.9199	0.92120186	0.9558	0.99551418	0.9199	0.94358902	0.9554	0.9558	0.9558
P. Intercooler	0.93741864	0.961	0.99835733	0.9197	0.92223958	0.9524	0.99835733	0.9197	0.93636518	0.9518	0.9524	0.9524
P. Mixing Box	0.93846779	0.9612	0.99825176	0.8986	0.92219734	0.9514	0.99825176	0.8986	0.9507	0.9507	0.9514	0.9514
P. Intake Runners	0.933826297		0.989266025		0.92038362		0.989266025		0.922249227		0	
P. Exhaust bank A	0.9689605	0.9998	0.97951582	1.023	0.98553123	1.016	0.97951582	1.023	1.0016111	1.018	1.016	1.016
P. Exhaust bank B	0.97496887	0.9998	0.98872068	1.023	0.99264691	1.016	0.98872068	1.023	0.99546804	1.018	1.016	1.016
P. Post Catalyst bank A	0.97960604	0.9996	0.97451146	1.022	0.99058084	1.016	0.97451146	1.022	0.98941468	1.016	1.016	1.016
P. Post Catalyst bank B	0.97480763	0.9996	0.96750779	1.022	0.9879639	1.016	0.96750779	1.022	0.98544246	1.016	1.016	1.016
	[K]	[K]	[K]	[K]	[K]	[K]	[K]	[K]	[K]	[K]	[K]	[K]
Temp. Heating box in	340.7223	331.5	339.941187	329.5	339.781366	327.8	339.941187	329.5	341.279433	333.3	340.571307	327.8
Temp. Heating box out	444.79966	414.2	394.00143	413	442.8196	411.8	394.00143	413	384.02369	411.8	441.57747	411.8
Temp. Mixed Air Manifold	425.47189	405.7	387.71163	404	423.25063	392.9	387.71163	404	376.54162	394.6	422.45167	392.9
Temp. Supercharger in	407.28164	405.8	403.94418	404	410.31005	392.9	403.94418	404	373.2631	394.6	410.12555	392.9
Temp. Supercharger out	400.65382	402.7	419.66695	407.7	406.24764	384.3	419.66695	407.7	374.44982	386.5	406.15252	384.3
Temp. Supercharger bypass	384.84003	402.7	402.41975	399.7	391.68702	399.7	402.41975	399.7	358.653682	386.5	390.88108	399.7
Temp. Intercooler	341.392339	320.5	342.502518	360.6	340.122073	318.4	342.502518	360.6	335.620355	326.9	338.418067	318.4
Temp. Intercooler Bypass throttle	381.83682	401	401.36133	399.7	388.56941	382.7	401.36133	399.7	357.429307	385	387.57111	382.7
Temp. Intercooler water in	324.452449	324	324.595859	324	324.137339	324	324.595859	324	324.318466	324	324.326264	324
Temp. Intercooler water out	325.093545		325.273099		325.581888		325.273099		325.205581		325.550009	
Temp. Mixing Box	364.409268	403.6	380.04579	396	367.41212	378	380.04579	396	346.162833	380.8	366.050626	378
Temp. Intake Runners (average)	362.2621727		378.28922		363.9601287		378.28922		350.0119313		362.8581975	
Temp. Engine Exhaust Valves		919.8		836.7		807		836.7		897		807
Temp. Exhaust Runners (average)	637.1954267		659.3542583		620.1703083		659.3542583		678.148695		620.412675	
Temp. Exhaust bank A		918.1		696		571		696		681		571
Temp. Exhaust bank B		918.1		696		571		696		681		571
Temp. Post Catalyst bank A	620.52809	917	657.69227	667	613.01974	523	657.69227	667	652.37623	637	621.46976	550
Temp. Post Catalyst bank B	639.13064	917	654.10148	667	599.52809	523	654.10148	667	670.57258	637	612.59443	550